

R-7138

GPO PRICE \$ \_\_\_\_\_

CFSTI PRICE(S) \$ \_\_\_\_\_

Hard copy (HC) 300

Microfiche (MF) .65

ff 653 July 65

# THERMODYNAMIC IMPROVEMENTS IN LIQUID HYDROGEN TURBOPUMPS (INTERIM REPORT)

**N68-19048**

FACILITY FORM 602	_____ (ACCESSION NUMBER)	_____ (THRU)
	<u>327</u> (PAGES)	_____ (CODE)
	<u>C1-93540</u> (NASA CR OR TMX OR AD NUMBER)	<u>28</u> (CATEGORY)



THERMODYNAMIC IMPROVEMENTS IN  
LIQUID HYDROGEN TURBOPUMPS

Contract No. NAS 8-20324

Interim Report

July 1967

13

Prepared For

National Aeronautics and Space Administration  
Propulsion and Vehicle Engineering Division  
George C. Marshall Space Flight Center  
Huntsville, Alabama

Prepared By

Advanced Projects & Turbomachinery Departments  
Large Engines  
Rocketdyne  
A Division of North American Rockwell Corporation  
Canoga Park, California

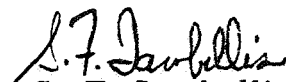


G. S. Wong  
Principal Engineer  
Supervisor, Advanced Turbomachinery



W. R. Wagner  
Supervisor, Heat Transfer

Approved:



S. F. Iacobellis  
Director  
Advanced Projects  
Large Engines



## FOREWORD

Rocketdyne, a Division of North American Rockwell Corporation, has prepared this interim report which documents the work performed in fulfillment of the program, "Thermodynamic Improvements in Liquid Hydrogen Turbopumps," during the period from 17 June 1966 to 17 June 1967. This program is sponsored by the National Aeronautics and Space Administration under Contract No. NAS8-20324. The work was performed by the Advanced Turbomachinery Unit of the Turbomachinery Department and by the Heat Transfer Unit of Advanced Projects Department. The program was administered by Mr. J. Suddreth of NASA Headquarters and by Messrs. T. W. Winstead, J. Vaniman, L. Gross and R. R. Fisher of Propulsion and Vehicle Engineering, NASA Marshall Space Flight Center. Mr. R. R. Fisher, as technical Project Manager, provided overall technical direction for the study.

## ABSTRACT

Analytical and experimental results are presented of an investigation to develop engineering criteria to analyze and improve liquid hydrogen turbopumps for rocket engine applications from the standpoint of alleviating the constraints of extensive pump thermal preconditioning and a narrow starting region envelope.

## ACKNOWLEDGMENT

This acknowledges contributions by D. G. Hodgdon and R. M. Vahedi of the Heat Transfer Unit and W. R. Bissell, F. C. Catterfeld, R. K. Hoshide, and W. M. McLaurin of the Advanced Turbomachinery Unit. Acknowledgment is also given to L. Manson of the Research Department for her contribution of the experimental hydrogen cooldown tests, to Systems Evaluation Unit of Advanced Projects, and to Systems Dynamics Unit of Design and Development.



Task IV: Study of Existing LH <sub>2</sub> Pumps . . . . .	229
Pump Characterization . . . . .	229
Effect of Engine Thrust Size on Pump Chillover . . . . .	233
Orbital Preconditioning of J-2 Turbopump . . . . .	246
Mark-15 LH <sub>2</sub> Turbopump Heat Soakback Analysis . . . . .	255
Mark-15 LH <sub>2</sub> Turbopump Chillover Analysis . . . . .	258
Mark 29 Turbopump . . . . .	263
350K LH <sub>2</sub> Turbopump Heat Soakback Study . . . . .	263
350K LH <sub>2</sub> Turbopump Chillover Analysis . . . . .	267
350K LH <sub>2</sub> Turbopump Ground Prechill Study . . . . .	272
M-1 Pump Chillover Study . . . . .	282
Slow-Chill Requirements of Existing Pumps . . . . .	282
Pump Vapor Tolerance . . . . .	288
Nomenclature . . . . .	291
References . . . . .	297

Appendix A

Distribution List for Interim Report NAS8-20324

Thermal Improvements in Liquid Hydrogen Turbopump . . . . .	A-1
---	-----

## ILLUSTRATIONS

1. Program Itemization . . . . .	7
2. Typical Pool Boiling Heat Flux . . . . .	16
3. LH <sub>2</sub> Nucleate and Transition Boiling Range (Ref. 6) . . . . .	17
4. Film Boiling Liquid Hydrogen . . . . .	18
5. Heat Transfer Data, Liquid Hydrogen . . . . .	20
6. Illustration of Boundary Layer Growth and Critical Regions of Pump Impellers . . . . .	21
7. Correlation of Liquid Hydrogen Straight-Tube Data with Rocketdyne Equation . . . . .	24
8. Local Heat Transfer Results for Helium and Hydrogen Gas . . . . .	25
9. Coolant Outlet Temperature vs Passage Geometry . . . . .	27
10. Hydrogen Stagnation Density-Acoustic Velocity Product at Pump Inlet Conditions . . . . .	28
11. $\rho^*/\rho_0$ vs $\gamma$ at Choked Condition . . . . .	29
12. $\Delta P$ to Velocity Head Conversion for Hydrogen Liquid Saturation Line Density . . . . .	30
13. Hydrogen Vapor Pressure vs Temperature . . . . .	32
14. Effect of Engine Starting Characteristics on Pump Performance . . . . .	34
15. LH <sub>2</sub> Turbopump Inertia Limited Start Times . . . . .	35
16. Typical Hydrogen Pump Start Transients for an LO <sub>2</sub> /LH <sub>2</sub> Engine . . . . .	36
17. Mark 15-F Turbopump Starting Test . . . . .	40
18. 30,000 lbf Engine Start Transient With Chill . . . . .	43
19. Typical Lunar Mission Profile . . . . .	45
20. Predicted Turbopump Temperatures in Orbit . . . . .	47
21. Single Surface Material Equilibrium Temperature in Earth Space . . . . .	48
22. Solar Heat Flux . . . . .	49

23.	Mars Powered Flyby (1973 Time Period)	51
24.	Rotor Conduction Distance vs Thrust Level	55
25.	Orbit Time to Conduction Time Comparison, 200 Mile Earth Orbit, Radiation and Feed line Conduction Neglected	57
26.	Radiation Function vs Initial to Sink (or Equilibrium) Temperature	60
27.	Approximate Pump Weight vs Thrust Level	64
28.	Approximate Turbine Weight vs Thrust Level	65
29.	Turbine Radiation Time to Pump Heat Conduction Time Ratio	67
30.	Vapor Volume Fraction and Density of Two-Phase Hydrogen	69
31.	Acoustic Velocity in Two-Phase Hydrogen at 36.8 R (14.7 psia)	72
32.	Acoustic Velocity in Two-Phase Hydrogen at 45.0 R, 48.0 psia	73
33.	Hydrogen Vapor Fraction Relationships	75
34.	Liquid and Vapor Properties for Constant-Quality Analysis	78
35.	Temperature vs Enthalpy Along Hydrogen Saturation Line	80
36.	Liquid Density vs Vapor Pressure Along Hydrogen Saturation Line	81
37.	Vapor Density vs Vapor Pressure Along Hydrogen Saturation Line	82
38.	Vapor Pressure vs Temperature Along Hydrogen Saturation Line	83
39.	Schematic of Inducer Geometry	86
40.	Effect of the Geometry of a Constant RMS Diameter Inducer on the Discharge Static Pressure When Pumping Two-Phase Hydrogen	87
41.	Effect of the Geometry of a Constant RMS Diameter Inducer on the Discharge Static Pressure When Pumping Two-Phase Hydrogen	88
42.	Effect of the Geometry of a Constant RMS Diameter Inducer on the Discharge Static Pressure When Pumping Two-Phase Hydrogen	89
43.	Effect of the Geometry of a Constant RMS Diameter Inducer on the Discharge Static Pressure When Pumping Two-Phase Hydrogen	90

44.	Effect of the Geometry of a Constant RMS Diameter Inducer on the Discharge Static Pressure When Pumping Two-Phase Hydrogen . . . . .	91
45.	Effect of the Geometry of a Constant RMS Diameter Inducer on the Discharge Static Pressure When Pumping Two-Phase Hydrogen . . . . .	92
46.	Effect of the Geometry of a Constant RMS Diameter Inducer on the Discharge Static Pressure When Pumping Two-Phase Hydrogen . . . . .	95
47.	Effect of the Geometry of a Constant RMS Diameter Inducer on the Discharge Static Pressure When Pumping Two-Phase Hydrogen . . . . .	96
48.	Experimental Inducer A . . . . .	101
49.	Experimental Inducer B . . . . .	101
50.	Experimental Inducer C . . . . .	102
51.	Model Mark-15 Fuel Inducer . . . . .	102
52.	Performance Summary . . . . .	105
53.	Candidate Pump Material Strength to Density Variation With Temperature . . . . .	109
54.	Critical Biot Number vs Fourier Number . . . . .	115
55.	Titanium Chillo down to Critical point ( $\alpha = 1/e$ ) . . . . .	126
56.	347 CRES Time to Chillo down ( $\alpha = 1/e$ ) . . . . .	127
57.	Copper Time to Chillo down ( $\alpha = 1/e$ ) . . . . .	128
58.	Kel-F Time to Chillo down ( $\alpha = 1/e$ ) . . . . .	129
59.	Wall Surface Chillo down vs Time . . . . .	132
60.	Wall Surface Chillo down vs Time . . . . .	133
61.	Wall Surface Chillo down vs Time . . . . .	134
62.	Material Chillo down to -420 F: Computer Solution . . . . .	135
63.	Wall Surface Chillo down vs Time . . . . .	136
64.	Surface Temperature of Teflon Coating vs Time . . . . .	137
65.	Surface Temperature of Teflon Coating vs Time . . . . .	138
66.	Surface Temperature of Teflon Coating vs Time . . . . .	139
67.	Surface Temperature of Teflon Coating vs Time . . . . .	140

68.	Surface Temperature of Teflon Coating vs Time . . . . .	141
69.	Teflon Coating Surface Temperature vs Heat Transfer Coefficient . . . . .	143
70.	Typical Section of a Coolant Passage Wall Chilled on One Side with a Cryogenic Fluid . . . . .	144
71.	Wall Temperature Variation With L/D and Fourier Number for a Hydrogen-Cooled Passage . . . . .	146
72.	Bulk Temperature Variation with L/D and Fourier Number for a Hydrogen-Cooled Passage . . . . .	147
73.	Wall Temperature Variation With L/D and Fourier Number for a Hydrogen-Cooled Passage . . . . .	149
74.	Wall Temperature Variation With L/D and Fourier Number for a Hydrogen-Cooled Passage . . . . .	150
75.	Wall Temperature Variation With L/D and Fourier Number for a Hydrogen-Cooled Passage . . . . .	151
76.	Wall Temperature Variation With L/D and Fourier Number for a Hydrogen-Cooled Passage . . . . .	152
77.	Wall Temperature Variation With L/D and Fourier Number for a Hydrogen-Cooled Passage . . . . .	154
78.	Wall Temperature vs Coating Thickness for Various L/D Values . . . . .	155
79.	Wall Temperature Variation With L/D and Fourier Number for a Hydrogen-Cooled Passage . . . . .	156
80.	Bulk Temperature Variation With L/D and Fourier Number for a Hydrogen-Cooled Passage . . . . .	157
81.	Thermocouple Location and Identification . . . . .	160
82.	Main Test Section . . . . .	161
83.	Vacuum Chamber Installation of Test Section . . . . .	162
84.	Cooldown of Metals in Liquid Hydrogen Flow Test Apparatus . .	163
85.	Flow Schematic . . . . .	164
86.	Cooldown of a Stainless-Steel Tube in Hydrogen Flow . . .	166
87.	Cooldown of a CRES 321 Tube in Hydrogen Flow . . . . .	168

88.	Cooldown of a K-monel (29-percent Cu) Tube in Hydrogen Flow . . . . .	168
89.	Cooldown of a Tens-50 Aluminum Tube in Hydrogen Flow . . . . .	169
90.	Cooldown of a Titanium (5-percent Al, 2.5- percent Sn) Tube in Hydrogen Flow . . . . .	170
91.	Cooldown of an OFHC Copper Tube in Hydrogen Flow . . . . .	171
92.	Nondimensional Time Parameter vs Insulation Temperature-Radiation Control Case . . . . .	178
93.	Time vs Pump Temperature-Insulation Control Case . . . . .	179
94.	Pump Temperature vs Insulation Temperature . . . . .	180
95.	$\delta$ (Insulation Thickness) for LH <sub>2</sub> Pumps vs $\psi$ (Time) . . . . .	182
96.	Insulation Thickness vs Mission Time for LH <sub>2</sub> Pump (Mark 15-F) . . . . .	185
97.	Heat Transferred by Turbine Shaft to Heat Radiated From Turbine Surface . . . . .	186
98.	Maximum Turbine Shaft Heat Dissipation vs Turbine Temperature . . . . .	188
99.	Turbine Shaft Heat Conduction vs Distance - Radiation Neglected . . . . .	189
100.	Heat Transferred by Downstream Ducting Compared to Heat Radiated From Turbine Surface . . . . .	191
101.	Turbine to Pump Isolation Distance vs Temperature . . . . .	192
102.	Sketch of Pump, Shaft and Turbine for Derivation of Eq. 1 . . . . .	196
103.	Time vs Pump Temperature, Insulation Control Case . . . . .	198
104.	Hydrogen Coolant Flow to Pump Weight vs Stanton--L/D Parameter at ( $\alpha= 1/e$ ) . . . . .	205
105.	Coolant Outlet Temperature vs Passage Geometry . . . . .	208
106.	Line Cooldown Test Data . . . . .	210
106a.	Effect of Turbine Cooling on LH <sub>2</sub> Turbopump Performance. . . . .	214
106b.	Effect of Turbine Cooling on LH <sub>2</sub> Turbopump Performance. . . . .	215

107.	Schematic of a Hydrogen-Cooled Turbine . . . . .	218
108.	Cooling of Critical Turbopump Components: Inlet Housing, Volute, and Turbine Exhaust Manifold . . . . .	219
109.	Thermal Barrier for Turbopumps . . . . .	221
110.	Schematic of Vented Flow Surface Liner and Vane . . . . .	222
111.	Regeneratively Cooled Thermal Barrier and Ball Spline Details . . . . .	223
112.	Thermal Isolation of Cryogenic Pump and Hot Turbine . . . . .	225
113.	Photomicrograph (100X) of KX635 Coated Aluminum With Top Coat . . . . .	226
114.	Pump Mean Hydraulic Diameter vs Thrust Level . . . . .	234
115.	Pump Mean Reynolds Number vs Thrust Level . . . . .	235
116.	LH <sub>2</sub> Pump Average Biot Number vs Thrust Level . . . . .	236
117.	Average Fourier Number vs Thrust Level . . . . .	237
118.	Turbopump Stator Blade . . . . .	239
119.	Typical Rotor Tip Blade Surface Velocities . . . . .	240
120.	Axial Pump Blade Scaling: Reynolds Number and Stanton Number . . . . .	244
121.	Axial Pump Blade Scaling: Biot and Fourier Numbers . . . . .	245
122.	Orbital Flight AS-203 Code Schematic . . . . .	247
123.	Pump Temperature History for Saturn Orbital Flight AS203 . . . . .	248
124.	Turbine Temperature History for Saturn Orbital Flight AS203 . . . . .	249
125.	Orbital Flight AS-203, Engine J2019, Date 5 July 1966 . . . . .	251
126.	J-2 Turbine Cooldown Temperature vs Time . . . . .	252
127.	J-2 Turbine Cooldown Temperature vs Time . . . . .	253
128.	J-2 Turbopumps, Engine Test, Skin Temperatures at Sea Level Ambient, Average of 4 Tests . . . . .	254
129.	Mark-15 Liquid Hydrogen Turbopump Nodal Points for a Thermal Analyzer Network . . . . .	256
130.	Mark-15 Hydrogen Turbopump Average Internal Temperature Distribution During Soakback . . . . .	257

131.	Pump Chilloidown Temperature vs Time for Mark-15 LH <sub>2</sub> Turbopump . . . . .	260
132.	Pump Chilloidown Temperature vs Time for Mark-15 LH <sub>2</sub> Turbopump . . . . .	261
133.	Pump Chilloidown Temperature vs Time for Mark-15 LH <sub>2</sub> Turbopump . . . . .	262
134.	Mark-29 Single-Stage Liquid Hydrogen Turbopump Nodal Point Distribution . . . . .	264
135.	A 350K LH <sub>2</sub> Turbopump Nodal Point Description . . . . .	265
136.	A 350,000 lbf LH <sub>2</sub> Turbopump Average Internal Temperature Distribution During Heat Soakback . . . . .	266
137.	Pump Chilloidown Temperature vs Time For a 350,000 lbf Breadboard LH <sub>2</sub> Turbopump . . . . .	268
138.	Pump Chilloidown Temperature vs Time For a 350,000 lbf Breadboard LH <sub>2</sub> Turbopump . . . . .	269
139.	Pump Chilloidown Temperature vs Time for a 350,000 lbf Breadboard LH <sub>2</sub> Turbopump . . . . .	270
140.	A 350K LH <sub>2</sub> Turbopump Chilloidown vs Time . . . . .	274
141.	Prechill Coolant Passages of 350K LH <sub>2</sub> Pump . . . . .	275
142.	A 350,000 lbf LH <sub>2</sub> Pump, Prechill Coolant Parameters . . . . .	276
143.	A 350,000 lbf Prechill Coolant Parameters, Test 5.01 . . . . .	277
144.	Analytical Wall Temperature Variation for a 350,000 lbf LH <sub>2</sub> Pump Prechill Coolant Passage . . . . .	278
145.	Study of a 350,000 lbf LH <sub>2</sub> Pump Prechill . . . . .	280
146.	A 350K Pump Prechill Test Data . . . . .	281
147.	M-1 Pump Wall Chilloidown vs Time . . . . .	283
148.	Pump Minimum Flow Passage Area vs Thrust Level . . . . .	284
149.	LH <sub>2</sub> --Limiting Chilloidown Flow vs Tank Pressure . . . . .	285
150.	Comparison of Maximum Chill Flow Allowable vs Thrust Level . . . . .	286
151.	Limiting Chilloidown Time vs Percent Mainstage Flowrate . . . . .	287
152.	LH <sub>2</sub> Pump Start Chilloidown Temperature vs Allowable Vapor Fraction . . . . .	289

TABLES

1. Comparative Heat Transfer Regimes . . . . .	23
2. Time Sequence of Events for a LO <sub>2</sub> /LH <sub>2</sub> Engine . . . . .	37
3. Comparison of Turbopump Starting Times . . . . .	39
4. Apollo Mission Profile . . . . .	46
5. Mars Powered Flyby Mission Profile . . . . .	52
6. Volume to Surface Areas for Various Simple Geometric Shapes Approximating Pump and Line Surfaces . . . . .	62
7. Summary of Turbopump Weights and Surface Areas . . . . .	63
8. Experimental Test Results, Inducer A ( $\phi_t = 0.153$ ) . . . . .	99
9. Experimental Test Results, Inducer A ( $\phi_t = 0.168$ ) . . . . .	99
10. Experimental Test Results, Inducer B ( $\phi_t = 0.0955$ ) . . . . .	100
11. Experimental Test Results, Inducer B ( $\phi_t = 0.116$ ) . . . . .	100
12. Experimental Test Results, Model MK-15 Fuel Inducer ( $\phi_t = 0.0935$ ) . . . . .	104
13. Comparison of Thermal Shock Rating Parameters for Candidate Pump Materials . . . . .	111
14. Relative Time for Chillover ( $N_{Bi} \ll 1, N_{Fo} \gg 1.0$ ) . . . . .	116
15. Chillover Thermal Factor for Moderate Film Coefficient. . . . .	118
16. Relative Chill Penetration for Film Coefficient ( $N_{Bi} \rightarrow \infty$ ) . . . . .	119
17. Relative Comparison of Material Chillover Characteristics . . . . .	120
18. Comparison of Kel-F and Teflon Heat Transfer Effectiveness. . . . .	122
19. Properties of Candidate Internal Coating Materials for LH <sub>2</sub> Turbopumps . . . . .	123
20. Limiting Critical Time ( $\alpha = 1/e$ ) Dependence Upon Material, Pressure and Temperature Parameters . . . . .	125

21.	Summary of Test Conditions, January 1967 Test Series . . . .	159
22.	Typical Tube Chillover Parameters for LH <sub>2</sub> Tests . . . .	173
23.	Comparative Evaluation of Thermal Conductivity and Density for External Insulations . . . . .	183
24.	Comparison of Isolated Turbopump Equilibrium Temperatures . .	194
25.	M-1 Pump Chillover Flow Requirements . . . . .	206
26.	Liquid Hydrogen Pumps . . . . .	230
26A.	Liquid Oxygen Pumps . . . . .	231
27.	Pump Characteristics . . . . .	232
28.	Comparative J-2 LH <sub>2</sub> Feed System Flow Areas . . . . .	290

## INTRODUCTION

Advanced cryogenic oxygen/hydrogen rocket engines for present and future mission applications must incorporate rapid start capability free of complex start and preconditioning sequences. To achieve this goal, the turbopump, as well as other related engine components, will require development of designs which allow rapid conditioning or chilling to cryogenic temperatures or which allow ingestion of vapor without serious loss in performance. Factors influencing rapid chilldown are numerous and include vehicle mission, space environment, engine design, and the basic structural configuration and hydrodynamic design of the turbopump.

The problem of chilldown of the liquid hydrogen pump arises as a result of the extremely low temperature to which the pump must be reduced before the pump can develop the required pressure and flow for an engine start. If the pump were insufficiently chilled, large vapor formation would result at subcritical pressures and large density changes would occur at supercritical pressures. Because of the inability of the pump to develop the required pressure with vapor, and the large vapor resistance downstream of the pump, the pump will stall, cavitate or surge and will prevent rapid engine start. An outline of the approach taken in the study program just completed to develop thermal design criteria for liquid hydrogen turbopumps is described below and is delineated into four task study areas.

For all applicable missions where single altitude start and restartable vehicles are involved, the primary problem to be considered is the degree of pump chilldown and conditioning required. Upon development of design and environmental criteria under Task I (Pump Thermal Design) and Task III (Preconditioning and Thermal Protection), alternative pump design approaches are established and a basis for design of an optimum pump is obtained. During Task I and Task II (Materials) both the severity of the heat transfer

problem (in terms of vapor time-rate generation), and the pump vapor swallowing capability are explored. This analysis provides the criteria for establishing start time required by various pump configurations associated with different start sequences and permits the effect of turbine drive cycles to be evaluated. Strength and chilldown capabilities of materials, including both metal and nonmetal coatings, are compared under Task II. Task III develops alternative and "system" solutions for alleviation of the pump chilldown problem either through preconditioning by hydrogen bleed through the pump before start or through external thermal insulation for environmental protection.

With the definition of the severity of the problem combined with development of the approach-solutions, either as redesign or system solutions, a critical examination of existing and proposed LH<sub>2</sub> turbopump designs is made during Task IV (Study of Existing LH<sub>2</sub> Pumps). Both a gross examination on the basis of average thermal scaling factors and detailed thermal network computer simulation are completed on several turbopumps. Where existing experimental data on chilldown are available, they are compared with analytical results.

The study of thermodynamic improvements for LH<sub>2</sub> turbopumps provides results that can be used for evaluating the chilldown problem for a range of engine thrust and chamber pressure. Specific improvements can be directed toward the following existing and advanced liquid hydrogen turbopumps:

J-2, J-2X, and J-2S	NASA
Advanced Engine Design Study, AEA	NASA
Advanced Engine Design Study, AEB	NASA
RL-10	NASA
M-1 Engine	NASA
Breadboard 5500-psi LH <sub>2</sub> Pump	NASA
Advanced Development Program (ADP) Engines	Air Force

During Task IV of the study, detailed analysis of several of these pumps is provided. Since several current engine programs have provided some experimental and analytical study data, the results from these programs were also applied.

## SUMMARY

The analytical study effort reported in the content of this volume is directed toward development of criteria for examination of the thermal problems associated with a liquid hydrogen turbopump. Delineation of the separate study areas associated with the pump and turbine and the respective aspects of start, shutdown, coast and restart were accomplished during this study. By necessity, due to the numerous facets of the overall undertaking, the approach used was to develop basic criteria and to provide supporting analysis which can be applied to a specific turbopump design. Development of general nondimensional parameter and rating groups was made wherever possible and thrust scaling approaches with proportionalities were provided. The thrust base assumed is representative of H<sub>2</sub>/O<sub>2</sub> fueled engine systems and application to nuclear and H<sub>2</sub>/O<sub>2</sub> propelled engine systems can be as a consequence obtained by a simple flowrate conversion.

Wherever possible, application of specific existing experimental data is made to compare with analytical values and trends. Moreover, a wide range of literature was surveyed to support the indicated representative experimental cases outlined in this report.

The complexity of the turbopump when analyzed by closed form heat transfer and fluid dynamic analysis approaches results in the use of two specific techniques. These were the employment of numerous simplifying assumptions for the closed form analysis cases and geometrical discretizing approaches for computer solutions. In the latter, the wide variety of geometrical sections inherent in a turbopump design, coupled with computer case time limitations, resulted in a less than ideal flow network for some analysis circumstances.

A summary of results for four definitive tasks is shown below. The tasks outlined in the summary and report include: Task I. - Pump Thermal Design;

Task II.— Materials; Task III.— Pump Preconditioning and Thermal Protection; and Task IV.— Analysis of Existing Turbopumps. A capsule view of programs undertaken is shown in Fig. 1.

#### TASK I. PUMP THERMAL DESIGN

Task I of this study developed the critical relationships for heat transfer coefficients, limiting flow and temperature relationships, critical time factors involved in engine start and application, and an evaluation of the two-phase flow pumping problem.

Analysis of the wide range of hydrogen temperature and pressure conditions led to the review of the relationships for all modes of convective and boiling heat transfer. Selection of appropriate equations indicative of boiling and/or forced convection was based on currently available literature. In the circumstance of subcritical-pressure  $\text{LH}_2$  film boiling with forced convection, further examination must be made due to apparent film coefficient sensitivity to wall temperature.

Limiting hydrogen flow mass velocity conditions for chilldown or at pump start were shown to be based on a choked vapor limitation or a liquid to kinetic energy conversion. As a result, enlargement of areas throughout the critical flow components coupled with higher tank or initial local pressures was seen to be advantageous.

A study of engine system and vehicle time factors developed the relative importance of the soakback of turbine heat and compared the time for radiation of the turbine heat content to the environment. Large thrust turbines were shown to result in a longer radiation cooldown due to the smaller ratio of surface area to mass. Additionally, the greater length of the larger turbopump designs results in a longer period for turbine heat soakback to the pump inducer. Several earth orbit and lunar and Mars excursion mission

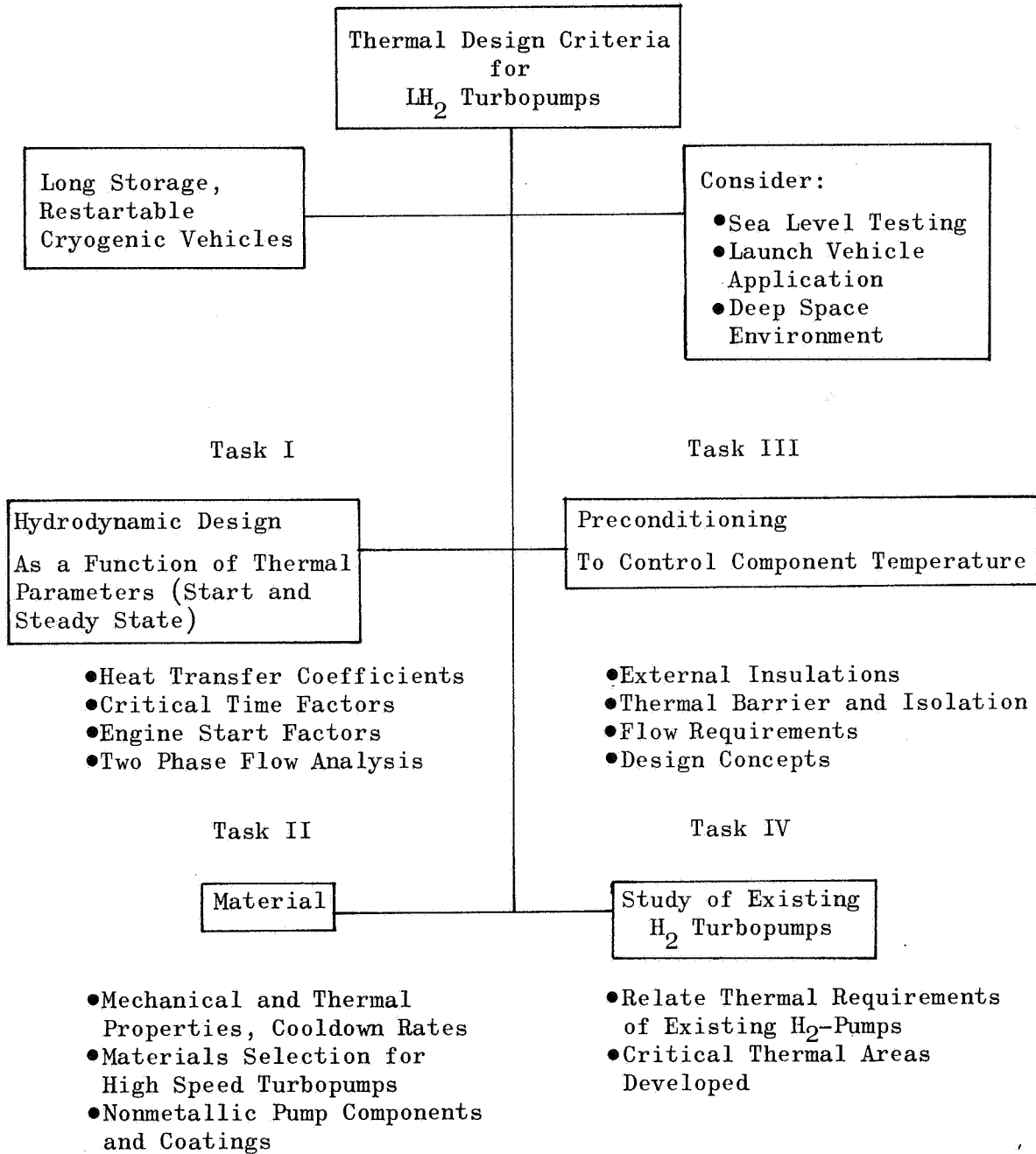


Figure 1. Program Itemization

time cases were postulated with large variances noted in the time elapsed between the successive restarts. As a result, it was seen that the general approaches for thermal conditioning employed must be suitable for a wide time range.

An investigation into two-phase flow ingestion in the pump was made. The case of vapor entering the pump impeller through the inlet line was examined. The two types of flow processes that were developed and analyzed were for hydrogen with constant quality and equilibrium flow. An analysis to determine the quantity of vapor generated on the pumping surfaces was initiated. Although shock wave effects were not considered in the analysis, they were studied along with their possible effects on pump performance. This study also provided background as to how a pump should be modified to handle two-phase flow, and provides mathematical descriptions of the two flow processes that form the boundaries of the actual flow process. The lack of adequate experimental data made it impossible to select the actual flow process.

## TASK II. MATERIAL

An evaluation of both metals and nonmetals was made during this study from the standpoints of strength to density ratio, thermal shock capability, and chilldown time behavior. The results of analytical study were favorably compared to experimental tests on tubes of various materials.

Consideration of both the strength and shock characteristics of the various materials was made. Titanium and Inconel were shown to be the highest strength to density ratio materials with titanium greater at low temperatures. The high strength character of the titanium would appear to allow a good thermal shock characteristic providing the thermal stresses remain below the yield value. A poor rating based on plastic behavior reflects a poor ductility at lower temperatures.

Consideration of partial and complete chilldown of the materials was made by both closed form analysis and numerous computer runs. For slow chilldowns where a minimum of coolant flow is to be used, a lightweight pump of high conductivity aluminum is the most suitable. For this circumstance the entire pump body was assumed to be reduced to the final cryogenic temperature. For more rapid chilldowns where the heat content is removed from the wetted surfaces only, the low conductivity of titanium or stainless-steel materials appears to offer advantage. For this latter case the pump heat content is bottled in the interior regions of the pump and allowed to bleed in at a tolerable rate during mainstage operation.

Computer examples were studied for both insulated coated surfaces and for surfaces of finite length. Flexible low conductivity insulating coatings such as Kel-F can be used for reducing the coating surface rapidly to the nucleate boiling temperature where heat transfer film coefficients are large. This results in a rapid metal chilldown. Alternatively, the coating can act as a thermal barrier to prevent the base metal heat from entering the coolant. Selection of these cases is provided by a stipulation of the coating Biot number.

Pumps with long passage length to hydraulic diameter ratios were shown to cause a considerable coolant bulk temperature rise which delays the cool-down of the downstream regions of the pump for fast chilldown circumstances. For maximum utilization of a slow chilldown flow with a minimized pump mass, the alternative of long pump passage length to hydraulic diameter ratios allows the greatest wetted surface area in relation to the pump weight.

Transient cooldown test data for K-monel, stainless steel, aluminum, titanium, and copper tube elements was reviewed. Confirmation of the time period required and heat transfer film coefficients correspondent to two-phase liquid hydrogen flow were verified.

### TASK III. PRECONDITIONING AND THERMAL PROTECTION

External insulation type and thickness requirements for storage of a chilled turbopump in space were established. Superinsulator application was shown to provide a substantial improvement over foam insulation matrices. Sensitivity of the multilayer insulation to penetrations and appendages and installation approaches is to be expected. Complete thermal isolation of the pump and turbine to eliminate heat soakback after shutdown appears to present a problem for both (1) pump mechanical isolation and (2) for pump insulation approaches. Designs for minimum contact between the pump and turbine and isolation by cooled turbine to pump supports were developed. Radiation of turbine heat content by improved surface area appeared attractive. Design concepts for a regeneratively cooled turbine to lower turbine heat content and to provide for a lower weight, less mass flow turbine indicated future promise.

Minimum chilldown flow solutions for complete pump chill were favorably compared with M-1 and 350K chilldown flow requirements. Coolant total weight flow for slow chill conditions was shown to be directly related to the pump weight-heat capacity.

### TASK IV. STUDY OF EXISTING LH<sub>2</sub> PUMPS

During Task IV study, application of the analysis derived for the preceding tasks was made to existing LH<sub>2</sub> turbopump designs. Examination was made of the thrust scaling of turbopumps on the chilldown time required. It was developed that the proportionately greater mass of large thrust pumps resulted in a longer time period required to provide a completely chilled pump.

Study of the J-2 MK-15 turbopump both in orbit and for ground conditions was accomplished. Good agreement of simplified analytical approaches for

orbital preconditioning and turbine cooldown with experimental Saturn AS203 flight data was noted. A detailed chilldown and heat soakback study of the MK-15 pump was also made. Critical areas within the pump for varying periods of soakback and prechill were analyzed. A similar analysis was performed on an LH<sub>2</sub> 350K pump to provide heat soakback and cooldown criteria. A favorable comparison of analysis with experimental test data for preconditioning was also shown.

For existing pump configuration limits, prechill flow tests for maximum flow utilization were studied. Allowable prechill flowrate percentages for low thermal conductivity titanium pumps were shown to be substantially below those for aluminum pumps. Higher pump inlet pressures and better pump geometrical characteristics were also explored.

## TASK I: PUMP THERMAL DESIGN

Task I study analysis was aimed at establishing guidelines for the subsequent task studies. It endeavored to provide the basic criteria for hydrogen heat transfer coefficients as a function of the hydrogen thermodynamic state and heat transfer rate intensity. Additionally, partial definition of the time periods involved in engine and pump startup, shutdown, orbiting, etc., to establish the time bounds necessary was developed. The effects of pump inducer and impeller geometry were comprehensively examined during Task I and the pumping ability for two-phase flow situations was determined.

### HEAT TRANSFER COEFFICIENTS

There are numerous possible heat transfer coefficient regimes that may occur during transient turbopump operation during startup until the relatively hot components reach thermal equilibrium with the hydrogen. The possible flow regimes and heat transfer conditions are listed below.

#### Boiling (Subcritical P and T)

##### Pool Boiling (Zero Velocity)

1. Nucleate
2. Transition
3. Film

##### Forced Convection with Boiling

1. Nucleate (local)
2. Transition (local)
3. Film (local)
4. Bulk Boiling: In order of increasing gas content -
  - a. Bubble flow (vapor bubbles in liquid stream)
  - b. Slug flow (alternating slugs of vapor and liquid)
  - c. Annular flow (vapor core, liquid annulus)
  - d. Mist flow (liquid droplets in gas stream)

## Forced Convection

### Boundary Layer Flow (Short Lengths)

### Fully Developed Channel Flow

During the course of turbopump startup periods, a series of sequential events occur at a given location in the pump which may be outlined as follows:

1. Large quantities of gas are generated, decreasing with time as the metal cools and hydrogen flow increases, which tend to retard the rise in hydrogen flowrate. During this phase of operation local film or transition boiling, and possible bulk boiling, are the more likely flow regimes.
2. As the metal surface continues to cool down to a value within 20 to 40 R above the saturation temperature, the heat flux will increase as the flow passes through the transition flow regime into nucleate boiling. If the hydrogen pressure or temperature has increased above the critical values, boiling will cease and only forced convection cooling will occur.
3. The final phase of the transient operation occurs when the forced-convection regime is encountered and ultimately cools the surface of the metal down to the hydrogen bulk temperature. The forced-convection regime may be reached by either passing through the boiling regimes, if the hydrogen pressure and temperature are below the critical point, or by virtue of a supercritical temperature or pressure condition. The film coefficient regime will vary at different locations in the pump since the hydrogen pressure and temperature rises and the component temperatures change as the flow progresses through the various components. In addition, the geometry presented to the flow changes from location to location in turbopumps. Thus, it is evident that the problem is a function of both time and geometry, and is extremely complex to treat practically.

## Pool Boiling

Pool boiling will occur in transient turbopump operation during the initial phase of startup if the hydrogen velocities are low and passage lengths are long. The three regimes of boiling, namely, nucleate, transition and film boiling, are shown in Fig. 2 at atmospheric pressure as an illustrative example. All three regimes are plotted in Fig. 3 for the bulk boiling case ( $T_B = T_{SAT}$ ), that is, without subcooling. The nucleate boiling regime is characterized by the formation of many isolated vapor bubbles, which maintain the wall temperature within about 20 R of the saturation temperature by an increase in boiling agitation when the heat flux is increased. The peak nucleate boiling heat flux marks the onset of transition to film boiling which results in the formation of a gaseous film at the surface of the wall. Once the maximum nucleate boiling heat flux is reached, the heat flux capability of the fluid is drastically reduced and the wall temperature is forced to increase to a very high value, well within the stable film boiling regime. Physically, nucleate boiling can accept a much larger heat flux, for a given temperature difference ( $T_W - T_B$ ), than the film boiling case because of the detrimental insulating nature of the gaseous film that occurs during film boiling. Figure 2 represents the simplest case for a boiling liquid since it is possible for the liquid bulk temperature to be at a value below the saturation temperature (subcooled), which results in local boiling only at the wall surface.

Figures 3 and 4 diagrammatically show the behavior of boiling hydrogen with subcooling. When a subcooled condition exists, the boiling is localized at the heated surface and the vapor collapses once it migrates into the bulk. It may be seen in Fig. 3 that the nucleate boiling regime extends over a very narrow range of subcooling, which indicates that the majority of turbopump operation will be in the film boiling regime at subcritical pressures. The effect of elevating pressure, and consequently the saturation temperature, is quite marked although the film boiling heat flux capacity is relatively low.

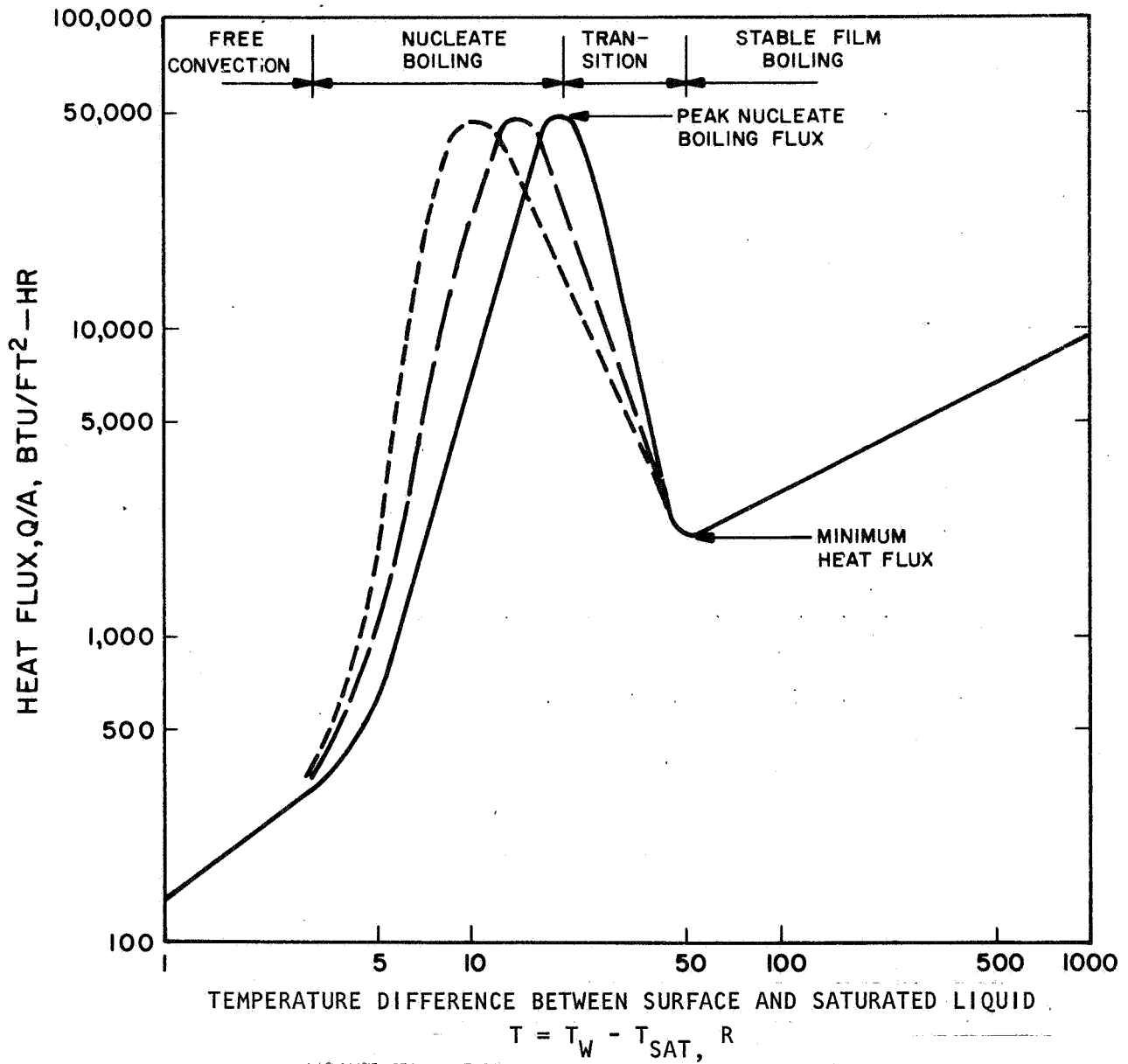


Figure 2. Typical Pool Boiling Heat Flux

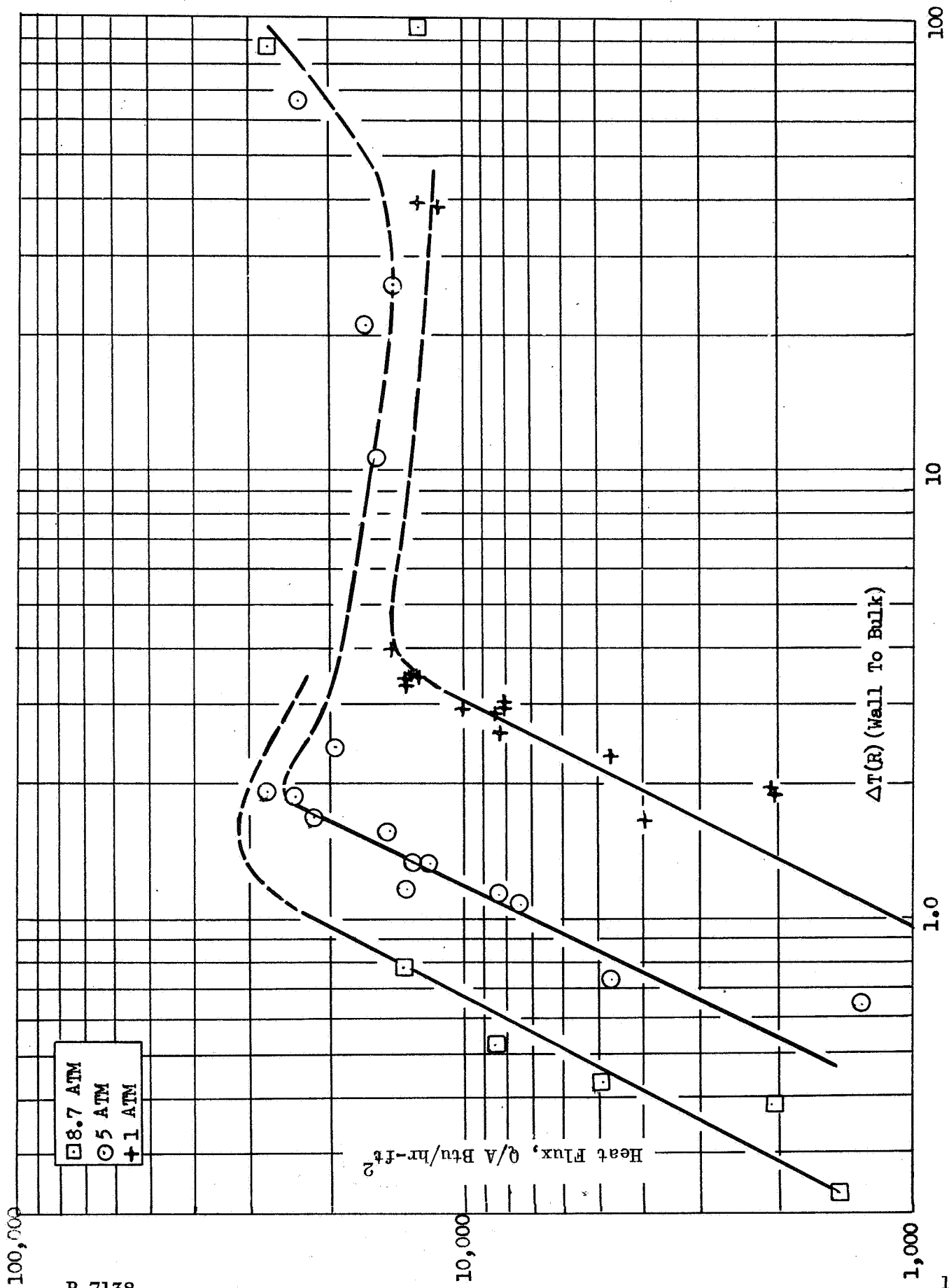


Figure 3. LH<sub>2</sub> Nucleate and Transition Boiling Range (Ref. 6)

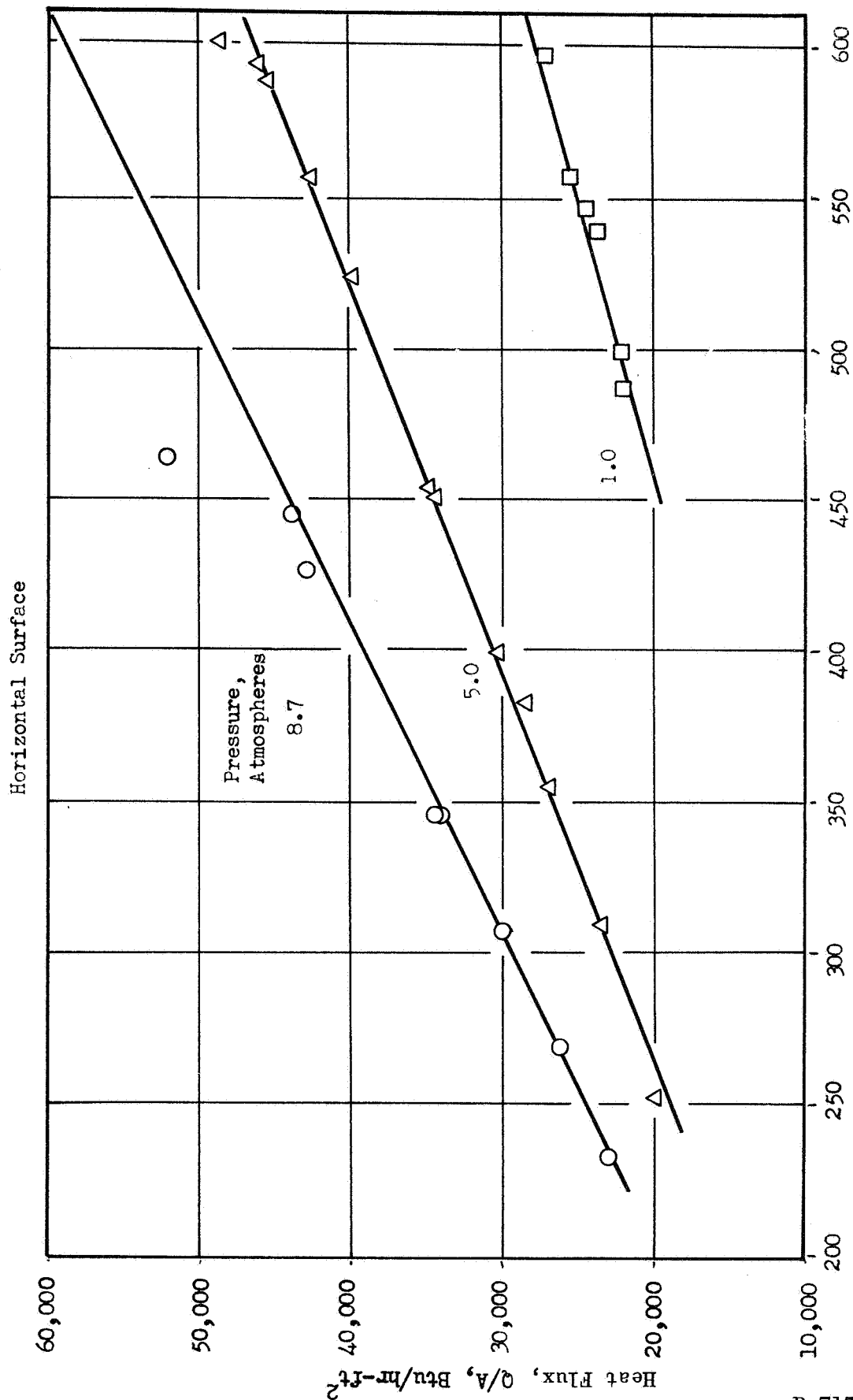


Figure 4. Film Boiling Liquid Hydrogen

### Forced Convection with Boiling

The same boiling regimes exist in a moving fluid as in the case of pool boiling. Some data are available (Refs. 24, 41) for forced convection with boiling. Figure 5 is a plot of some data for the boiling case. The 100 percent quality point data appear to be somewhat higher than the two-phase flow data. In general, the influence of fluid velocity is to raise the heat flux capability considerably above the pool boiling values, and use of pool boiling data for predicting hydrogen film coefficients would provide low values for this circumstance.

The selection of the dimensional correlating parameter shown in Fig. 5 ( $hd^{0.2}/G_{\infty}^{0.8}$ ) was made for simplification purposes in the near critical temperature region due to the strong fluid property variation with varying wall to coolant temperature ratios. Confirmation of this selected parameter was seen under Task II study where cooldown studies of individual metal tubes were examined.

Within the critical temperature region a substantial lowering of the Stanton number (based on freestream properties) is noted. Whereas for highly supercritical pressure and temperature at a reasonably high Reynolds number, a value of  $\approx .002$  is representative, for film boiling with forced convection, reductions of 4 to 5 can occur. Further analytical study is necessary to compare experimental Stanton number behavior with both wall to bulk temperature changes and fluid quality in the near critical temperature region.

### Boundary Layer Flow

Boundary layer theory can be used to calculate hydrogen heat transfer coefficients on a body with varying pressure gradients in short length-to-diameter passages. Figure 6 illustrates the cross section of an

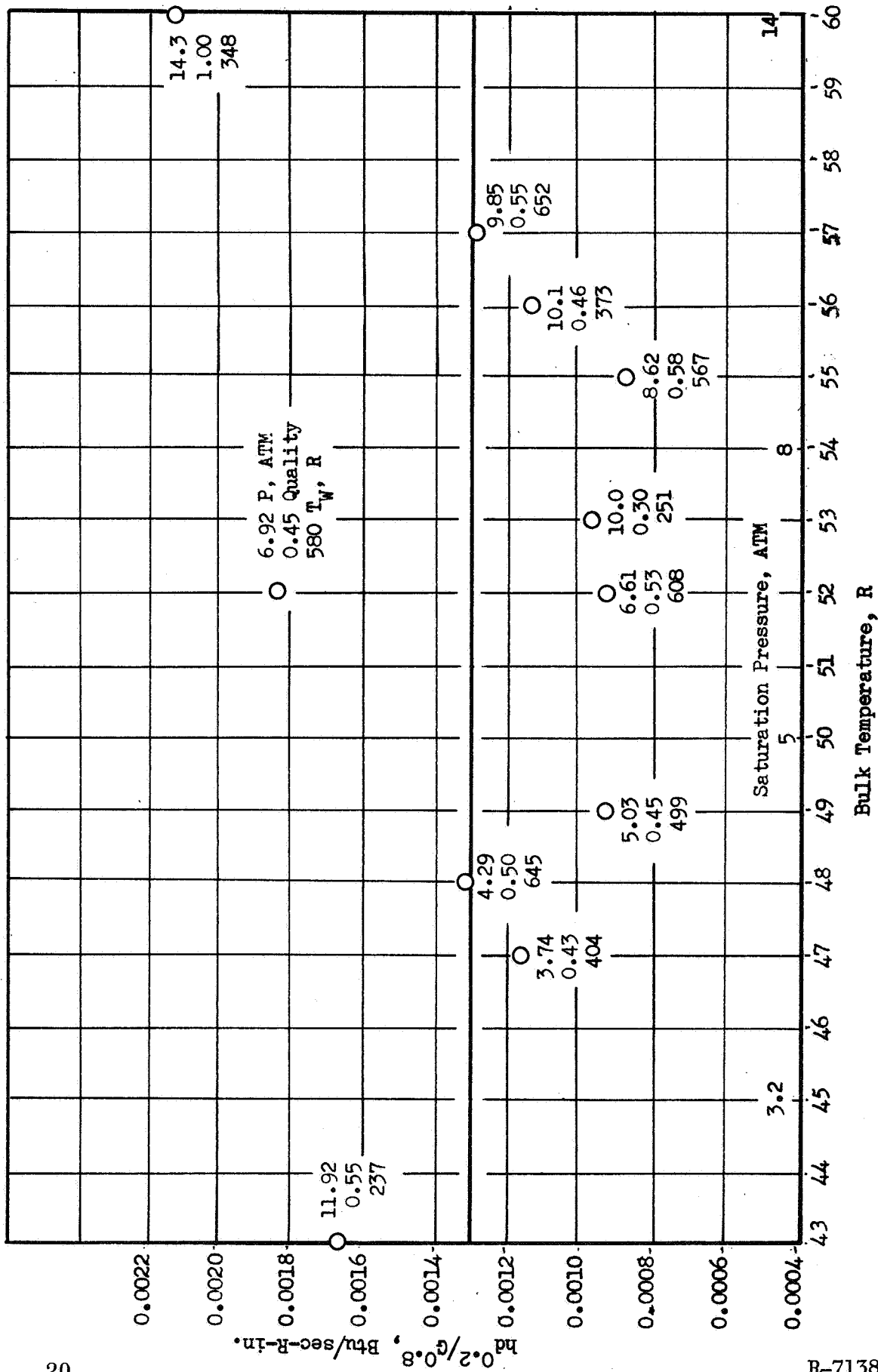


Figure 5. Heat Transfer Data, Liquid Hydrogen

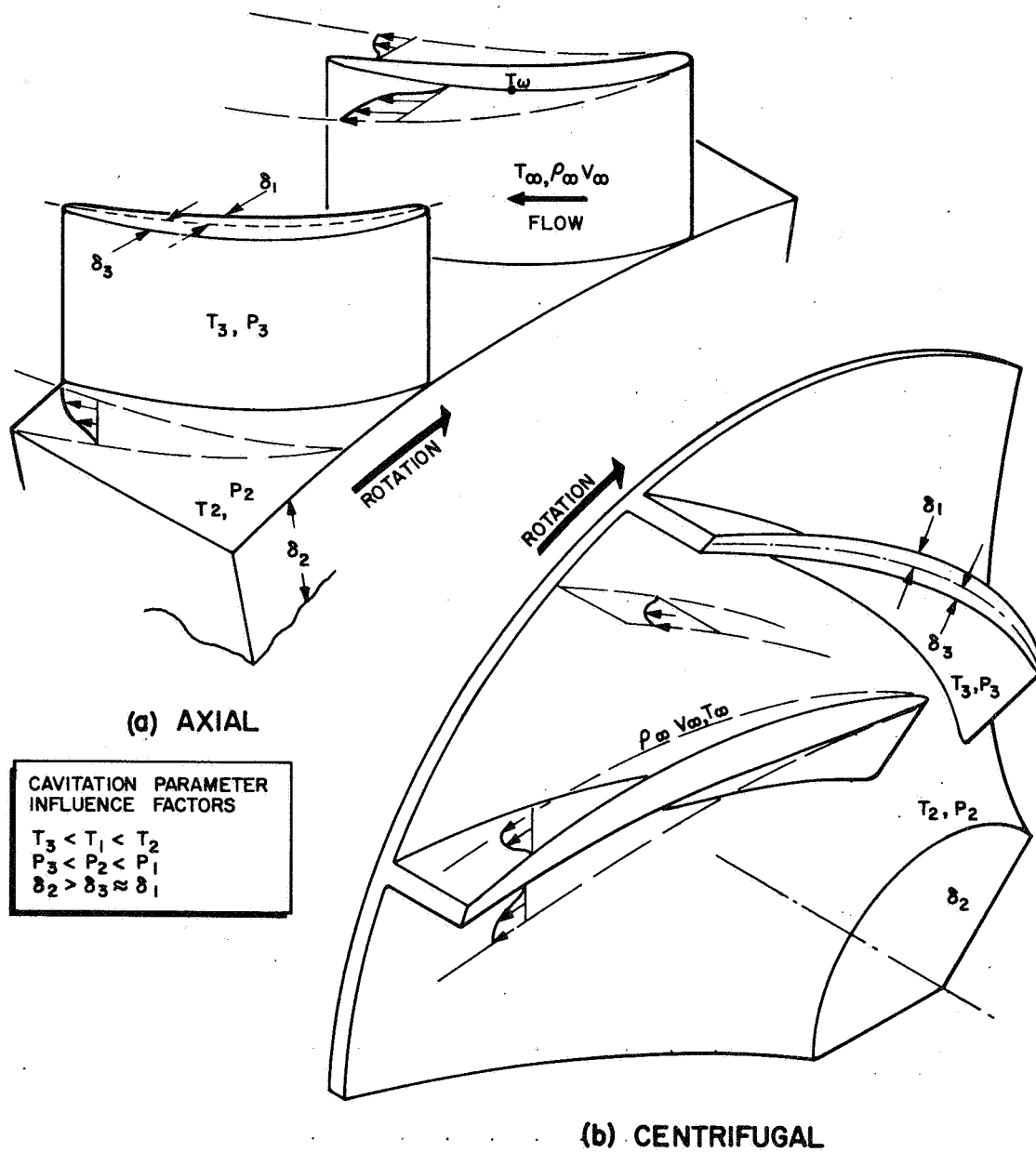


Figure 6. Illustration of Boundary Layer Growth and Critical Regions of Pump Impellers

impeller blade for typical axial and centrifugal LH<sub>2</sub> pumps. The boundary layer forms at the leading edge of the blades with an initial finite thickness and grows along the length of the blade. The boundary layer growth depends upon the contour of the blade surfaces and on the fluid velocity and pressure distributions. Although exact solutions of boundary layer equations are associated with mathematical difficulties, approximate integral methods of solution have been developed for practical applications.

The solution which is obtained from the boundary layer energy equation (Ref. 19) is based upon the Von Karman integral energy equation for laminar or turbulent boundary layer flows with a pressure gradient. This equation is valid for incompressible or compressible fluids with a nonadiabatic wall temperature. Its application requires an empirical description of the Stanton number behavior with energy thickness-based Reynolds number.

The integral energy equation can be written as:

$$\frac{d\phi}{ds} = C_H \left( \frac{T_{AW} - T_W}{T_o - T_W} \right) - \phi \left[ - \left( \frac{1}{T_o - T_W} \right) \frac{dT_W}{ds} + \frac{1}{\rho U} \frac{d(\rho U)}{ds} + \frac{1}{r} \frac{dr}{ds} \right] \quad (1)$$

where  $C_H = f(N_{Re}, N_{Pr})$  (1a)

An empirical equation for the Stanton number ( $C_H$ ) with the integral energy equation will permit the energy thickness and heat transfer coefficients to be determined at the wall boundary.

After evaluating the integral energy equation, the smooth surface Stanton coefficient is known. A recent thesis by Dipprey (Ref. 14) for pipeflow led to the equation for heat transfer in terms of heat transfer coefficients for flow in rough pipes:

$$N_{ST} = \frac{h}{\rho V C_P} = \frac{C_{H_o}}{1 + \sqrt{C_{H_o}}} \left[ f(\epsilon^*, N_{Pr}) - 8.48 \right] \quad (2)$$

$$\epsilon^* = N_{Re} \sqrt{C_{H_0}} \left( \frac{\epsilon}{D} \right) \quad (2a)$$

where the value of  $f(\epsilon^*, N_{Pr})$  is dependent on surface roughness  $\epsilon^*$ . High hydrogen Reynolds number conditions encountered over the blade surfaces can result in strong surface roughness effects.

### Fully Developed Channel Flow

Extensive data exist on fully developed channel or pipe flow, which allows accurate prediction of hydrogen film coefficients in the liquid- and single-phase forced-convection regimes. Typical cooling curves are shown in Fig. 7 and 8, which encompass a wide range of bulk temperatures and pressures.

The following table summarizes the conditions required for the possible boiling and nonboiling hydrogen flow regimes.

TABLE 1  
COMPARATIVE HEAT TRANSFER REGIMES

Mode	Q/A	V <sub>H</sub>	Bulk	T <sub>WC</sub>	T <sub>B</sub>	P <sub>B</sub>	
I Pool Boiling							
1. Nucleate	High	0	Boiling	T <sub>WC</sub> ≈ T <sub>SAT</sub>	T <sub>B</sub> ≤ T <sub>SAT</sub>	Sub-Critical	
2. Transition	Low	0	if T <sub>B</sub> = T <sub>SAT</sub>	T <sub>WC</sub> > T <sub>SAT</sub>	↓		
3. Film	High	0	Nonboiling	T <sub>WC</sub> ≫ T <sub>SAT</sub>	↓		
if T <sub>B</sub> < T <sub>SAT</sub>							
II Boiling and Forced Convection							
1. Nucleate	High	Finite	Boiling	T <sub>W</sub> ≈ T <sub>SAT</sub>	T <sub>B</sub> ≤ T <sub>SAT</sub>	Sub-Critical	
2. Transition	Low	↓		if T <sub>B</sub> = T <sub>SAT</sub>	T <sub>WC</sub> > T <sub>SAT</sub>		↓
3. Film	High			T <sub>WC</sub> ≫ T <sub>SAT</sub>	↓		
4. Bulk Boiling	High	↓	Nonboiling	T <sub>WC</sub> ≫ T <sub>SAT</sub>	↓		
if T <sub>B</sub> < T <sub>SAT</sub>							
III Forced Convection							
	Low to High	Finite	Nonboiling	-----	-----	Super-Critical	
	Low	Finite	Nonboiling	T <sub>WC</sub> < T <sub>SAT</sub>	T <sub>B</sub> < T <sub>SAT</sub>	Sub-Critical	

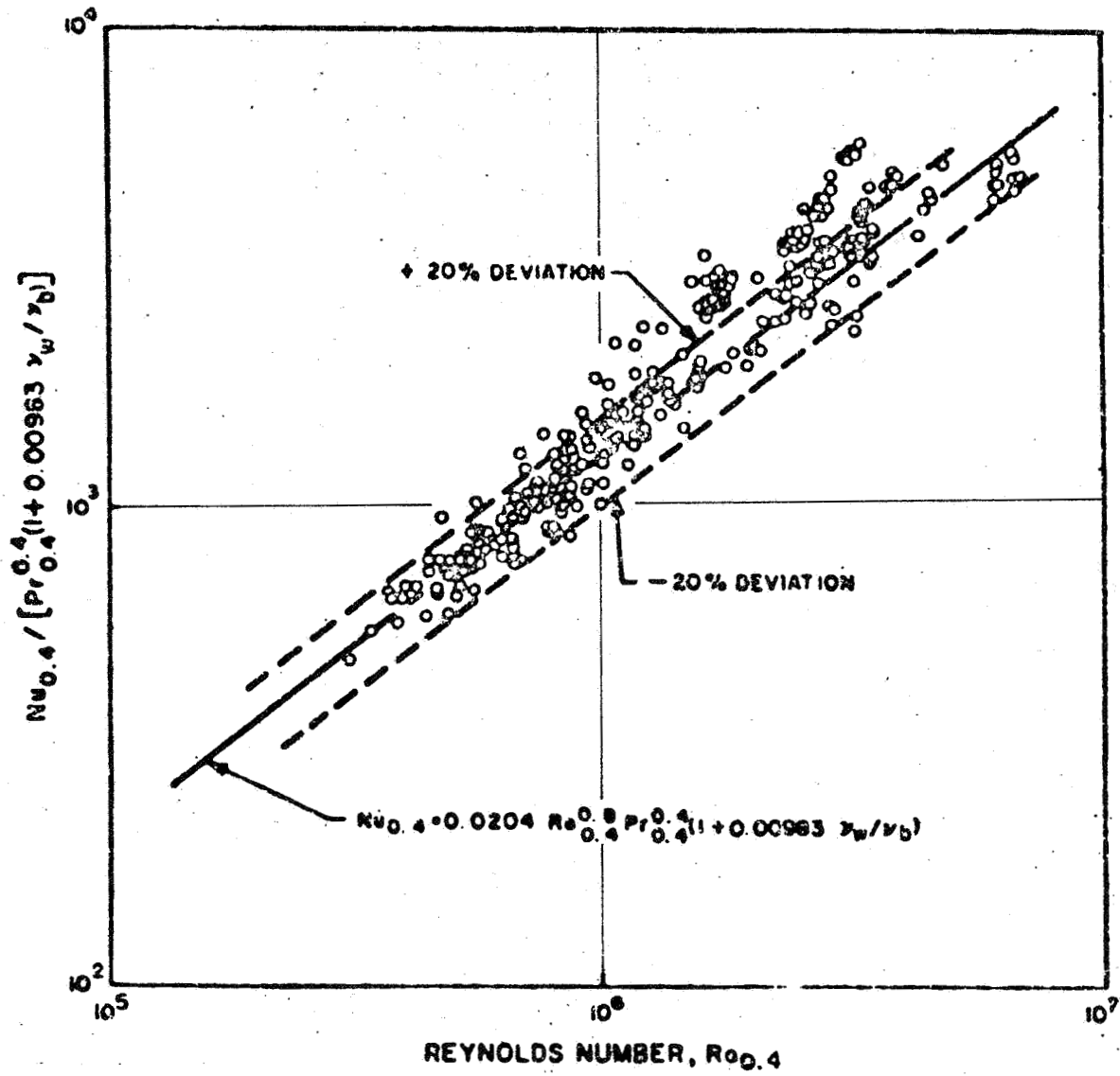


Figure 7. Correlation of Liquid Hydrogen Straight-Tube Data with Rocketdyne Equation

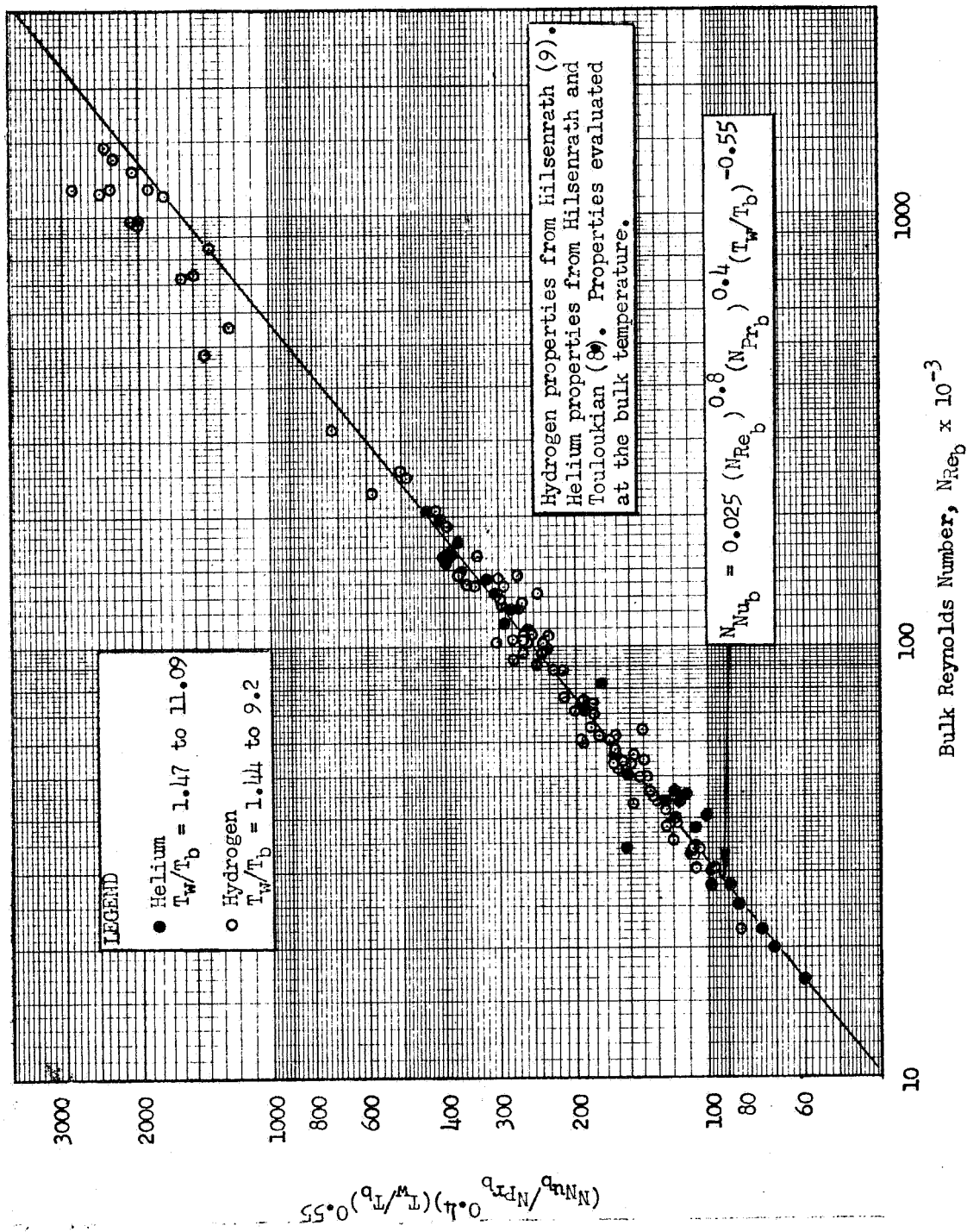


Figure 8. Local Heat Transfer Results for Helium and Hydrogen Gas (Properties Evaluated at the Bulk Temperature, Total  $L/D = 20.9, 30.2, 42.6,$  and  $67.0$ )

## LIMITING FLUID VELOCITY AND TEMPERATURE CONDITIONS

During the pump initial start period when the pump surfaces are warm and the pump pressures are at tank head value, an evaluation of the maximum liquid and vapor mass velocity ( $\rho_{\infty} V_{\infty}$ ) is required for determination of local heat transfer coefficients. For long fluid passage circuits within the pump (as illustrated in Fig. 9) at the beginning of flow onset, the pump fluid outlet temperature can be greater than 50 percent of the warm wall to coolant temperature difference. As a result, for pumps subject to restart in a warm condition, initial coolant outlet temperatures may approach 520 R. A limiting flow mass-velocity condition for the pump with a vapor state is the choked condition. Figure 10 illustrates for inlet pressure conditions of 14.7 and 40 psia the stagnation density acoustic velocity product. Over the temperature range the local static to stagnation density ratio may be determined from Fig. 11. The local maximum gas mass velocity may be evaluated by the relationship

$$(\rho_{\infty} V_{\infty})_{\text{choked}} = (\rho_o C) \left( \frac{\rho_{\infty}}{\rho_o} \right) = \left( \frac{2}{\gamma + 1} \right)^{\frac{1}{\gamma-1}} \rho_o C \quad (3)$$

Evaluation of the maximum liquid mass velocity was accomplished by assuming a conversion of the inlet pressure head to a velocity head as shown in Fig. 12. A range of coolant mass velocity which might be expected for a 40-psia inlet condition would be 0.5 lb/in.<sup>2</sup>sec (200 R gas) to 6 lb/in.<sup>2</sup>sec (42 R liquid). Evaluation of local maximum mass velocity condition within the pump at start can be calculated from the minimum flow area location (pump, thrust chamber or injector) and local Stanton number and heat transfer coefficients may be thus determined.

Chiltdown in the pump to the temperature value consistent with the NPSH and pump performance is required during the course of a specific chiltdown study. For suppression of nucleate or film boiling, wall surface and coolant temperature at locations of pressure below the critical ( $P_{\text{crit}} = 188 \text{ psia}$ )

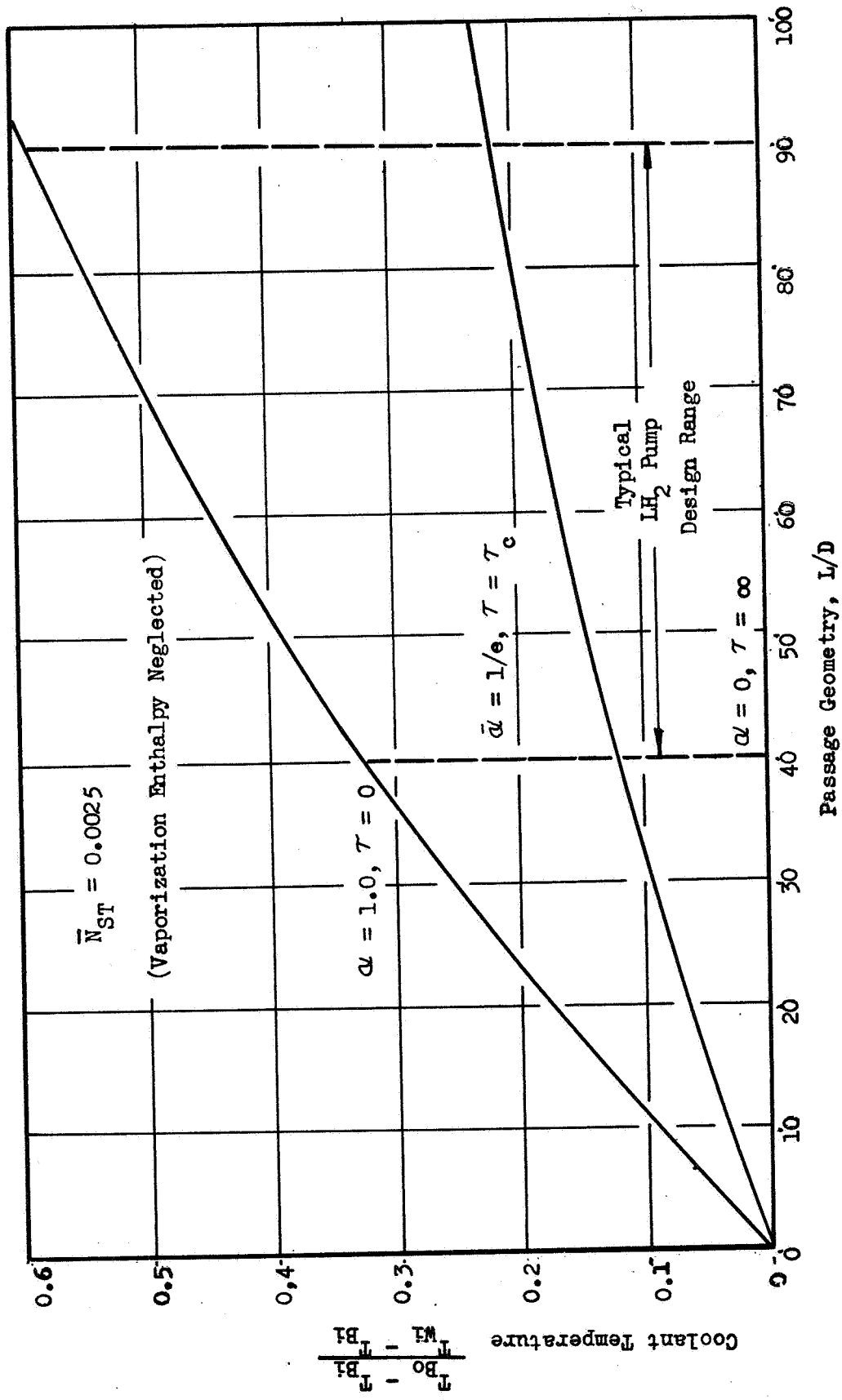


Figure 9. Coolant Outlet Temperature vs Passage Geometry

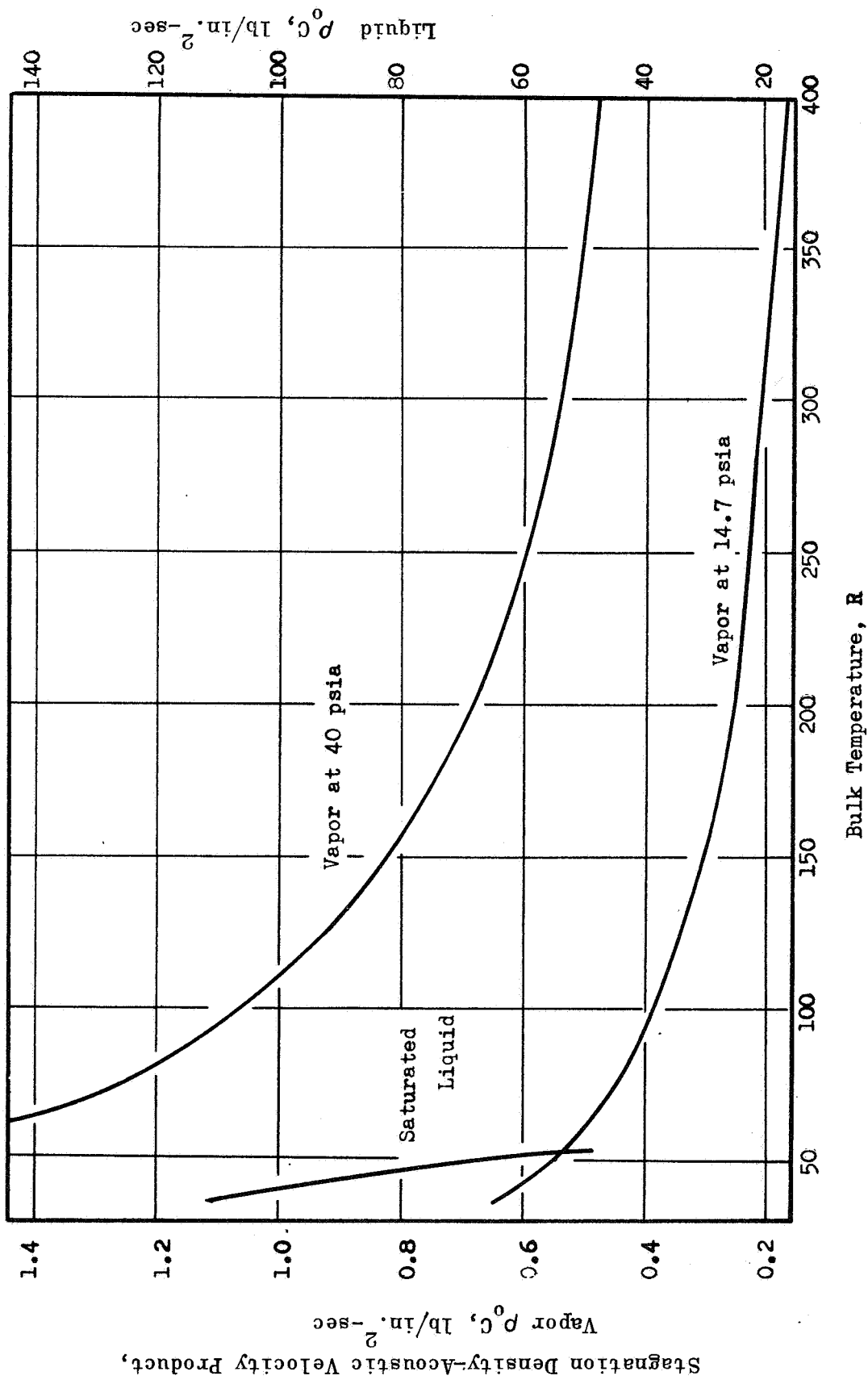


Figure 10. Hydrogen Stagnation Density-Acoustic Velocity Product at Pump Inlet Conditions

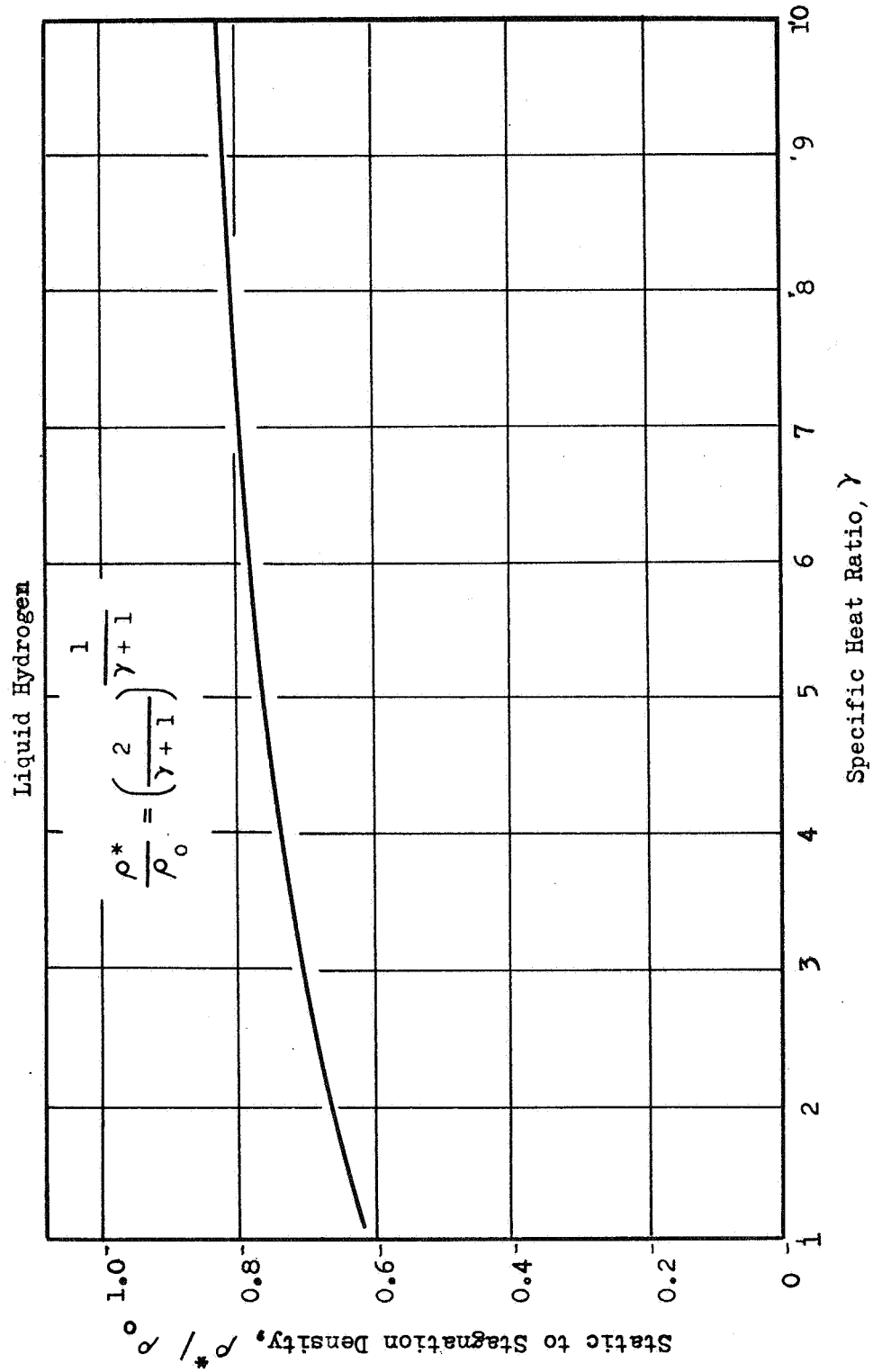


Figure 11.  $\rho^*/\rho_0$  vs  $\gamma$  at Choked Condition

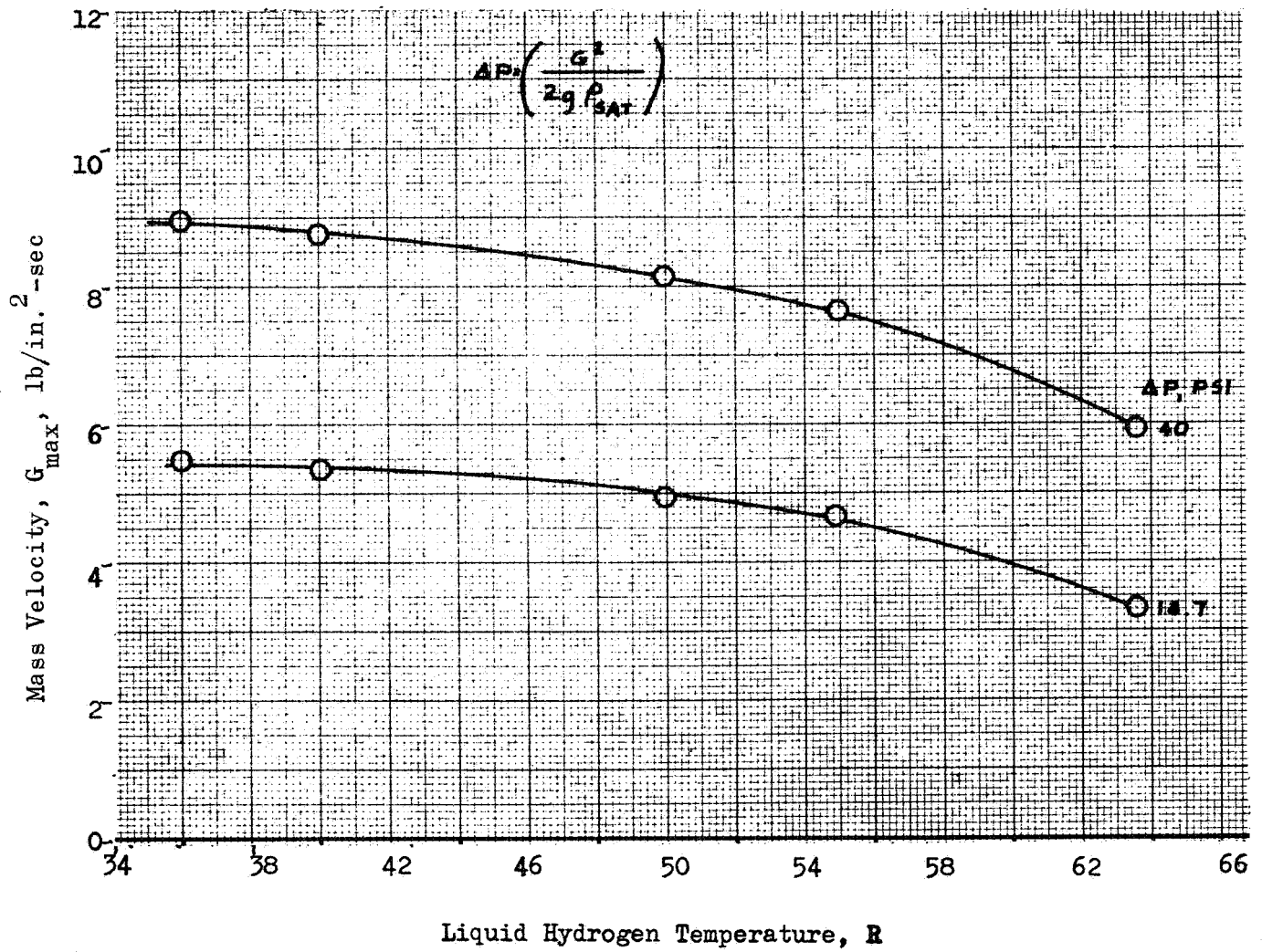


Figure 12.  $\Delta P$  to Velocity Head Conversion for Hydrogen  
Liquid Saturation Line Density

must be below 60 R (Fig. 13). For initial tank head pressures of 40 psia wall surface temperatures must be reduced below 43 R. As a result any preconditioning or chill that is prescribed must be fairly complete before a condition of no vapor formation is provided. Tolerance of the LH<sub>2</sub> pump to large and small vapor flowrates is provided in a later section of this report.

### CRITICAL TIME FACTORS

In evaluation of the transient operating period for a cryogenic pump, a number of critical time constants affecting its thermal response must be thoroughly considered. These are: (1) engine start time, (2) lower time limit of pump start, (3) coolant transit time through the pump and line plumbing, and (4) line plumbing and pump body time response. In addition, for an engine restart, the following time factors must also be considered: space storage time, space radiation time, and time between starts for turbine heat soakback. The evaluation of relative critical time constant allows an immediate stipulation of the relative importance of each factor on the pump overall mechanical and hydrodynamic performances.

#### Engine Start Times

The goal for engine startup is to achieve minimum time from initial to mainstage thrust with present target times for typical O<sub>2</sub>/H<sub>2</sub> engines being in the range of 1 to 5 seconds. Limitations to this minimum value are encountered if either pump cavitation or stall is initiated. Absorption of heat by the cryogenic propellants from the warm line, valve, pump, and thrust chamber surfaces can result in an evolution of high volume of low-density gas during the initial time period when flow and pressures are low.

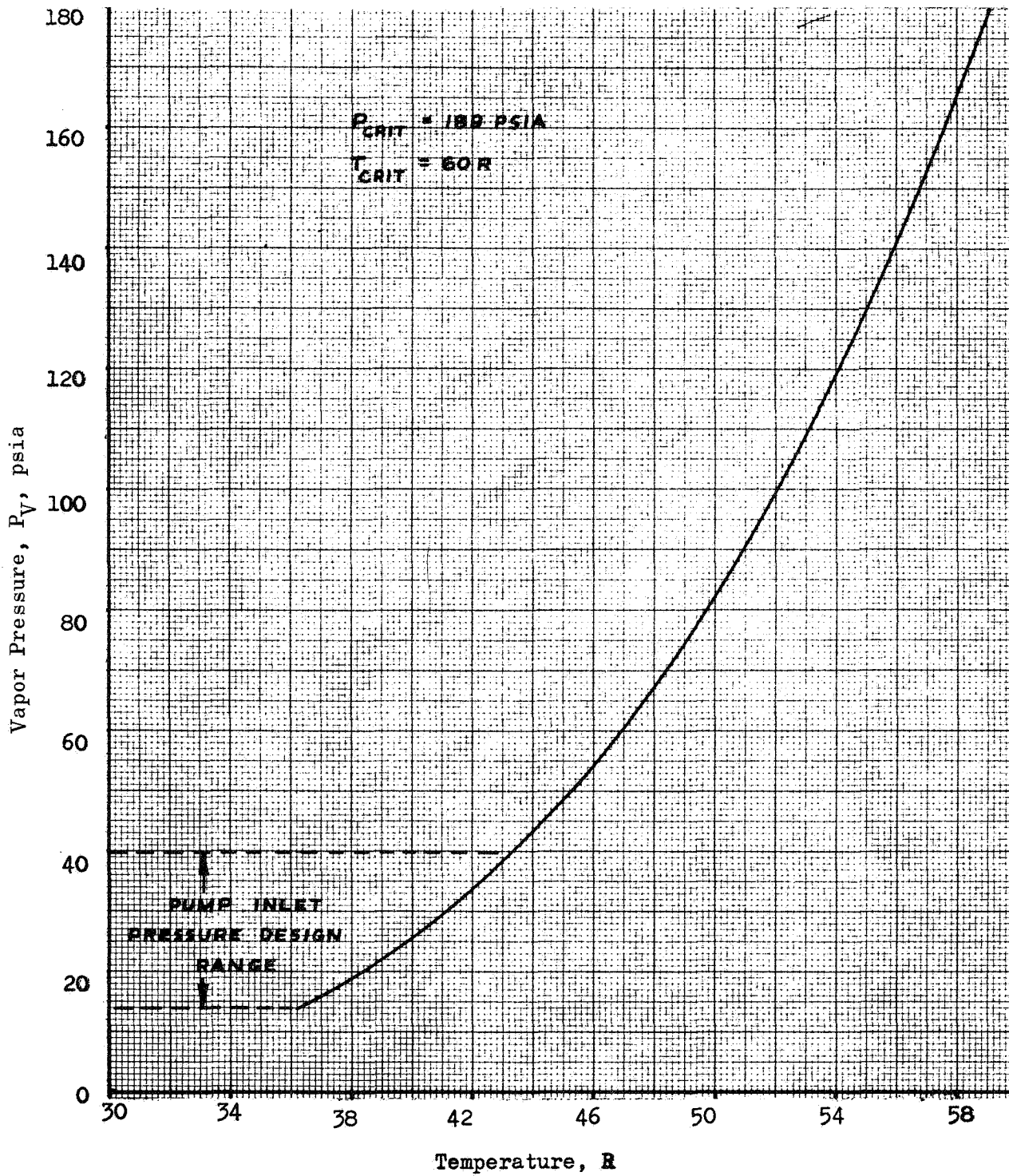


Figure 13. Hydrogen Vapor Pressure vs Temperature

The pump is only one of many components in the engine system that is involved in a warm start; therefore, it must be studied only in terms of its performance as it influences the start cycle. It should be kept in mind that the ultimate objective is to attain a rapid and efficient start that is not penalized by the initially warm engine. The inter-related effects of all the engine components on the engine start are illustrated by the combined engine and pump operating lines (Fig. 14). The high system resistance line shown in Fig. 14 can control the flow if the pump, tube bundle, and other engine parts are all warm. The reason for the high resistance is that flow passages are sized for dense liquid and are too small for the large volumes of gas generated by the warm surfaces. This high system resistance is undesirable since it reduces the flowrate and prolongs the start cycle. Moreover, the pump also operates inefficiently at off-design conditions.

A low system resistance at start will accelerate the warm starting cycle because it permits the flow of a large quantity of fluid in a short time. This can promote rapid chilling of the pump. Low system resistance can be obtained by bypassing flow directly to the injector instead of through the high resistance tube bundle.

The curve labeled "desired start transient" is representative of a rapid, efficient start cycle. The turbopump operates in an efficient region of performance and will accelerate rapidly. During a design study, turbopump parameters should be investigated that will permit operation in a desirable region during warm starting. The engine starting dynamics are typically shown on the performance map of LH<sub>2</sub> turbopump in Fig. 16 with time intervals indicated. The time sequence of events is summarized in Table 2.

#### Turbopump Start Time

The start time of "dry" turbopumps, where acceleration is limited only by the inertia of the turbine rotor assembly, is shown in Fig. 15. This sets

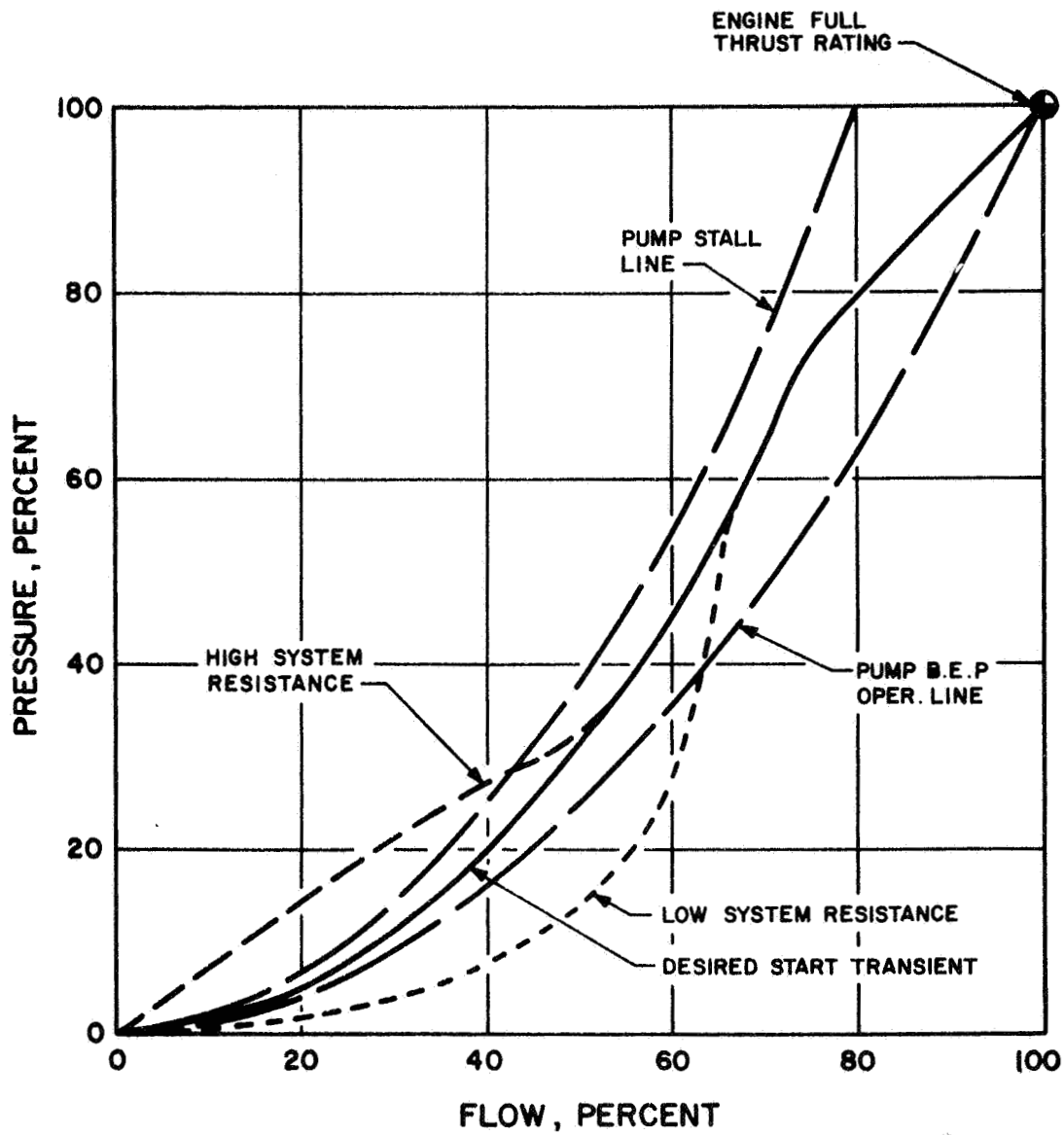


Figure 14. Effect of Engine Starting Characteristics on Pump Performance

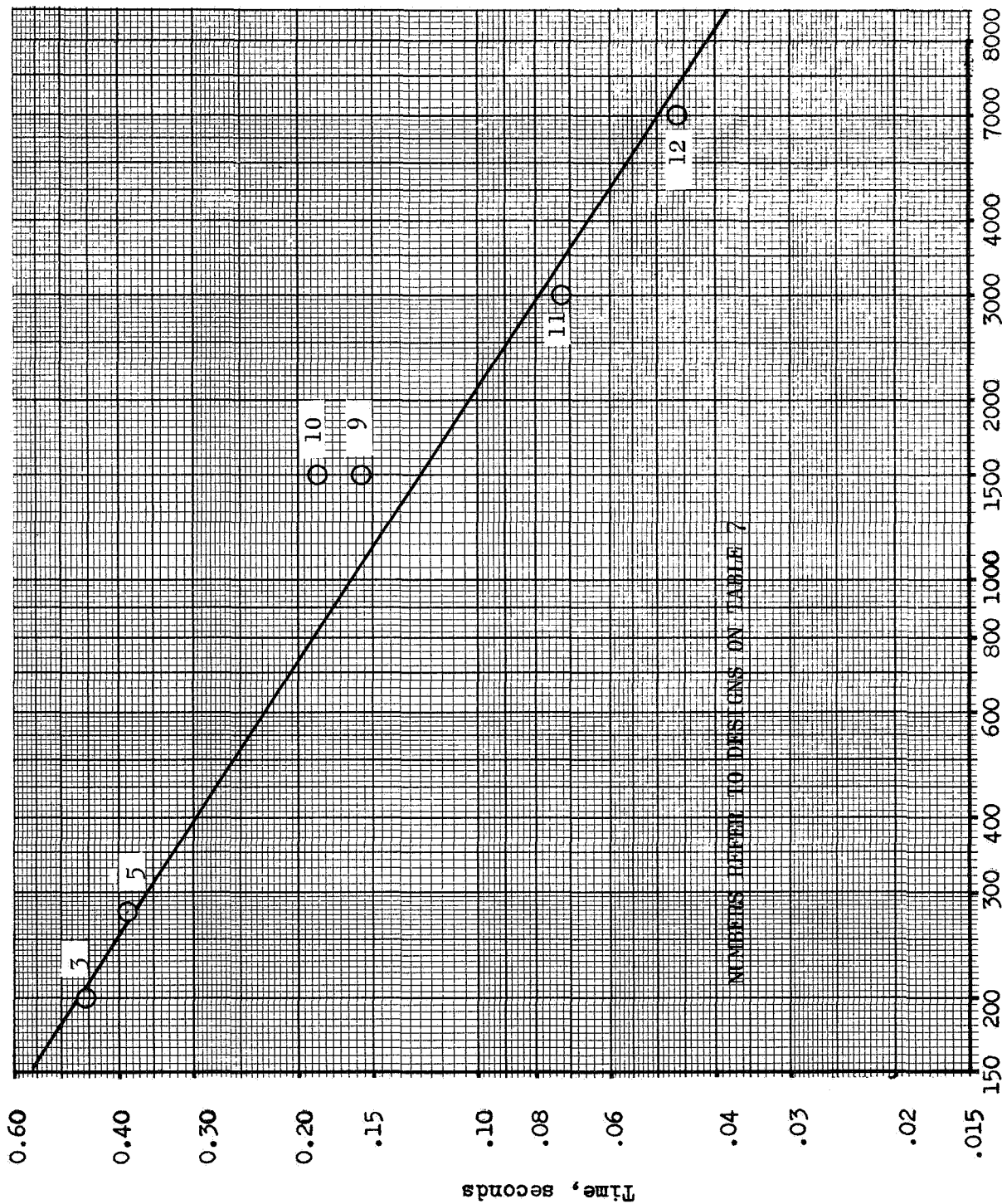


Figure 15. LH<sub>2</sub> Turbopump Inertia Limited Start Times (Dry Pump Conditions)

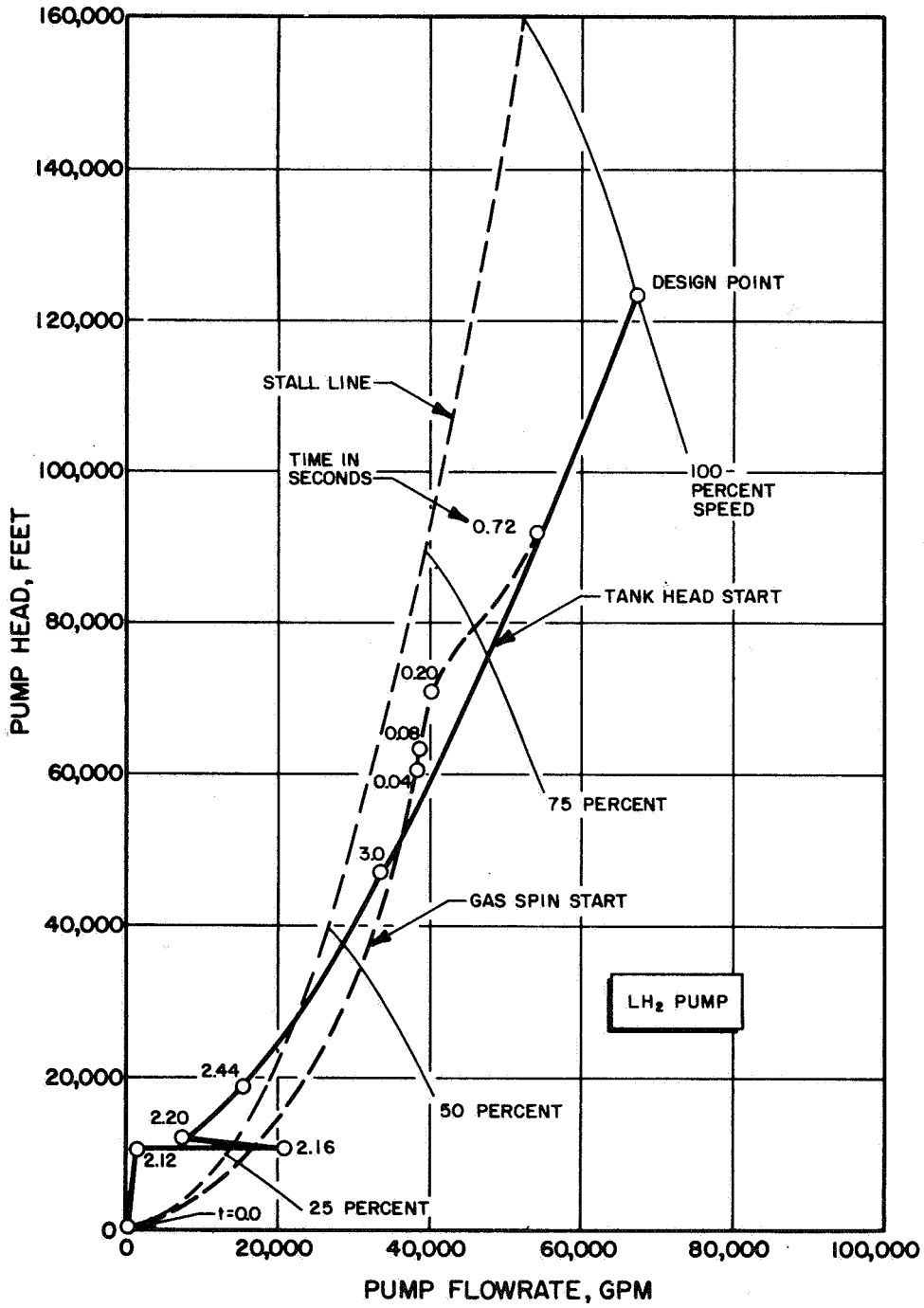


Figure 16. Typical Hydrogen Pump Start Transients for an LO<sub>2</sub>/LH<sub>2</sub> Engine

TABLE 2

TIME SEQUENCE OF EVENTS FOR A LO<sub>2</sub>/LH<sub>2</sub> ENGINE

Event	Time of Event, seconds		
	Tank Head Start		Gas Spin Open
	LO <sub>2</sub> Tank Aft	LO <sub>2</sub> Tank Forward	LO <sub>2</sub> Tank Forward
Gas Generator Fuel Valve Starts to Open	0	0	0
Gas Generator Oxidizer Valve Starts to Open	0	0	0
Gas Generator Fuel Primes	0.04	0.04	0.01
Gas Generator Oxidizer Primes	0.04	0.04	0.01
Gas Generator Fuel Valve Full Open	0.10	0.10	0.10
Gas Generator Oxidizer Valve Full Open	0.10	0.10	0.10
Main Fuel Valve Starts to Open	2.15	2.14	0
Main Oxidizer Valve Starts to Open	2.15	2.14	0
Igniter Valve Starts to Open	2.15	2.14	0
Igniter Primes Thrust Chamber	2.16	2.16	0.03
Oxidizer Primes Thrust Chamber	2.16	2.17	0.03
Fuel Primes Thrust Chamber	2.17	2.19	0.04
Igniter Valve Full Open	2.20	2.19	0.05
10-Percent Thrust	2.25	2.24	0.042
Main Fuel Valve Full Open	2.45	2.44	0.30
Main Oxidizer Valve Full Open	2.45	2.44	0.30
Igniter Valve Closed	2.65	2.64	0.40
90-Percent Thrust	3.98	3.97	1.04

the limit of the fastest start time for the study of the transient chill-down problem. Actual start times for some existing turbopumps are shown in Table 3 and, except for geared turbopumps, the start times of  $\text{LO}_2/\text{LH}_2$  turbopumps are on the order of two or three seconds. The start transient for a prechilled J-2  $\text{LH}_2$  turbopump is shown in Fig. 17. (Since the engine system gas generator, mixture ratio control, etc., influences the start time to a large extent as shown in the following section, a typical reference value of 2.5 seconds was used for most of the ensuing analysis). The engine start time will be one limited by system considerations which include the pump downstream resistance, pump inlet flow conditions, and pump cavitation or stall criteria.

The ability of a warm turbopump to develop pressure during the first few seconds of a warm start cycle will be primarily a function of the heat input to the fluid from the warm metal surfaces. For thick or uninsulated surfaces, the controlling parameter will be the relative amount of surface the fluid will contact before pump pressure can be generated. For example, for a given metal temperature, if a pump impeller can generate pressure faster than the vapor pressure can increase due to heat addition, the pump will develop substantially full design head and will not reduce the warm start capability of the engine. In other words, warm starting would then be essentially an engine system rather than a pump problem.

#### Turbine Drive and Start Method Effects

In order to evolve an engine starting sequence or to study the transient characteristics of major components, a complete engine analysis must be conducted. Examination of whether the start is powered, or tank head start based on a timer or on level of engine operation, must be specified.

TABLE 3

## COMPARISON OF TURBOPUMP STARTING TIMES

Parameter	F-1	Atlas	H-1	J-2
	MK 10 Direct Turbine Drive LO <sub>2</sub> + RP1	MK3 - MA5 Geared Turbine Drive LO <sub>2</sub> + RP	MK 3H Geared Turbine Drive LO <sub>2</sub> + RP1	MK 15-F Direct Turbine Drive LO <sub>2</sub> + LH <sub>2</sub>
Angular Velocity (Design Point) $W_d$ , rad/sec	581.9	3103.6	3483.2	2717.5
Start Time $\tau$ ( $W = 0$ to $W_d$ Test Data), sec	2.50	0.60	0.60	2.35
Average Acceleration, rad/sec <sup>2</sup>	232.8	5172.7	5805.3	1156.8
Mass Moment of Inertia (Wet Rotating Parts), lb-sec <sup>2</sup> -in.	250.14	0.530	0.636	2.89
Turbine Pitch Diameter $D_m$ , inches	34.9	9.0	9.0	12.5
Turbine Nozzle Area, in. <sup>2</sup>	17.040	2.286	2.214	2.353
Turbine Pressure Ratio	16.7	15.7	19.3	6.5

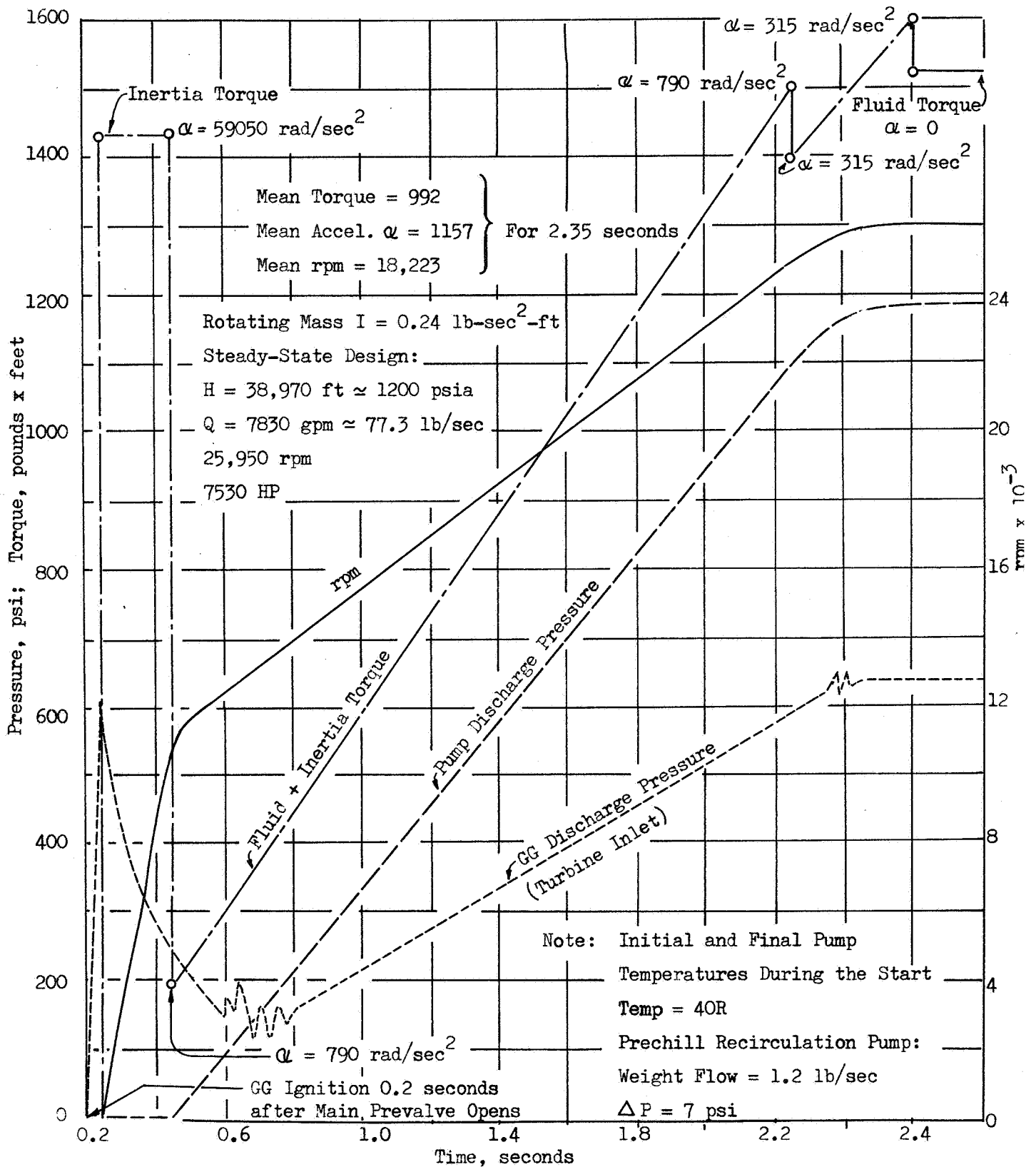


Figure 17. Mark 15-F Turbopump Starting Test

LH<sub>2</sub> engines can be classified in general categories for start transients. The first is one which uses cold liquid or gas to chill the hardware and uses auxiliary power for turbine starting (J-2 Basic). The second type (J-2S) uses a more powerful source for starting the engine, allows for mixed-phase propellants at the pump inlet but still requires some hardware chilling prior to start. The third type (J-2X) uses main tank pressures to start with no auxiliary power supply. In order to achieve start the engine is well chilled both prior to start and during the long start transient itself. Rather high main tank pressures are required. A fourth approach employs only main tank pressures to start but is designed to start without chilling prior to the start signal. In any of the four systems the start sequence allows for sufficient chilling during start to avoid pump stall or surge. In addition, a typical engine must have additional chilling and additional tank pressure so that it can produce excess pump torque at any operating point while avoiding adverse temperatures at the thrust chamber wall and on the turbine blades.

Hydrogen readily changes phase and will always experience a significant density reduction in flowing through the cooling jacket. At full thrust the density entering the thrust chamber jacket will be near 4.4 lb/ft<sup>3</sup> and decrease perhaps an order of magnitude before passing through the injector. During start the density will be even more variable, dropping as low as 0.05 lb/ft<sup>3</sup>. The start density variation is a function of early mixture ratio, initial thrust chamber temperature and absolute pressure levels. Variations in the density show up as injector and tube bundle pressure drop and can reflect back to the fuel pump pressure to force the fuel pump into stall or surge.

Basically a high-energy start simplifies the feedback controls required in the engine system. Critical problem regions can be traversed quickly. A low-energy start, such as tank head, requires a more sophisticated feedback control system. Nevertheless, a great advantage in overall capability

such as multiple restarts and long noncritical coast periods can be realized. Start studies conducted on a typical 30K engine analyzed a start system which has the capability of achieving satisfactory starts under a wide range of fuel pump and thrust chamber initial temperatures. The initial temperature of the pump was found to be much more significant than the temperature of the thrust chamber. The time transients of chamber pressure are shown in Fig. 18.

Starting an engine with gaseous hydrogen and a warm thrust chamber presents the problem of high mixture ratio excursions and potentially high turbine temperatures. For quick restarts a fuel-rich cutoff will lower the bulk thrust chamber temperature and alleviate the above problem. J-2 experience with a 400-millisecond fuel valve closure shows final thrust chamber temperatures below ambient. Studies of the J-2X engine using chilled hardware also show that the time to mainstage is also a very strong function of fuel tank pressure and that by varying the tank pressure from 100 to 30 psia, minimum starting times from 3 to 15 seconds could be achieved.

Although it is yet to be shown in detail, it appears that the long starting time is also dependent on the time required to precondition the turbine power supply system. It is first necessary to chill the pump, or to provide a design so that even low speeds can produce a pressure rise through the pump. It is then necessary to chill the system that feeds liquid to the combustion device which supplies gas to the turbine. In a system start, both chill times are equally important. These chill times may be controlled by controlling heat transferred to the propellant, or by controlling the amount of fluid flowing through the warm hardware.

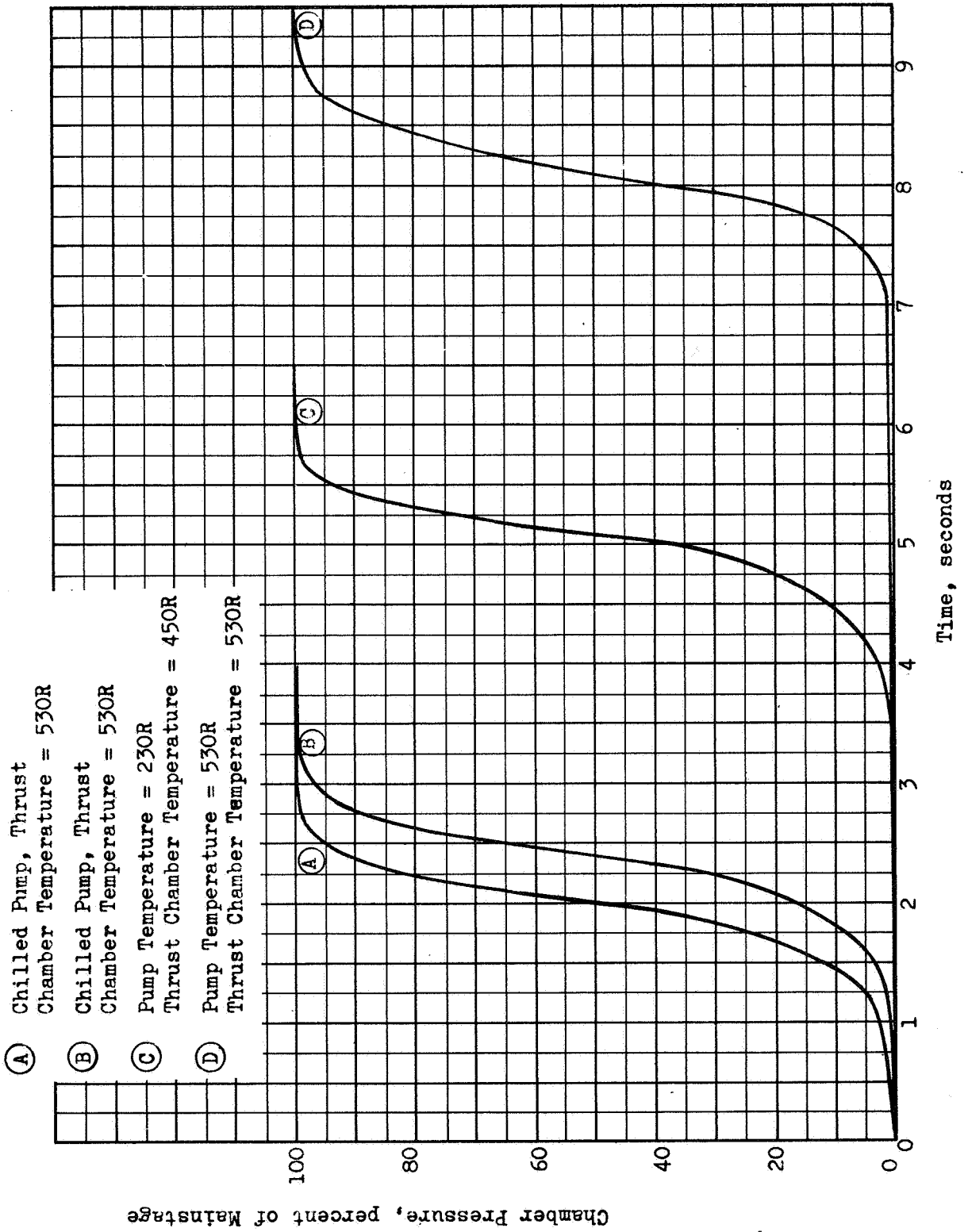


Figure 18. 30,000 lbf Engine Start Transient With Chill

### Vehicle Mission Time

The study of heat transfer in  $\text{LH}_2$  turbopumps depends upon an analysis of the turbopump application and a definition of the turbopump environmental influences. A variety of uses currently exists for cryogenic propulsion systems, and more are expected to arise in future missions. Missions and vehicles must be reviewed to specify the operational requirements for turbopumps in terms of starts, length of operation, and the environment for each operation. Typical missions representing these considerations are described below for establishing criteria necessary for overall thermal analysis as a function of time.

Apollo Mission. The mission profile portion for landing on the moon is shown on Fig. 19 and the associated propulsion system operations during flight are described on Table 4. Flight prior to third-stage operation is deleted for brevity on Table 4 and only space operations are depicted. Thermal analysis in determining turbopump temperatures has already been conducted considering prelaunch and boost flight to orbit. These representative temperatures are shown on Fig. 20. Continued analysis for the complete mission will then determine temperatures resulting at any time for the propulsion modules required for mission accomplishment.

As conditions for thermal analysis depend greatly on active or passive thermal control, interrelation with spacecraft and other component influences, engine operations, spatial location, sun exposure, and material thermal properties, a complete heat balance is required. For example, material thermal characteristics and surface exposure can dominate resulting temperatures as shown on Fig. 21. These temperatures result in near earth space that would be experiencing a solar heat flux of  $444 \text{ Btu/hr-ft}^2$ . Other locations in space will require changed solar heat fluxes as shown on Fig. 22. Single surface temperatures can be

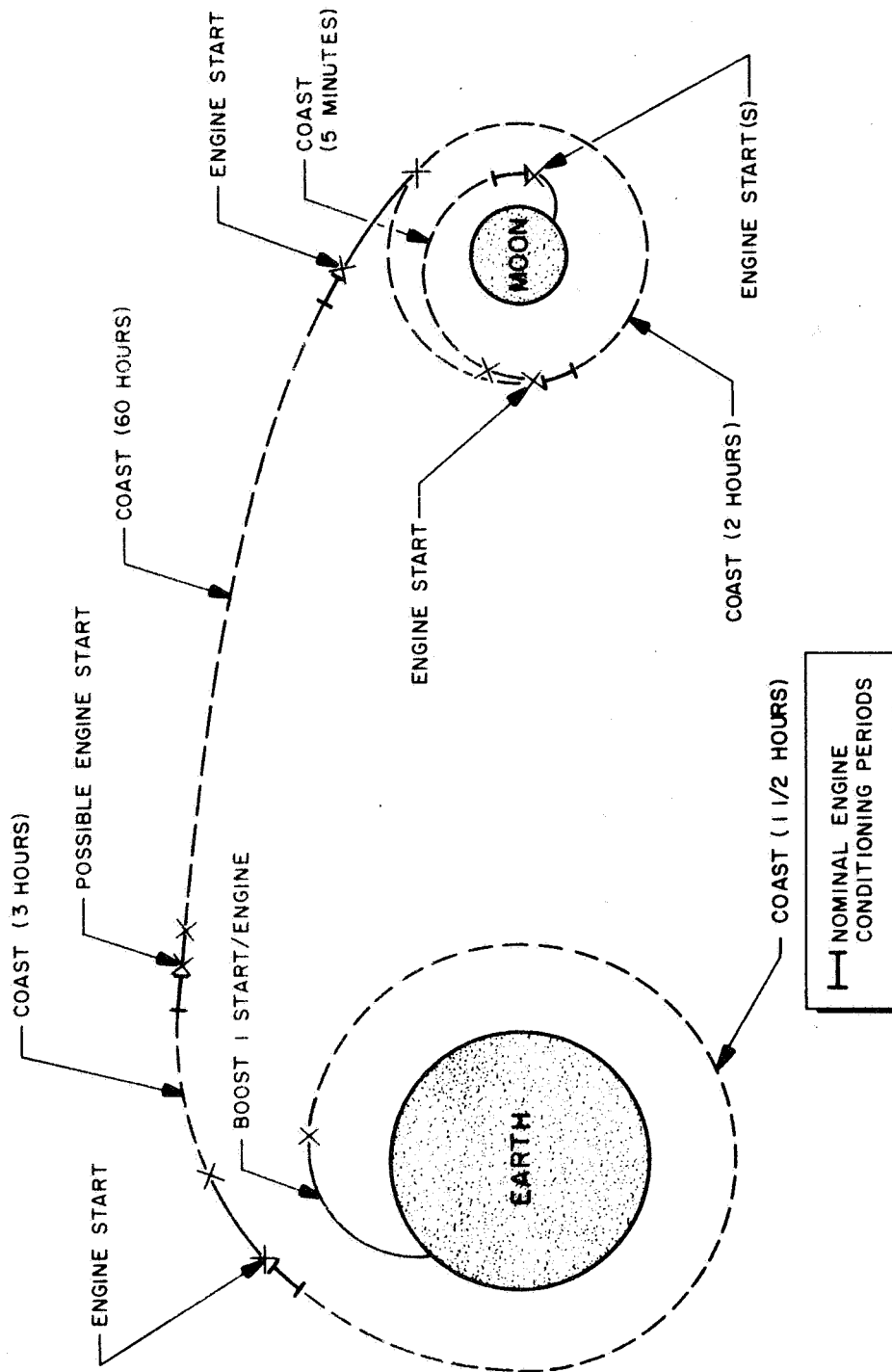


Figure 19. Typical Lunar Mission Profile

TABLE 4

APOLLO MISSION PROFILE  
(14-Day Mission)

Module	Function	Propulsion System Operation	Starts	Remarks
S-IVB	Third-Stage Boost to Low Earth Orbit	145 Seconds at Full Thrust	1	Vehicle remains in orbit (100 n mi) for 1.5 to 4.5 hours after cutoff
	Translunar Injection	325 Seconds at Full Thrust	1	Cutoff at approximately 1,029,000 feet followed by 1-to 3-hour coast where transposition and docking maneuver performed and S-IVB jettisoned. SM, LEM, and command module (CM) continue to moon
Service Module (SM)	Midcourse Corrections	Short-Interval Thrust Bursts	Multiple	Periodically operated during 60-hour coast period
	Lunar Orbit Insertion (also return flight)	Main Engine Burn for 5 Minutes for Lunar Orbit	1	Establishment of 80 n mi lunar orbit and then coast for about 2 hours
Lunar Excursion Module (LEM)	Lunar Descent from Orbit	Retro Thrust Burn for Short Duration	1	CM and SM remain in lunar orbit
	Lunar Land	Descent Engine Firing for 8 Minutes	Multiple	Land and explore for 10 to 14 days on lunar surface*

\*Return flight will launch and rendezvous in lunar orbit, coast, transearth inject, coast, and re-enter Earth corridor.

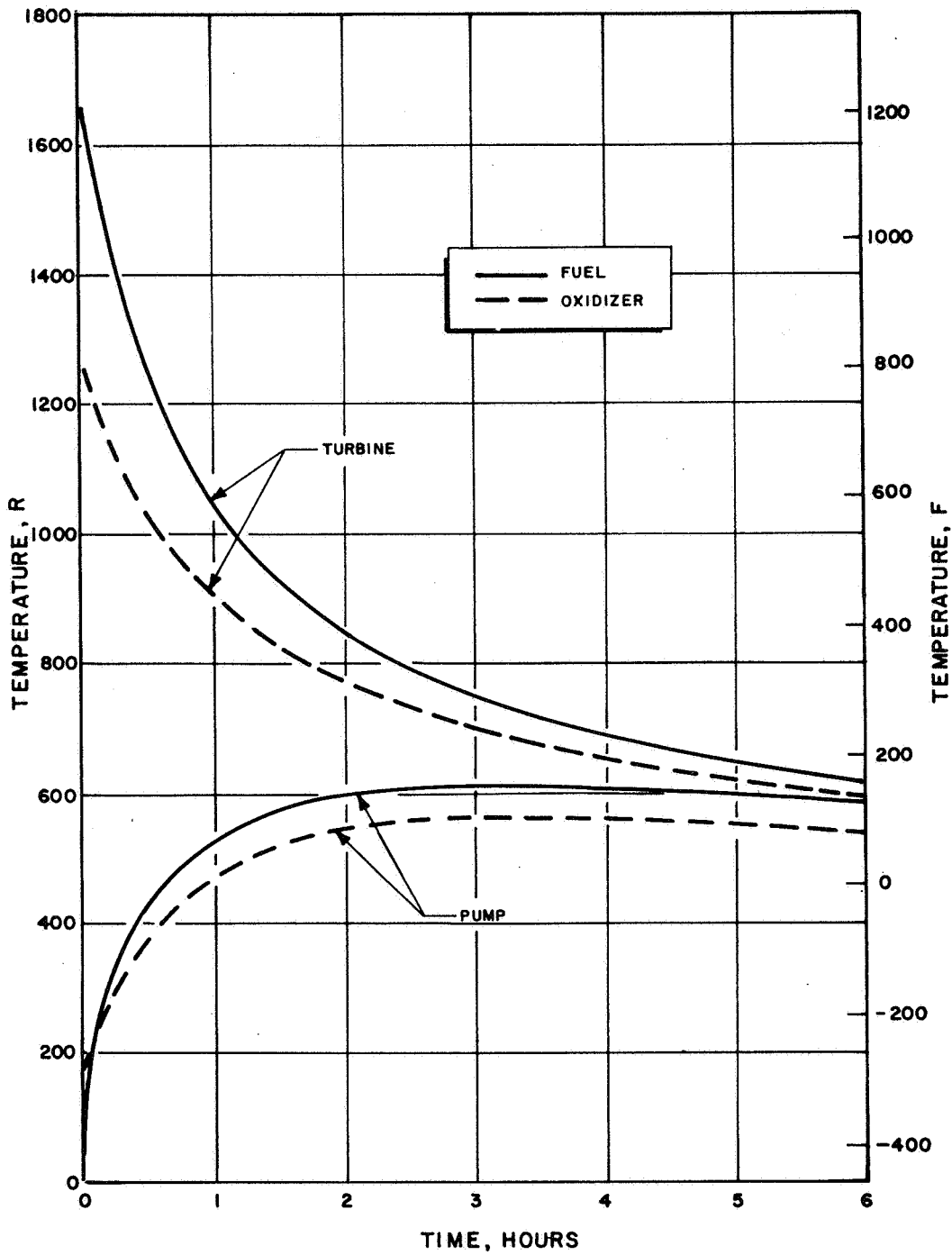


Figure 20. Predicted Turbopump Temperatures in Orbit

$A_p$  is Projected Surface Area  
 $A_s$  is Total Surface Area

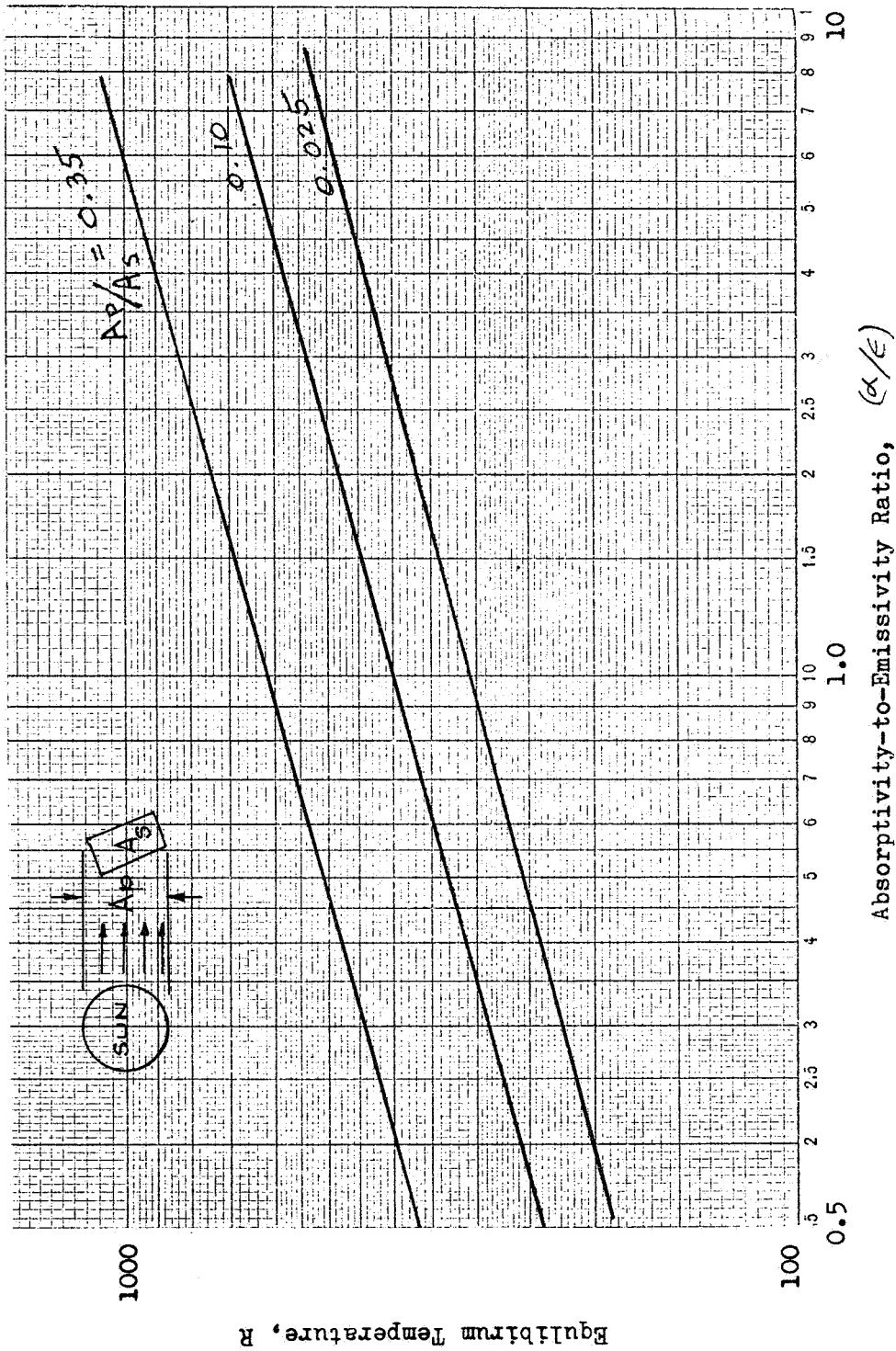
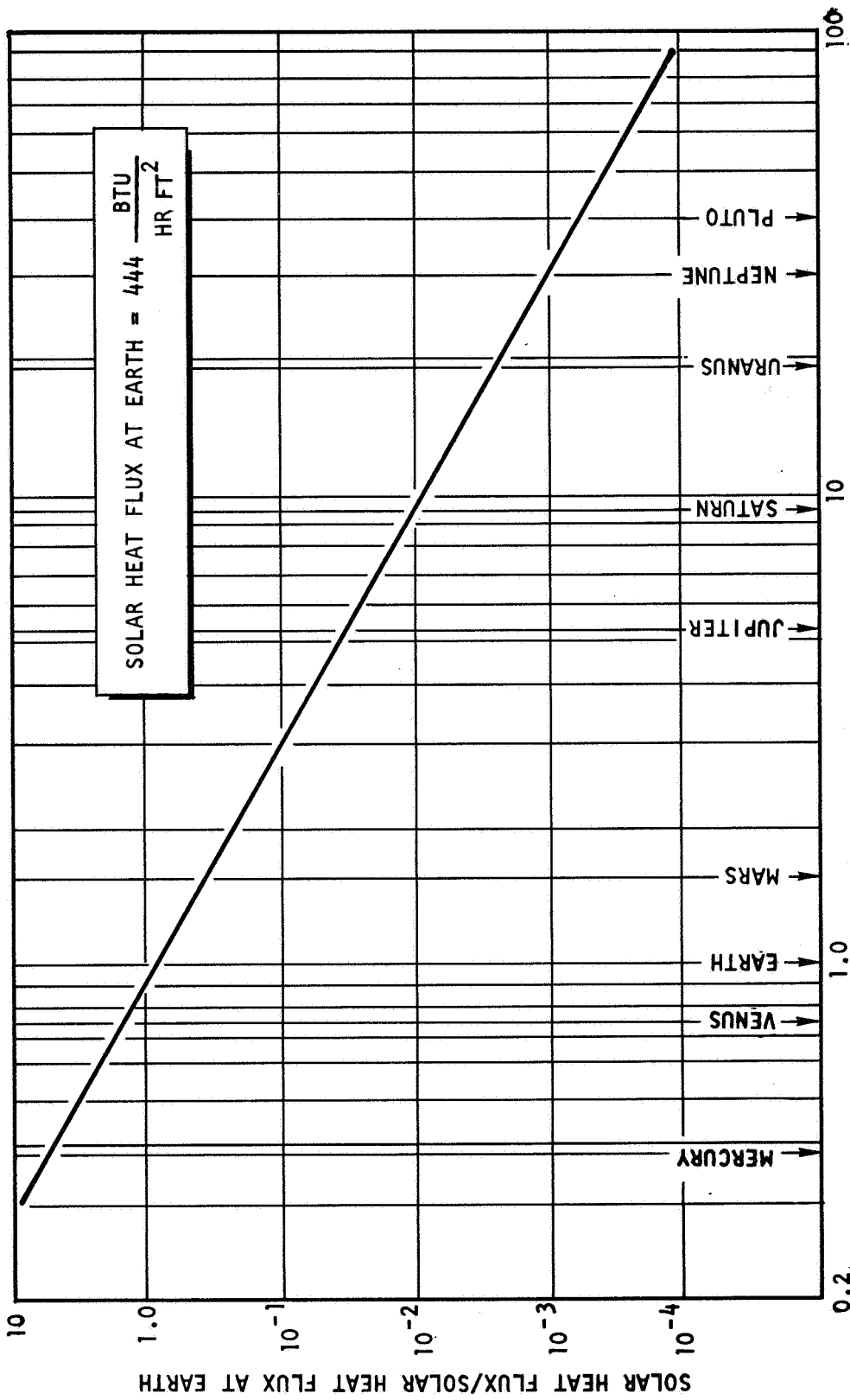


Figure 21. Single Surface Material Equilibrium Temperature in Earth Space



DISTANCE FROM SUN, ( $\frac{R}{R_0}$ )

Figure 22. Solar Heat Flux

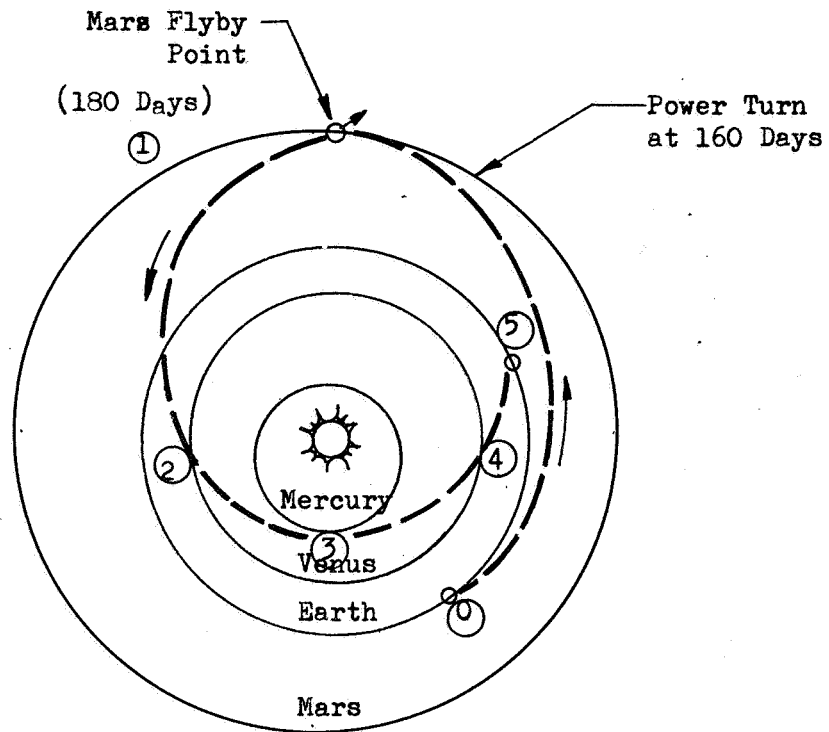
estimated for other space locations by employing the equation

$$\frac{T_{\text{space}}}{T_{\text{earth}}} = \left( \frac{I_{\text{space}}}{I_{\text{earth}}} \right)^{1/4} \quad (4)$$

where  $I_{\text{space}}/I_{\text{earth}}$  is heat flux ratio from Fig. 22.

Mars Flyby Mission. Many Mars missions can be chosen for analysis and will vary as a function of mission purpose and launch date. Mission durations can vary from fast trips (450 days) to as long as 1000 days depending upon stay time at Mars. The mission trajectory shown on Fig. 23 represents a fast-trip powered flyby of Mars. From a thermal analysis standpoint the trajectory flown involves varying solar heat flux inputs relative to vehicle and sun position. For the trajectory flown the vehicle return flight will pass close to a Mercury orbit and receive fairly high solar heat flux values due to nearness to the sun. Possible propulsion system operations for this mission profile are shown on Table 5. Temperatures will require overall heat balance determinations as a function of time.

An analysis will also require the determination of effects of turbopump preconditioning, possible propellant loss in preparing for engine start, and thermal protection methods on the capability of the vehicle and propulsion system to complete the mission successfully. This evaluation will identify the advantages or penalties of the various methods of eliminating or reducing turbopump preconditioning requirements. The effect of preconditioning time on the initiation and completion of the mission must be weighed against any component weight or propellant penalty.



- ① Launch from Earth Orbit
- ② Arrival at Mars - 180 Days
- ③ Venus Orbit Encounter - 357 Days
- ④ Near Mercury Orbit Encounter - 387 Days
- ⑤ Second Venus Orbit Encounter - 420 Days
- ⑥ Return to Earth - 450 Days (Total Trip Time)

Figure 23. Mars Powered Flyby (1973 Time Period)

TABLE 5

MARS POWERED FLYBY MISSION PROFILE  
(450-Day Mission)

Module	Function	Propulsion System Operation	Starts	Remarks
Midcourse and Power Turn Stage	Trajectory Orientation	10K thrust for 160 seconds or 50K thrust for 32 seconds every 50 days	3	Outbound Flight
	Power Turn	10K thrust for 3200 seconds or 50K thrust for 640 seconds at 160-day trajectory point	1	Flyby at Mars
	Trajectory Orientation	10K thrust for 60 seconds or 50K thrust for 12 seconds at 50-day intervals	6	Return Flight

### Coolant Transit Time

The heat input from the warm metal surfaces to the coolant (propellant) are greatest during the coolant transit time through the pump and line passages in the initial pump priming period. Comparison of coolant transit periods can be derived from a summative relationship through a j number of passages of length  $\ell$  as:

$$\tau = \sum_{n=1}^j \frac{\ell_n (\rho_c)_n}{(G_c)_n} \quad (5)$$

For long passage lengths and low coolant mass velocity, the coolant transit time will be long and will result in high heat input to a unit of flow. Coolant transit times through the pump were evaluated during Task III study and found to be small as reported in a later section.

### Turbopump Wall Time Response

The critical thermal time response period for the turbopump body structure can be developed from the transient heat-conduction equations for three extreme cases using one-dimensional heat conduction, constant film coefficient assumptions. These limiting cases are for (1) a finite wall thickness (t) with an infinite thermal conductivity (k), (2) an infinite wall thickness with finite thermal conductivity, and (3) an infinite film coefficient. The evaluation of the wall response is comprehensively covered under Task II discussion.

### Heat Conduction Critical Time

Penetration of heat from the turbine housing to the colder pump body during orbital flight after initial start was examined on a simplified

basis assuming no isolation of the pump from the turbine body. For this case the solution of the Fourier conduction equation becomes

$$\frac{T_T - T}{T_T - T_{Pi}} = \operatorname{erf} \frac{x}{2 \sqrt{\alpha \tau}} = \operatorname{erf} \left( \frac{1}{2 N_{F_0}^{1/2}} \right) \quad (6)$$

For a temperature rise at a distance  $x$  of  $1/e$  of the total temperature difference of the turbine to pump value

$$\frac{T_T - T}{T_T - T_{Pi}} = 1/e \quad (7)$$

the above solution becomes

$$N_{F_0} = \frac{\alpha \tau_c}{l^2} = \frac{e^2}{\pi} \quad (\text{conduction time}) \quad (8)$$

It is seen that the length of time for heat penetration from the turbine to the pump inducer section becomes a function of the pump length squared and the material thermal diffusivity. Aluminum pump housings in this respect are seen to allow a conduction time of 10 to 15 times shorter than an equivalent Inconel, nickel or titanium pump body. It would appear as a result that the isolation requirements of the pump from the turbine are considerably more severe with the aluminum pump body selection.

Figure 24 illustrates a summary of the pump rotor lengths for various axial and centrifugal flow machines listed in Table 27. Approximate agreement with the square root with thrust scaling rule is shown although in general the centrifugal flow pumps will have a shorter rotor conduction length and pose a more severe problem in this regard. Referring to Eq. 8 it is seen that as a result the critical time dependence for conduction

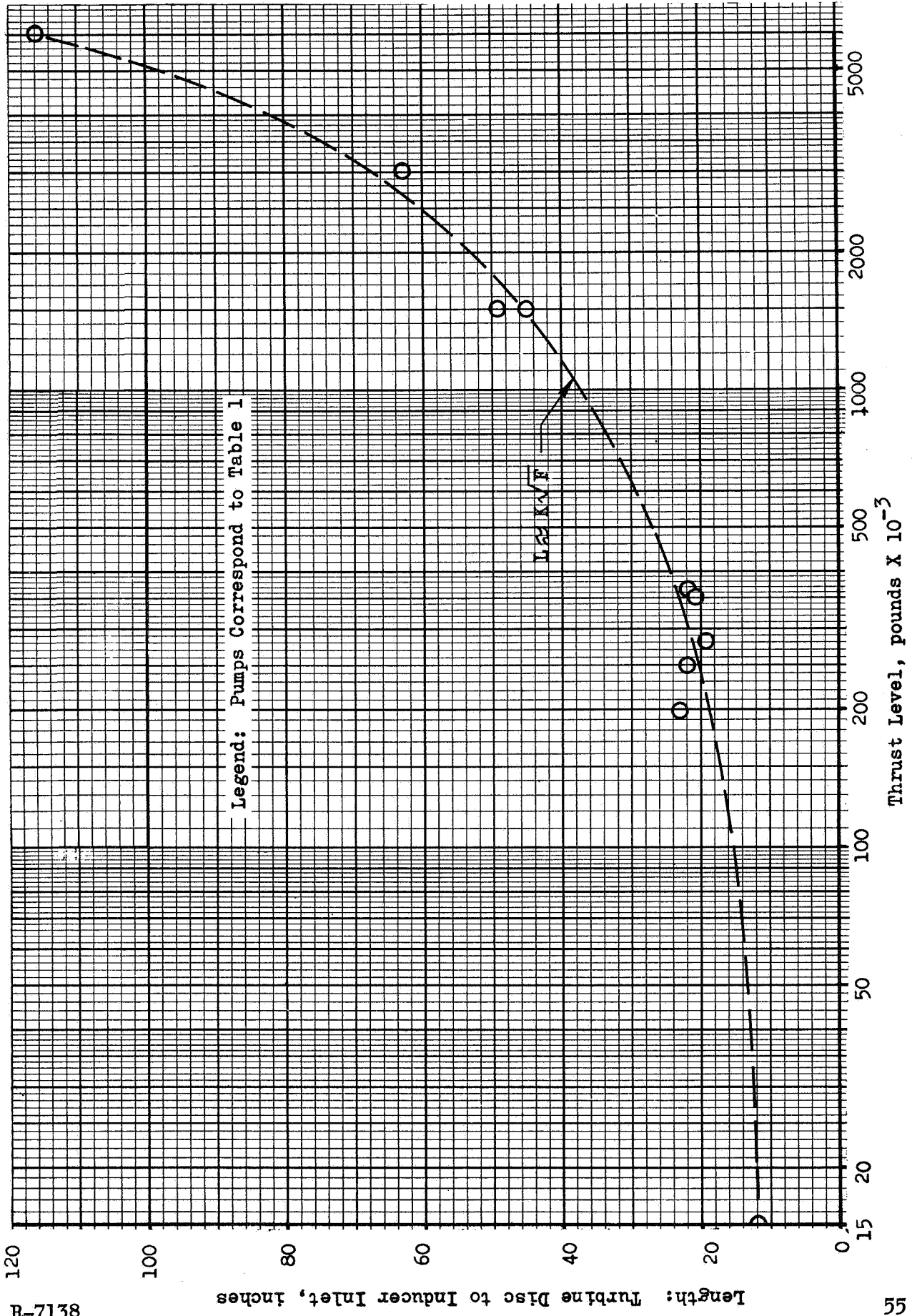


Figure 24. Rotor Conduction Distance vs Thrust Level

of heat from the turbine to the pump inducer section is

$$\frac{\tau_{c1}}{\tau_{c2}} = \left( \frac{F_1}{F_2} \right) \quad (\text{conduction time}) \quad (9)$$

with the critical conduction time linearly dependent upon thrust.

#### Orbit to Conduction Time Comparison

Earth orbit periods were compared to the time of heat soak through the rotor or pump housing length. Earth orbital times may be expressed in terms of the orbit and earth radii as

$$\tau_o = 1.41 \left( \frac{r_o}{r_e} \right)^{3/2} \quad (\text{hours}) \quad (10)$$

The ratio of orbit to conduction time then becomes

$$\frac{\tau_o}{\tau_c} = \frac{1.41 \pi \left( \frac{r_o}{r_e} \right)^{3/2} \alpha}{e^2 \ell^2} \quad (11)$$

where  $r_o$  is the radius of the orbit measured from the earth center,  $\alpha$  is the thermal diffusivity, and  $\ell$  is the length of the pump. A comparison of this time, required for heat penetration from the turbine to the inducer section, with the period of a 200-mile single orbit is shown in Fig. 25. This indicates that a large-thrust pump will not come to thermal equilibrium within the period of a single orbit and, for missions where restart occurs within the time period of a single orbit, any preconditioning requirements for the pump could be minimized if external thermal insulation to prevent environmental heat input is employed.

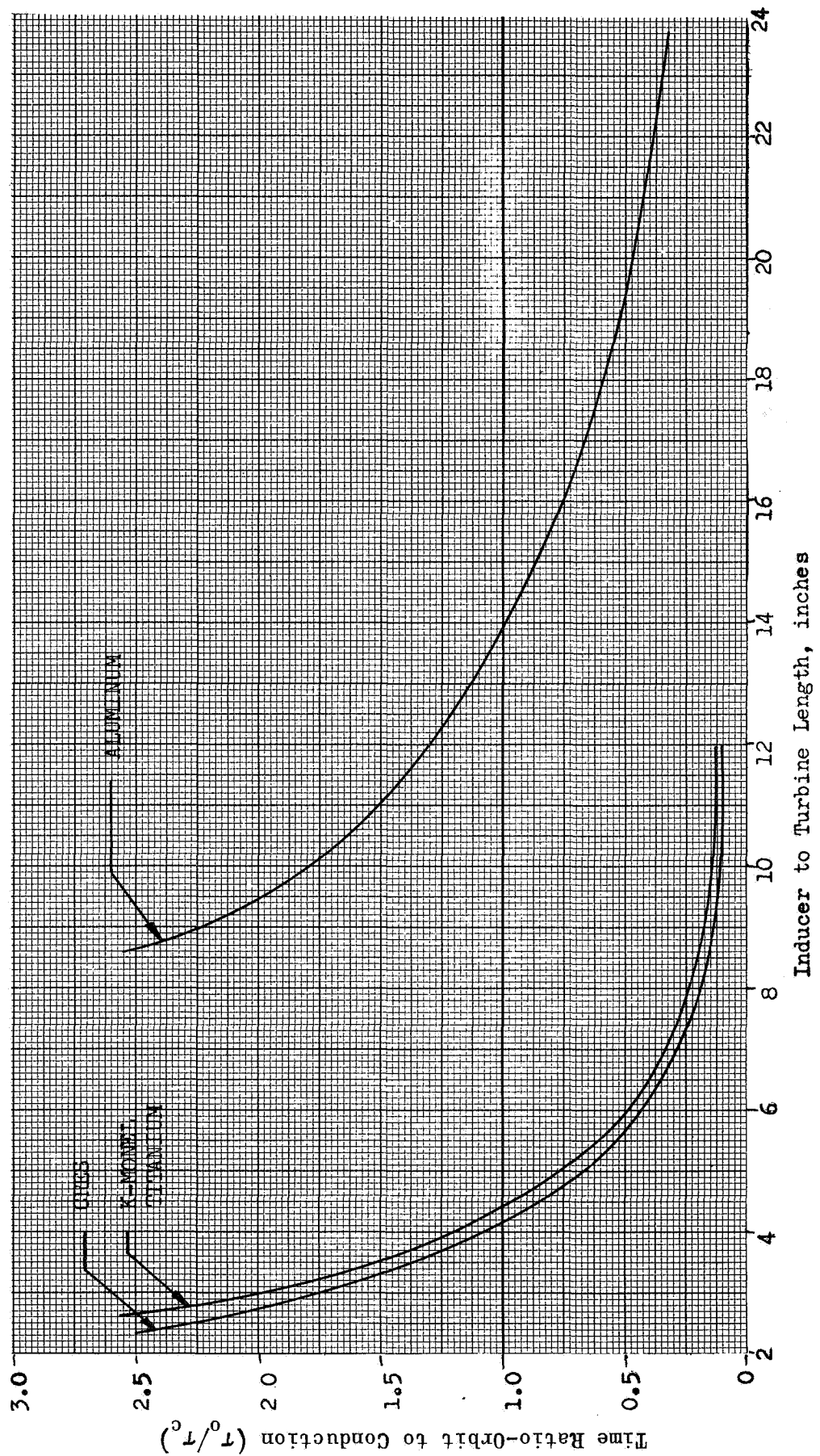


Figure 25. Orbit Time to Conduction Time Comparison, 200 Mile Earth Orbit, Radiation and Feedline Conduction Neglected

The above analysis represents the shortest time period for heat conduction through the pump. In reality exhaustion of the turbine heat through radiation to environment, conduction to the inlet and outlet turbine ducting, and the absorption of the turbine heat content by the heat capacity of the pump, will, combined with pump to turbine isolation, lengthen the period of thermal conduction as described under Task III. Writing the heat balance equation

$$\frac{\zeta \epsilon F A_s \tau}{W C_p} = - \int_{T_i}^T \frac{dT}{T^4 - T_s^4} \quad (12)$$

A simplified solution is allowed when

$$\left(\frac{T_s}{T}\right)^4 \ll 1.0 \quad \frac{\zeta \epsilon F A_s \tau T^3}{W_T C_{PT}} = \frac{1}{3} \left[ 1 - \left(\frac{T}{T_i}\right)^3 \right] \quad (13)$$

It is seen that the turbine chilldown time in space becomes directly proportional to the weight heat capacity product, inversely as the emissivity and surface area and inversely as the cube of the specified final temperature.

Integration of the exact solution to Eq. 12 yields

$$\frac{\zeta \epsilon F A_s \tau T_i^3}{W_T C_{PT}} = \frac{1}{2} \left(\frac{T_i}{T_s}\right)^3 \left[ \tan^{-1} \left(\frac{T}{T_s}\right) - \tan^{-1} \left(\frac{T_i}{T_s}\right) + \frac{1}{2} \log_e \left(\frac{T + T_s}{T - T_s}\right) - \frac{1}{2} \log_e \left(\frac{T_i + T_s}{T_i - T_s}\right) \right] \quad (14)$$

An expression for the achievement of a near equilibrium temperature can be made by the following relationship

$$\frac{T - T_s}{T_i - T_s} = \frac{1}{e} \quad (15)$$

For  $T_i/T_s \rightarrow \infty$  the  $1/e$  equilibrium temperature value of the turbine can be developed in terms of the time function as

$$\frac{\zeta \epsilon F A_s \tau_c T_i^3}{W_T C_{PT}} = \frac{e^3 - 1}{3} = 6.33 \quad (16)$$

An expression of the function  $\beta$  for other finite ratios of  $T_i/T_s$  may be seen in Fig. 26.

Criteria for turbine and pump scaling, as developed in a following section, indicate that large-thrust turbines require a greater chilldown time (every thing else being equal) due to a higher compactness factor, i.e., higher weight or volume to surface area ratio. This results in a turbine chilldown due to radiation along the approximate scaling rule

$$\frac{\tau_{c1}}{\tau_{c2}} = \left( \frac{F_1}{F_2} \right)^{1/2} \quad (17)$$

An example of the approximate time required for turbine chilldown may be expressed from solution of Eq. 14 for the following conditions for a J-2 turbine

$$\begin{aligned} \frac{W_T}{A_s} &= 0.534 \text{ lb/in.}^2 \\ \epsilon &= 0.8 \\ F &= 1.0 \\ C_{PT} &= 0.12 \text{ Btu/lb-F} \\ T_i &= 1600 \text{ R} \\ \zeta &= 3.31 \times 10^{-15} \text{ Btu/in.}^2 \text{ sec R}^4 \end{aligned}$$

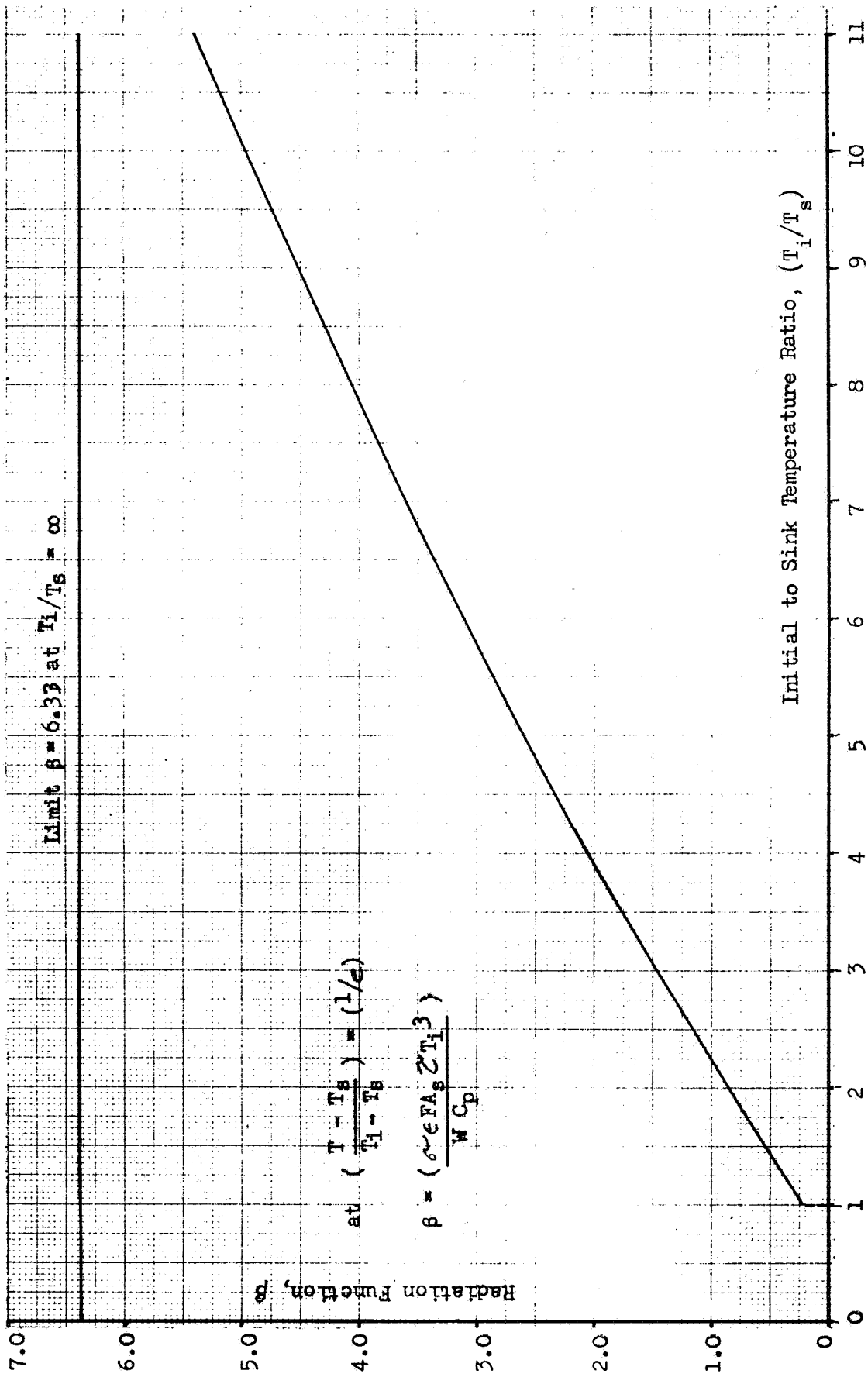


Figure 26. Radiation Function vs Initial to Sink (or Equilibrium) Temperature

A value of 10.4 hours is computed for a 0-degree sink condition. In reality conduction of heat to the cold pump body and to turbine inlet and exhaust ducting will reduce required radiation times below that predicted analytically. A comparison of the predicted J-2 fuel and turbine chill-down time with Saturn flight data is made in a later section of this report.

Table 6 illustrates a summary of approximate pump and turbine weights and external surface areas for existing turbopumps and for some detailed paper designs. It is seen that larger-thrust turbopumps in general have a larger weight to surface area. In general, if the characteristic dimension of the pump increases by the square root of the thrust and the percentage of void within the pump remains the same with scaling, the volume to surface area can be translated to a weight to surface area as (with reference to Table 7)

$$\frac{W}{A_s} = \frac{\rho C_v V}{A_s} \propto \rho C_v D_{\text{characteristic}} \propto \sqrt{F} \quad (18)$$

Agreement with the above relationship and Table 7 results were found to be good.

As a consequence from the radiation relationship shown in Eq. 14, small-thrust turbines will chill more rapidly and small-thrust pumps will warm to an equilibrium temperature more rapidly than large-thrust turbopumps. Consequently a greater pump insulation thickness is required on small turbopumps to prevent warming from a prechilled or final-state condition.

TABLE 6

VOLUME TO SURFACE AREAS FOR VARIOUS SIMPLE GEOMETRIC SHAPES  
APPROXIMATING PUMP AND LINE SURFACES

<u>Geometry</u>	<u>V/A<sub>s</sub></u>
Cylinder (L = ∞)	D/4
Cylinder (L = <∞)	L/4 (L/D + 1/2)
Sphere	D/6
Slab	t/2
Long Hollow Cylinder	t

Figures 27 and 28 illustrate LO<sub>2</sub> and LH<sub>2</sub> pump and turbine weights from Task IV study, respectively, without regard for pump material or operating pressure. A near linear correspondence between pump and turbine weight with thrust is shown. High-pressure pumps and lightweight titanium pumps would be expected to fall above and below a specific weight reference line. The greater weight of the larger-thrust turbines and pumps coupled with a greater weight per unit surface area results in a more difficult chilldown problem for the larger-thrust turbopumps.

Radiation to Conduction Time Comparison

Analysis was performed of the comparative time period for conduction along the pump length to the inducer section and the time period for radiation from the turbine body without significant turbine temperature deterioration due to pump soak of the turbine heat. For this analysis a simplified radiation chilldown relationship was chosen representing a near zero temperature sink and a high initial turbine temperature. The radiation time from this expression was compared with the conduction relationship

$$\frac{\tau_r}{\tau_c} = \frac{\pi}{3_e^2} \frac{W_T C_{P_t} \alpha \left( 1 - \left( \frac{T_R}{T_i} \right)^3 \right)}{\zeta \epsilon F A_{s_t} T_R^3 \ell^2} \quad (19)$$

TABLE 7  
SUMMARY OF TURBOPUMP WEIGHTS AND SURFACE AREAS

Code No.	Name	Weight, pounds				External Surface						Turbine W/A, $\frac{W}{A_s}$ , $\frac{lb}{in.}^2$	Pump W/A, $\frac{W}{A_s}$ , $\frac{lb}{in.}^2$
		Rotating Parts		Stationary Parts		Pump			Turbine				
		Pump	Turbine	Pump	Turbine	Axial Length	Diameter	Area, $in.^2$	Axial Length	Diameter	Area, $in.^2$		
<b>LH<sub>2</sub> PUMPS</b>													
1	P&WA RL10	6	6	31	12	8	9.3	234	5	7.0	110	0.16	0.16
3	MK 15-F	72	54	108	97	20	9.8	615	6	15.0	283	0.53	0.29
4	MK 30-F	69	55	184	141	20	14.3	897	11	12.5	432	0.45	0.28
5	MK 29-F	59	55	305	120	15	16.0	752	9	15.5	440	0.40	0.48
6	P&WA HG-3	146	42	387	80	38	14.4	1,716	18	13.2	332	0.37	0.31
7	P&WA HG-3A	113	42	290	80	18	15.8	896	8	13.2	332	0.37	0.45
8	MK 25-F	72	54	108	97	20	9.8	615	6	15.0	283	0.53	0.29
9	Aerojet M-1	1030	780	1630	1330	45	25.5	3,610	14	33.0	1460	1.4	0.74
10	RD 1.5M	930	700	1470	1200	41	19.9	2,570	12	30.4	1280	1.5	0.93
11	RD 3.0M	1870	1400	2830	2500	57	28.1	5,030	17	43.0	2300	1.7	0.94
12	RD 6.0M	3750	2800	5650	5000	83	40.7	10,600	25	62.3	4800	1.6	0.89
<b>LO<sub>2</sub> PUMPS</b>													
3	MK 15-0	16	57	140	72	8	15.0	378	9	17.0	470	0.28	0.41
4	MK 30-0	28	56	60	143	13	11.0	450	11	15.0	517	0.39	0.20
6	P&WA HG-3	67	59	204	240	34	12.6	1,350	10	20.0	628	0.48	0.20
7	P&WA HG-3	34	59	144	240	17	11.7	625	10	20.0	628	0.48	0.29
9	Aerojet M-1	170	600	1230	640	22	34.0	2,345	20	41.0	2580	0.48	0.60

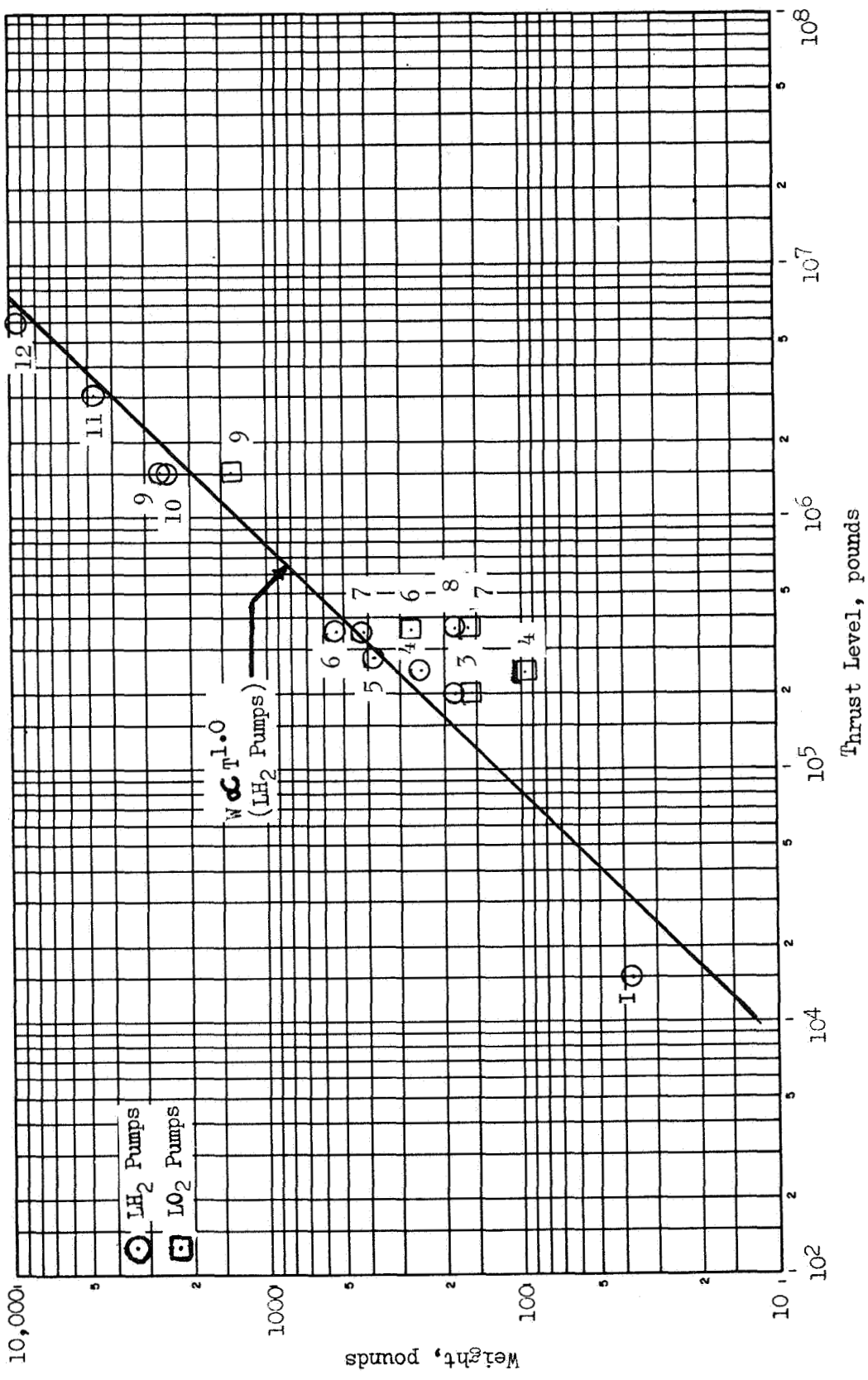


Figure 27. Approximate Pump Weight vs Thrust Level

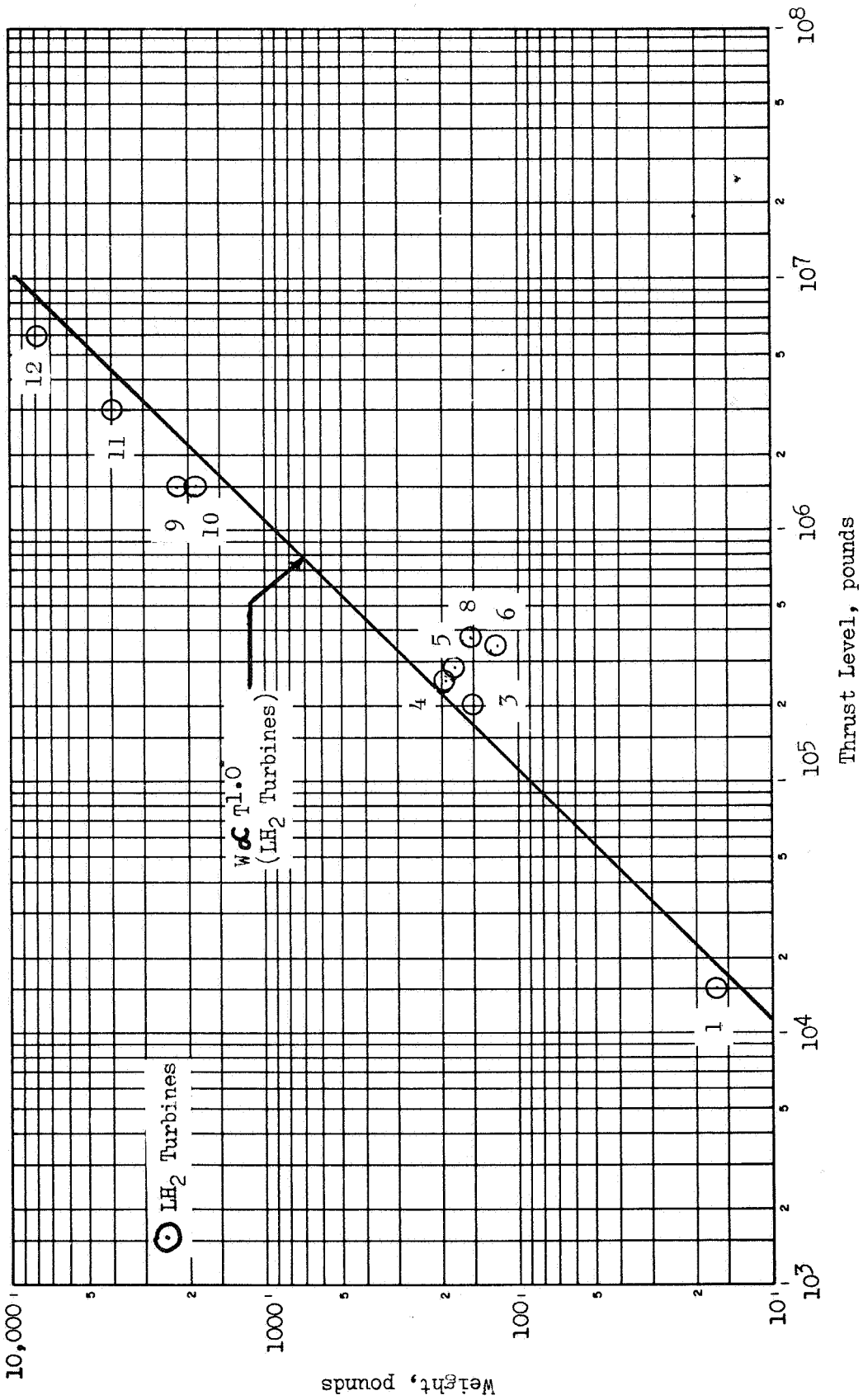


Figure 28. Approximate Turbine Weight vs Thrust Level

Figure 29 illustrates a typical solution of this relationship for aluminum, K-monel and titanium pumps with a turbine of Inconel ( $C_{PT} = 0.11$  Btu/lb F). For the example chosen it is shown that appreciable chilldown of the turbine has occurred through radiation before conduction has occurred through the length of the pump for pump materials of low thermal diffusivity such as titanium and K-monel. Aluminum on the other hand conducts the heat too rapidly to allow appreciable radiation chilldown of the turbine. The above analysis assumes no isolation of the pump and turbine and as a result represents the worst case for heat conduction to the pump. Pump to turbine isolation techniques are reviewed in Task III.

#### TWO-PHASE FLOW PUMP ANALYSIS

The objective of this study was to maximize the pump discharge pressure during initial mixed-phase operation. If the pump can deliver mixed-phase propellants satisfactorily, the problems of inlet line chilldown and of propellant settling can be greatly alleviated. In order to fulfill these objectives the pump discharge pressure must be related to the pump geometry, rotational speed, flowrate, inlet pressure, inlet quality, heat transfer coefficient between the impeller and the flow, flow passage temperature, time from start, etc. Such a prediction approach can then be used to determine the pump geometry and the operating conditions that will provide the optimum performance during mixed-phase operation.

During this study the pump impeller performance was related to the impeller geometry and to the operating conditions for the external vapor source case, (i.e., the case in which any vapor that exists enters the impeller through the inlet line). Other pump components downstream of the impeller, such as the diffuser vanes and the volute, were not treated. Since the propellant was hydrogen, the neglecting of the vapor generated on the suction surface of the inducer leading edge (an internal vapor source) may be reasonable due to the large thermodynamic suppression head properties of hydrogen.

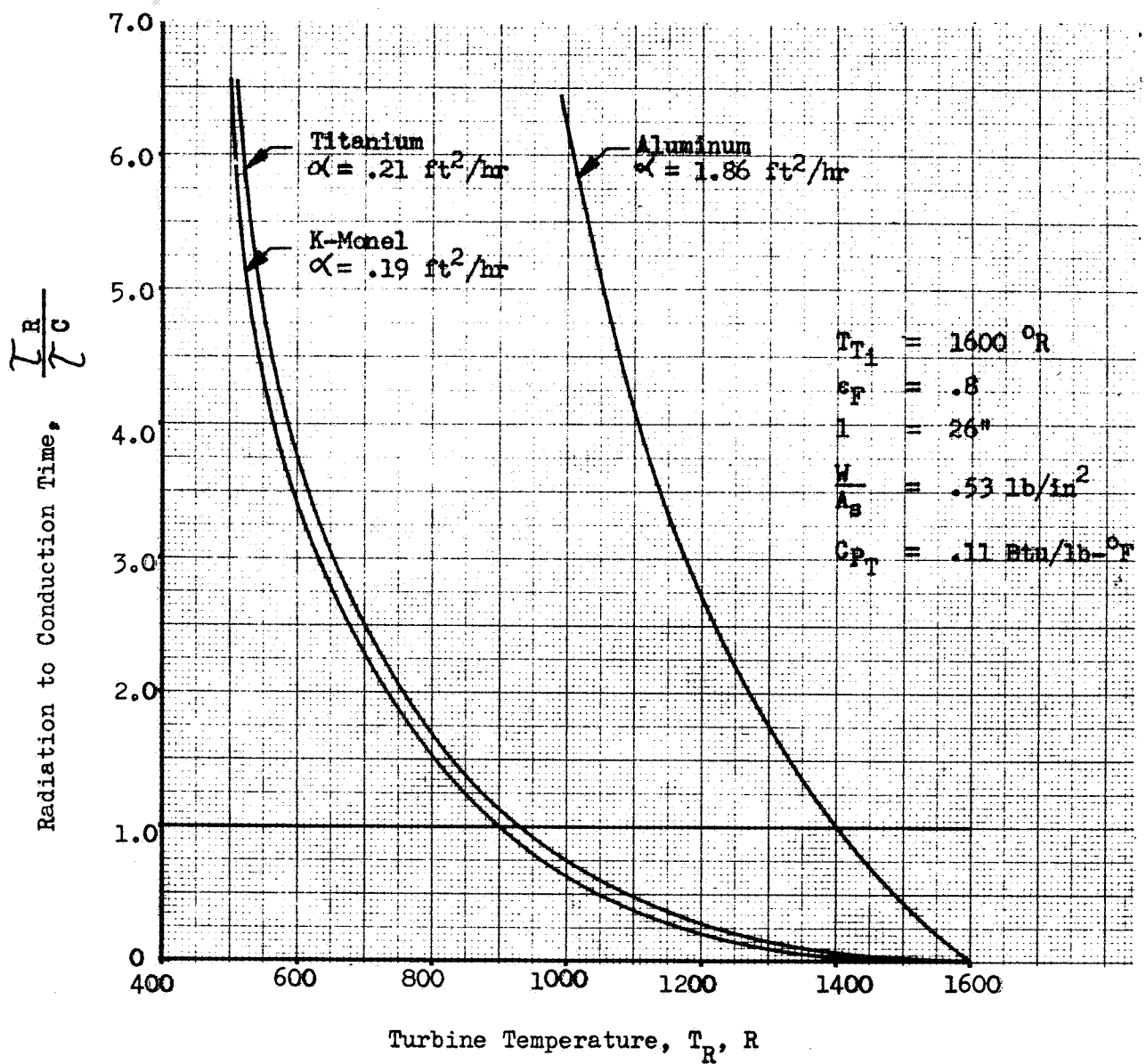


Figure 29. Turbine Radiation Time to Pump Heat Conduction Time Ratio

However, for any other propellants, this inducer vapor would have to be considered in order to obtain a realistic prediction. Since inducer vapor generation must be treated, approaches to analysis of the quantity generated were made.

The two types of impeller flow processes that were developed and analyzed were the constant quality and equilibrium cases. Shock wave effects were neglected and the impeller temperature was assumed to be equal to the flow temperature, thereby neglecting the vapor formed by heat transfer from a hot impeller (the other internal vapor source).

This study gives insight into the two-phase pumping problem, provides approaches to pump modifications for two-phase flow, and provides descriptions of the two flow processes that form the boundaries of the actual flow process. The lack of adequate experimental data made it impossible to select the actual flow process. Although shock wave effects were not considered in the analysis, they were studied (Ref. 17) and are discussed along with their possible effects on pump performance. Subsequent studies will have to include shock wave analyses because they can have a large effect on performance.

#### General Characteristics of Mixed-Phase Flow

One of the two basic reasons why a pump will develop less pressure rise under two-phase flow conditions is that the pressure rise is directly proportional to density. For an inlet hydrogen quality of 5 percent, for example, the two-phase flow density is only 1/4 the liquid density (Fig. 30) and therefore the pump pressure can be only approximately 1/4 of that obtained with liquid. The other reason for the low-pressure rise is that the flow velocity in the pump can be much higher than the acoustic velocity of the two-phase fluid. Since the pump is a liquid (incompressible) device which converts kinetic energy to static pressure by increasing the

Fluid Condition: Saturation at atmospheric pressure

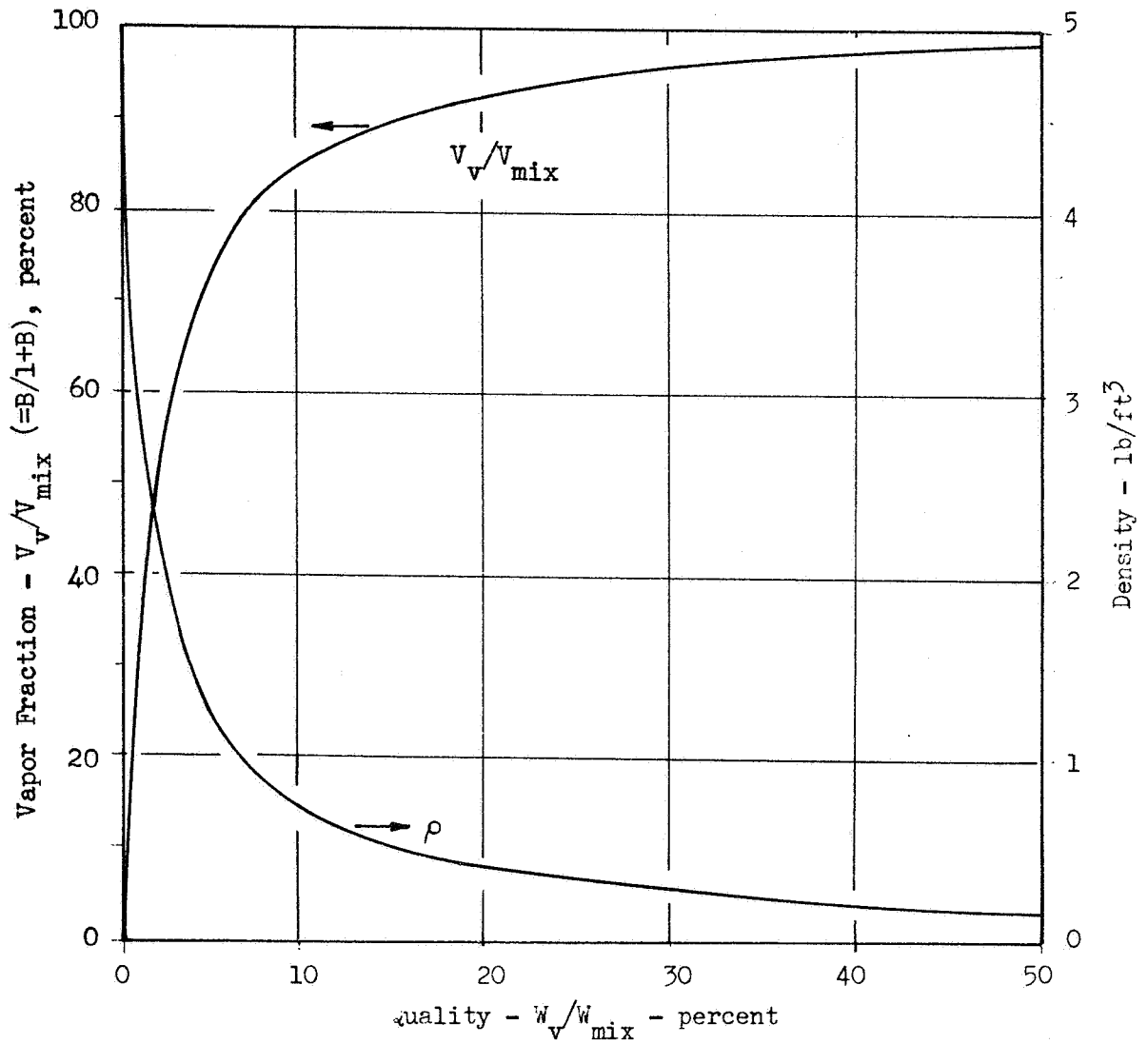


Figure 30. Vapor Volume Fraction and Density of Two-Phase Hydrogen

area of the flow passages, a flow condition above acoustic velocity will increase the kinetic energy of the flow, thereby decreasing rather than increasing the static pressure rise across the pump.

The two-phase flow process is also quite important to pump design and performance. The two types of flow processes which provide the boundaries of the actual flow process are equilibrium and constant quality. The difference between the two processes is in the assumption of the vaporization and condensation rates with the equilibrium process assuming that these rates are high enough to maintain equilibrium between the vapor and the liquid phases. Conversely, the constant-quality process assumes that these rates are very low and no vaporization or condensation takes place. Therefore, the quality of the flow is assumed to remain constant as it passes through the pump.

#### Acoustic Velocities

To determine the conditions under which acoustic velocity can be exceeded in a constant-quality, two-phase flow, the acoustic velocity relationship for a constant-quality process was derived and evaluated as a function of vapor to liquid volume ratio and compared to that for equilibrium two-phase flow. The constant-quality acoustic velocity relationship (Ref. 28) is expressed by Eq. 20.

$$c = \frac{c_L (1 + B)}{\sqrt{\left(\frac{\rho_V}{\rho_L} B + 1\right) \left[1 + \left(\frac{c_L}{c_V}\right)^2 \frac{\rho_L}{\rho_V} B\right]}} \quad (20)$$

The density ratio (Eq. 21) was obtained by empirically correlating the saturated hydrogen data in Ref. 38. The correlation and comparison with data are presented in Fig. 36 and 37. The liquid to vapor density may be expressed approximately by

$$\frac{\rho_L}{\rho_V} = \frac{805}{P} - 1.75 \quad (P = \text{psia}) \quad (21)$$

The acoustic velocities of the liquid and the vapor phases were obtained from Ref. 38 and are tabulated as follows:

T, R	P, psia	C <sub>L</sub> , ft/sec	C <sub>V</sub> , ft/sec
36.8	14.7	3610	1140

The equilibrium acoustic velocity relationship is shown in Eq. 22, 23, and 24.

$$C = \frac{\left[ 1 + X \left( \frac{\rho_L}{\rho_V} - 1 \right) \right] \sqrt{g}}{\sqrt{\frac{1+X}{144} \left( \frac{d\rho_L}{dP} \right) + \frac{X}{144} \left( \frac{\rho_L}{\rho_V} \right)^2 \frac{d\rho_V}{dP} - \left( \frac{\rho_L}{\rho_V} - 1 \right) \left( \frac{\rho_L}{144} \frac{dX}{dP} \right)}} \quad (22)$$

where

$$\frac{\rho_L}{144} \frac{dX}{dP} = \frac{(H_V - H_L) \left[ 1 + X \left( \frac{\rho_L}{\rho_V} - 1 \right) \right] - T \left( \frac{\rho_L}{\rho_V} - 1 \right) \left[ (1-X) \frac{dH_L}{dT} + X \frac{dH_V}{dT} \right]}{J (H_V - H_L)^2} \quad (23)$$

and

$$X = \frac{B}{B + \frac{\rho_L}{\rho_V}} \quad (24)$$

The acoustic velocities for constant-quality and equilibrium processes in two-phase hydrogen were obtained as a function of vapor to liquid volume ratio by solving Eq. 20 and 22, respectively. The results are presented on Fig. 31 and 32.

A two-phase flow with a constant-quality process presents less of an acoustic velocity problem in a pump than if it followed an equilibrium process as illustrated in Fig. 31 and 32. For a constant-quality process the acoustic problem will be encountered in existing pumps between a

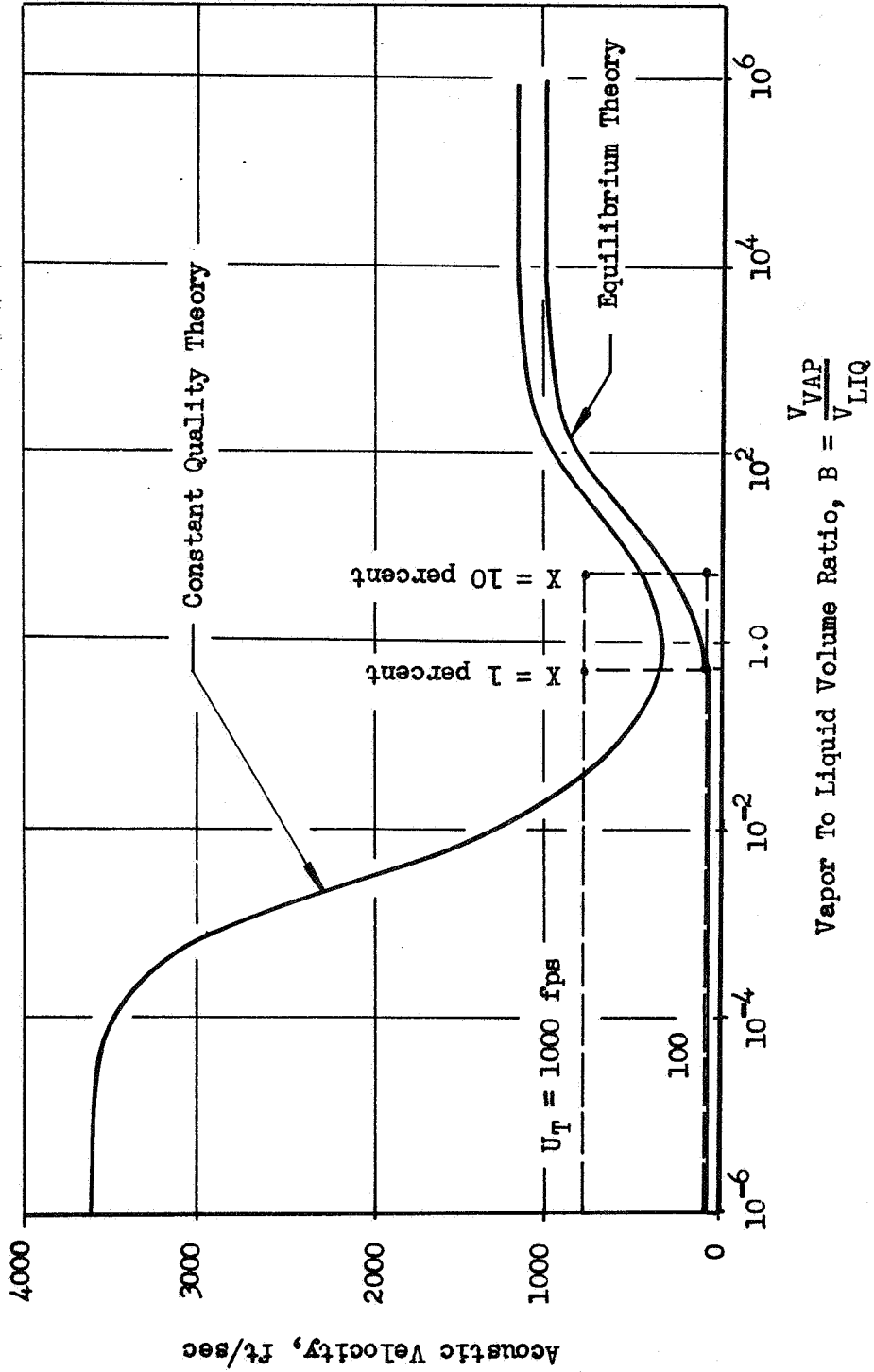


Figure 31. Acoustic Velocity in Two-Phase Hydrogen at 36.8 R (14.7 psia)

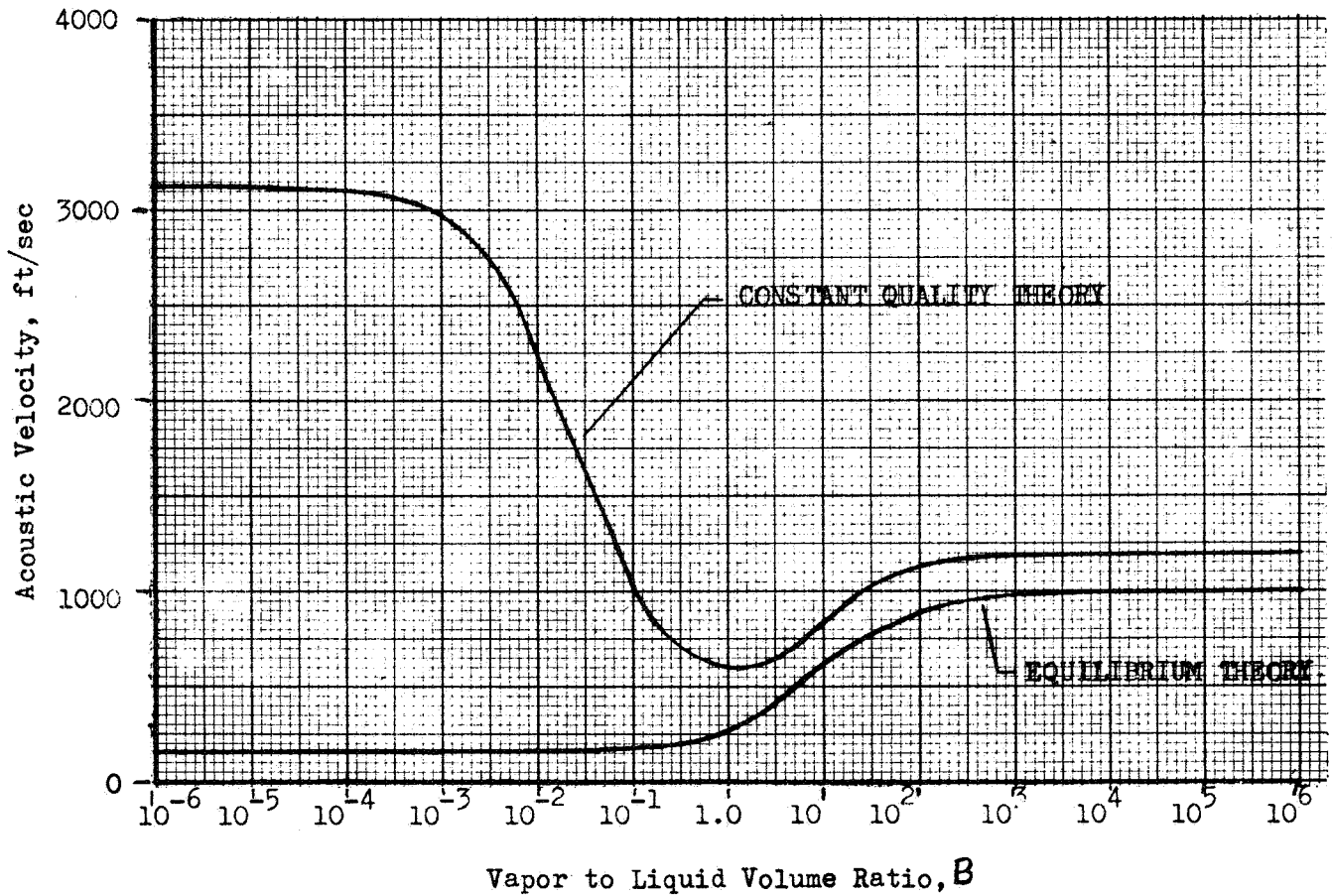


Figure 32. Acoustic Velocity in Two-Phase Hydrogen at 45.0 R, 48.0 psia

vapor to liquid volume ratio of 0.1 and 10. Operating a pump in this region would require reducing the inducer tip speed to stay below the acoustic velocity, or a low tip-speed preinducer can be placed upstream of the main inducer. If the flow in the pump follows an equilibrium process where the acoustic velocities are even lower in the same region of vapor to liquid volume ratios, a rather severe acoustic problem will exist even at low quality operation (Fig. 33 relates quality to vapor to liquid volume ratio).

The acoustic velocity can be increased by increasing the inlet pressure, as indicated by comparing Fig. 31 (14.7 psi) with Fig. 32 (48.0 psi).

### General Hydrodynamic Equations

To relate impeller performance to impeller geometry and operating conditions, the following one-dimensional equations for impellers were derived. Since they have heat addition, these initial equations include internal vapor source terms.

1. Energy equation

$$N_{ST} H \left( \frac{T_W}{T} - 1 \right) \frac{dA_W}{A} + \frac{U}{gJ} dU - \frac{W}{gJ} dW = dH \quad (25)$$

2. Momentum equation

$$\frac{144}{\rho} \frac{dP}{A} + f \frac{W^2}{2g} \frac{dA_W}{A} = \frac{U}{g} dU - \frac{W}{g} dW \quad (26)$$

3. Continuity equation

$$W = \frac{\dot{W}}{\rho A} \quad (27)$$

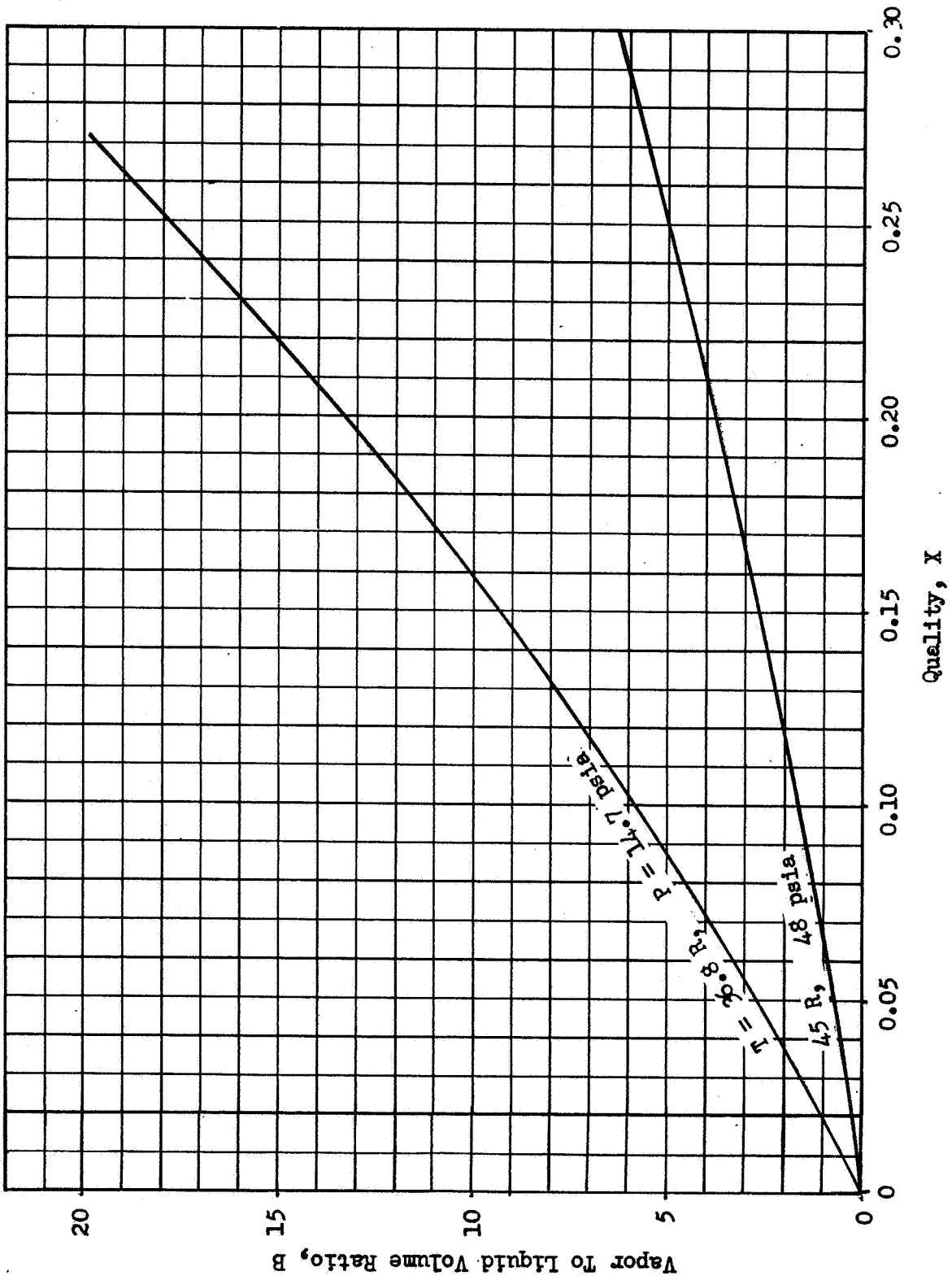


Figure 33. Hydrogen Vapor Fraction Relationships

In applying these equations to the external vapor source, two-phase flow case, the following assumptions were made:

1. The flow is one dimensional.
2. The two phases are homogeneously mixed.
3. The two phases are at the same pressure and velocity.
4. The impeller wall temperature equals the flow temperature.
5. The fluid friction losses are negligible.
6. The flow is shock free.

Therefore, the following are the general hydrodynamic equations that were used to analyze the impeller flow characteristics during operation with external vapor source, two-phase flow:

1. Energy equation

$$dH = \frac{U}{gJ} dU - \frac{W}{gJ} dW \quad (28)$$

2. Momentum equation

$$\frac{144}{\rho} dP = \frac{U}{g} dU - \frac{W}{g} dW \quad (29)$$

3. Continuity equation

$$W = \frac{\dot{W}}{\rho A} \quad (30)$$

### Constant-Quality Analysis

For the constant-quality analysis, the hydrogen properties were obtained from Ref. 38 by assuming an isentropic compression of each of the two individual phases beginning on the saturation line at atmospheric pressure.

In this flow process the quality remains constant while the temperatures of the two phases differ. A comparison of the empirical hydrogen property equations derived (Eq. 31 through 34) with data obtained from Ref. 38 are shown on Fig. 34. These correlations are similar to the classical relationships of incompressible flow for liquid and of perfect gas law for vapor.

$$\rho_L = 4.5 \text{ lb/ft}^3 \quad (31)$$

$$H_L = u + \frac{144 P}{\rho_L J} = -110 + \frac{144 P}{\rho_L J} \quad (32)$$

$$\frac{144 P}{\rho_V T_V} = R = 720 \quad (33)$$

$$H_V = C_p T_V = 2.28 T_V \quad (34)$$

$$\gamma = \frac{R}{1 - \frac{R}{J C_p}} = 1.685 \quad (35)$$

The final constant-quality flow process equations which relate the discharge static pressure to the discharge to inlet area ratio (normal to the relative velocities) for given values of inlet flow condition, geometry, and tip speed were obtained by simultaneously solving Eq. 28 through 38 and are presented below.

The continuity equation is

$$\frac{A_2}{A_1} = \frac{\rho_1/\rho_2}{W_2/W_1} \quad (36)$$

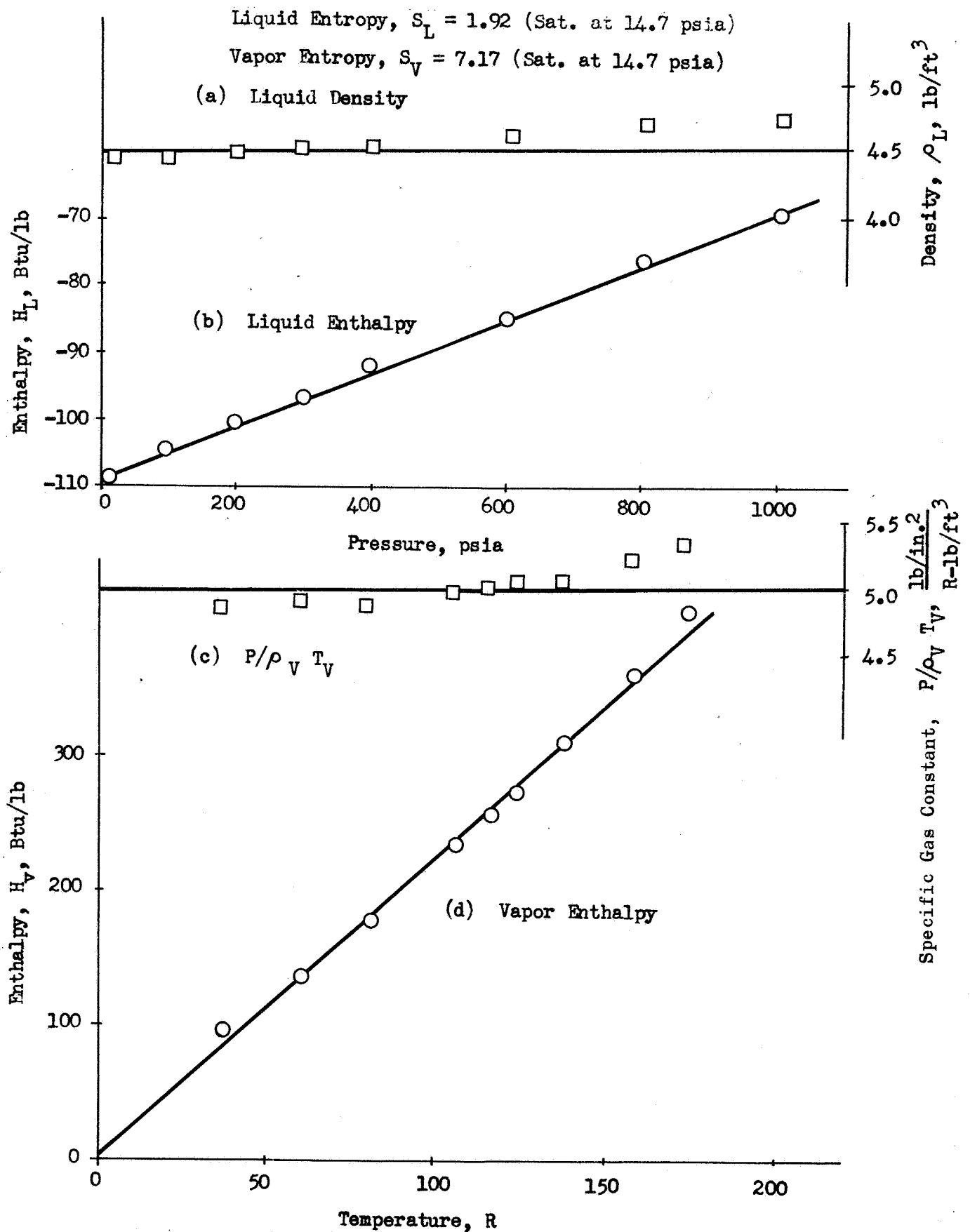


Figure 34. Liquid and Vapor Properties for Constant-Quality Analysis

The density ratio is

$$\frac{\rho_1}{\rho_2} = \frac{\frac{1 - X_1}{\rho_L} + \frac{X_1 R T_1}{144 P_1} \left(\frac{P_1}{P_2}\right)^{\frac{1}{\gamma}}}{\frac{1 - X_1}{\rho_L} + \frac{X_1 R T_1}{144 P_1}} \quad (37)$$

and the relative velocity ratio at the pump mean diameters is

$$\frac{W_2}{W_1} = \sqrt{\frac{\left(\frac{d_2}{d_1}\right)^2 + \frac{\phi_1}{2} - \frac{144 P_1}{J \rho_L} (1 - X_1) \left(\frac{P_2}{P_1} - 1\right) + X_1 C_P T_1 \left[\left(\frac{P_2}{P_1}\right)^{\frac{\gamma-1}{\gamma}} - 1\right]}{1 + \phi_1^2 - (1 + \phi_1^2) U_1^2 / 2gJ}} \quad (38)$$

Note that  $\frac{d_2}{d_1}$ ,  $\phi_1$ ,  $W_2/W_1$ , and  $U_1$  are at the rms diameters.

### Equilibrium Analysis

For the equilibrium analysis the hydrogen properties along the saturation line were obtained from Ref. 38. The empirical hydrogen property equations (Eq. 39 through 42) are compared with the data from Ref. 38 in Fig. 35 through 37. These relationships are not similar to the classical relationships for vapors and liquids. Clapeyron's equation was used to obtain the vapor pressure vs temperature relationship (Eq. 45) from the enthalpy and density correlations. This relationship is compared with the data from Ref. 38 in Fig. 38.

$$H_L = -232 + 3.32 T \quad (\text{Fig. 35}) \quad (39)$$

$$H_V = 82 \quad (\text{Fig. 35}) \quad (40)$$

$$\rho_L = 4.6 - P/100 \approx 4.4 \quad (\text{Fig. 36, approximation is for } T < 45 \text{ R}) \quad (41)$$

$$\rho_V = P/175 \quad (\text{Fig. 37}) \quad (42)$$

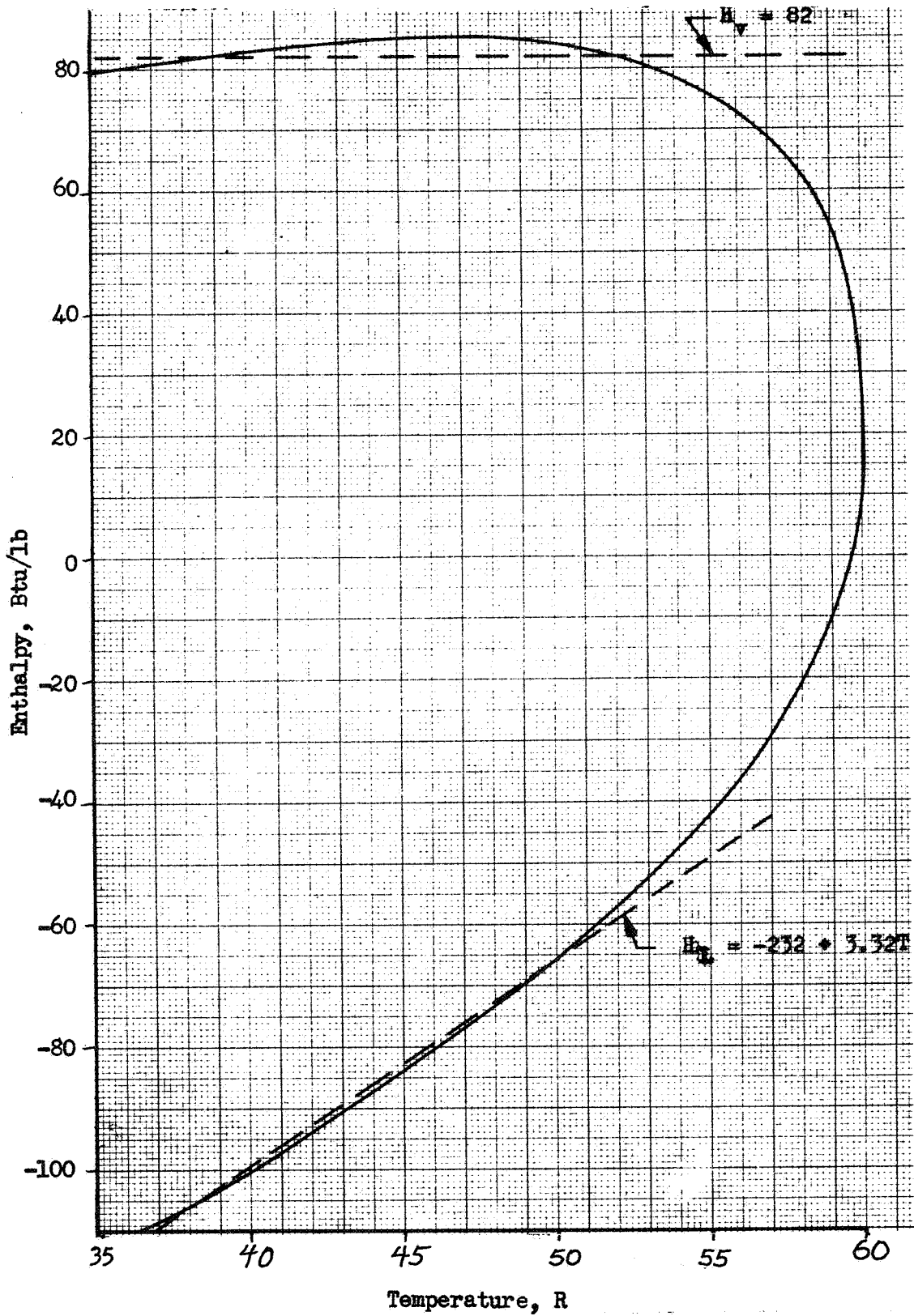


Figure 35. Temperature vs Enthalpy Along Hydrogen Saturation Line

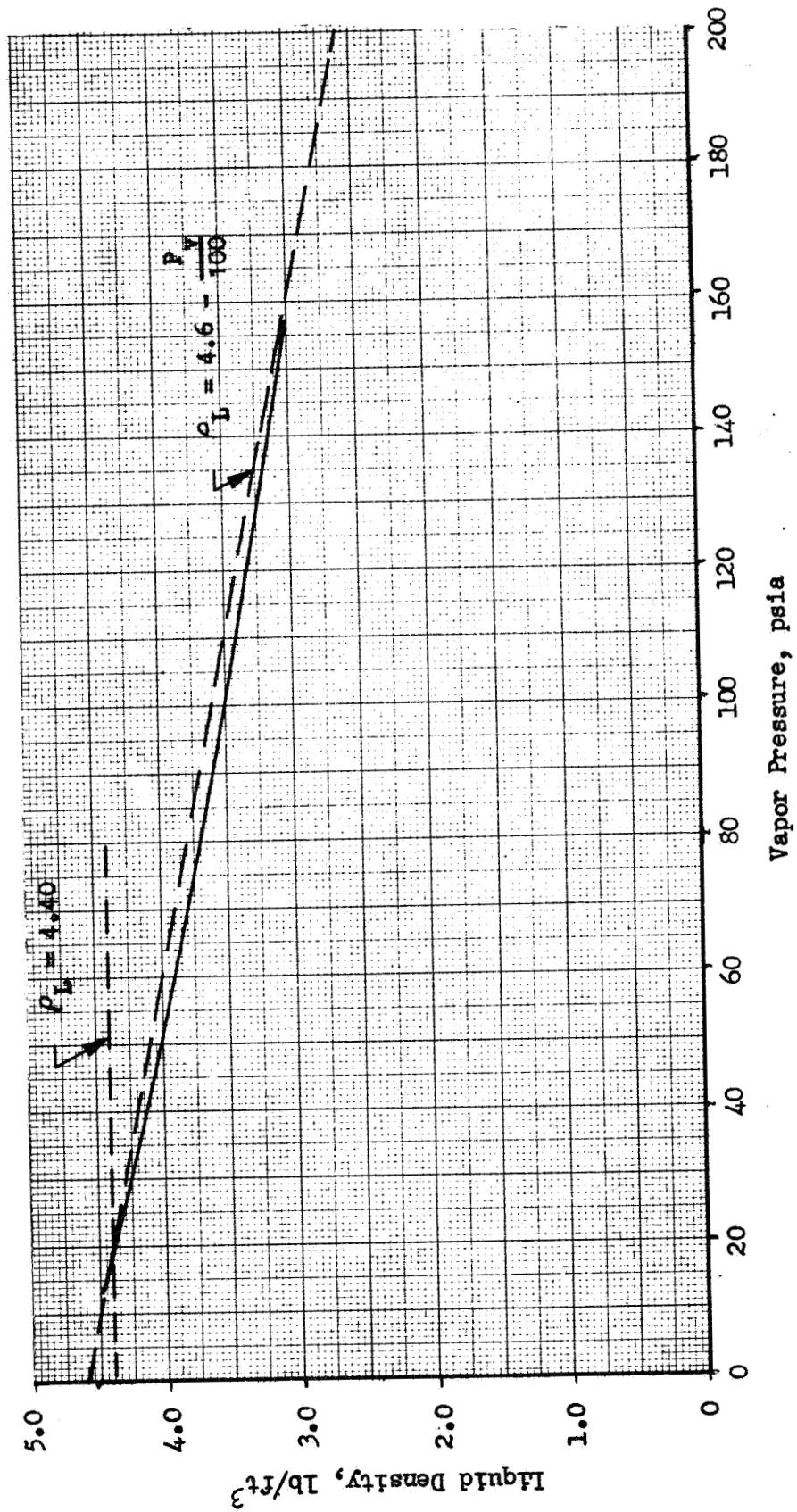
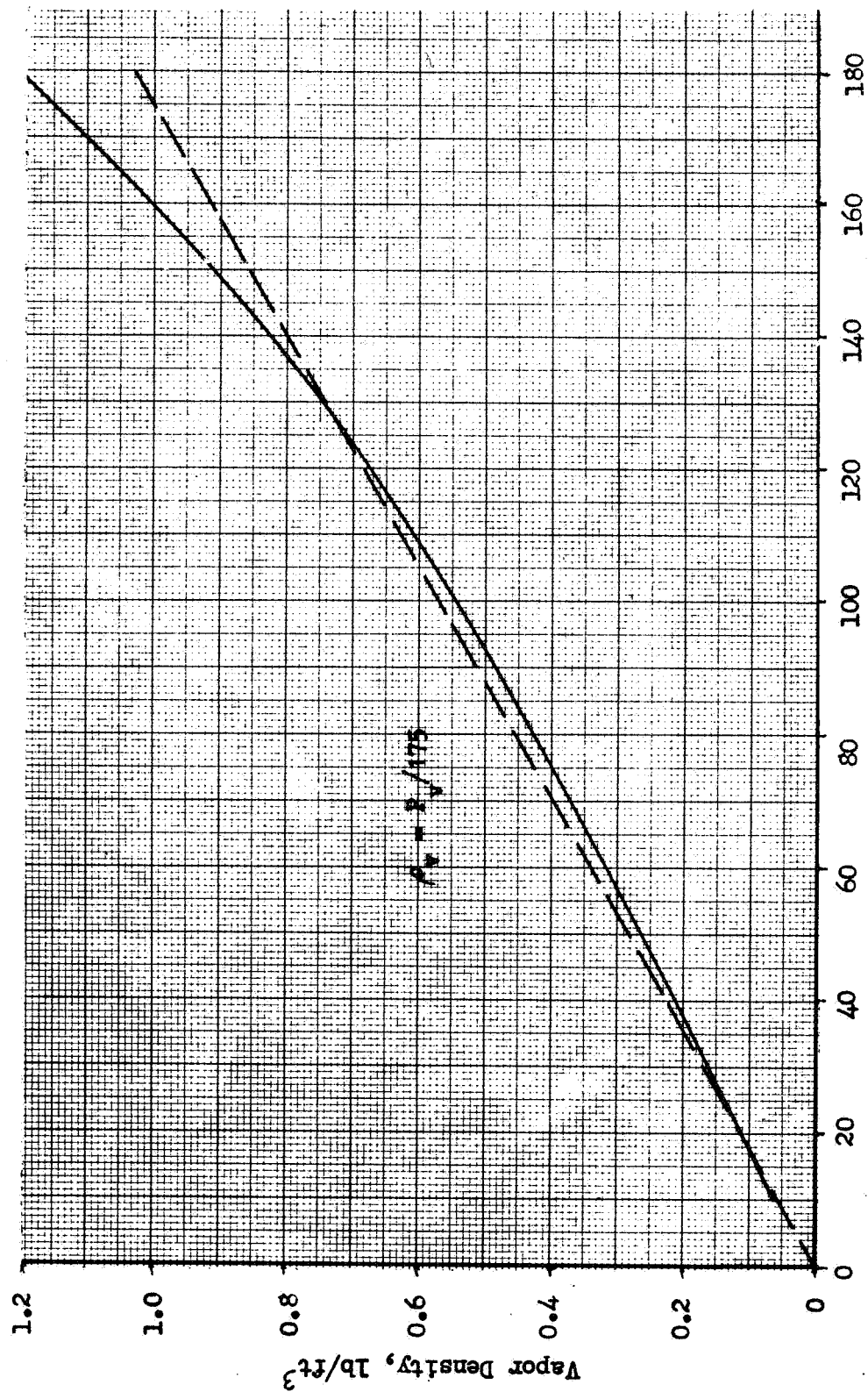


Figure 36. Liquid Density vs Vapor Pressure Along Hydrogen Saturation Line



Vapor Pressure, psia  
 Vapor Density vs Vapor Pressure Along Hydrogen Saturation Line

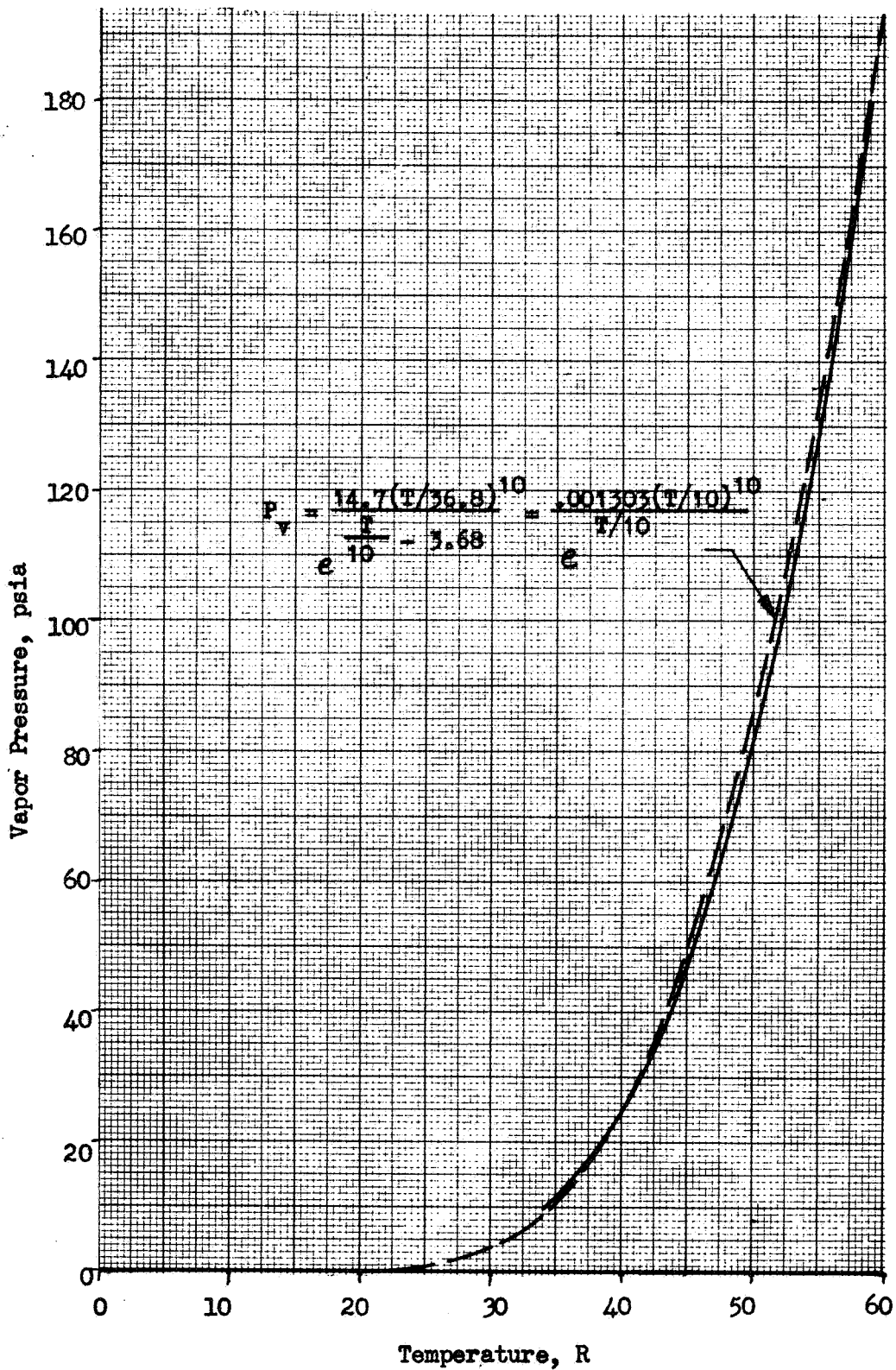


Figure 38. Vapor Pressure vs Temperature Along Hydrogen Saturation Line

$$1/\rho \approx 0.227 + 175X/P \quad (\text{For } T < 45 \text{ R}) \quad (43)$$

$$H = -232 + 3.32 T + X (314 - 3.32 T) \quad (44)$$

$$P = \frac{14.7 (T/36.8)^{10}}{e^{T/10 - 3.68}} = \frac{0.001303 (T/10)^{10}}{e^{T/10}} \quad (\text{Fig. 38}) \quad (45)$$

For this flow process the vapor-liquid mixture is compressed isentropically beginning at atmospheric pressure and temperature. During the compression the quality varies while condensation (or vaporization) occurs to keep the temperatures of the two phases equal.

Assuming that the temperature never exceeds 45 R, which is a satisfactory assumption as long as the inlet quality never exceeds 10 percent at a vapor pressure of 14.7 psia, the following equations were obtained by simultaneously solving Eq. 28 through 30 and 39 through 45 and were used to relate two of the most significant parameters, the static pressure and the discharge to inlet area ratio. The discharge quality is related to the inlet properties and the discharge temperature by

$$X_2 = \frac{X_1 \left( \frac{314}{T_1} - 3.32 \right) - 3.32 \ln \left( \frac{T_2}{T_1} \right) + \frac{144}{J \rho_L} \int_1^2 \frac{dP}{T}}{314/T_2 - 3.32} \quad (46)$$

where the last term in the numerator is

$$\frac{144}{J \rho_L} \int_1^2 \frac{dP}{T} = 0.216 \left\{ \frac{1}{e^{T_2/10}} \left[ \frac{(T_2/10)^9}{8!} - \sum_{M=0}^{M=8} \frac{(T_2/10)^M}{M!} \right] - \frac{1}{e^{T_1/10}} \left[ \frac{(T_1/10)^9}{8!} - \sum_{M=0}^{M=8} \frac{(T_1/10)^M}{M!} \right] \right\} \quad (47)$$

The static pressure and the mixture density relationships are expressed by Eq. 45 and 43, respectively. The relative velocity ratio at the impeller mean diameter is

$$\frac{W_2}{W_1} = \sqrt{\frac{\left(\frac{d_2}{d_1}\right)^2 + \phi_1^2}{1 + \phi_1^2} - \frac{3.32 [T_2 (1-X_2) - T_1 (1-X_1)] + 314 (X_2 - X_1)}{(1 + \phi_1^2) U_1^2 / 2gJ}} \quad (48)$$

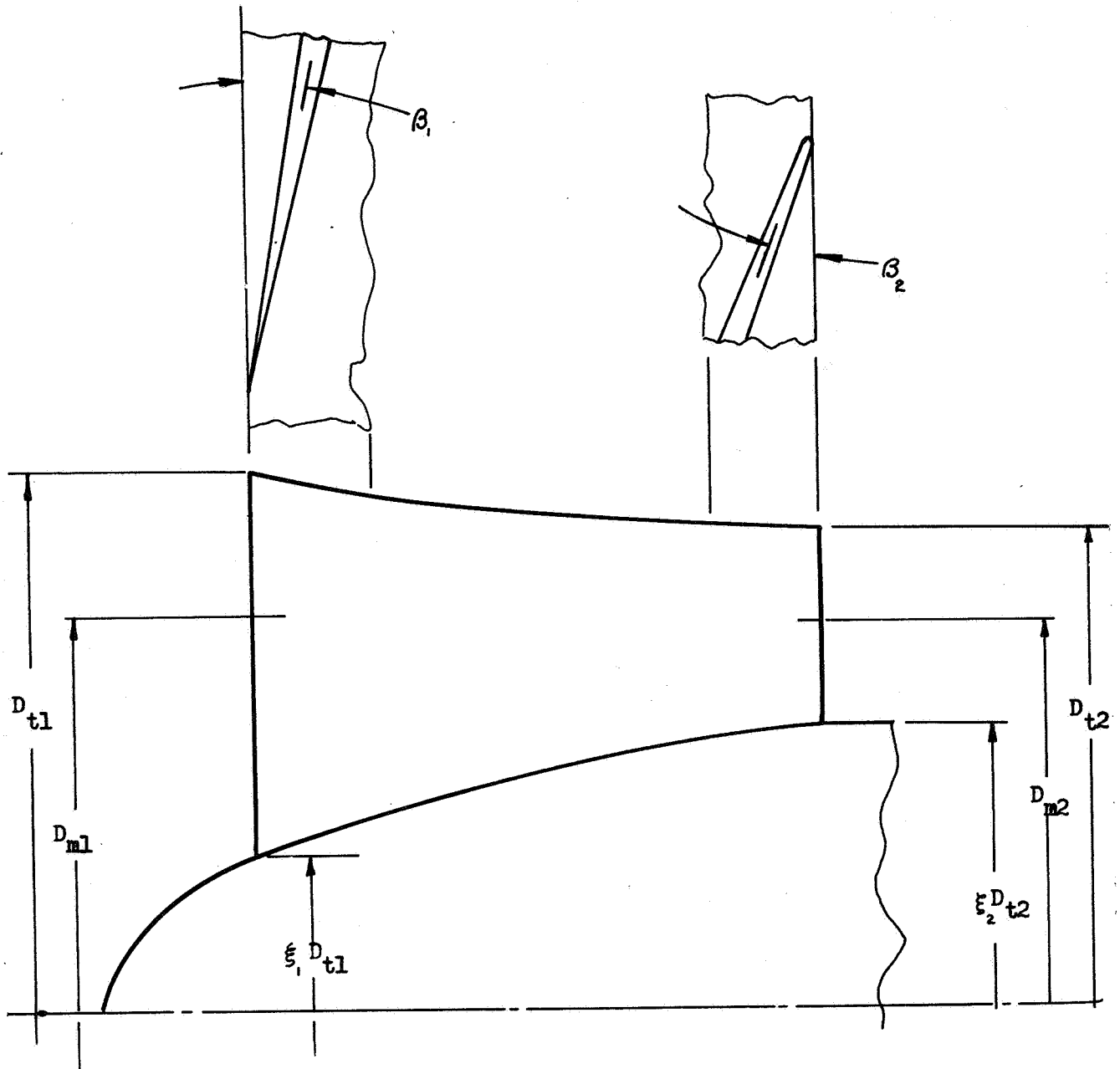
and finally, the impeller area ratio (normal to the relative velocities) is

$$\frac{A_2}{A_1} = \frac{\rho_1}{\rho_2} \frac{W_1}{W_2} \quad (49)$$

The values of  $d_2/d_1$ ,  $\phi_1$ ,  $W_2/W_1$ , and  $U_1$  are at the rms diameters.

#### Analysis of Results

Flow calculations were made for both processes at inlet qualities of 0 (liquid), 0.01, 0.10, and 1.0 (vapor) and at inducer tip speeds of 1000, 600, 300 and 100 ft/sec. The geometry analyzed was a constant rms diameter inducer, as shown schematically on Fig. 39. The computed results consist of inducer discharge static pressure vs inducer discharge to inlet area ratio. These parameters were chosen because they indicate the magnitude of the effect of both the pump geometry and the operating conditions on the acoustic phenomena and on the resulting low density. To provide a comparison, the liquid analysis is presented in Fig. 40 and 41. Figures 42 and 43 are constant-quality processes at inlet qualities of 0.01 and 0.10, respectively. Figures 44 and 45 are for equilibrium processes at inlet qualities of 0.01 and 0.10, respectively. The high-pressure rises and subacoustic velocity characteristics of inducers while operating in a liquid are shown in Fig. 40. The subacoustic velocity characteristic is indicated by the positive slope of each curve at an area ratio of one.



$$\frac{D_{m2}}{D_{m1}} = 1.0$$

$$A_1 = \frac{\pi D_{t1}^2 (1 - \xi_1^2) \sin \beta_1}{4}$$

$$A_2 = \frac{\pi D_{t2}^2 (1 - \xi_2^2) \sin \beta_2}{4}$$

Figure 39. Schematic of Inducer Geometry

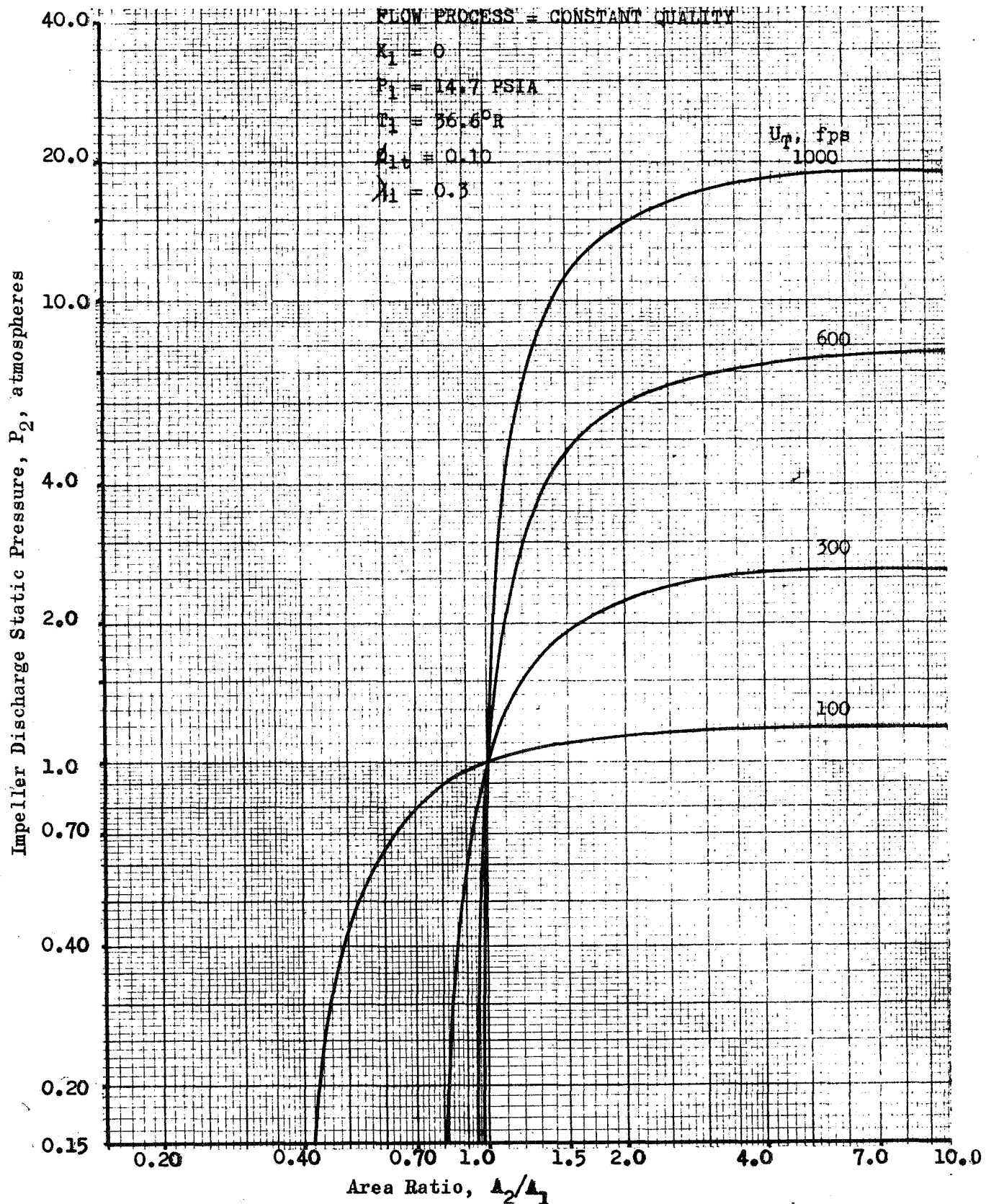


Figure 40. Effect of the Geometry of a Constant RMS Diameter Inducer on the Discharge Static Pressure When Pumping Two-Phase Hydrogen

Flow Process = Equilibrium

$X_1 = 0$

$P_1 = 14.7$  psia

$T_1 = 36.6$  degrees R

$\phi_{lt} = 0.10$

$\lambda_i = 0.3$

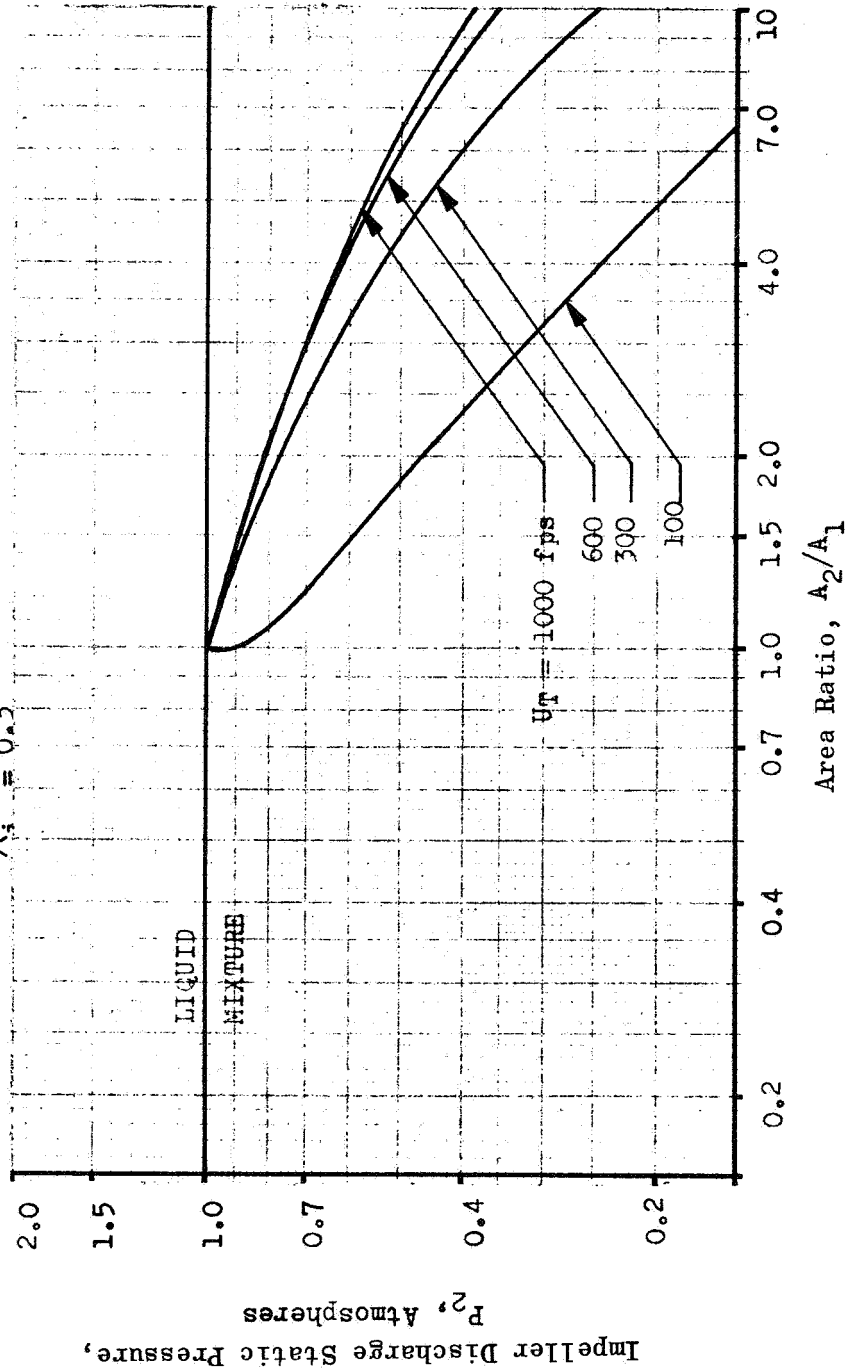


Figure 41. Effect of the Geometry of a Constant RMS Diameter Inducer on the Discharge Static Pressure When Pumping Two-Phase Hydrogen

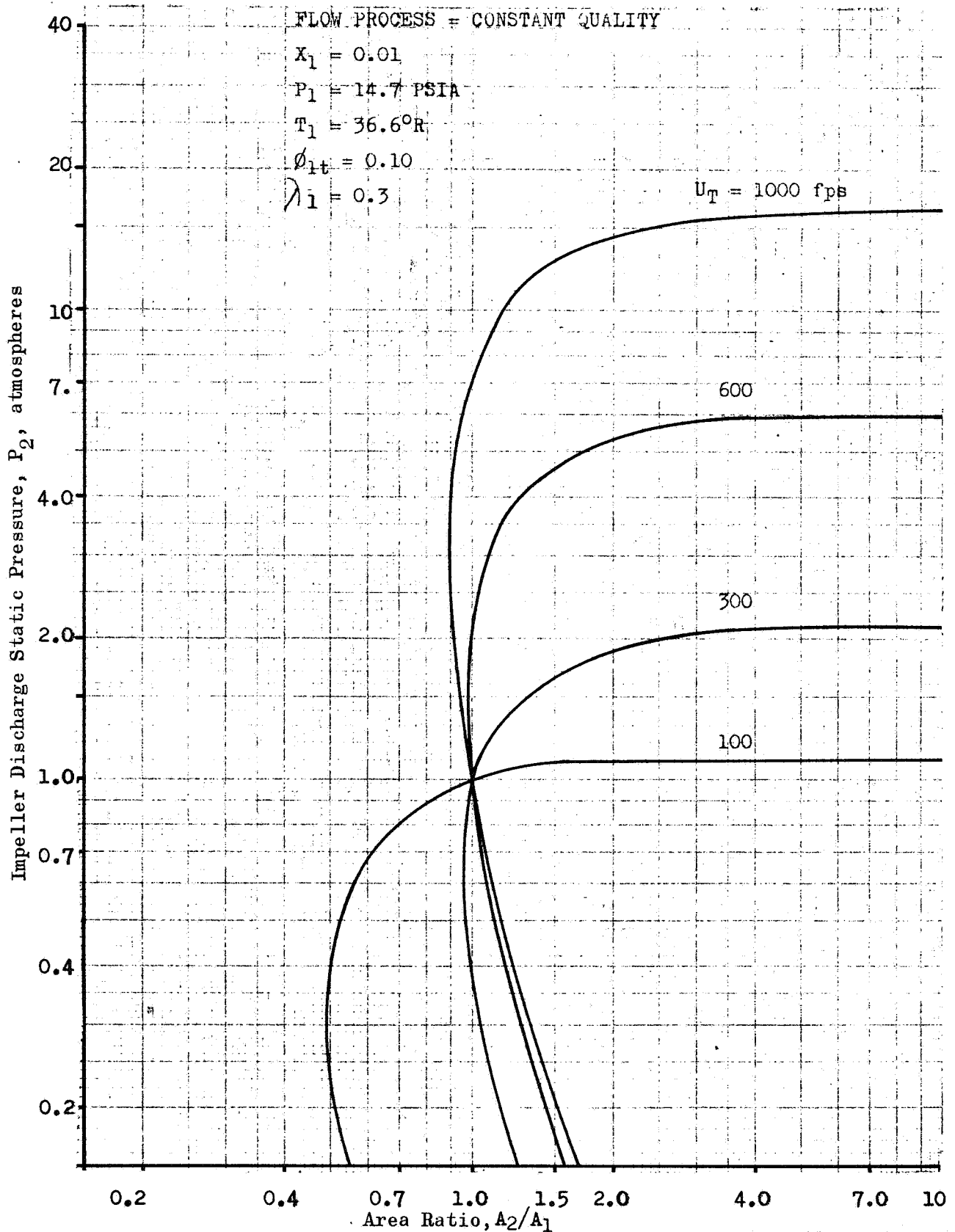


Figure 42. Effect of the Geometry of a Constant RMS Diameter Inducer on the Discharge Static Pressure When Pumping Two-Phase Hydrogen

Flow Process = Constant Quality

$X_i = 0.10$

$P_i = 14.7$  psia

$T_i = 36.6$  degrees R

$\phi_{it} = 0.10$

$\lambda_i = 0.3$

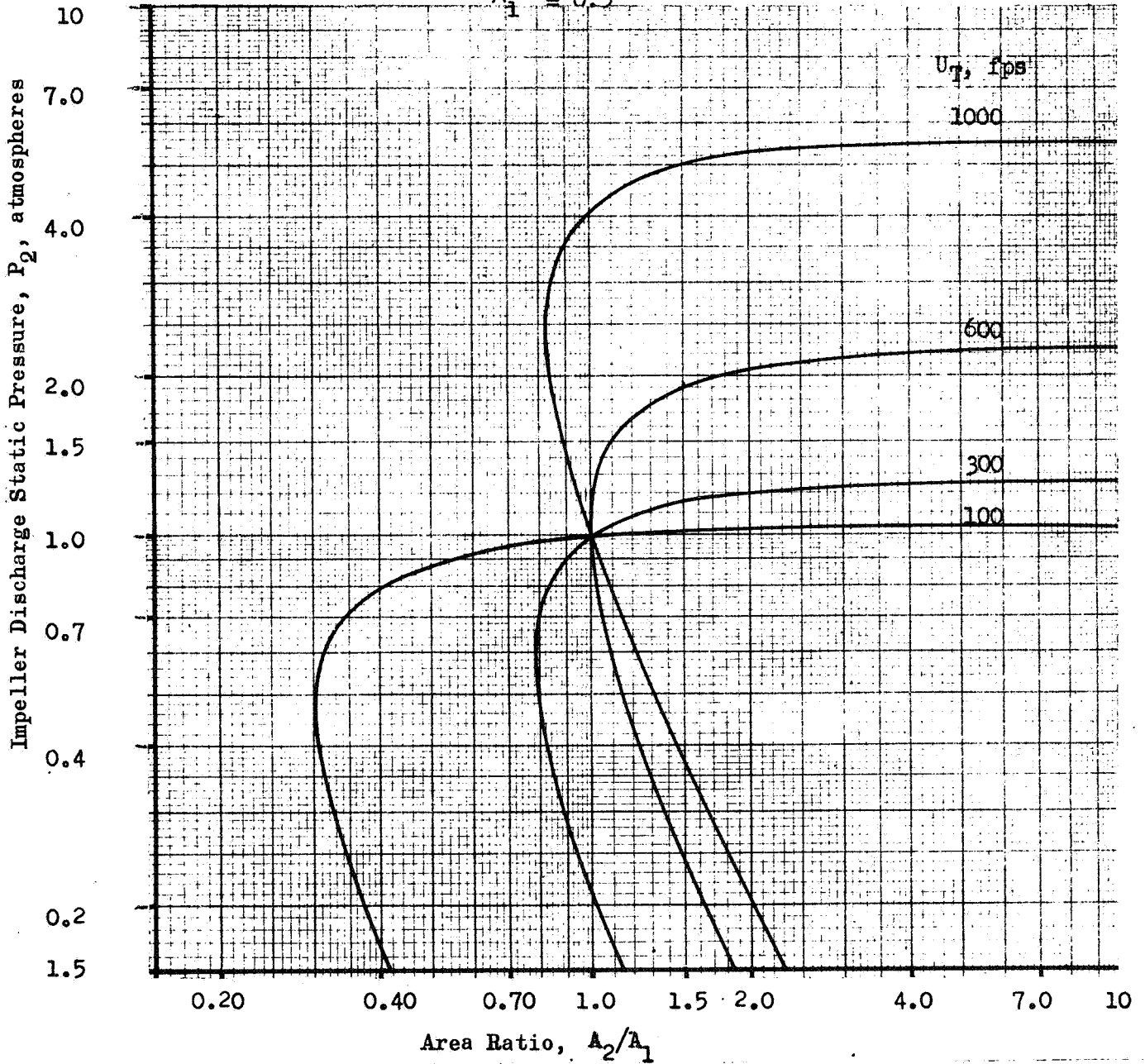


Figure 43. Effect of the Geometry of a Constant RMS Diameter Inducer on the Discharge Static Pressure When Pumping Two-Phase Hydrogen

Flow Process = Equilibrium

$x_1 = 0.01$

$P_1 = 14.7 \text{ psia}$

$T_1 = 36.6 \text{ degrees R}$

$\phi_{it} = 0.10$

$\lambda_1 = 0.3$

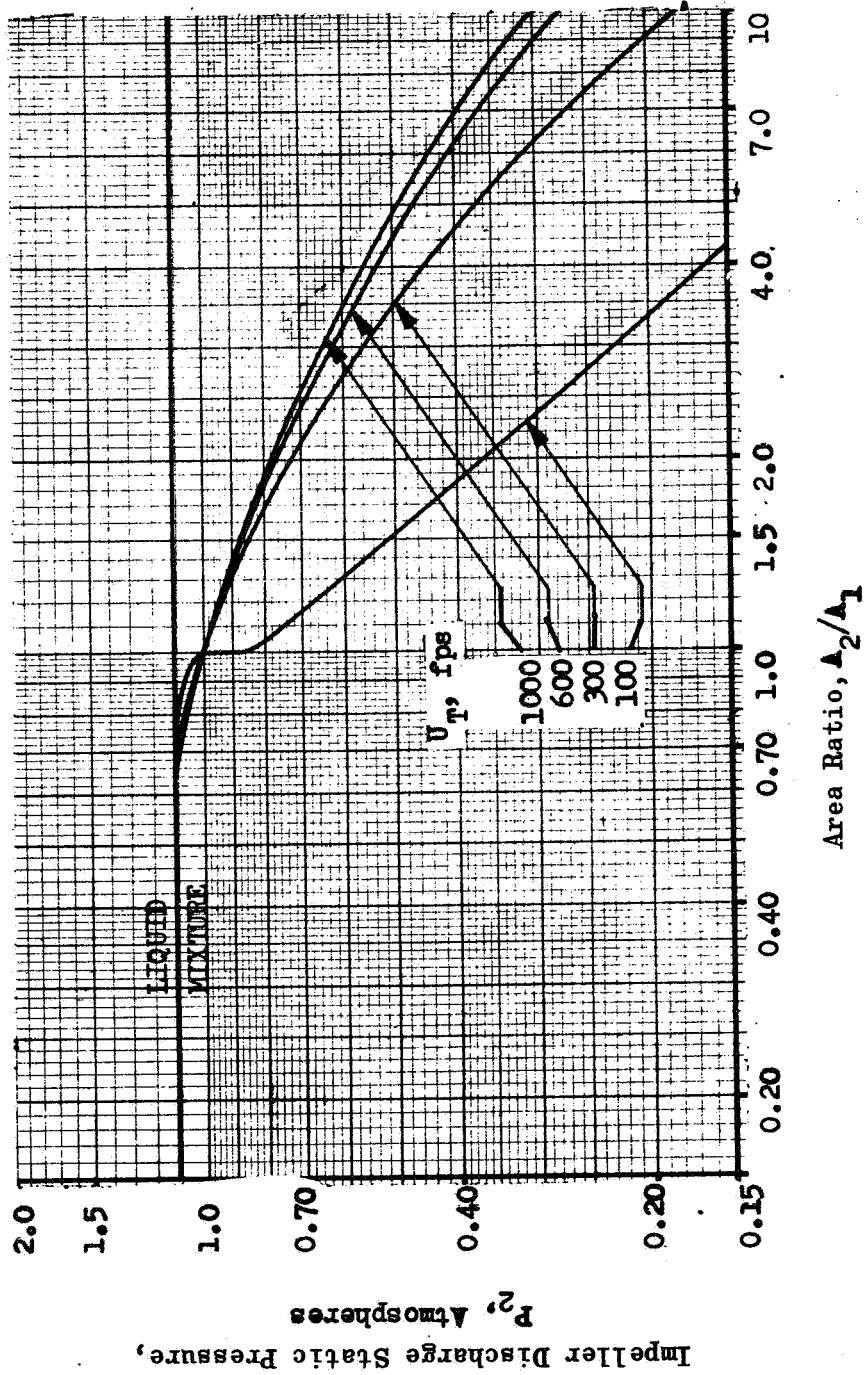


Figure 44. Effect of the Geometry of a Constant RMS Diameter Inducer on the Discharge Static Pressure When Pumping Two-Phase Hydrogen

Flow Process = Equilibrium

$X_1 = 0.10$

$P_1 = 14.7$  psia

$T_1 = 36.6$  degrees R

$\phi_{1t} = 0.10$

$\lambda_i = 0.3$

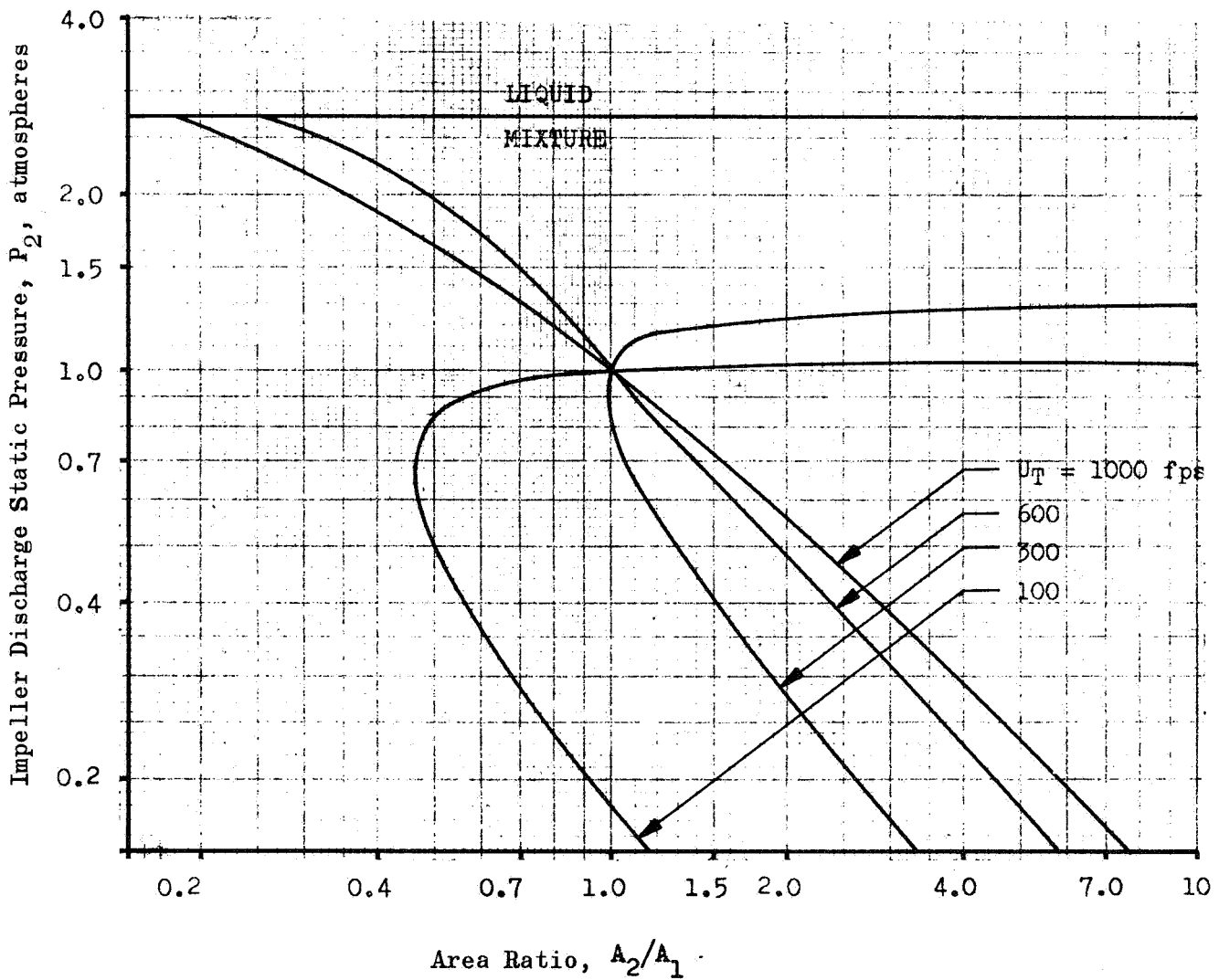


Figure 45. Effect of the Geometry of a Constant RMS Diameter Inducer on the Discharge Static Pressure When Pumping Two-Phase Hydrogen

Figure 41 illustrates how a liquid would perform if the flow process were equilibrium. The portion of the curve that is above the inlet static pressure of one atmosphere would be similar to the same region in Fig. 40. The region below one atmosphere in Fig. 41 indicates that equilibrium flow is above the acoustic velocity at tip speeds above 100 ft/sec. However, test data at inlet static pressures of one atmosphere indicate that the constant quality case illustrated in Fig. 40 is the most accurate and that the flow process is either constant quality or, if equilibrium, never gets into the above acoustic velocity region indicated in Fig. 41.

For a constant-quality process Fig. 42 and 43 show how increasing the inlet quality decreases the static pressure rise and causes above acoustic velocity operation at tip speeds above 500 ft/sec. This condition is indicated by the negative slopes of the 1000- and 600-ft/sec lines at area ratios of 1. Therefore, if the flow is constant quality the usual design with diverging flow passages will cause a static pressure decrease if operated at a tip speed greater than 500 ft/sec. However, a slight area contraction at these high tip speeds could convert the flow to a below acoustic velocity condition. Such a converging-diverging approach would limit flexibility by choking and would interfere with cavitation performance during normal operation with a liquid. Variable geometry is also a possible solution. Another possible solution would be to provide a high head-rise, low tip-speed preinducer at some distance upstream. This preinducer could raise the static pressure by operating below the acoustic velocity of the two-phase flow and the separation between its discharge and the main inducer inlet would allow time for the flow to condense to a pure liquid before entering the main pump. This solution would have the additional advantage of satisfactory operation during the normal pumping of a pure liquid.

For an equilibrium process Fig. 44 indicates that the flow is always above the acoustic velocity of the two-phase flow if the tip speed exceeds 100 ft/sec and if the quality is 0.01. A possible design that could handle this case would be initially to contract the flow passage to convert the two-phase flow to liquid and then diverge to recover static pressure. However, as with the constant-quality case, this would result in decreased flexibility due to choking and would seriously penalize cavitation performance during normal operation with a liquid. Again, a possible solution would be a variable geometry pump.

For an equilibrium process with an inlet quality of 0.10 the flow would be above acoustic velocity at tip speeds greater than 300 ft/sec and the static pressure rise at tip speeds less than 300 ft/sec would be exceedingly small due to the low density of the flow, as shown in Fig. 45. The area contractions required to convert the two-phase flow to liquid at tip speeds greater than 500 ft/sec would be so great that even variable geometry would be a questionable solution. Constant-quality and equilibrium processes with saturated vapor (quality = 1.0) at the pump inlet are illustrated in Fig. 46 and 47, respectively. These curves indicate that both processes would be below acoustic velocity over the entire tip-speed range investigated, and the flow densities are so low that the pressure rises obtainable in a pump would be quite small.

Due to the lack of test data, the question arises of whether two-phase hydrogen follows an equilibrium process, a constant-quality process, or a process somewhere in between. References 22 and 29 tend to support the constant-quality approach because acoustic velocities in boiling water agree with constant-quality theory. However, finite amplitude pressure wave testing does not simulate the high velocity flow situation that occurs in a pump impeller. In addition, water may not be similar to two-phase hydrogen behavior.

Flow Process = Constant Quality

$X_1 = 1.0$

$P_1 = 14.7$  psia

$T_1 = 36.6$  degrees R

$\phi_{1t} = 0.10$

$\lambda_1 = 0.3$

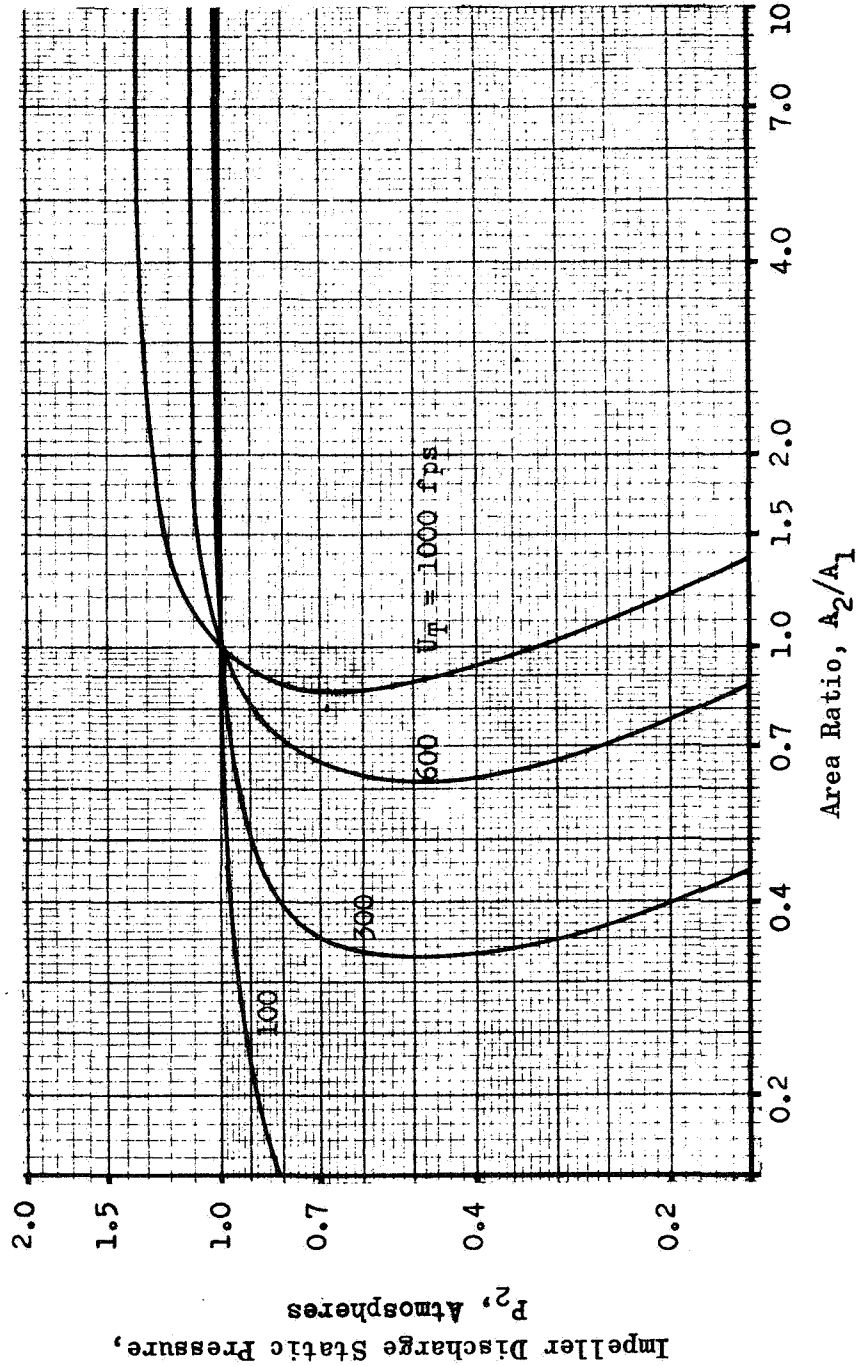


Figure 46. Effect of the Geometry of a Constant RMS Diameter Inducer on the Discharge Static Pressure When Pumping Two-Phase Hydrogen

Flow Process = Equilibrium

$$X_1 = 1.0$$

$$P_1 = 14.7 \text{ psia}$$

$$T_1 = 36.6 \text{ degrees R}$$

$$\phi_{lt} = 0.10$$

$$A_i = 0.3$$

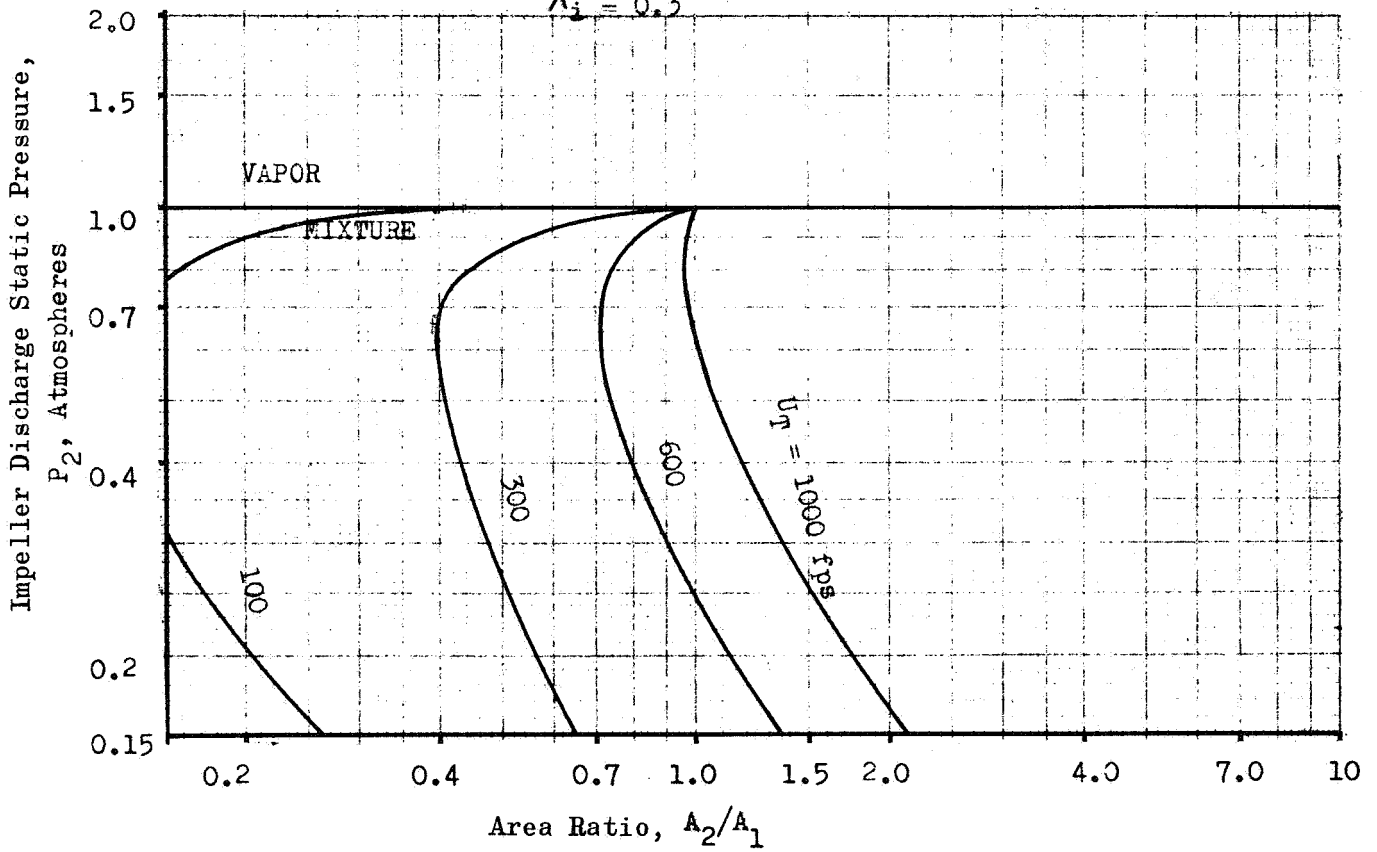


Figure 47. Effect of the Geometry of a Constant RMS Diameter Inducer on the Discharge Static Pressure When Pumping Two-Phase Hydrogen

The two-phase hydrogen pump testing conducted at NASA Lewis tends to support the constant-quality case because the test pump produced a pressure rise with 15-percent vapor by volume at the inlet. However, the same result could probably have been obtained in equilibrium flow if a shock wave had occurred at the right location.

It may be concluded that the type of flow process and, consequently, the optimum two-phase pump design cannot yet be established. However, the two most likely flow processes have been mathematically described and, if no severe shock waves occur, the upper and lower limits on impeller performance can be established.

#### Inducer Experimental Results

In order to study the effect of mixed-phase flow on engine start, the effect of vapor ingestion or vapor generation on pump performance must be ascertained. In the case where the effects of vapor are assumed similar to the effects of cavitation on pump performance, a study was initiated to correlate vapor volume with inducer cavitation performance. For this mixed-phase flow approach the cavity theory described in Ref. 1 was used to correlate the experimental data obtained from three experimental inducers.

From the relationship of the cavitation coefficient  $\tau$  with blade cavitation number  $k_e$ ,

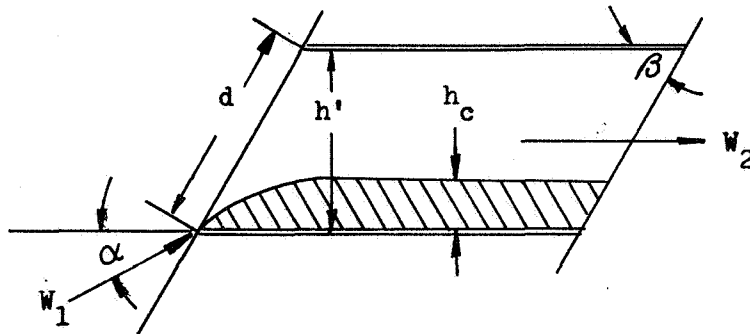
$$\tau = (k_e + 1) (\phi^2 + 1) - 1 \quad (50)$$

The relative velocity ratio  $R = \frac{W_2}{W_1}$  can be obtained from the following equation based on cascade geometry and flow continuity:

$$k_e = \frac{(1/R + R) - 2 \cos \alpha}{\cos \alpha - R + \sin \alpha \cot (\beta - \alpha)} \quad (51)$$

From cavity theory the cavity height  $h_c$  can be obtained from the following expression:

$$h_c = d \sin \beta \left[ 1 - R \frac{\sin (\beta - \alpha)}{\sin \beta} \right] \quad (52)$$



If the assumption is made that the amount of vapor, in percent of the total volume, passing through the inducer is  $h_c/h'$ , then the percent of vapor by volume can be computed for a given inducer design and correlated with its experimental performance. Also by assuming that the inducer can be represented by a one-dimensional analysis, the critical point (corresponding to a given head-loss as a result of cavitation) can be related to a critical vapor volume or flow quality passing through the inducer.

The experimental performance of three cylindrical hub and tip helical inducers was briefly studied and the results are shown in Tables 8 through 11. The effect of cavity volume growth on inducer head-loss is also shown in these tables. Figures 48, 49, and 50 indicate the various points at which the head was related to the NPSH for inducers A, B and C, respectively. For these performances in water the computed critical vapor volume was taken at the 10-percent inducer head-loss point (defined as the critical point).

TABLE 8

EXPERIMENTAL TEST RESULTS, INDUCER A ( $\phi_t = 0.153$ )

H <sub>2</sub> O					
Point	$\psi$	$\tau$	$k_e$	$h_c$ , inches	$h_c/h'$ , percent
1	0.124	0.37	0.340	0.252	21.8
2	0.124	0.185	0.159	0.325	28.2
3	0.122	0.148	0.123	0.349	30.2
4	0.1178	0.111	0.0866	0.378	32.8
5	0.1197	0.074	0.0504	0.420	36.4
6	0.1148	0.0629	0.0395	0.438	38.0
<u>7</u>	0.1053	0.0592	0.0359	0.444	<u>38.5</u>
8	0.061	0.055	0.0381	0.453	39.3

TABLE 9

EXPERIMENTAL TEST RESULTS, INDUCER A ( $\phi_t = 0.168$ )

H <sub>2</sub> O					
Point	$\psi$	$\tau$	$k_e$	$h_c$ , inches	$h_c/h'$ , percent
1	0.1067	0.37	0.333	0.169	14.7
2	0.1054	0.185	0.152	0.261	22.6
3	0.1041	0.148	0.1167	0.282	24.5
4	0.1002	0.111	0.0808	0.309	26.8
5	0.1028	0.0925	0.0628	0.327	28.4
6	0.1043	0.08325	0.0538	0.338	29.3
7	0.1035	0.074	0.0448	0.350	30.4
8	0.1017	0.0703	0.0412	0.358	31.0
<u>9</u>	0.0971	0.0666	0.0376	0.362	<u>31.4</u>
10	0.0897	0.06475	0.0378	0.365	31.7
11	0.074	0.0629	0.0340	0.368	31.9

TABLE 10

EXPERIMENTAL TEST RESULTS, INDUCER B ( $\phi_t = 0.0955$ )

H <sub>2</sub> O					
Point	$\psi$	$\tau$	$k_e$	$h_c$ , inches	$h_c/h'$ , percent
1	0.0668	0.179	0.168	0.149	18.1
2	0.0676	0.119	0.109	0.167	20.3
3	0.0648	0.0994	0.0895	0.175	21.3
4	0.0662	0.0795	0.0697	0.185	22.6
5	0.0621	0.0596	0.0500	0.198	24.1
<u>6</u>	0.0599	0.0398	0.0304	0.215	<u>26.2</u>
7	0.0608	0.0338	0.0245	0.222	27.0
8	0.0547	0.0328	0.0235	0.223	27.1
9	0.0298	0.0326	0.0233	0.223	27.2

TABLE 11

EXPERIMENTAL TEST RESULTS, INDUCER C ( $\phi_t = 0.116$ )

H <sub>2</sub> O					
Point	$\psi$	$\tau$	$k_e$	$h_c$ , inches	$h_c/h'$ , percent
1	0.1063	0.370	0.350	0.138	16.5
2	0.1058	0.204	0.186	0.176	21.0
3	0.1082	0.148	0.131	0.196	23.3
4	0.1082	0.111	0.0955	0.208	24.8
5	0.1045	0.0925	0.0766	0.223	26.6
6	0.1017	0.0740	0.0583	0.236	28.1
7	0.1032	0.0462	0.0310	0.262	31.2
8	0.1008	0.0426	0.0273	0.266	31.8
<u>9</u>	0.0936	0.0407	0.0255	0.269	<u>32.1</u>
10	0.9841	0.0388	0.0237	0.272	32.4
11	0.0693	0.037	0.0219	0.275	32.8

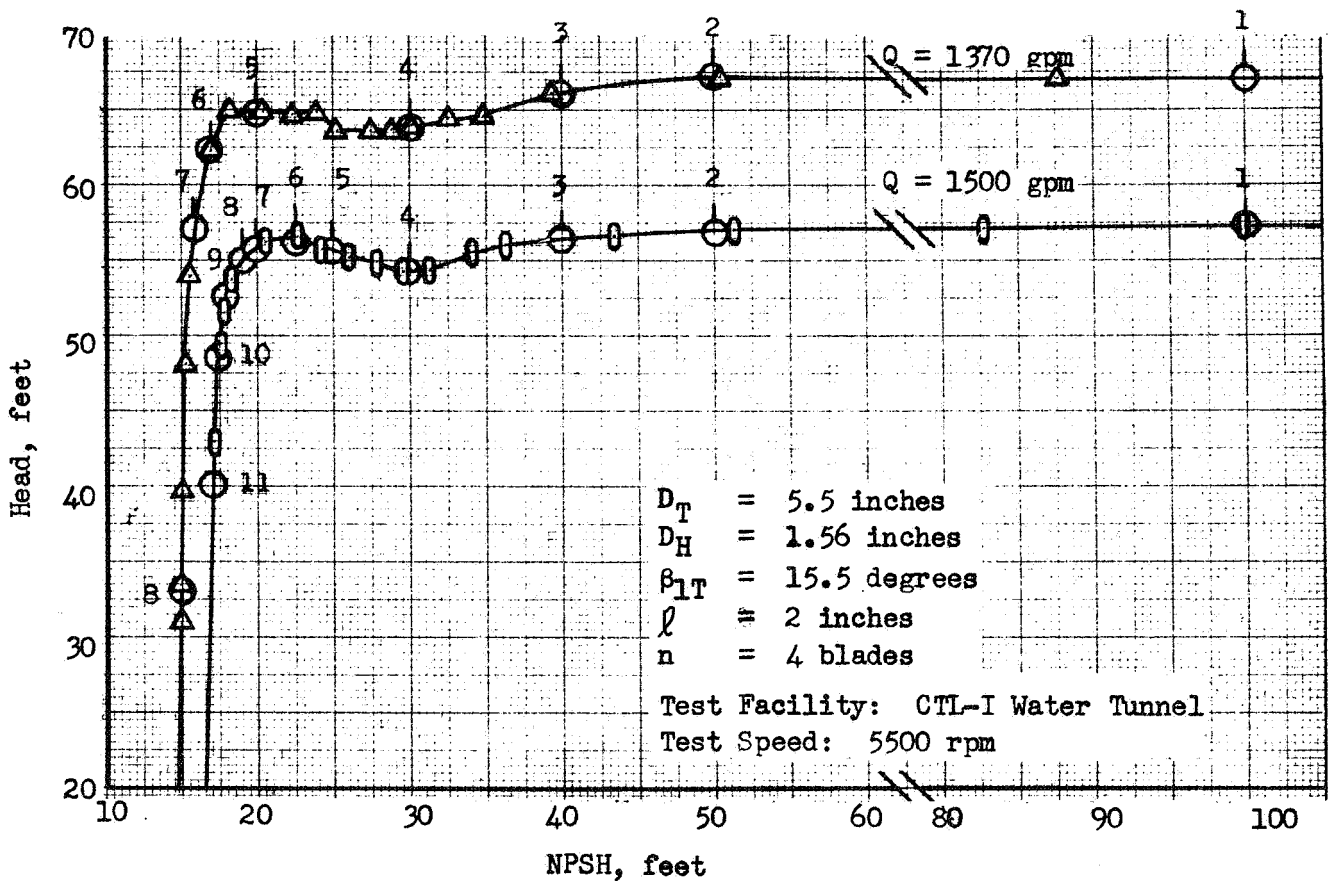


Figure 48. Experimental Inducer A

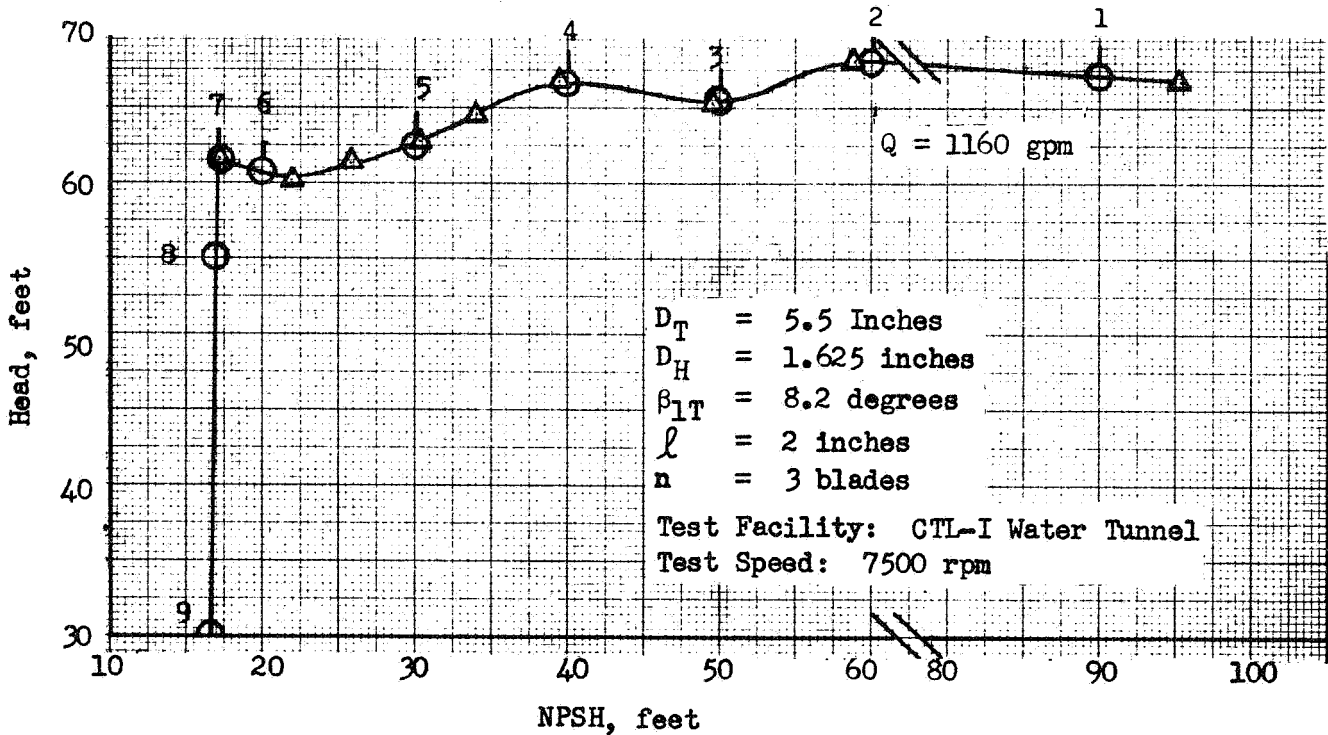


Figure 49. Experimental Inducer B

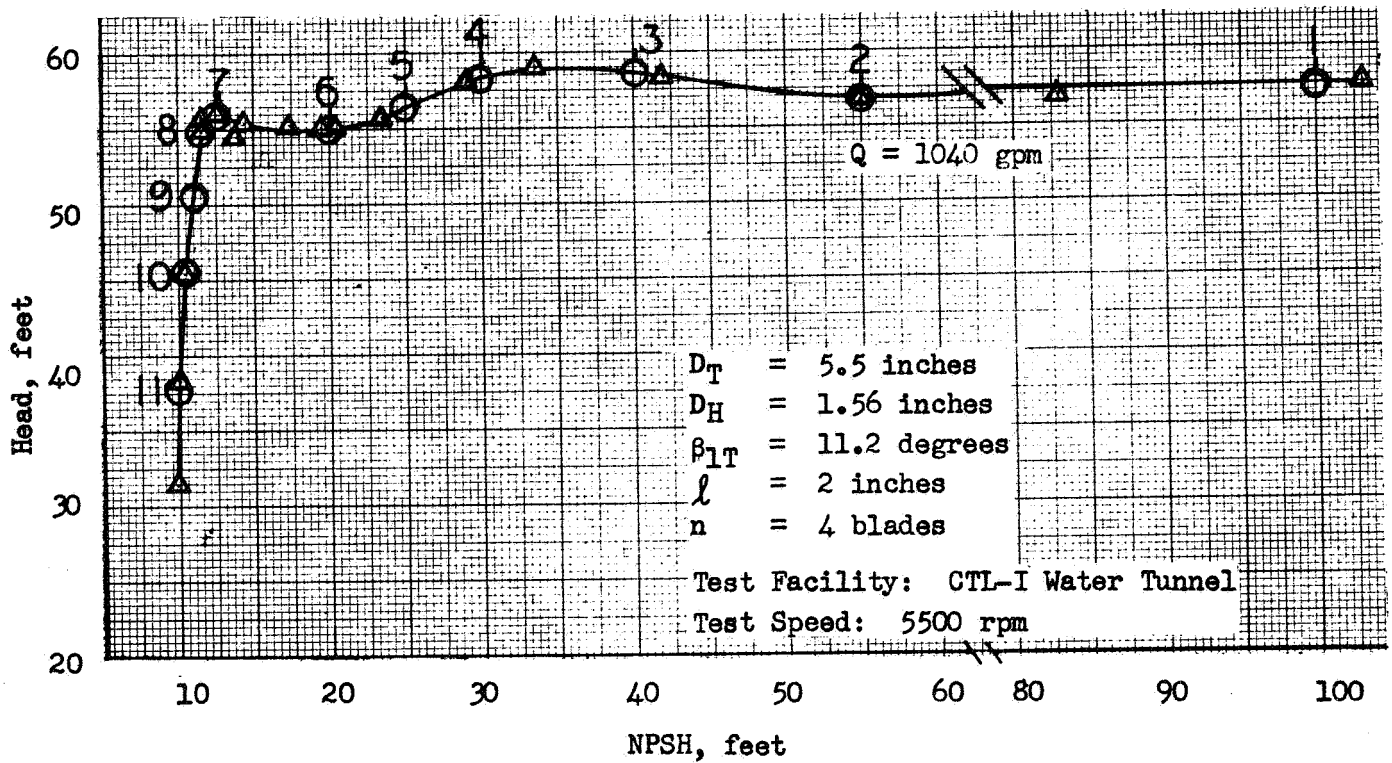


Figure 50. Experimental Inducer C

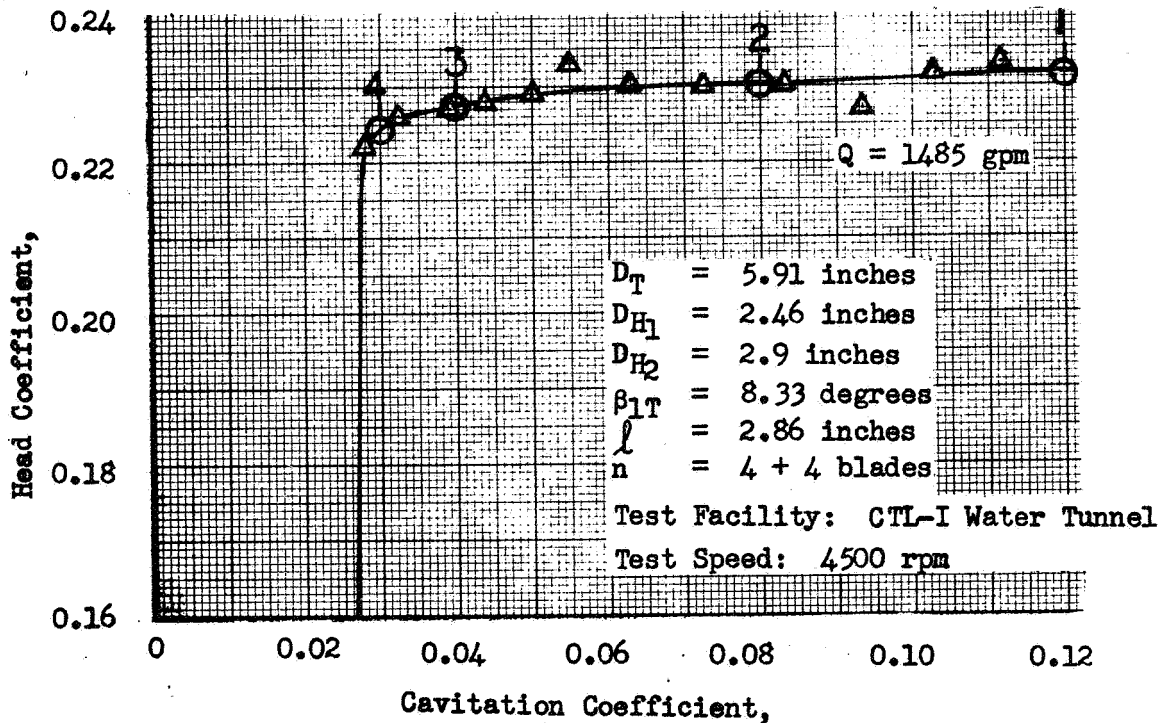


Figure 51. Model Mark 15 Fuel Inducer

A brief study on the experimental performance of a tapered-hub, cylindrical-tip model MK 15 fuel (J-2) inducer is shown in Table 12. Both water and LH<sub>2</sub> data are shown for this inducer. Its corresponding points for which the inducer head coefficient was related to the cavitation coefficient is shown in Fig. 51.

The critical vapor volumes of these inducers were plotted against their respective incidence to blade angle ratio ( $\alpha/\beta$ ) and are shown in Fig. 52. Maximum inducer suction specific speed ( $S_s$ ) values have been obtained experimentally when the  $\alpha/\beta$  ratio is equal to about 0.426 (design flow coefficient equal to  $\beta \times 10^{-2}$ ). From the limited data examined the critical vapor volume of about 36.5 percent was obtained at the maximum inducer  $S_s$  (Fig. 52). Also shown in Fig. 52 are the corresponding  $S_s$  of these inducers. Note that the critical vapor volume is not dependent on the inducer  $S_s$  but is a function of the inducer  $\alpha/\beta$  ratio.

#### Shock Wave Effects

Reference 17 has shown experimentally that both normal and conical shock waves occur in mixtures of gaseous nitrogen and water (effectively, this is a constant-quality mixture) and, given the flow conditions upstream of the shock, has accurately predicted the shock losses and the downstream flow conditions. Since this verifies the existence of shock waves in two-phase mixtures and since in many cases a two-phase mixture will exceed its acoustic velocity when passing through a pump, some sort of shock waves are probable and, depending upon their type, can further complicate the two-phase pump analysis. For example, if a normal shock wave occurs somewhere in the diverging impeller passage, the location of the shock and, consequently, the impeller discharge static pressure is dependent upon the static pressure at the impeller discharge. If a stable normal shock can be established, it would be of great benefit because it would raise the flow density and thereby increase the static pressure rise between the shock wave and the impeller discharge.

TABLE 12

EXPERIMENTAL TEST RESULTS, MODEL MK 15 FUEL INDUCER  
 ( $\phi_t = 0.0935$ )

H <sub>2</sub> O					
Point	$\psi$	$\tau$	$k_e$	$h_c$ , inches	$h_c/h'$ , percent
1	0.233	0.12	0.111	0.353	22.5
2	0.231	0.08	0.072	0.331	25.0
3	0.227	0.04	0.032	0.298	28.8
<u>4</u>	0.225	0.03	0.022	0.286	<u>30.2</u>
LH <sub>2</sub>					
1	0.233	0.103	0.0933	0.0931	11.9
2	0.231	0.063	0.0536	0.1769	22.6
3	0.227	0.023	0.0140	0.2152	27.4
<u>4</u>	0.225	0.013	0.0041	0.2486	<u>31.7</u>

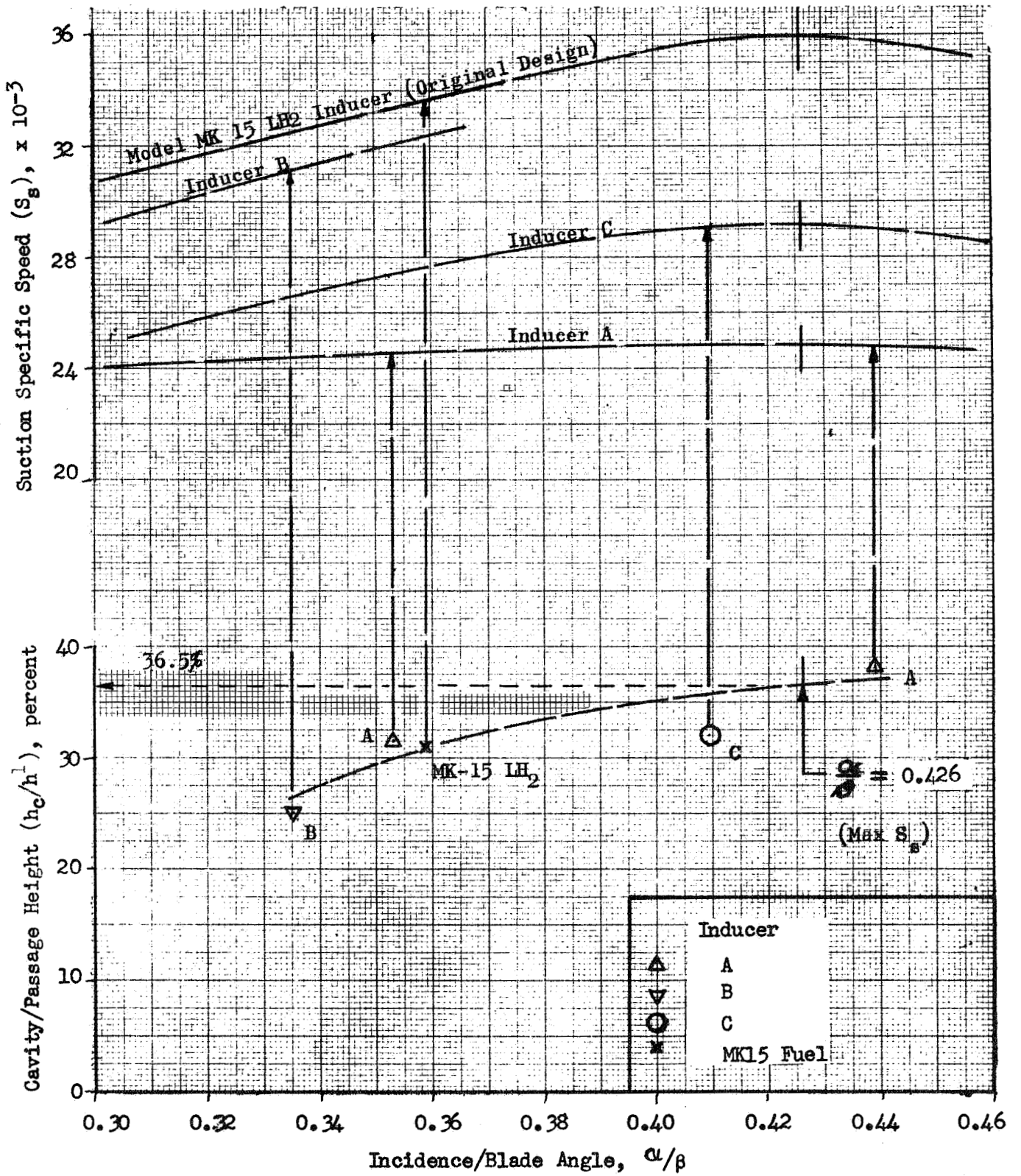


Figure 52. Performance Summary

Conical shock waves may occur at other locations within a pump. For example, even if the relative velocity leaving the impeller is subsonic, the absolute velocity approaching the volute vanes may be supersonic, particularly if the impeller is centrifugal. This would cause a conical shock wave and some total pressure drop at the vane leading edges. If the flow enters the inducer supersonically, a conical shock wave will form at the inducer leading edge, thereby altering the downstream flow conditions and, consequently, affecting the pump performance.

It is apparent that any complete analysis of pumps during two-phase operation must include an analysis of shock wave losses and effects. This can lead to severe complications, particularly if the pump performance is dependent upon the system back pressure.

## TASK II: MATERIALS

The selection of a candidate LH<sub>2</sub> pump material must be based on a myriad of constraints including strength, weight, ductility, modulus, heat capacity, thermal conductivity, etc. The purpose of Task II is the comparative evaluation of the material candidates from a structural standpoint followed by a comprehensive evaluation of the thermal response characteristics of the materials under a wide range of chilldown conditions. The confirmation of the analytical closed form and computer predictions is followed by experimental test results provided by a related study.

### MATERIAL CHILLDOWN PHILOSOPHY

The philosophy of material chilldown can be considered as composed of two alternative possibilities. For engine start situations where little or no preconditioning has been provided, a minimum propellant flow and minimum time period of start are indicated. For this circumstance the question of complete chilling of the pump vs chilling of only the wetted surface arises. For the former condition a high material conductivity and low-density heat capacity product are indicated. In addition for this condition the surface coatings which enhance the boiling at the wetted surface without providing a strong insulating influence for the base material will be optimum. For rapid chill situations where only the pump wetted surfaces are chilled, the interior of the pump material remains warm and bleeds a tolerable heat level slowly into the pump during the mainstage portion of operation. For this condition the use of thermally insulating surface coatings will prevent the heat content of the pump from entering the chilldown fluid. In this latter case an increased insulation thickness can provide increased benefit.

From a thermal shock and required strength standpoint consideration of start with the main interior of the pump in a warm condition must be assessed. Since materials generally increase in strength at low temperatures, the

desirability of a completely cold pump or a warm pump with a chilled surface must be evaluated. During the course of a design study consideration of both cases must be ascertained from these standpoints. The analysis undertaken during this study included both slow, moderate, and fast chill circumstances.

Design of a pump from a chilldown standpoint regardless of material type should be toward a lighter weight pump except under the singular case where turbine weight is large and a resultant high pump equilibrium temperature results prior to a restart condition. For conditions where a long period of preconditioning is allowed and where maximum utilization of the prechill flow is available, the spreading of the minimized LH<sub>2</sub> pump weight over a long flow passage length (large length to hydraulic diameter L/D) is desirable. If the rapid start with only a chilled surface condition present is acceptable, the pump weight should be toward obtaining a small flow passage length to hydraulic diameter ratio. In this latter approach the pump heat capacity will be isolated from the hydrogen wetted surfaces. In accordance with this method, materials with low thermal diffusivity and thermal conductivity are to be selected. Materials of this type are titanium-nickel alloys and stainless steel as opposed to aluminum or high conductivity nickel materials.

#### Material Strength to Density Ratio

Minimization of the pump mass by employment of minimum thickness sections is a primary requirement to promoting a rapid chilldown. A study review of maximum yield strength to density ratio indicated titanium and Inconel 718 provide the highest values as shown in Fig. 53. The effect of material strength increase with decreased temperature results in a necessary comparison to be made of the desirability of (1) completely chilling a lightweight pump for strength factors or (2) partial chilling of a heavier pump which

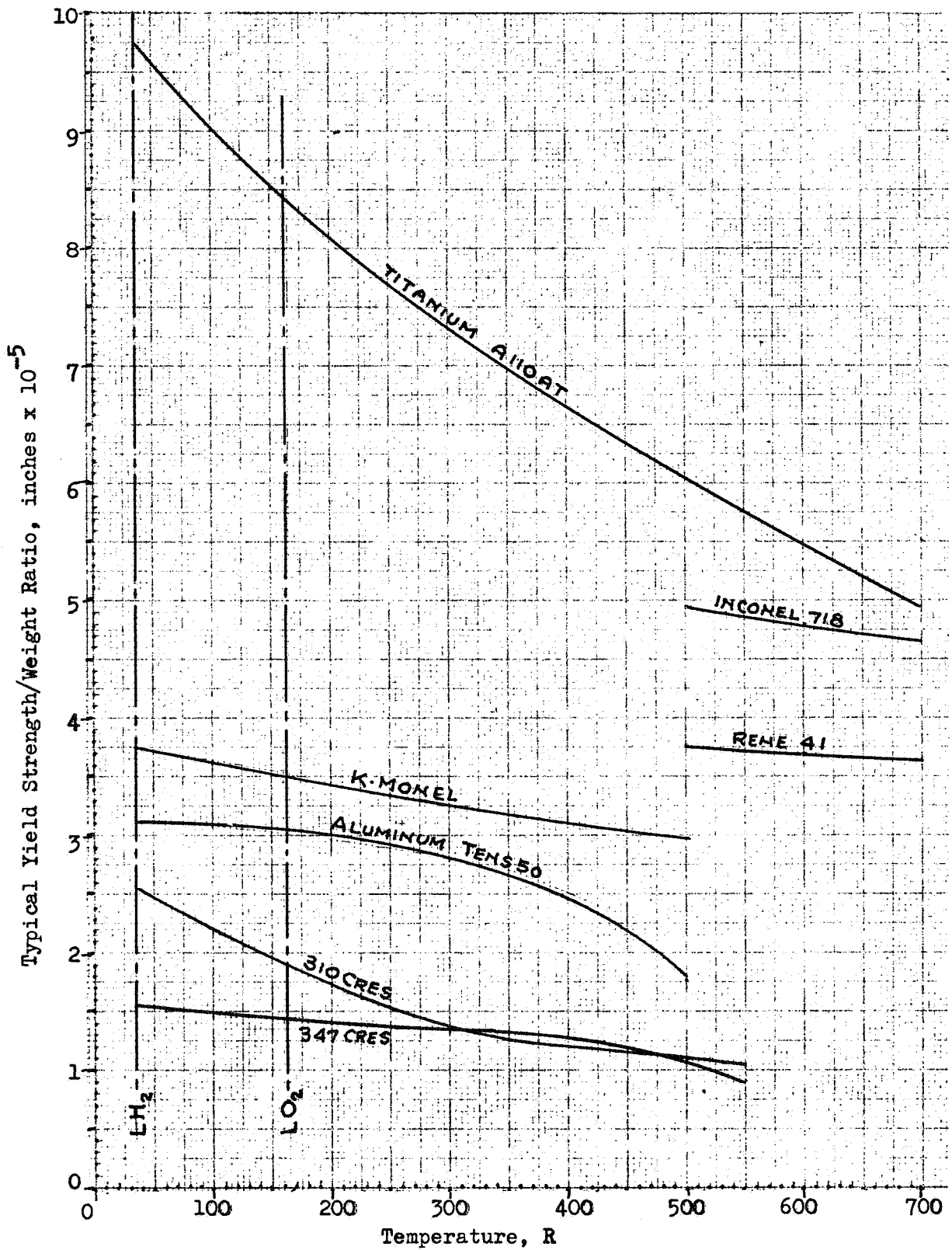


Figure 53. Candidate Pump Material Strength to Density Variation With Temperature

does not require the temperature-dependent strength. Under the assumptions made a consideration to what extent minimum thickness sections governs the pump weight must be included.

### Thermal Shock Characteristics

The thermal shock character of materials studies was analytically assessed from the standpoints of allowing thermal strains to remain within the yield stress value or from a standpoint of allowing yielding due to thermal strain. For the former a high density to modulus ratio is desired; for the latter a high fracture ductility and plastic strain absorption capability is necessary. The rating employed used the following relationships for assessing material desirability. Table 13 illustrates the comparative parameter ratings,

$$N_B = \left( \frac{\alpha \Delta T}{\sigma_y / E} \right) \quad (\text{elastic rating parameter}) \quad (53)$$

$$N_D = \left( \frac{\alpha \Delta T}{D(1-\mu)} \right)^2 \quad (\text{plastic rating parameter}) \quad (54)$$

Further comparison of thermal expansion differences of proposed insulating coating to base material properties and coating plasticity is necessary prior to final selection.

### MATERIAL TIME RESPONSE

The critical thermal time response period for the turbopump body structure can be developed from the transient heat-conduction equations for three cooling limit cases using one-dimensional heat conduction, constant heat transfer coefficient assumptions. These limiting cases are for (1) a

TABLE 13

COMPARISON OF THERMAL SHOCK RATING PARAMETERS  
FOR CANDIDATE PUMP MATERIALS

Material	$N_B$		$N_D \times 10^4$	
	Elastic Rating Parameter 70 to -200 F	70 to -420 F	Plastic Rating Parameter 70 to -200 F	70 to -420 F
Aluminum (Tens 50)	0.810	1.162	1.78	5.64
Inconel-X	0.555	0.856	1.85	4.03
K-Monel	0.409	0.531	1.08	1.88
Rene-41	0.371	0.483	0.89	2.09
Titanium (ALLOAT)	0.158	0.208	1.24	3.84
310 CRES	1.075	1.455	0.20	0.72
347 CRES	0.822	1.080	1.42	1.05

NOTE: Low values of  $N_B$  and  $N_D$  are desirable.

finite wall thickness ( $t$ ) with an infinite thermal conductivity ( $k$ ), (2) an infinite heat transfer coefficient, and (3) an infinite wall thickness with finite thermal conductivity. The equations for heat conduction may be expressed in terms of a nondimensional temperature ratio, a Biot number (a measure of coolant-side film coefficient), and a Fourier number (a measure of time). By arranging the solution of Ref. 21 in terms of these dimensionless parameters, the equation for heat conduction in a finite thickness slab ( $k \rightarrow \infty$ ) becomes:

$$\alpha = e^{-N_{Fo} N_{Bi}} \quad (55)$$

$$\alpha = \frac{T_w - T_c}{T_i - T_c} \quad (56)$$

$$N_{Bi} = \frac{ht}{K} \quad (57)$$

$$N_{Fo} = \frac{\alpha \tau}{t^2} \quad (58)$$

where the subscripts  $w$ ,  $c$ , and  $i$  are for wall, coolant, and initial values, respectively.

A critical time constant can be defined as the time when the wall-to-coolant temperature ratio (or heat flux) reduces to  $1/e$  of its initial value, i.e.,

$$\alpha_{crit} = \left(\frac{1}{e}\right) = 0.367 \quad (59)$$

Solving the two above equations results in:

$$N_{Fo} N_{Bi} = 1.0 \quad (\text{Case I slow chill}) \quad (60)$$

A comparison of typical materials may be made by comparing density, heat capacity, and thermal conductivity factors defined by the time constant equations as will be shown below.

Under conditions where very vigorous boiling is combined with forced convection, the wall surface and propellant interface is reduced to the local bulk temperature in a very short period of time. Comparisons of wall thickness response for an infinite coolant heat transfer coefficient may be approximately expressed by rapid chill relationship:

$$N_{Fo} \approx \left( \frac{e^2}{\pi} \right) \quad (\text{Case II rapid chill}) \quad (61)$$

$$t_{\text{eff}} = \left( \frac{\sqrt{\pi}}{e} \right) \left( \sqrt{\frac{K \tau}{\rho C_p}} \right) \quad (62)$$

Similarly, for the case of the infinite thickness slab, the dimensionless form of the heat conduction equation becomes

$$\alpha = \text{erf} \frac{1}{2} (N_{Fo})^{-1/2} + e \left[ N_{Bi} + N_{Bi}^2 N_{Fo} \right] \text{erfc} \frac{N_{Fo}^{-1/2}}{2} + N_{Bi} N_{Fo}^{1/2} \quad (63)$$

For this case the solution may be developed for  $\alpha_{\text{crit}}$  with  $N_{Bi} N_{Fo} > 1.0$ , and the result is

$$N_{Fo}^{1/2} N_{Bi} = \left( \frac{e}{\sqrt{\pi}} \right) \quad (\text{Case III moderate chill}) \quad (64)$$

In terms of critical time the limits for two cases become

$$\tau_c = \frac{\rho C_p t}{h_c} \quad \text{finite slab } K \rightarrow \infty \quad (N_{Bi} \rightarrow 0) \quad (65)$$

$$\tau_c = \frac{e^2}{\pi} \frac{t^2}{\alpha} \quad \text{infinite film coefficient} \quad (N_{Bi} \rightarrow \infty) \quad (66)$$

$$\tau_c = \frac{e^2}{\pi} \frac{\rho C_p k}{h_c^2} \quad \text{finite slab } (N_{Bi} N_{Fo} \approx 1.0) \quad (67)$$

A comparison of the first and third time bounds with the exact solution to the heat-conduction equation is shown in Fig. 54. For the time conditions (Fourier number) representative of rapid pump and engine startup time without prechill, the infinite slab solution time constant is most closely representative of the actual time for chilldown. For most turbo-pump materials of reasonably large wall thickness and small times (of approximately 1 to 5 seconds), this solution is approximately correct.

#### Slow Chilldown Time Material Response

For conditions of low heat transfer coefficient with a long time period (slow chill) or thicker wall ( $N_{Bi} < 1.0$ ,  $N_{Fo} > 1.0$ ), the thermal conductivity of the wall is of secondary importance as shown by Eq. 65. For long chill periods the total heat capacity or enthalpy indicates the time for heat removal.

Two material chill situations were examined for a range of materials (Table 14). These were a chilldown from ambient to 36 R and a chill from 180 to 36 R. An examination of the results based upon the material properties of Ref. 8 and 18 show that the largest fraction of heat content is in the temperature range of 540 to 180 R with only 10 to 15 percent remaining in the 180 to 36 R due to a drastic reduction in thermal heat capacity at low temperatures. A comparison of the chilldown characteristics over the entire temperature range indicates the light metals such as magnesium, beryllium, titanium, and aluminum indicate the best slow chill characteristics. In the nonmetals the Teflon (and Kel-F) materials have the lowest heat content.

#### Moderate Chilldown Time Material Response

From Eq. 67 where the chilldown of the cooled surface is considered, the product of density, heat capacity and thermal conductivity is the controlling

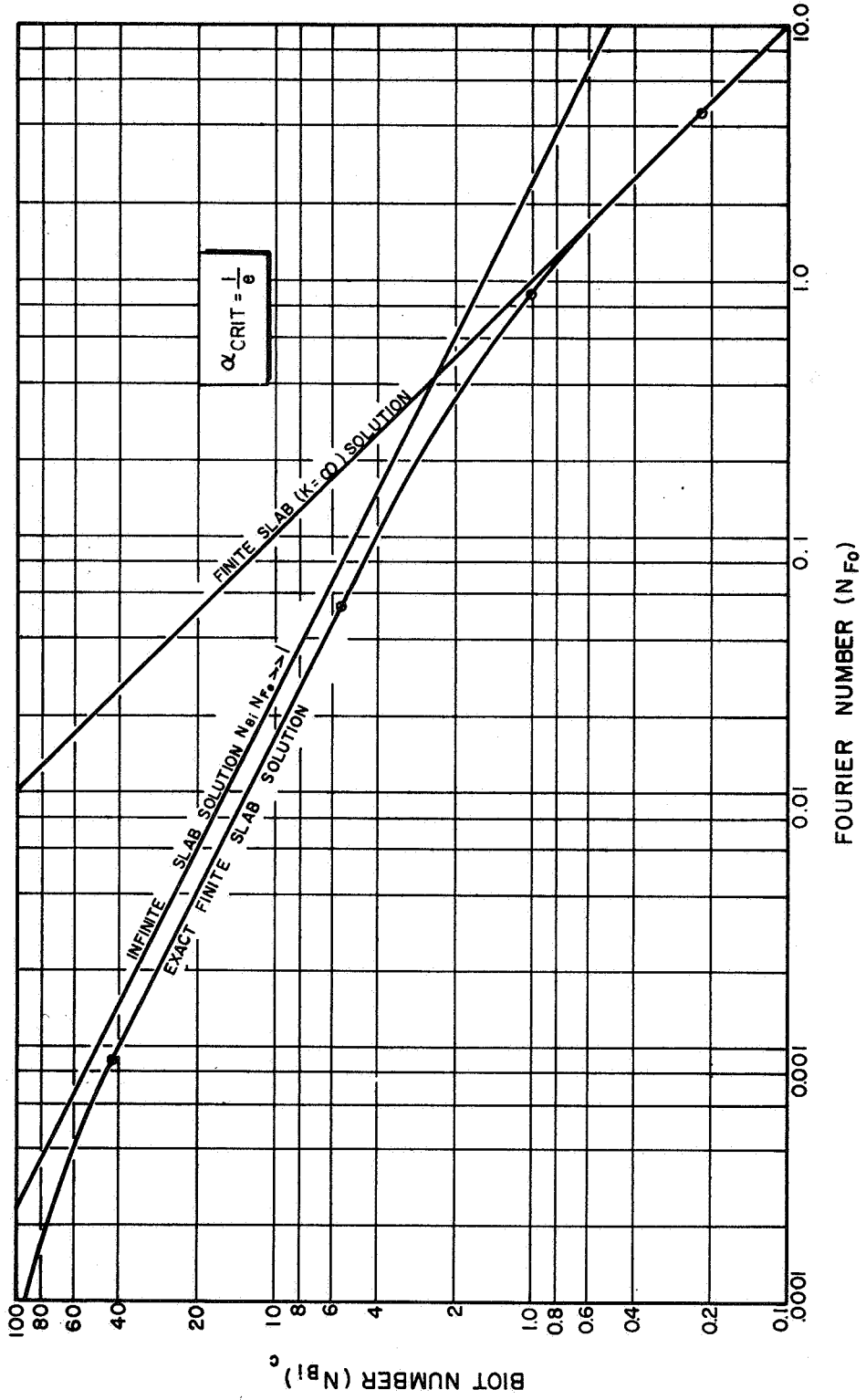


Figure 54. Critical Biot Number vs Fourier Number

TABLE 14

RELATIVE TIME FOR CHILLDOWN ( $N_{Bi} \ll 1, N_{Fo} \gg 1.0$ )

Material	180 to 36 R $\rho \Delta H$	Material	540 to 36 R $\rho \Delta H$
Beryllium	0.131	Magnesium	5.60
Chromium	0.668	Beryllium	6.68
Magnesium	0.711	Titanium	7.20
Aluminum	0.744	Aluminum	7.25
Molybdenum	0.828	Molybdenum	7.62
Titanium	0.852	Tantalum	8.2
Steel	0.97	Tungsten	8.5
Tungsten	1.11	Chromium	8.8
Nickel	1.12	Steel	10.1
Manganese	1.23	Manganese	10.3
Tantalum	1.44	Nickel	10.7
Copper	1.51	Copper	11.1
Carbon	0.38	Teflon	5.77
Teflon	0.68	Carbon	6.6
Polyethylene	0.78	Polyethylene	8.95

influence. Table 15 indicates this product for a range of materials at -250 and 60 F. It is shown that titanium is substantially better than K-monel and stainless steel due to a low thermal conductivity preventing heat soak from the pump interior. For normal forced convection circumstances this moderate chilldown criterion is controlling.

#### Minimum Surface Chilldown Time

For conditions where the applied heat transfer coefficient approaches a high value ( $N_{Bi} \rightarrow \infty$ ,  $N_{Fo} < 1.0$ ) the thermal diffusivity controls the diffusion of heat to the chilled surface. A comparison of the thermal diffusivity values at temperatures of 400, 60, and -250 F is shown in Table 16 for a range of pump materials. For this condition the common pump materials of Inconel, stainless steel, K-monel, and titanium appear about equal. Materials with high thermal conductivity are shown to have substantially higher thermal diffusivity values.

Table 17 compares the candidate pump metals on a qualitative basis from the previous charts. From fast and moderate surface chill standpoints the titanium is excellent. From a very slow chill standpoint it also appears good. Materials such as aluminum exhibit good slow chill characteristics but poor fast chill characteristics.

#### Pump Internal Coating Materials

From a materials study of thermal properties it appears that for the provision of insulators on the pump internal wetted surfaces, ductile materials with a low thermal conductivity appear useful. From a comparison of the thermal properties groupings it was indicated that Teflon and Kel-F materials have low thermal conductivity, density, and heat capacity with good low-temperature ductility. A comparison of Kel-F and Teflon for a range in

TABLE 15

CHILLDOWN THERMAL FACTOR FOR MODERATE  
FILM COEFFICIENT

Material	$\rho C_p K \left[ \text{Btu}^2 / (\text{hr ft}^4 \text{ R}^2) \right]$	
	at 60 F	at -250 F
Titanium	139	37.3
Manganese	333	102
K-monel	534	273
347 CRES	441	262
Inconel	559	365
Magnesium	1,170	532
Aluminum	2,350	778
Beryllium	6,530	817
Tantalum	1,030	980
Nickel	2,930	1,520
Chromium	3,360	1,790
Molybdenum	3,410	2,430
Tungsten	3,790	3,050
Copper	11,300	10,000

TABLE 16

RELATIVE CHILL PENETRATION FOR FILM COEFFICIENT

 $(N_{Bi} \rightarrow \infty)$ 

Material	$\alpha$ ft <sup>2</sup> /hr		
	at 400 F	at 60 F	at -250 F
Manganese		0.115	0.12
Inconel	0.140	0.132	0.150
347 CRES	0.161	0.160	0.179
K-monel	0.217	0.191	0.190
Titanium		0.18	0.21
Tantalum		0.933	1.25
Magnesium	2.00	1.74	1.27
Nickel	0.410	0.678	1.33
Aluminum	2.50	2.03	1.86
Molybdenum	1.74	2.07	3.73
Chromium		1.46	4.22
Tungsten		2.38	4.72
Copper		4.35	6.75
Beryllium		2.21	27.5

TABLE 17

RELATIVE COMPARISON OF MATERIAL  
CHILLDOWN CHARACTERISTICS

Material	Fast Chill (Low $K/\rho C_p$ )	Moderate Chill (Low $\rho C_p K$ )	Slow Chill (Low $\rho C_p$ )
Titanium	Excellent	Excellent	Good
Beryllium	Poor	Poor	Excellent
Aluminum	Poor	Fair	Good
Magnesium	Fair	Fair	Excellent
Inconel	Excellent	Good	Fair
347 CRES	Excellent	Good	Fair
K-monel	Excellent	Good	Poor
Nickel	Fair	Fair	Poor
Copper	Poor	Poor	Poor

chilldown circumstances is shown in Table 18. For moderate chilldown times the table indicates that Kel-F coatings require approximately 50 percent of the thickness required for Teflon. Comparative evaluation of other non-metal coating candidates such as aluminum and zirconium oxide, etc., is shown in Table 19. Adherence of the coating and pump ingestion of flaked coating would apparently limit selection to flexible soft materials and those which are easily applied to the line or pump part. Discussion of the promise of applied or surface treating techniques for pump rotating and stationary parts is provided under Task III discussion.

#### Limiting Critical Chilldown Time

The critical time for wall material chilldown was shown by solutions for slow, moderate, and fast chill conditions by the expressions:

$$\tau_c = \frac{\rho_w C_{P_w} t_w}{h_c} \quad \text{slow chill } (N_{Bi} \rightarrow 0) \quad (68)$$

$$\tau_c = \frac{e^2}{\pi} \left( \frac{\rho_w C_{P_w} K_w}{h_c^2} \right) \quad \text{moderate chill } (N_{Bi} N_{Fo} \approx 1.0) \quad (69)$$

$$\tau_c = \frac{e^2}{\pi} \left( \frac{\rho_w C_{P_w} t_w^2}{K_w} \right) \quad \text{fast chill penetration} \quad (70) \\ (N_{Bi} \rightarrow \infty)$$

In the latter case with high film coefficients where the surface chills extremely rapidly, the penetration of the chill through the body thickness becomes a function of the thermal diffusivity and thickness. For the finite film coefficient cases the film coefficient directly affects the time to chilldown.

It can be shown that the maximum flow mass velocity ( $\rho_{\infty} V_{\infty}$ ) may be expressed for a gas condition based on the choked vapor condition and for a liquid flow

TABLE 18

COMPARISON OF KEL-F AND TEFLON  
HEAT TRANSFER EFFECTIVENESS\*

T, R	$\rho C_p$	$\rho C_p^K$	$\left(\frac{K}{\rho C_p}\right)$
Teflon			
500	27.6	4.06	0.00532
400	24.8	3.6	0.00584
300	20.7	2.9	0.00677
200	14.5	1.96	0.00932
100	8	0.99	0.0154
50	4.8	0.92	0.0225
Kel-F			
500	26.8	1.96	0.00272
400	24.1	1.76	0.00303
300	20.1	1.47	0.00363
200	14.1	0.92	0.0046
100	7.7	0.39	0.0065
50	4.65	0.19	0.0086

\*Values in Btu/hr-ft-R units

TABLE 19

PROPERTIES OF CANDIDATE INTERNAL COATING MATERIALS  
FOR LH<sub>2</sub> TURBOPUMPS

Material	Specific Gravity	Thermal Conductivity, Btu/ft-hr-F		Specific Heat, Btu/lb-F		Tensile Stress, psi
		77 F	-423 F	77 F	-423 F	
Neoprene	1.25	1.3				
Teflon	2.2 to 2.4	1.3		0.132	0.018	3,000
Hypalon	1.2					500 to 3500
Butyl Rubber	0.9	0.6				2,200
Polyurethane	1.25					8,000
Kel-F (KX-675)	1.2					
Kel-F	2.12	0.97	0.39	0.22		2500 to 3500
Nylon	1.08	2.3	0.7	0.6		
Silicone Rubber	1.25	1.4				
Polyethylene	0.92	2.1	1.5	0.55		
Zr <sub>2</sub> O <sub>3</sub>	5.7	1.1		0.11		19,000
Al <sub>2</sub> O <sub>3</sub>	4.0	16.2		0.21		37,000
Si <sub>2</sub> O <sub>3</sub>	2.5	0.8		0.18		
Ti O <sub>2</sub>	4.1	3.8		0.17		
Ti C	4.6	12.8		0.20		

based on the conversion of total pressure to a velocity head. The expression for the film coefficient in terms of a relatively insensitive Stanton number becomes

$$N_{ST} = \frac{h}{\rho_{\infty} V_{\infty} C_P} \quad (71)$$

This may be related to a choked gas flow condition and a maximum liquid flow velocity

$$\rho_{\infty} V_{\infty} = \frac{f(\gamma, R) P_0}{\sqrt{T_0}} \quad (\text{gas}) \quad (72)$$

$$\rho_{\infty} V_{\infty} = \sqrt{2g \rho P_0} \quad (\text{liquid}) \quad (73)$$

An expression for the limiting minimum critical chilldown time for H<sub>2</sub> liquid and gas is as shown in Table 20. For conditions of fixed pump geometry the stagnation pressure becomes the strongest influencing factor for reduction of prechill time. Higher pump inlet and tank pressures will proportionally decrease the chilldown time. For rapid starts without preconditioning the influence is seen to be proportional to the square of the inlet pressure. It is indicated that the lower pressure, small flow area sections of the pump such as the inducer can provide the limitation during early pump speedup due to existing low-pressure conditions.

#### MATERIAL CHILLDOWN TIME EXAMPLES (ANALYTICAL COMPARISON)

Comparisons of low typical material surface chilldown times as a function of film coefficient are shown in Fig. 55 to 58 for titanium, stainless, copper (reference) and Kel-F insulator. For these examples the time to achieve a temperature ratio with 1/e of the final value were compared using the previously described limiting conditions for a finite wall

TABLE 20

LIMITING CRITICAL TIME ( $\alpha = 1/e$ ) DEPENDENCE UPON  
MATERIAL, PRESSURE AND TEMPERATURE PARAMETERS

Parameter	$\tau_c$	
	Liquid Flow	Gas Flow
Thin Wall (slow chill)	$\frac{\rho_w C_{p_w} t}{N_{ST} C_{p_H} \sqrt{2g} \rho_H P_H}$	$\frac{\rho_w C_{p_w} t \sqrt{T_H}}{N_{ST} C_{p_H} P_H f(\gamma, R)}$
Thick Wall (rapid chill)	$\frac{\rho_w C_{p_w} k_w (e^2/\pi)}{2N_{ST}^2 C_{p_H}^2 g \rho_H P_H}$	$\frac{\rho_w C_{p_w} k_w T_H (e^2/\pi)}{N_{ST}^2 C_{p_H}^2 P_H^2 f(\gamma, R)^2}$

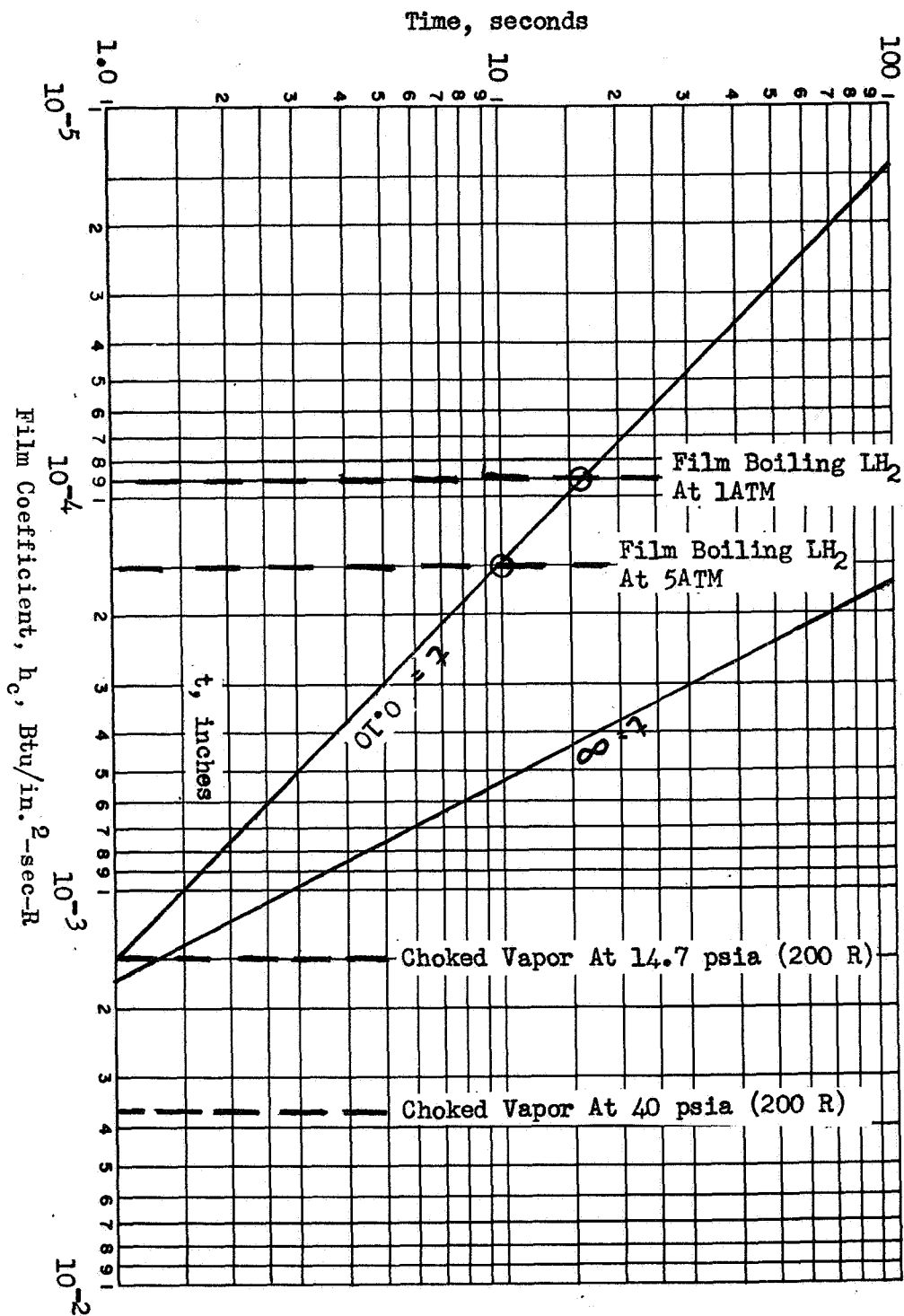


Figure 55. Titanium Chillo down to Critical Point ( $\alpha = 1/e$ )

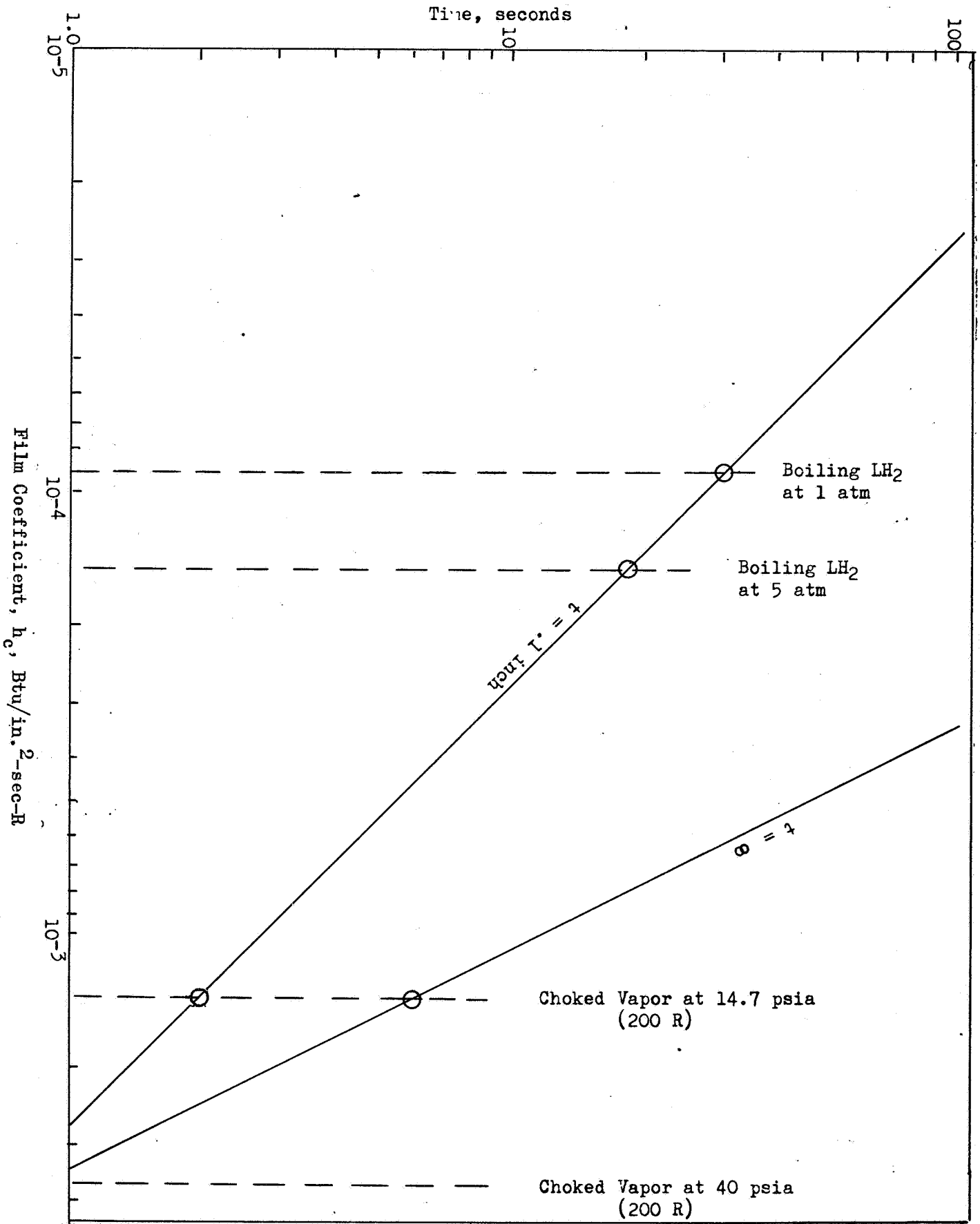


Figure 56. 347 CRES Time to Chardown ( $\alpha = 1/e$ )

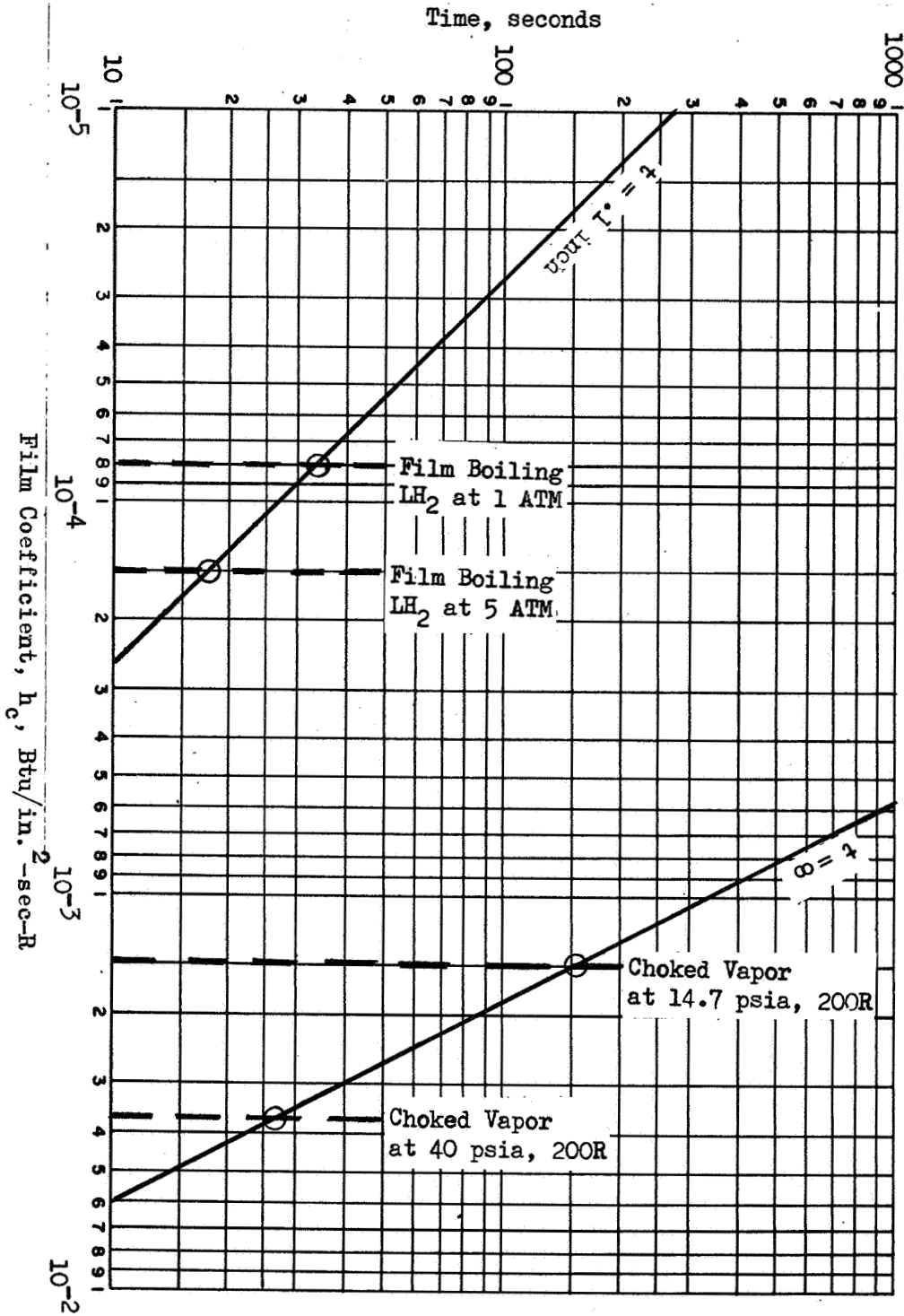


Figure 57. Copper Time to Chilloff of Surface ( $\alpha = 1/e$ )

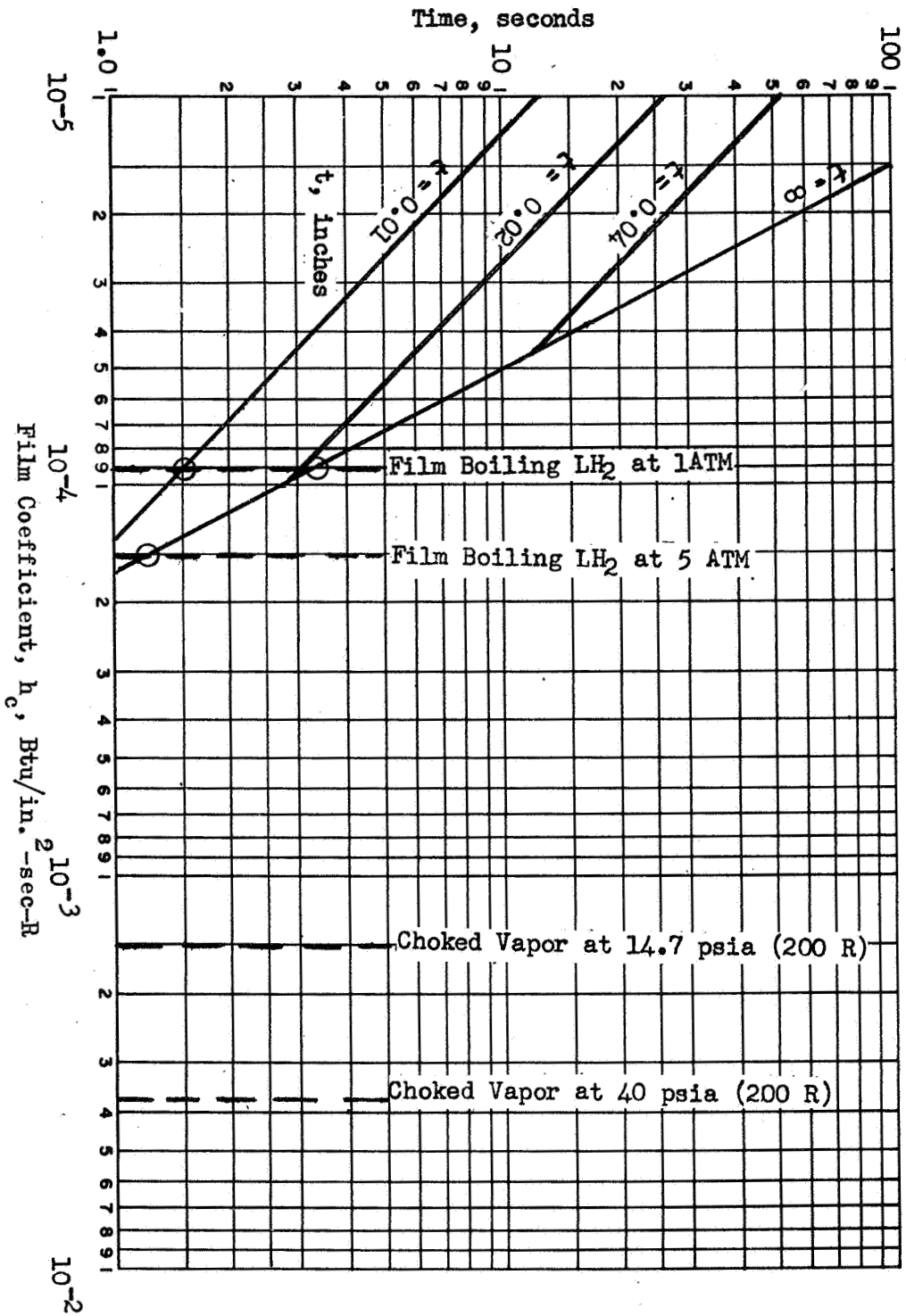


Figure 58. Kel-F Time to Chillover ( $\alpha = 1/e$ )

thickness with a high thermal conductivity and a finite film coefficient for a thick wall. Material properties for this analysis were based upon an average between ambient and -210 F ( $\alpha = 1/e$ ). It is seen that for high conductivity materials a wide difference exists between the solutions for thin and thick wall surfaces. For lower conductivity wall materials a small thickness (<0.1 inch) acts similar to a thick wall due to the small chill penetration depth over the start time period. A comparison of the chilldown times to  $\alpha = 1/e$  may be seen illustrated below for a low film coefficient case (IH<sub>2</sub> film boiling at 5 atm pressure) and a high film coefficient (choked vapor) case.

Material	Time, seconds	
	at $h_c = 1.5 \times 10^{-4}$	at $h_c = 1.4 \times 10^{-3}$
Titanium (0.1 inch)	9.5	1
Titanium ( $t = \infty$ )	120	1.5
Stainless (0.1 inch)	18	2
Stainless ( $t = \infty$ )	500	6
Copper ( $t = 0.1$ inch)	17.5	1.75
Copper ( $t = \infty$ )	12,000	150
Kel-F ( $t = 0.1$ inch)	1.2	0.1
Kel-F ( $t = \infty$ )	1.2	0.1

NOTE: Surface chilldown ambient to 210 R

It is shown that the material comparison charts previously shown are in agreement with the above results. The critical time relationship equations can as a consequence be used for approximate estimate comparisons.

#### MATERIAL CHILLDOWN FOR ZERO LENGTH SURFACES

A more exact computer analysis considering variable material properties of conductivity and specific heat was performed using the Tap II program

(Ref. 48) with varying material properties with temperature and a variety of imposed coolant film coefficients. Chillydown was assessed from ambient to a chilled condition of -420 F with a coolant bulk temperature of -426 F. Figures 59 and 60 compare titanium with stainless material under a low film coefficient circumstance (pool film boiling at 5 atm pressure,  $h_c = 1.5 \times 10^{-4}$  Btu/in.<sup>2</sup>-sec). Comparison of the titanium with the stainless steel indicates a more rapid surface chilling to -420 F. For a 0.1-inch material thickness 15 seconds are required for titanium compared with 60 seconds for stainless steel. Figure 61 compares titanium chillydown with a higher film coefficient. As expected, the time for chillydown is substantially reduced. In addition, it is indicated that the back side wall temperature lags the more rapid chillydown of the cooled surface. A comparison over a range in coolant film coefficients is shown in Fig. 62. The shorter time periods associated with higher film coefficients are shown.

#### Material Coating Study

Applications of insulating surface coatings such as Kel-F and Teflon over the base metal were examined with the aid of the Tap II program (Ref. 48) for transient heat transfer analysis. Wall thicknesses of 0.1 and 1.0 inch were evaluated with surface coatings of 0.010, 0.050, and 0.100 inch with film coefficients ranging from pool film boiling to strong forced convection conditions. Figures 62 to 68 illustrate the effects of surface coating thickness and film coefficient on the chillydown time for a 1.0-inch titanium wall. For low values of film coefficient (pool film boiling) the effect of coating thickness is pronounced; however, within an acceptable time period the surface is not reduced to near the coolant bulk temperature. For higher film coefficients (forced-convection LH<sub>2</sub>) the surface temperature decrease is quite marked. The surface is shown to bleed into the coolant a low heat rate after the initial surface temperature reduction. The effect of increasing the forced convection coefficient is seen to provide a quicker surface chill and to require a smaller coating thickness for

$h_c = 1.5 \times 10^{-4} \text{ Btu/in}^2\text{-sec-}^\circ\text{R}$   
(Pool Film Boiling)  
0.1 inch Titanium  
 $\text{LH}_2$  Bulk Temperature - 425 F

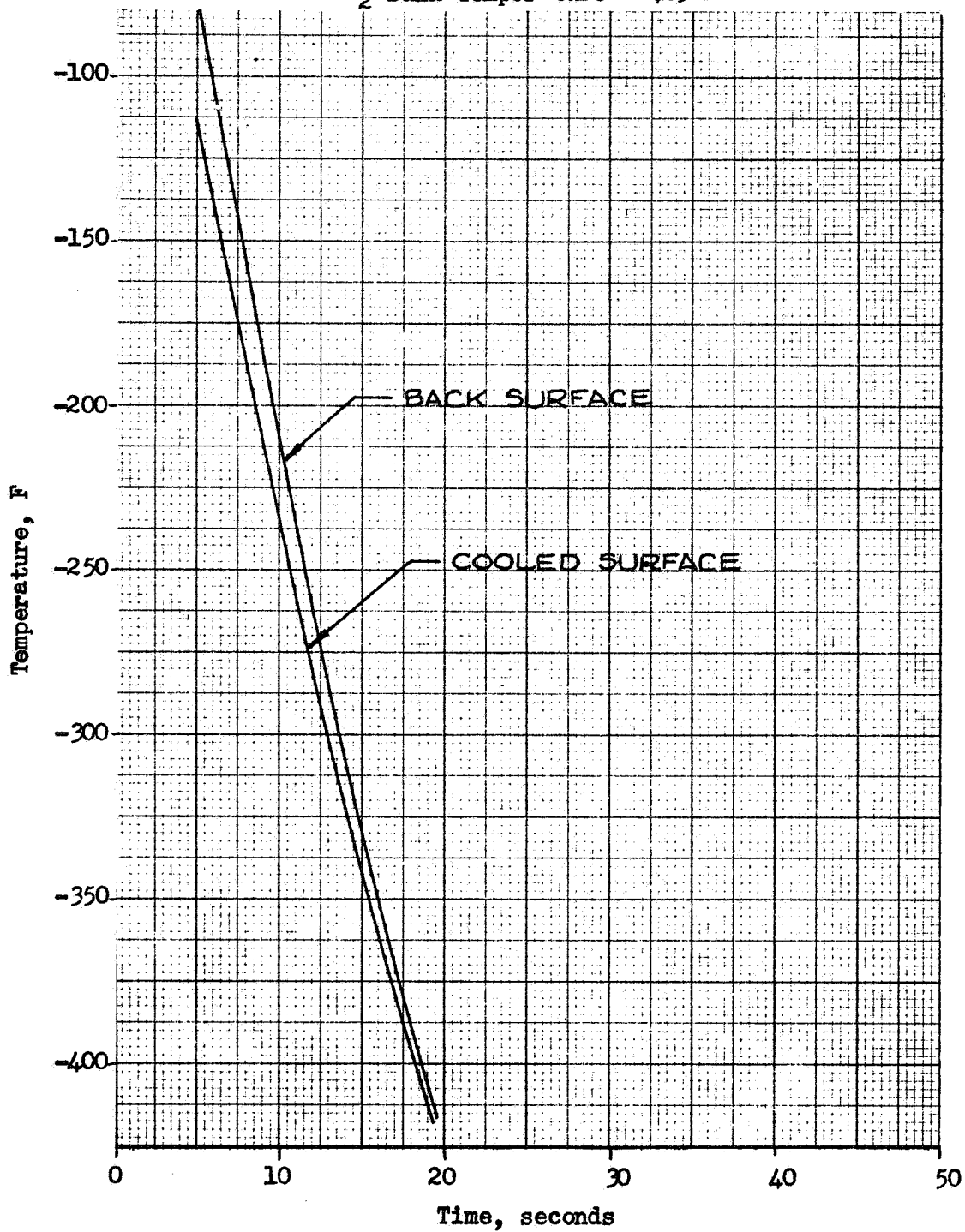


Figure 59. Wall Surface Chilldown vs Time

347 CRES (0.1 inch)  
Pool Film Boiling  
 $h_c = 1.5 \times 10^{-4}$

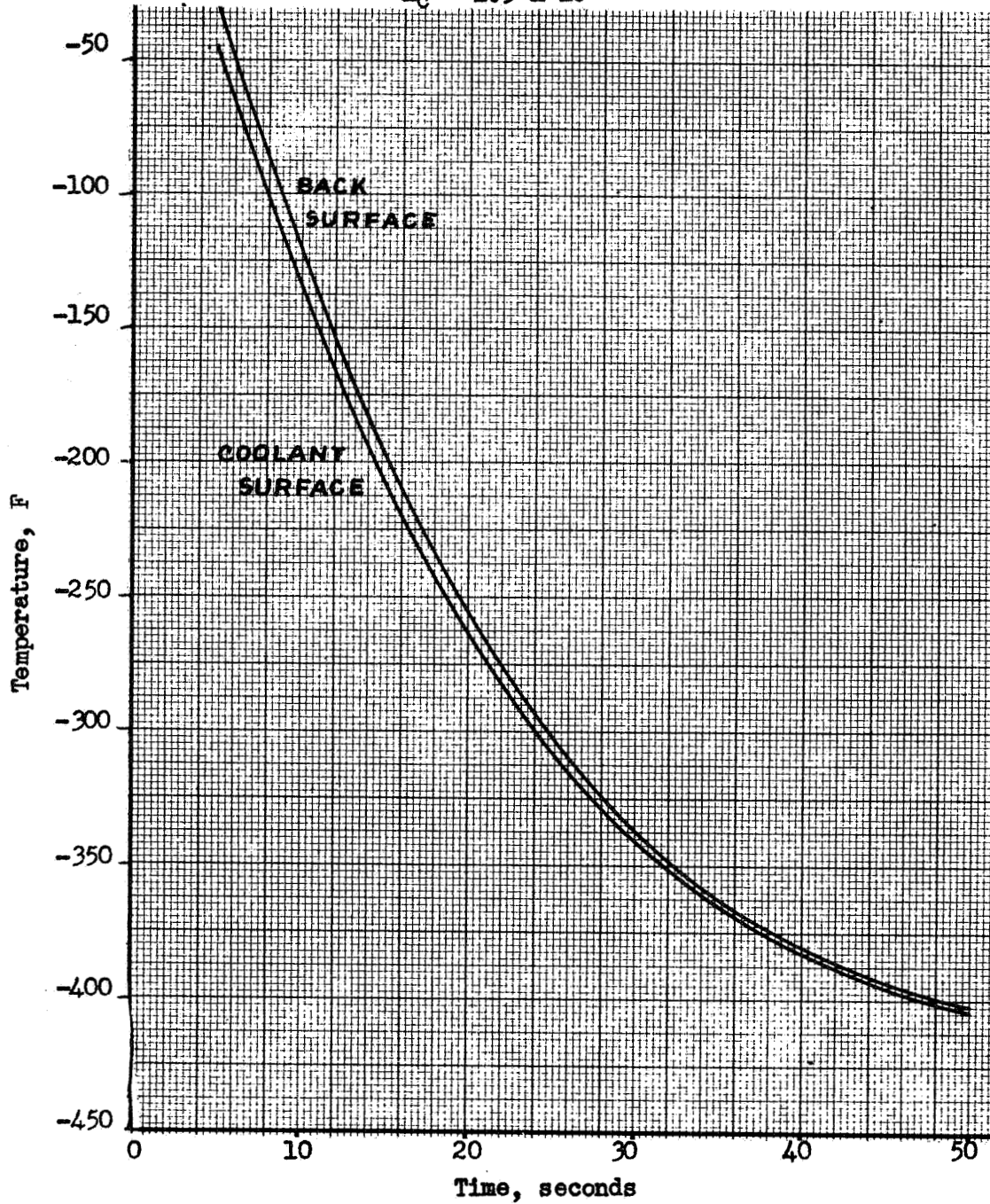


Figure 60. Wall Surface Chillover vs Time

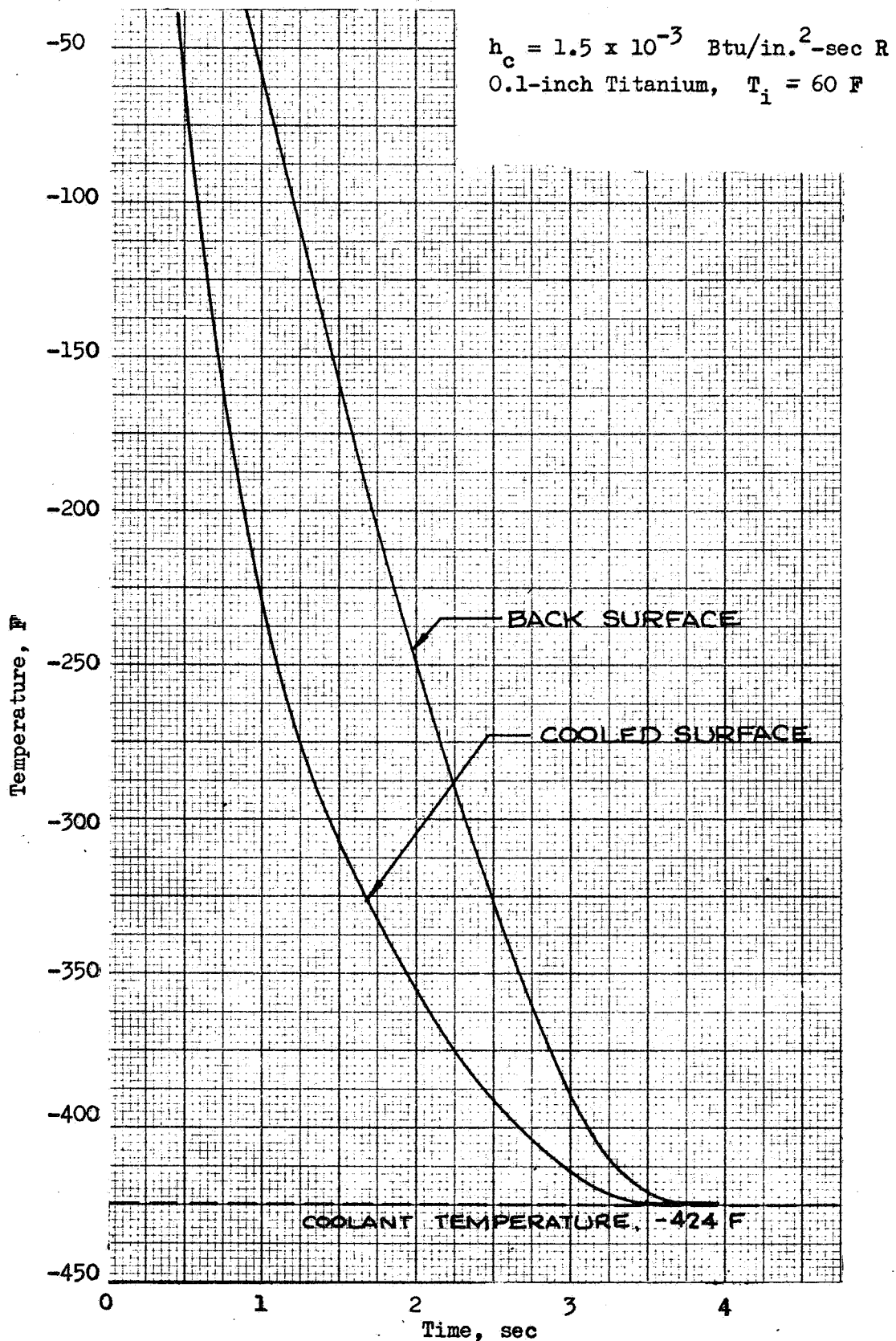


Figure 61. Wall Surface Chilldown vs Time

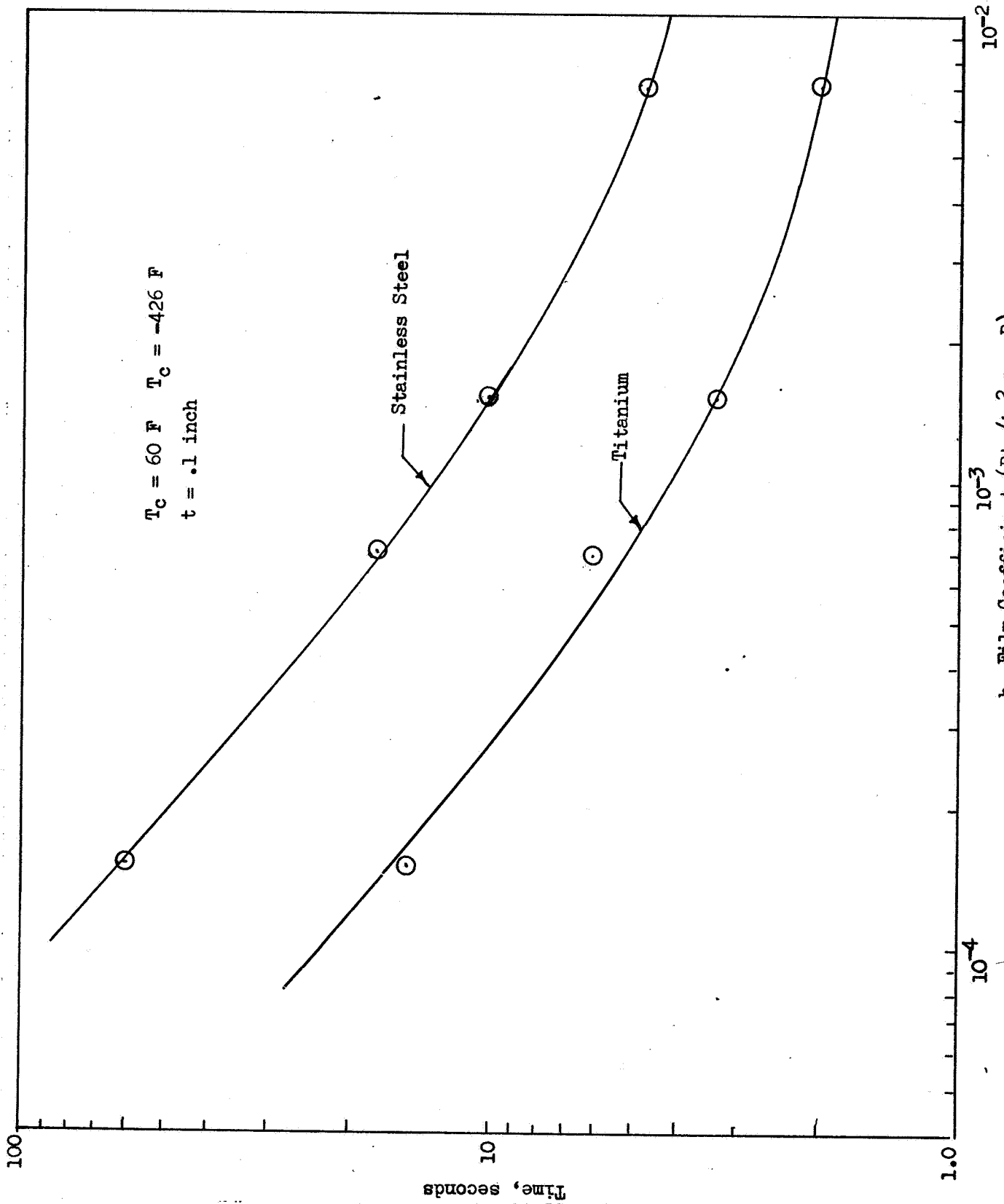


Figure 62. Material Chilldown to -420 F: Computer Solution

$h_c = 1.5 \times 10^{-4} \text{ Btu/in}^2\text{-sec-}^\circ\text{R}$   
(Pool Film Boiling)  
1.0 inch Titanium  
LH<sub>2</sub> Bulk Temperature - 425 F

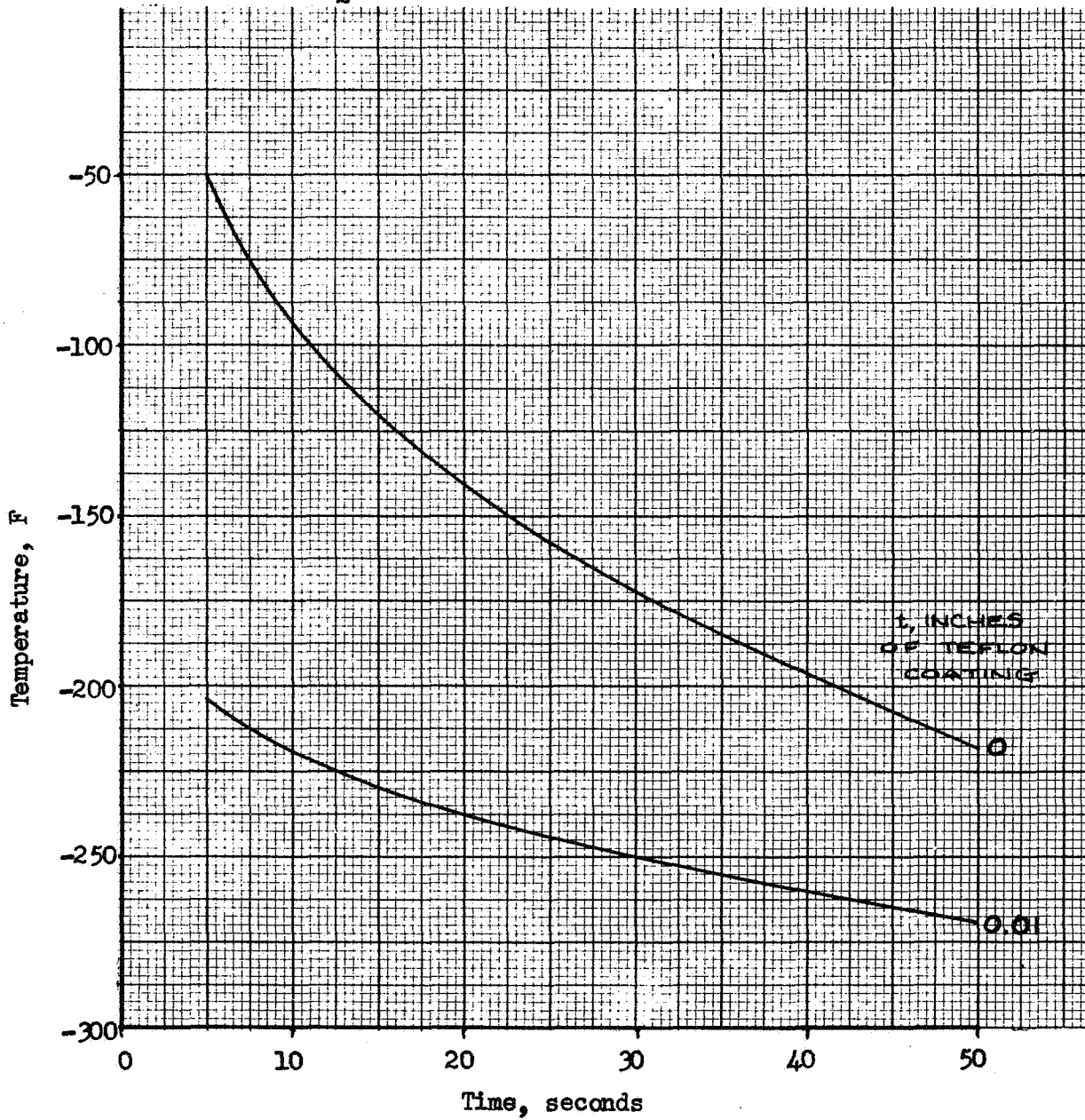


Figure 63. Wall Surface Chillover vs Time

Base Metal	Titanium
Base Metal Thickness	1.0 inch
Teflon Coating Thickness	0.010 inch
LH <sub>2</sub> Bulk Temperature	-425.0 F
Initial Material Temperature	60.0 F

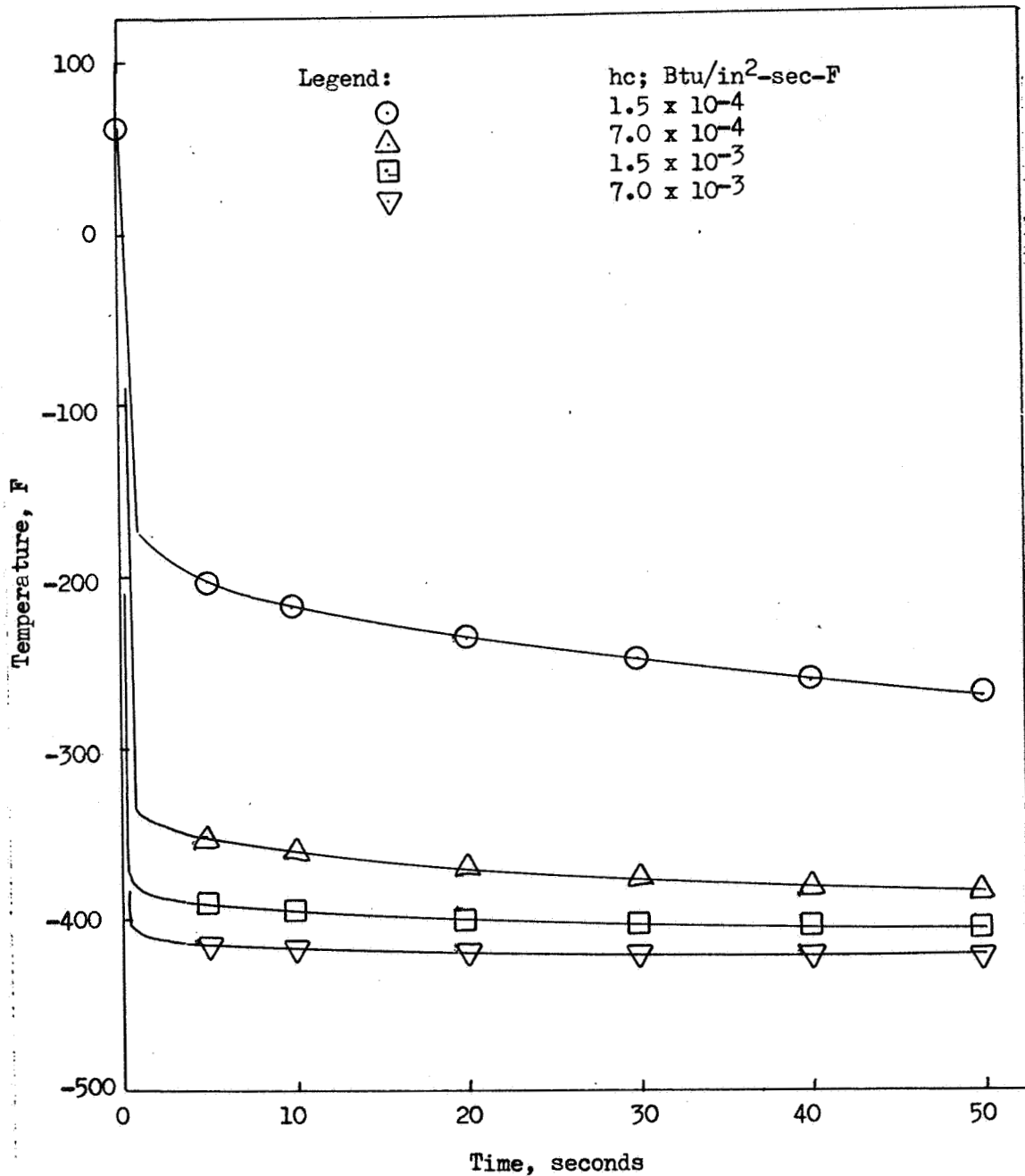


Figure 64. Surface Temperature of Teflon Coating vs Time

Base Metal	Titanium
Base Metal Thickness	1.0 inch
Teflon Coating Thickness	0.050 inch
LH <sub>2</sub> Bulk Temperature	-425.0 F
Initial Material Temperature	60.0 F

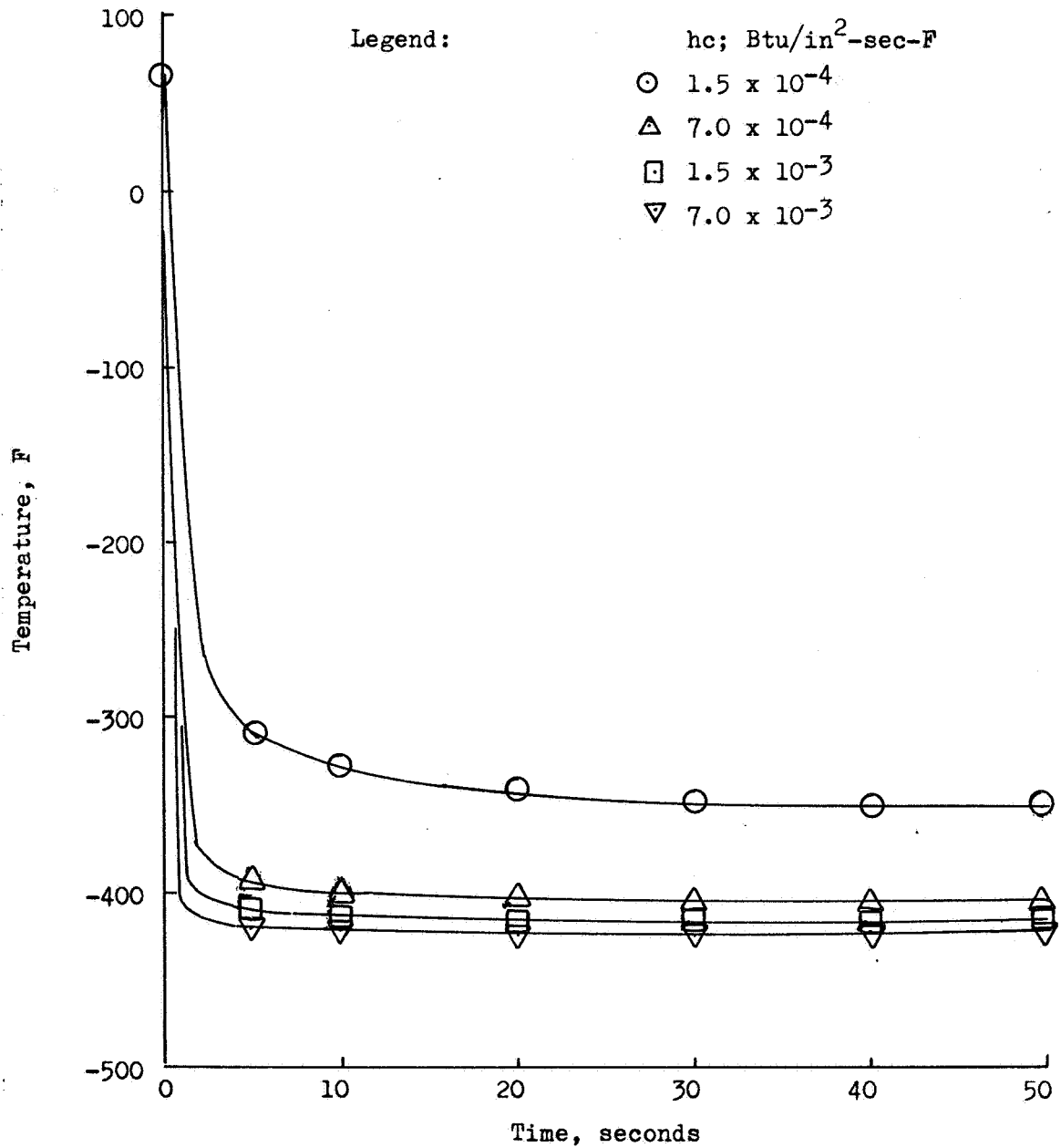


Figure 65. Surface Temperature of Teflon Coating vs Time

Base Metal	Titanium
Base Metal Thickness	1.00 inch
Teflon Coating Thickness	0.100 inch
LH <sub>2</sub> Bulk Temperature	-425.0 F
Initial Material Temperature	60.0 F

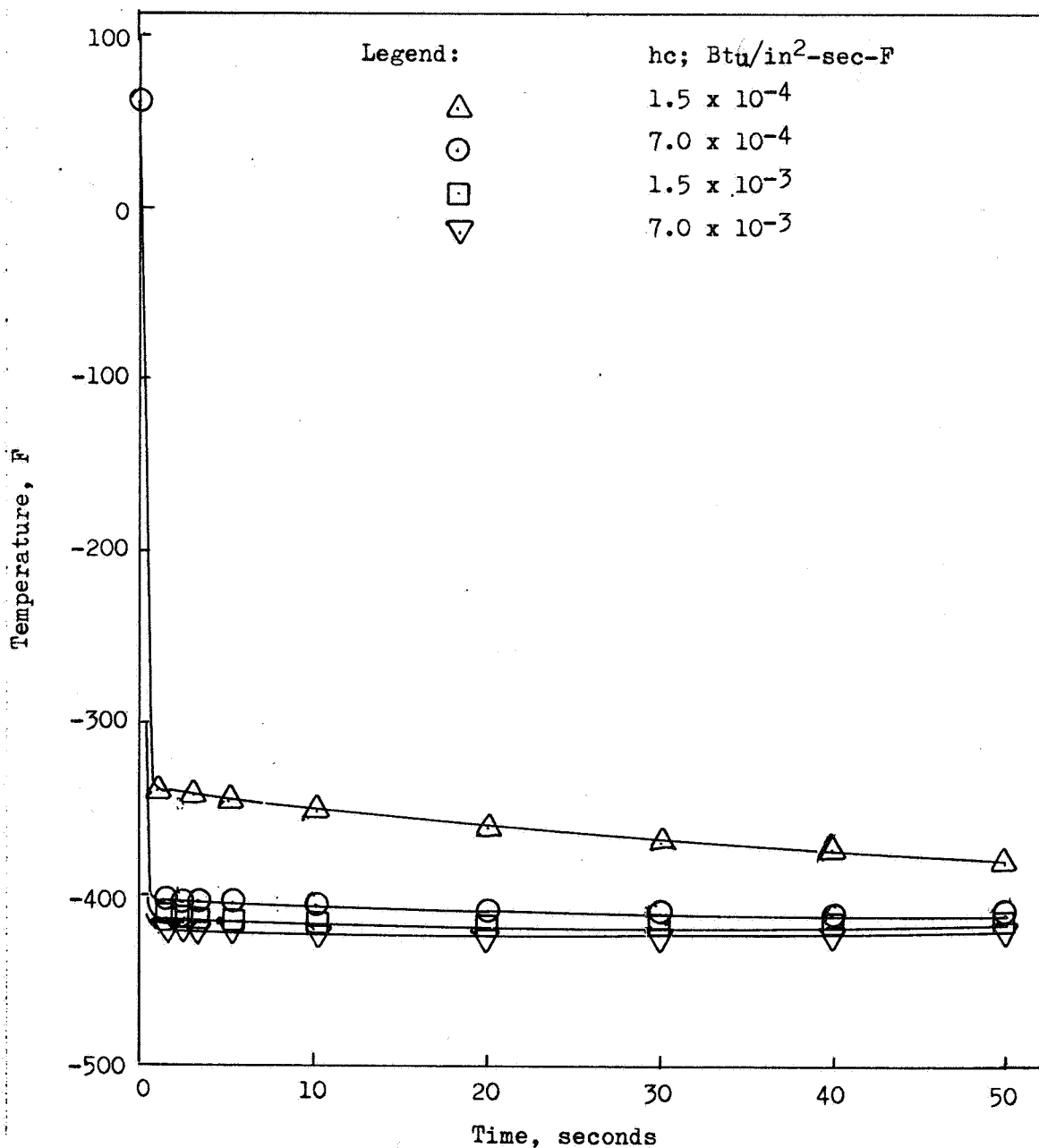


Figure 66. Surface Temperature of Teflon Coating vs Time

Base Metal	347 S.S.
Base Metal Thickness	1.0 inch
Teflon Coating Thickness	0.010 inch
LH <sub>2</sub> Bulk Temperature	-425.0 F
Initial Material Temperature	60.0 F

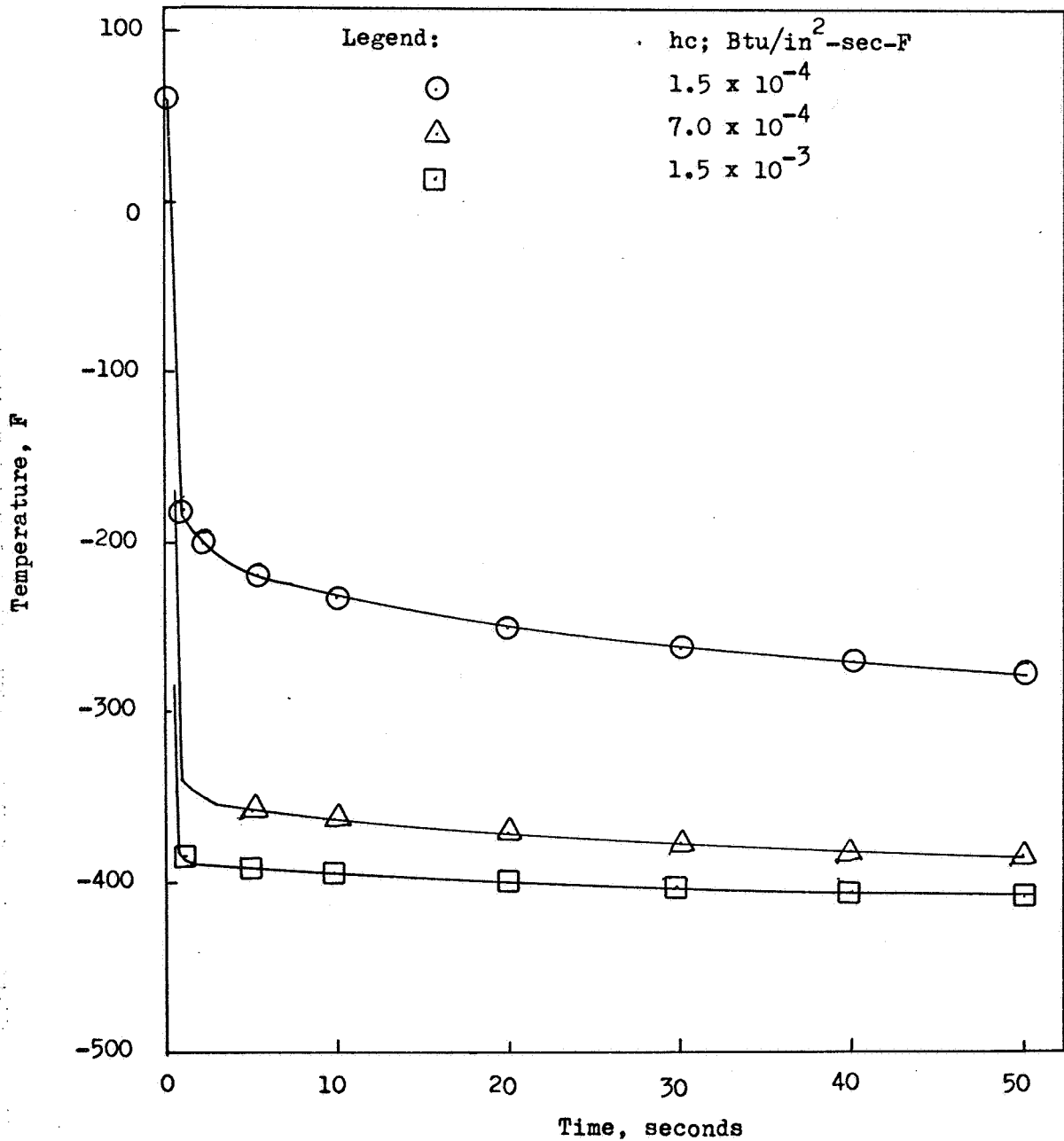


Figure 67. Surface Temperature of Teflon Coating vs Time

Base Metal 347 S.S.  
 Base Metal Thickness 1.0 inch  
 Teflon Coating Thickness 0.050 inch  
 LH<sub>2</sub> Bulk Temperature -425.0 F  
 Initial Material Temperature 60.0 F

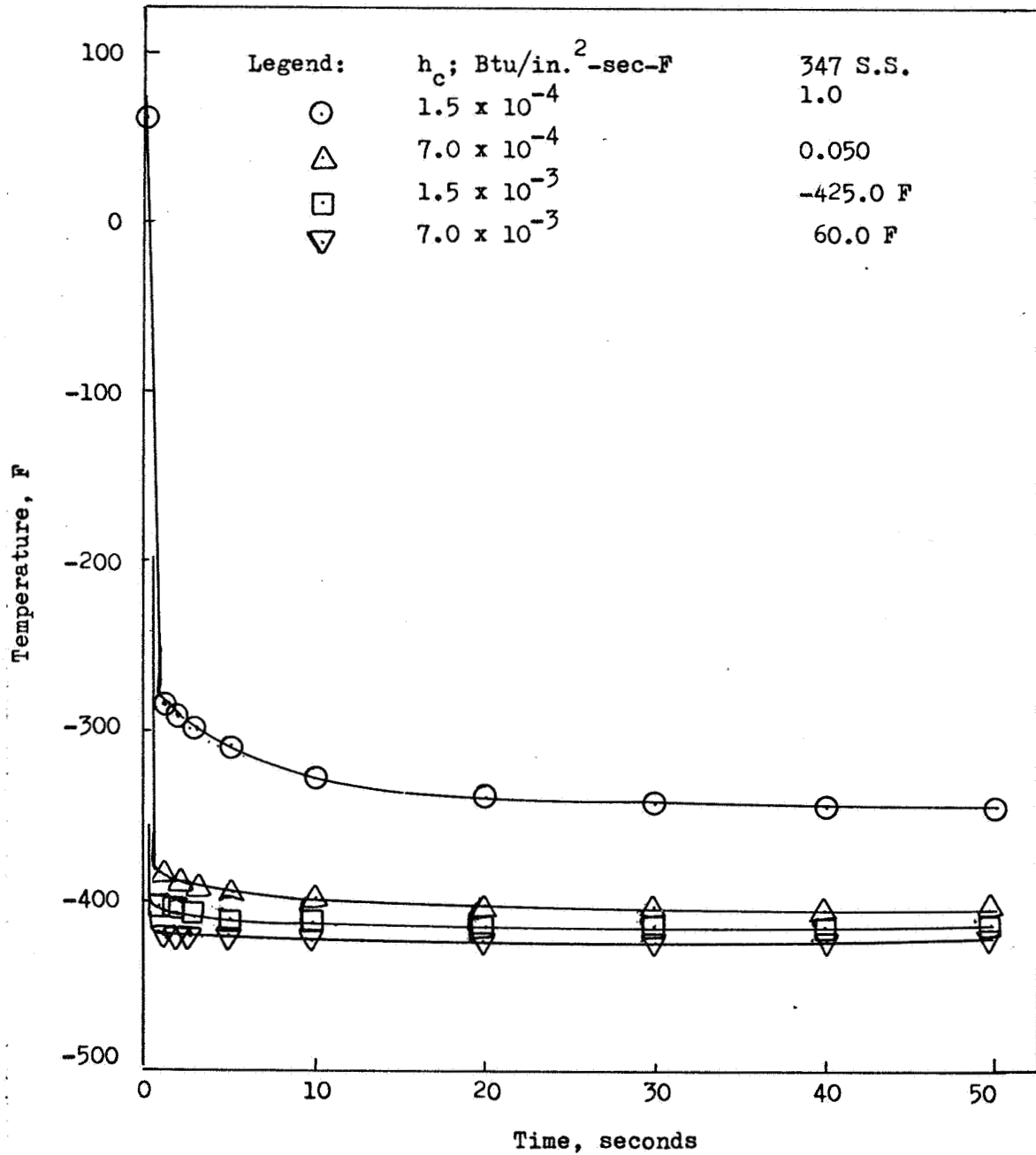


Figure 68. Surface Temperature of Teflon Coating vs Time

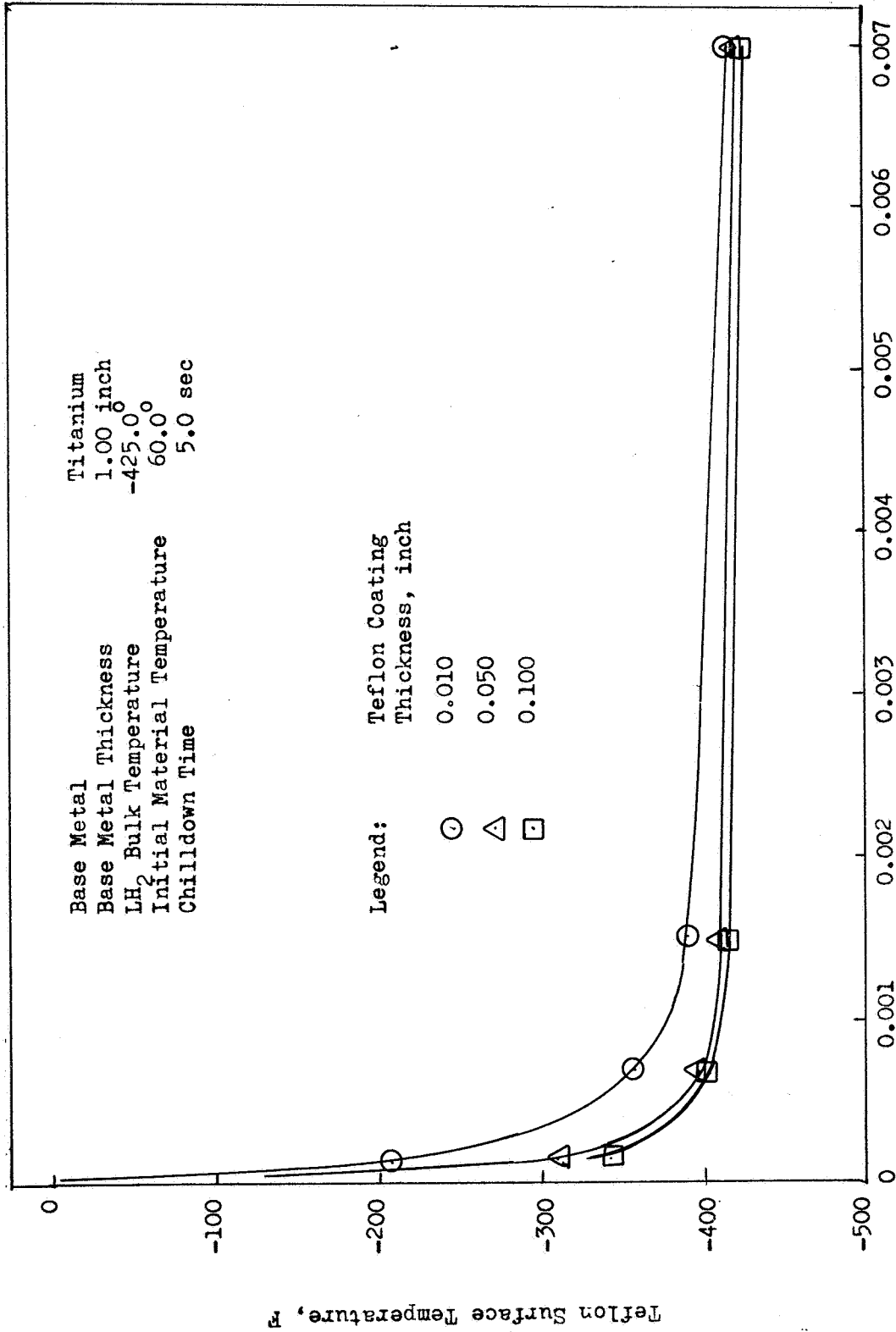
a given time period. Comparable figures for 1.0-inch thickness stainless material is shown in Fig. 67 and 68. For the higher applied film coefficients and thicker surface coatings the effects of the metal base material properties are minimized. Figure 69 illustrates a graph of surface temperature vs heat transfer coefficient after a 5-second period. Benefits of increased coating thickness above 0.050 inch (Teflon) are seen to be beneficial only for low film coefficient values ( $<0.001 \text{ Btu/in.}^2\text{-sec-F}$ ). For the pump and line surfaces as a consequence it is seen that the requirement of a small coating thickness on high fluid velocity surfaces and a large thickness on low fluid velocity surfaces is indicated. As a result, thin pump blading need only be coated with a minimum thickness insulator.

#### MATERIAL CHILLDOWN FOR FINITE LENGTH SURFACES

A further computer investigation of the chilldown characteristics of long pump fluid passages was made with several candidate pump materials, wall thicknesses, film coefficients and wall coatings to complete the previous ( $L/D = 0$ ) work just described. A section of fluid passage typical of a hydrogen pump was analyzed to determine the wall and fluid temperatures as a function of passage length to equivalent hydraulic diameter ratio ( $L/D$ ). The developed fluid passage is assumed to typically have a nominal equivalent diameter of  $1/\pi$  inches. This is shown in the sketch of Fig. 70. The thermal analyzer computer program was modified to include the effect of bulk temperature rise along the passage length and was employed for this parametric analysis.

The various parameters were expressed in terms of the Stanton, Biot, and Fourier numbers listed below:

$$\text{Stanton number} = \frac{h}{G_{\infty} C_{P_{\infty}}} \quad (74)$$



Heat Transfer Coefficient, Btu/in.<sup>2</sup>-sec-F

Figure 69. Teflon Coating Surface Temperature vs Heat Transfer Coefficient

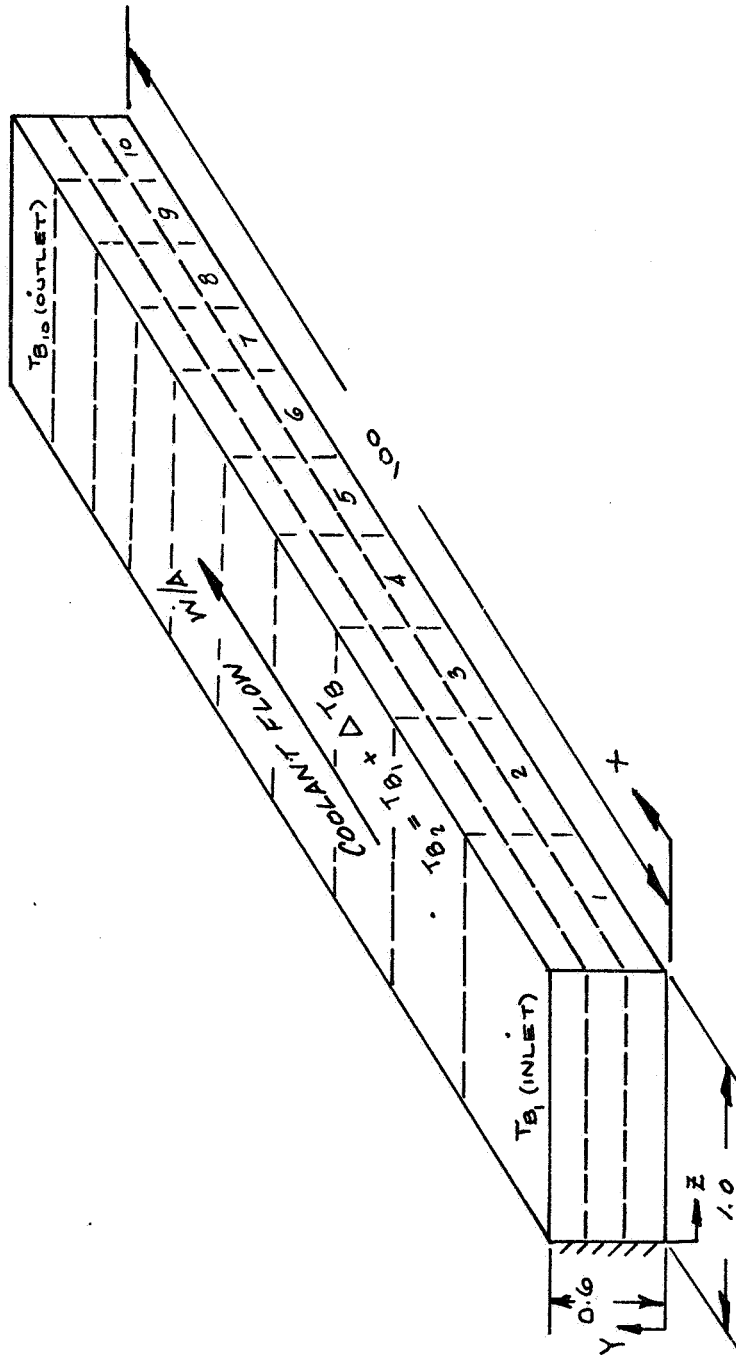


Figure 70. Typical Section of a Coolant Passage Wall Chilled on One Side with a Cryogenic Fluid

$$\text{Biot number} = \frac{h t_w}{k_w} \quad (75)$$

$$\text{Fourier number} = \frac{\alpha \tau}{t_w^2} \quad (76)$$

These nondimensional parameters allow a degree of generality in the results by which moderate changes in some parameters may be predicted and comparisons made for differing conditions. A typical value for the Stanton number in the hydrogen-cooled passage was taken as 0.00218 with the hydrogen properties evaluated at an average temperature of 200 R.

The film coefficient was varied by an order of magnitude from 0.001 representing forced convection down to 0.0001 Btu/sec-in.<sup>2</sup>-R representing pool film boiling. A typical case chosen for consideration was a hydrogen-cooled passage through an aluminum wall of 0.6-inch thickness. In all cases the wall was assumed initially at an ambient temperature of 530 R. The coolant enters at 60 R and experiences a bulk temperature rise along the passage. At 10 seconds after start of chilldown the wall temperature at an L/D of zero near the inlet has reached 225 R and, due to a higher fluid temperature, rises rapidly with L/D to near the initial wall temperature as shown in Fig. 71. Within 2 minutes time the wall has completely chilled to an L/D of 150 and within 50 degrees at an L/D of 300.

The corresponding bulk temperature of the coolant is plotted in Fig. 72. For the high film coefficient of 0.001 the hydrogen bulk temperature has a dominant influence on chilldown with the wall temperature following closely the fluid temperature with increased time.

The wall surface temperature drops rapidly at an L/D of 300 and rather slowly at L/D values above approximately 100 due to this rapid rise in the accompanying bulk temperature.

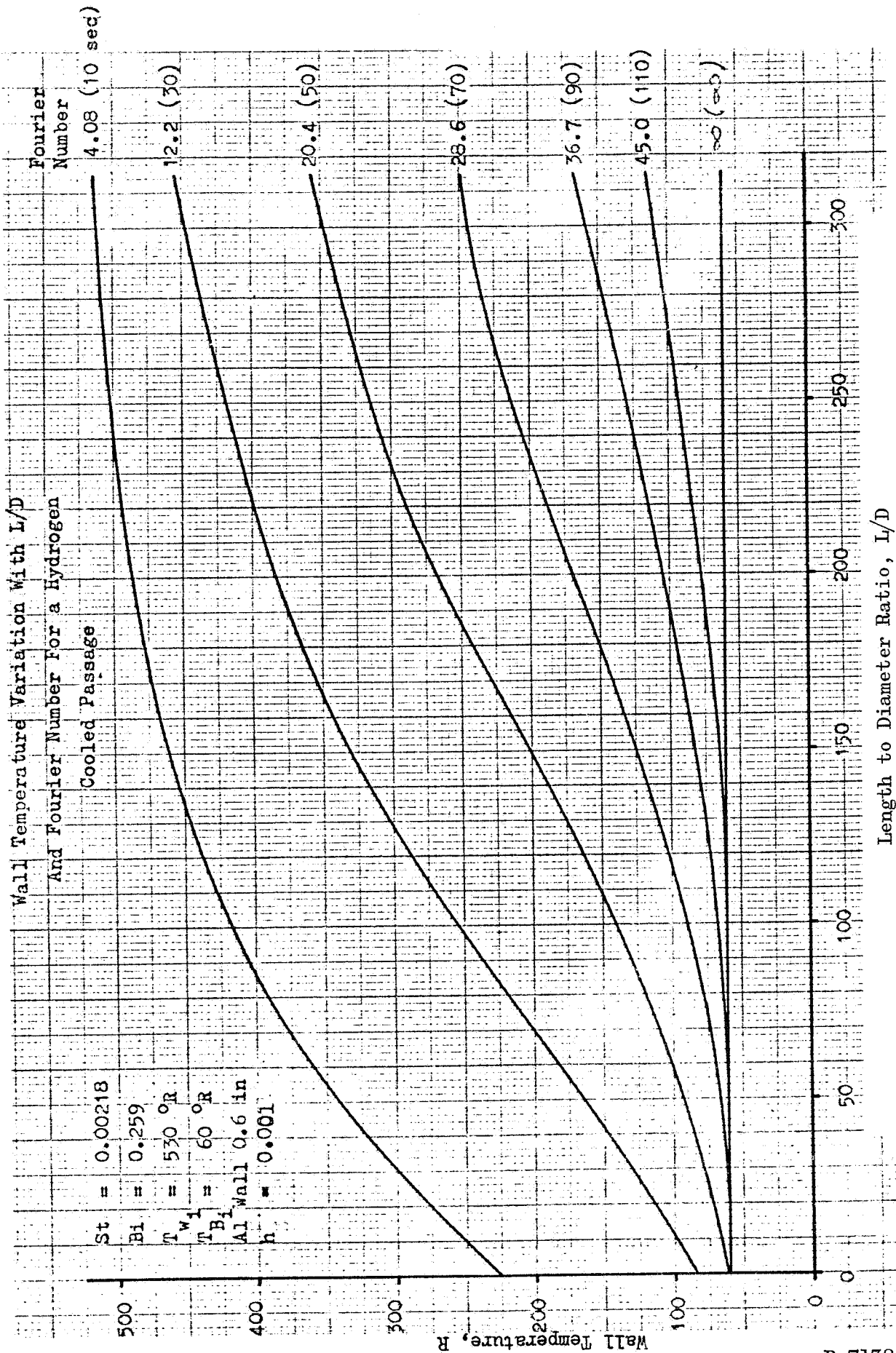


Figure 71. Wall Temperature Variation With L/D and Fourier Number for a Hydrogen-Cooled Passage

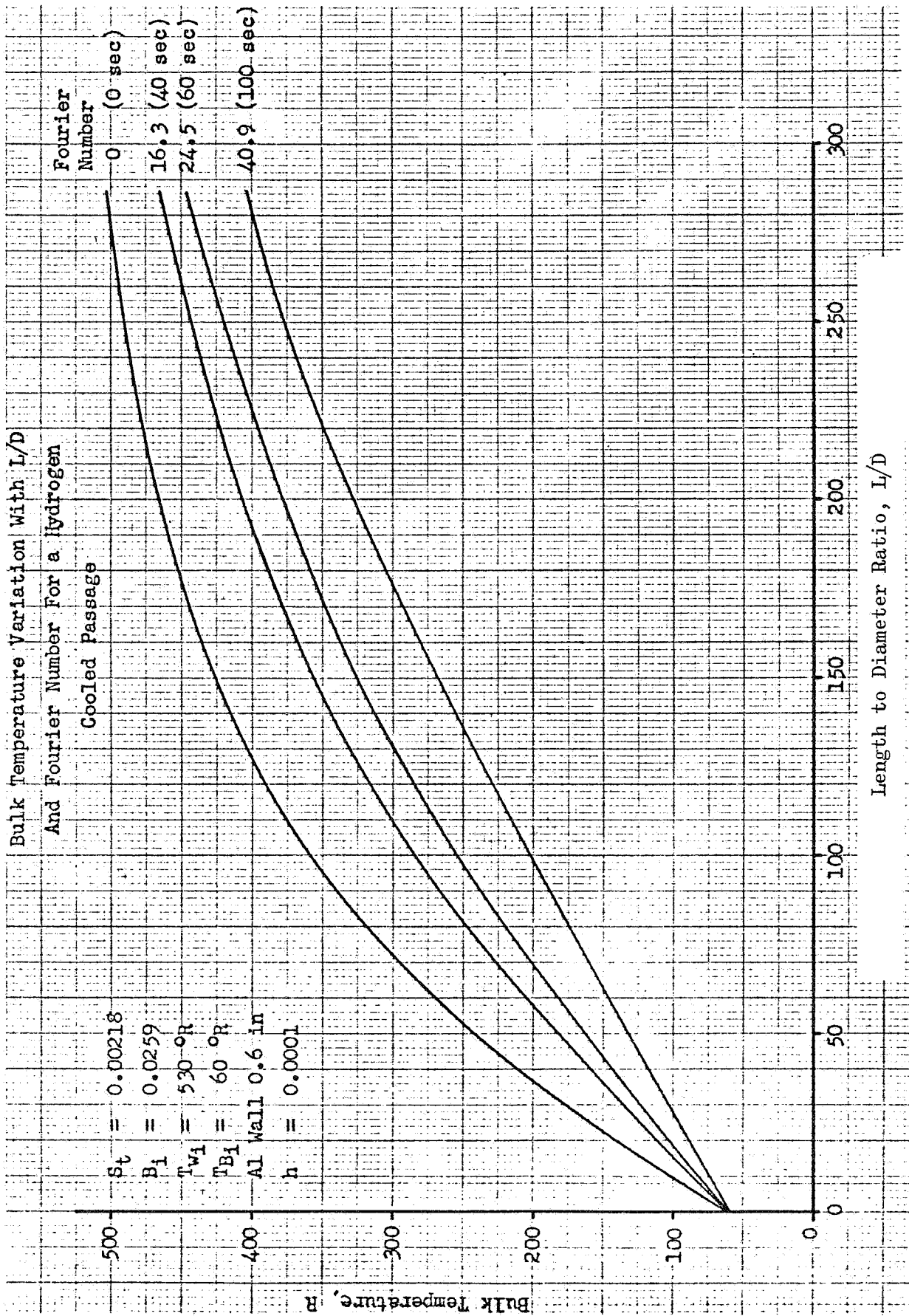


Figure 72. Bulk Temperature Variation with L/D and Fourier Number for a Hydrogen-Cooled Passage

This indicates that an L/D of 100 to 150, modeling hydrogen pump and line passages, may require a considerably longer chilldown period. The predicted chilldown times by a transient analysis of the wall without considering the bulk temperature rise through the passage ( $L/D = 0$ ) will be shorter.

The 0.1-inch aluminum wall shown in Fig. 73 chills much more rapidly at low L/D values but only slightly faster at high L/D values. The chill is almost completely down to bulk temperature at an L/D of zero within 10 seconds and throughout for an L/D of 300 within 2 minutes. This indicates the thin wall is of considerable advantage in chilling short passages but of little benefit in chilling long passages. Similar curves are plotted for 347 CRES in Fig. 74 and titanium in Fig. 75. The 0.6-inch CRES wall chills somewhat less than the aluminum at high Fourier numbers and L/D values since its heat content  $\rho C_p$  is approximately 50 percent greater. The titanium surface chills more rapidly at low L/D values, due to low thermal diffusivity ( $\alpha$ ), and at the same rate as aluminum at high L/D values since they have approximately the same total heat content ( $\rho C_p$ ). These wall temperatures are also controlled largely by the bulk temperature which is similar to Fig. 72 for high film coefficients.

For the same thickness of wall and high film coefficient the material selection has little bearing on chilldown rate at high L/D and Fourier numbers and a moderate effect at an L/D of zero and low Fourier numbers.

Decreasing the Biot number or film coefficient by a factor of 1/10 increases the chilldown time appreciably as may be seen for an 0.6-inch aluminum wall in Fig. 76. This indicates under low coolant flowrates and film coefficient the chilldown will be very slow with high bulk temperature persisting throughout a long chilldown period as in Fig. 76. This condition is to be avoided for a rapid LH<sub>2</sub> turbopump start.

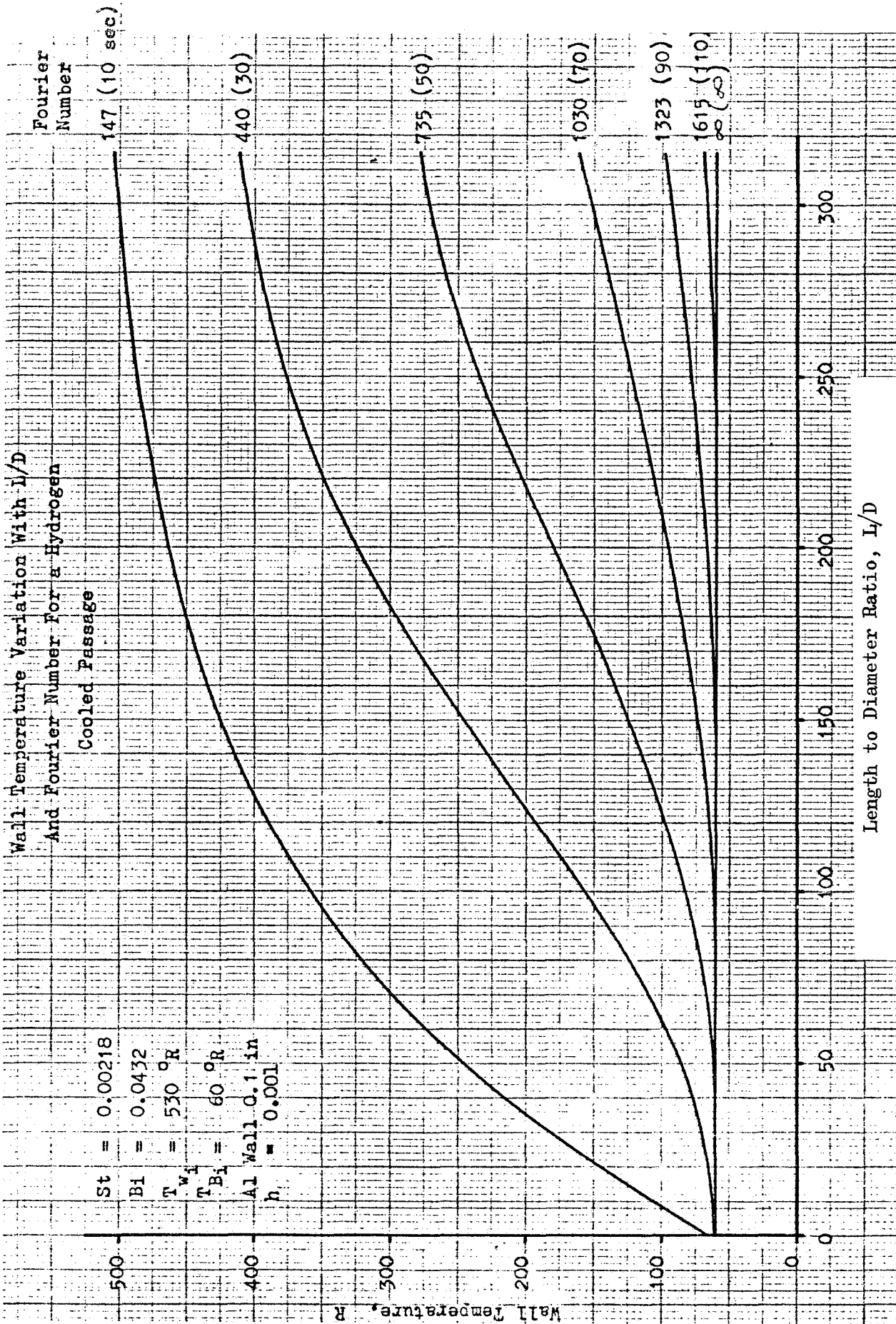


Figure 73. Wall Temperature Variation With  $L/D$  and Fourier Number for a Hydrogen-Cooled Passage

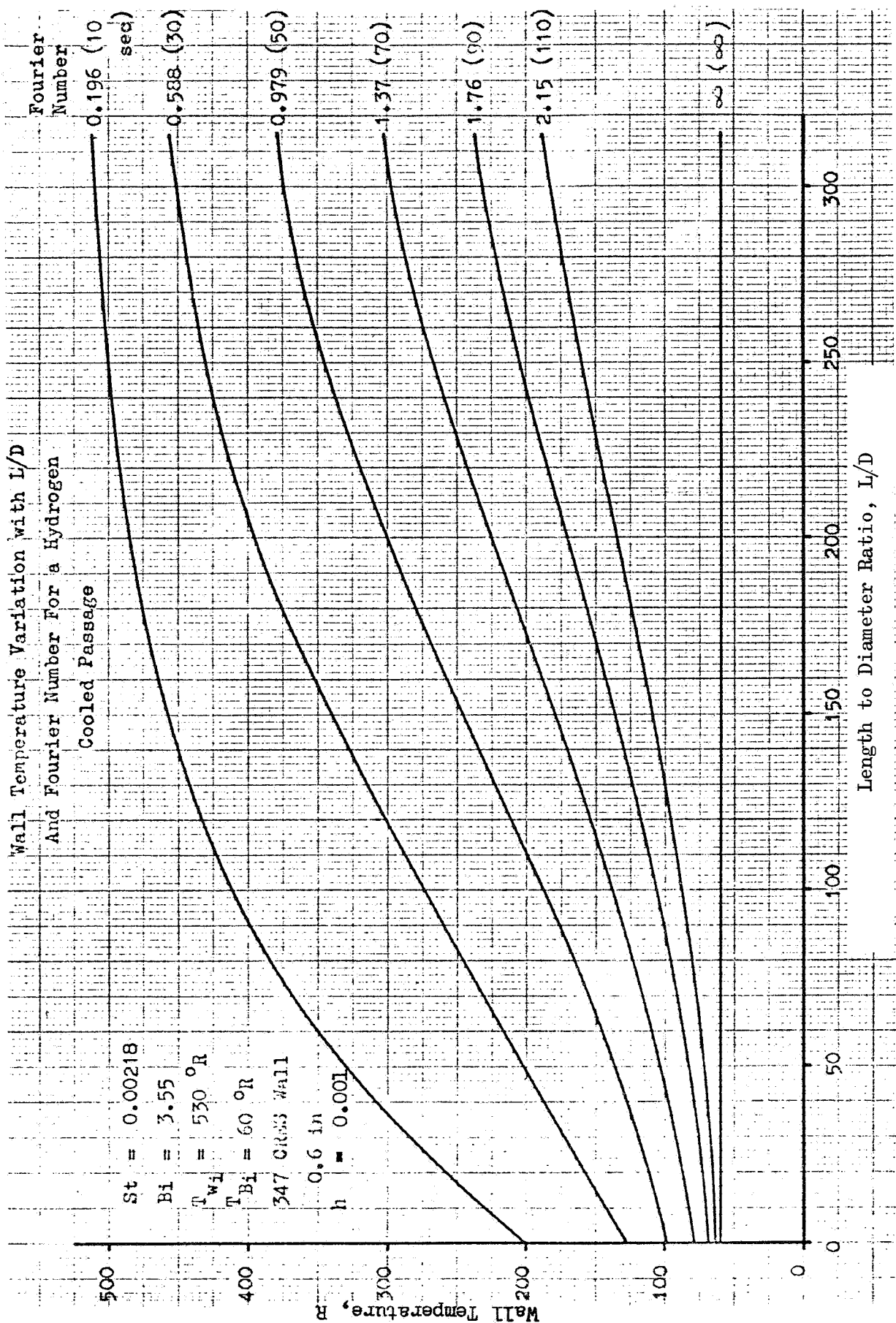


Figure 74. Wall Temperature Variation With L/D and Fourier Number for a Hydrogen-Cooled Passage

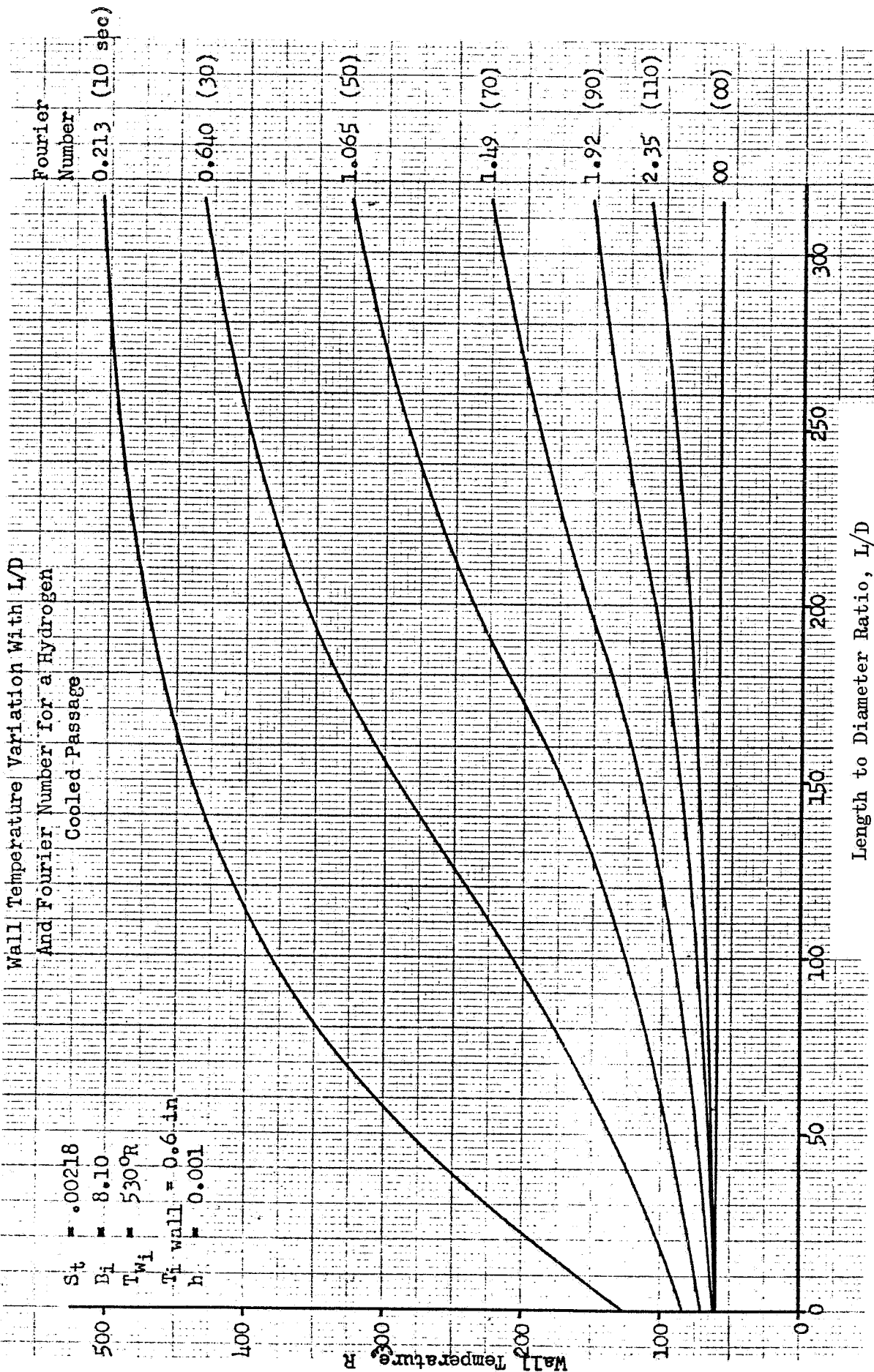


Figure 75. Wall Temperature Variation With L/D and Fourier Number for a Hydrogen-Cooled Passage

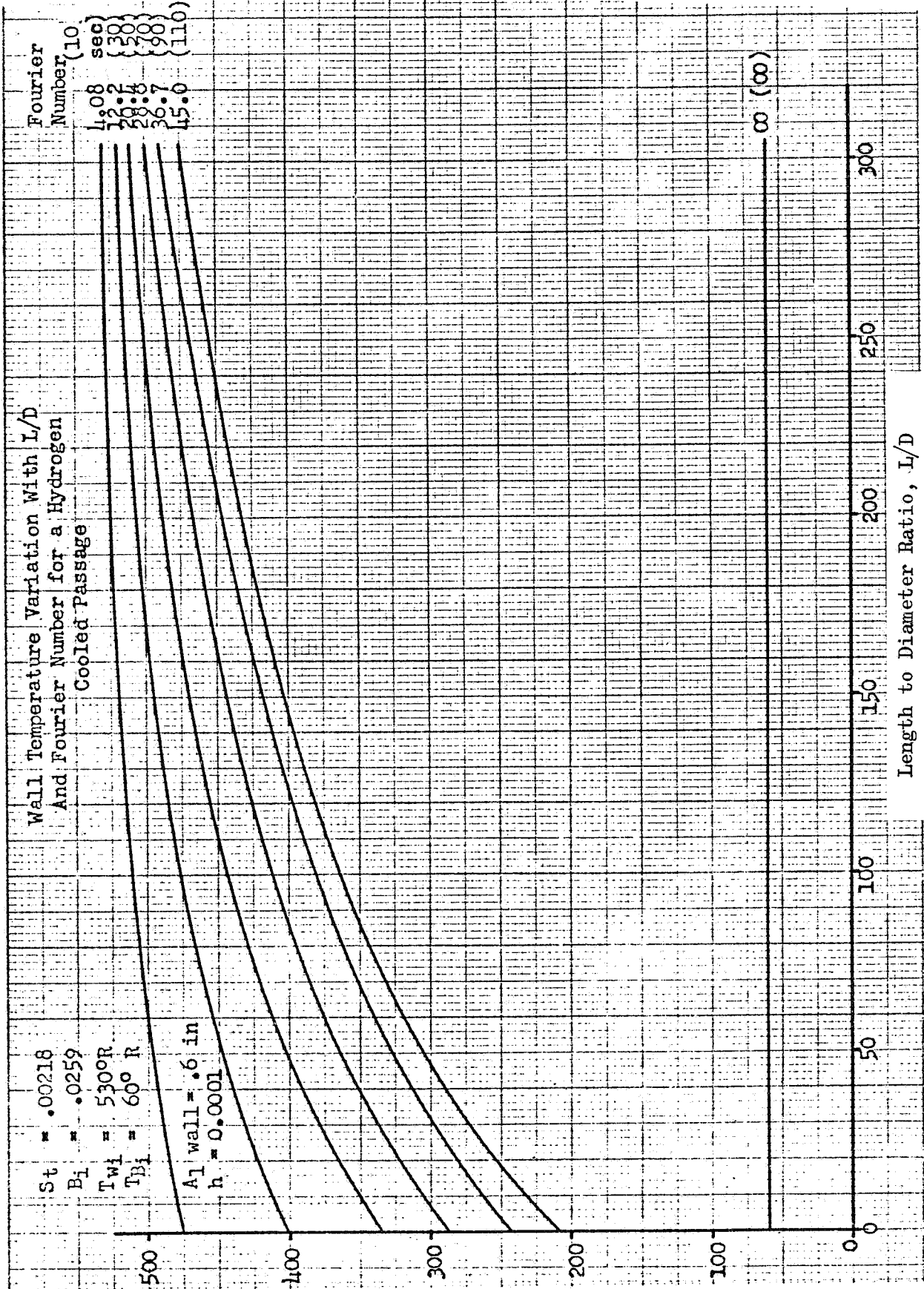


Figure 76. Wall Temperature Variation With L/D and Fourier Number for a Hydrogen-Cooled Passage

A logical alternative when a rapid chilldown is not possible for low flow-rates and large metal masses, is to retard the heat input to fluid through use of a high thermal resistance coating. To determine the effect on a long fluid passage, a Kel-F coating of 0.050 inch applied to the 0.6-inch aluminum wall was analyzed. This resulted, as seen in Fig. 77, in a substantial drop in wall surface temperature at low  $L/D$  values and only a slight decrease at high  $L/D$  and intermediate Fourier numbers as compared with no coating case in Fig. 71.

The optimum coating thickness for the operating conditions of Fig. 77 is indicated by the variation of wall surface temperature with coating thickness plotted in Fig. 78. For low  $L/D$  values from 0 to approximately 100, coating thickness of 0.010 to 0.020 inch ( $h = 0.001 \text{ Btu/in.}^2\text{-sec-R}$ ) appear to yield most of the benefit available from a coating. It appears that coating a high  $L/D$  passage is of little advantage due to the large fluid temperature rise encountered. The coating is of considerable benefit in providing a rapid surface chill with low film coefficients and coolant flow. This is seen in comparing the surface temperatures of Fig. 79 with those of Fig. 77.

The thermal analyzer program employed did not include the effect of variation in hydrogen specific heat with bulk temperature. A brief hand calculation including the change in specific heat serves to show its effect is small and diminishes rapidly with time. The coolant initial bulk temperature distribution along the wall for an 0.6-inch CRES wall is shown in Fig. 80 as calculated within the program. If each bulk temperature rise is corrected for  $C_p$ , the resultant curve will be shifted a maximum of approximately 8 percent higher in bulk temperature at the lower  $L/D$  values as shown in Fig. 80. This diminishes the heat transfer rate only slightly at the initial time period. At 20 seconds the differences in bulk temperature becomes negligible, thus introducing little error in the time for chill-down. The effect of  $C_p$  variation will be damped out earlier with a smaller time increment for bulk temperature change.

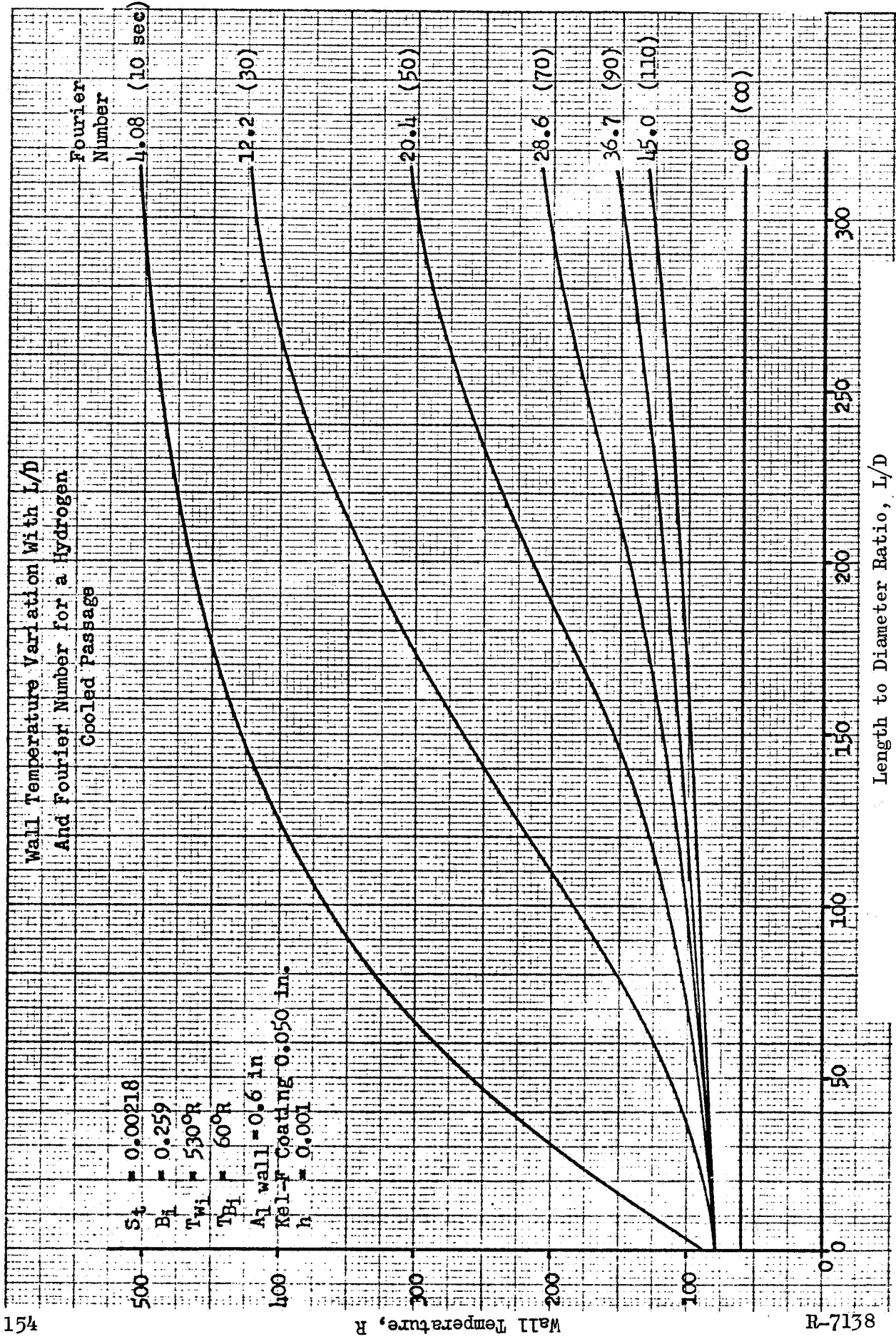


Figure 77. Wall Temperature Variation With L/D and Fourier Number for a Hydrogen-Cooled Passage

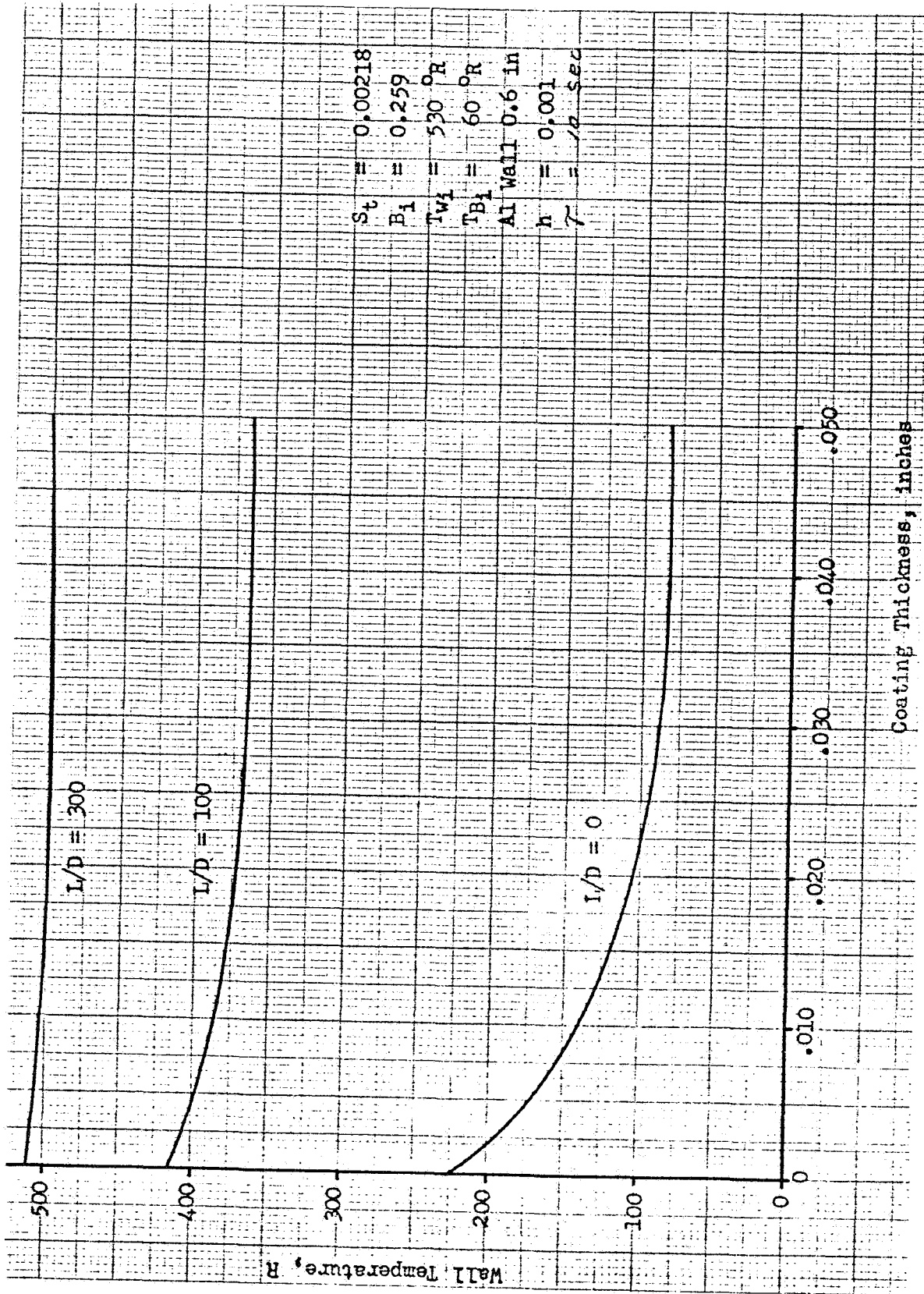


Figure 78. Wall Temperature vs Coating Thickness for Various L/D Values

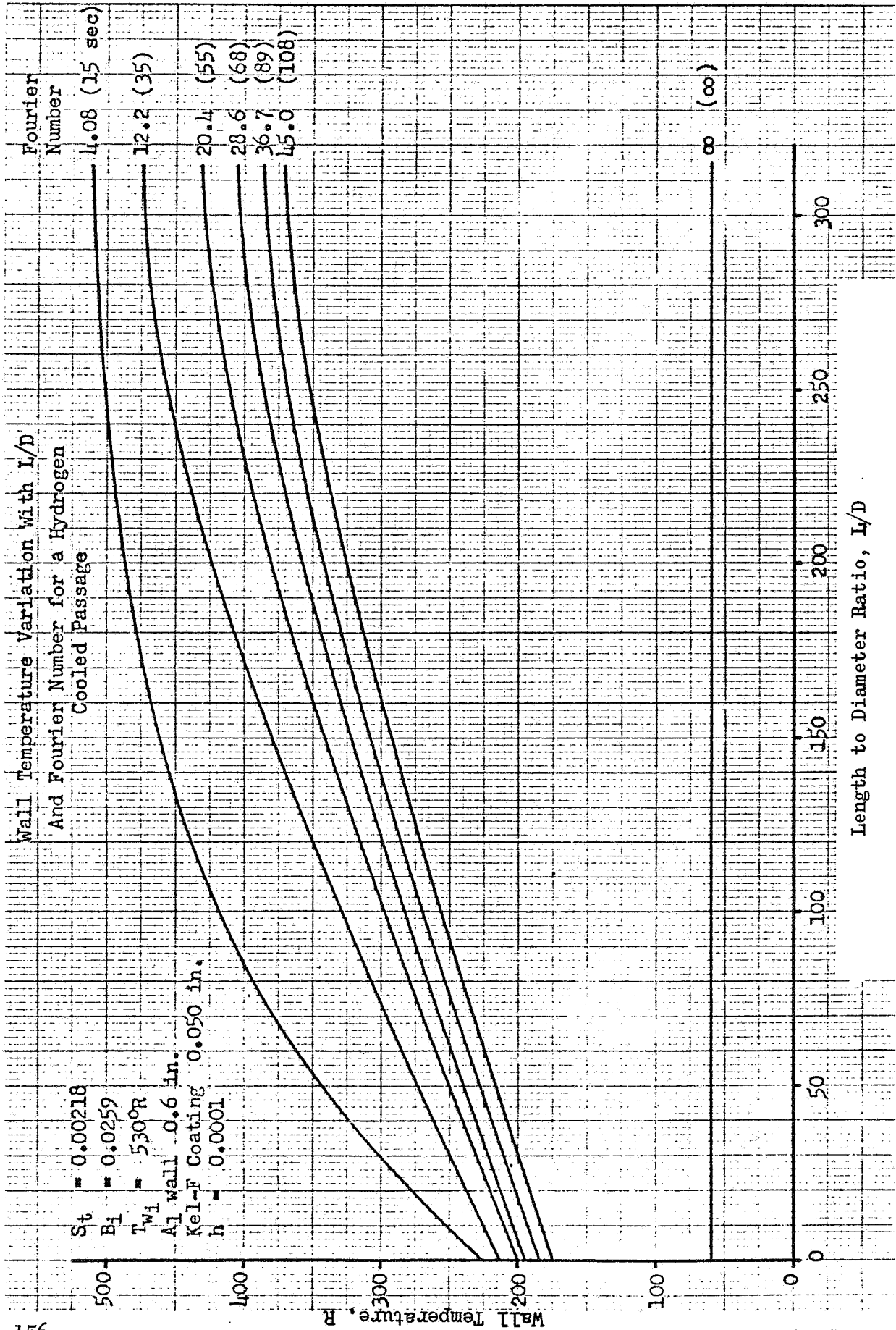


Figure 79. Wall Temperature Variation With L/D and Fourier Number for a Hydrogen-Cooled Passage

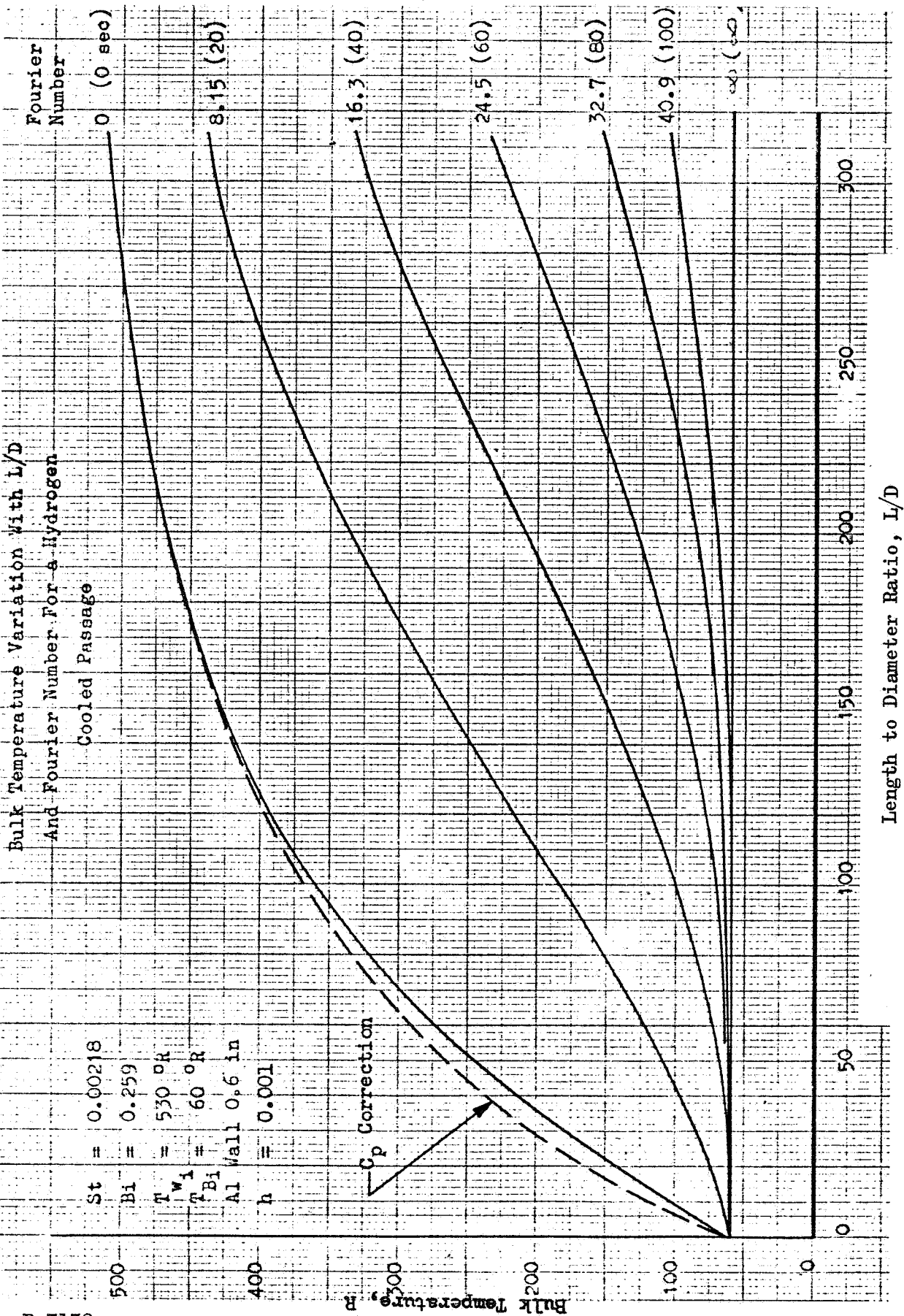


Figure 80. Bulk Temperature Variation With L/D and Fourier Number for a Hydrogen-Cooled Passage

## TRANSIENT TWO-PHASE HYDROGEN HEAT TRANSFER

Under an associated program study, experimental transient two-phase hydrogen flow heat transfer data were obtained for uncoated tubes made of the candidate pump materials; CRES 321 stainless steel, titanium (5Al-2.5 Sn), aluminum alloy (Tens 50), and K-monel, with OFHC copper used as a reference material (Table 21). A total of 87 tests was run with tank pressures varying between 25 and 150 psig and initial tube temperatures ranging from ambient to 30 R. The chilldown was considered complete when steady liquid flow was obtained at the exit of the tube test section. A minimum of two tests was run for each test condition. A test summary is shown in Table 21. (The thickness of each tube chosen was such that the amount of heat dissipated when the tube cooled from ambient to liquid hydrogen temperatures was approximately the same for all five tubes.)

A drawing of a typical test specimen is shown in Fig. 81. Photographs of a typical test specimen, test apparatus, vacuum chamber, and flow schematic are shown in Fig. 82 to 85.

The experimental data collected during the tests included:

1. Temperature histories obtained from nine chromel-constantan thermocouples located on the outer surfaces of the tubes and three chromel-constantan thermocouples located in 1/8-inch-deep wells for the steel and the K-monel tubes
2. Temperature of the liquid hydrogen in the reference junction pool measured by a Rosemount platinum resistance thermometer
3. Bulk temperatures of the hydrogen flow immediately upstream and immediately downstream of the test section (These were measured by chromel-constantan thermocouples fabricated from 0.003-inch-diameter wires.)

TABLE 21

SUMMARY OF TEST CONDITIONS, JANUARY 1967  
TEST SERIES

Test Specimen (tubes)	Run No.	Initial Temperature (Nominal*), R	Tank Pressure (Nominal*), R
Steel(CRES 321) 0.500-inch ID 0.750-inch OD L/D = 24	4 to 12	500	25 to 150
Copper(OFHC) 0.500-inch ID 0.750-inch OD L/D = 24	13 to 23 24 to 29	500 160	25 to 150 25 to 150
K-monel(29-Percent Copper) 0.500-inch ID 0.750-inch OD L/D = 24	30 to 40 41 to 47	500 160	25 to 150 25 to 150
Titanium(5-Percent Al) 0.500-inch ID 0.850-inch OD L/D = 24	63 to 82 83 to 87	500 160	25 to 150 25 to 150
Aluminum(Tens 50) 0.500-inch ID 0.850-inch OD L/D = 24	40 to 57 58 to 62	500 160	25 to 150 25 to 150

\*Nominal temperatures and pressures are the target test conditions.



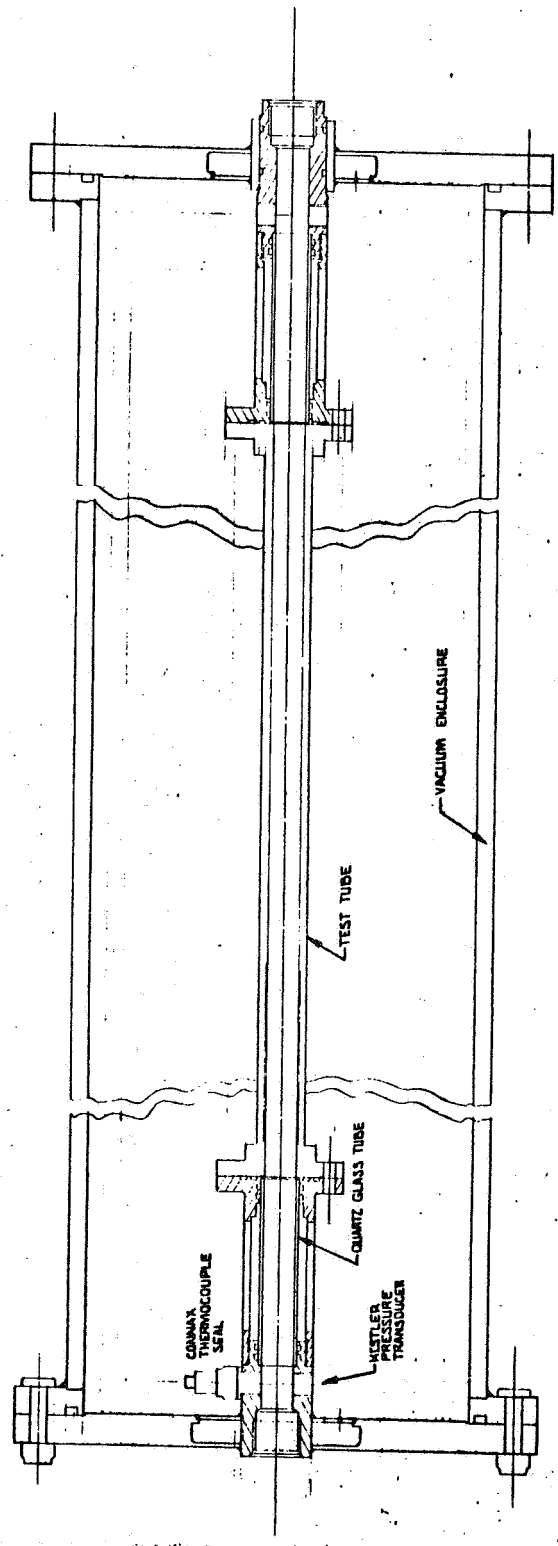


Figure 82. Main Test Section

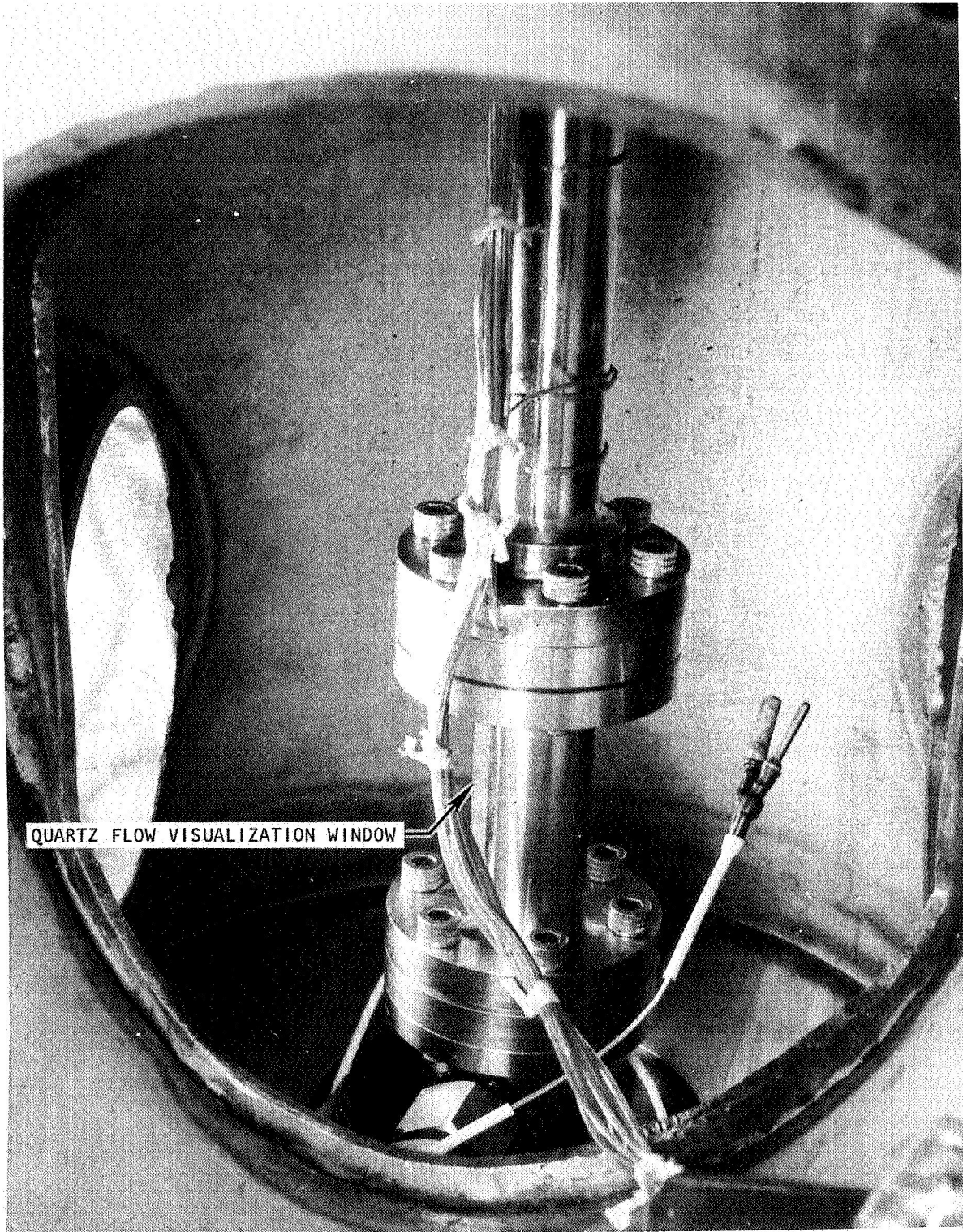


Figure 83. Vacuum Chamber Installation of Test Section

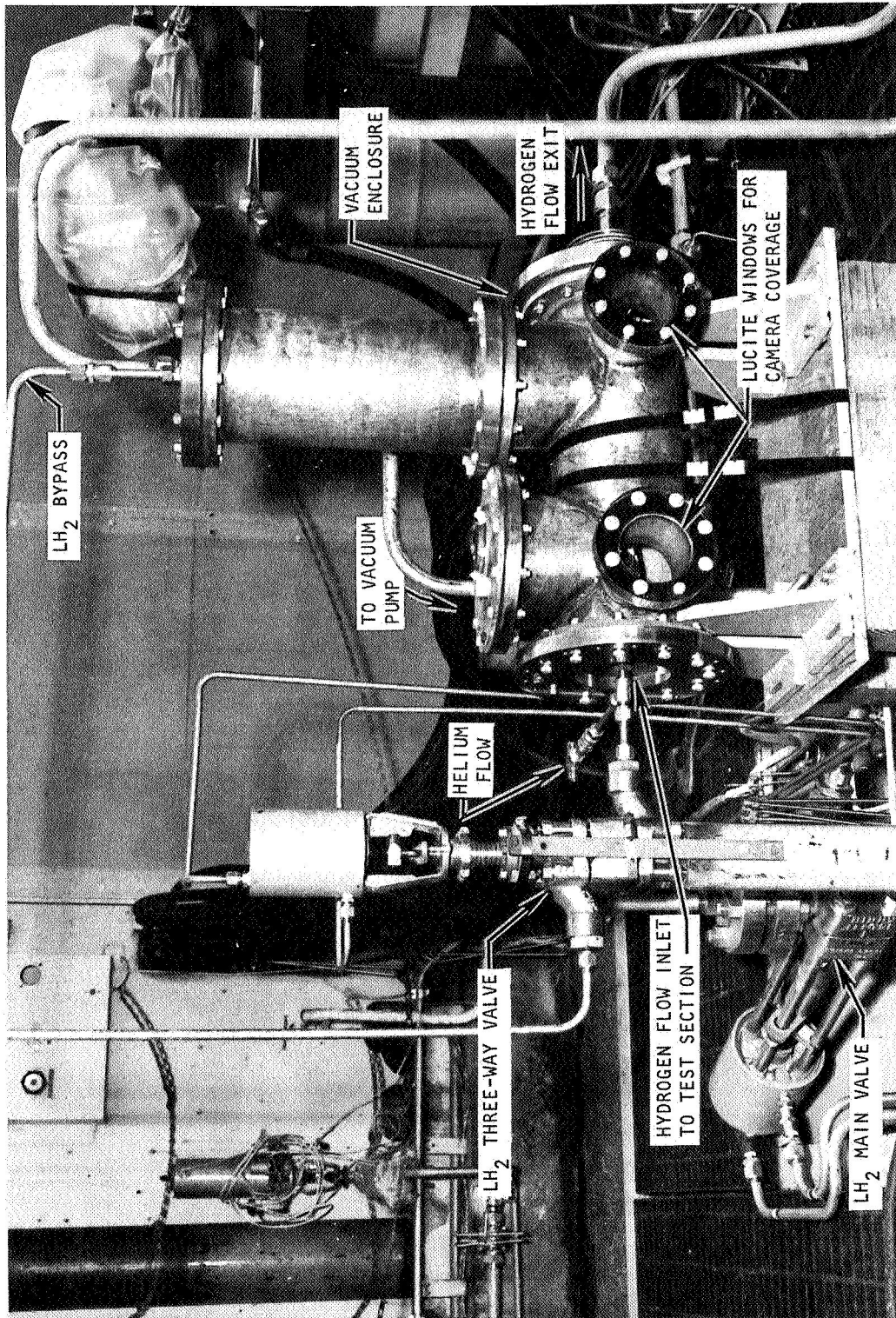


Figure 84. Cooldown of Metals in Liquid Hydrogen Flow Test Apparatus

- Valves 1, 2, 3 Annin Valves (#2 cooled by LH<sub>2</sub> By-Pass Line)
- Valves 4, 5, 6, 7 Helium Valves
- TC 1 and 2 Hydrogen Temperatures
- TC 3 Tube Wall Temperatures
- P1 and P2 Pressure Pickups

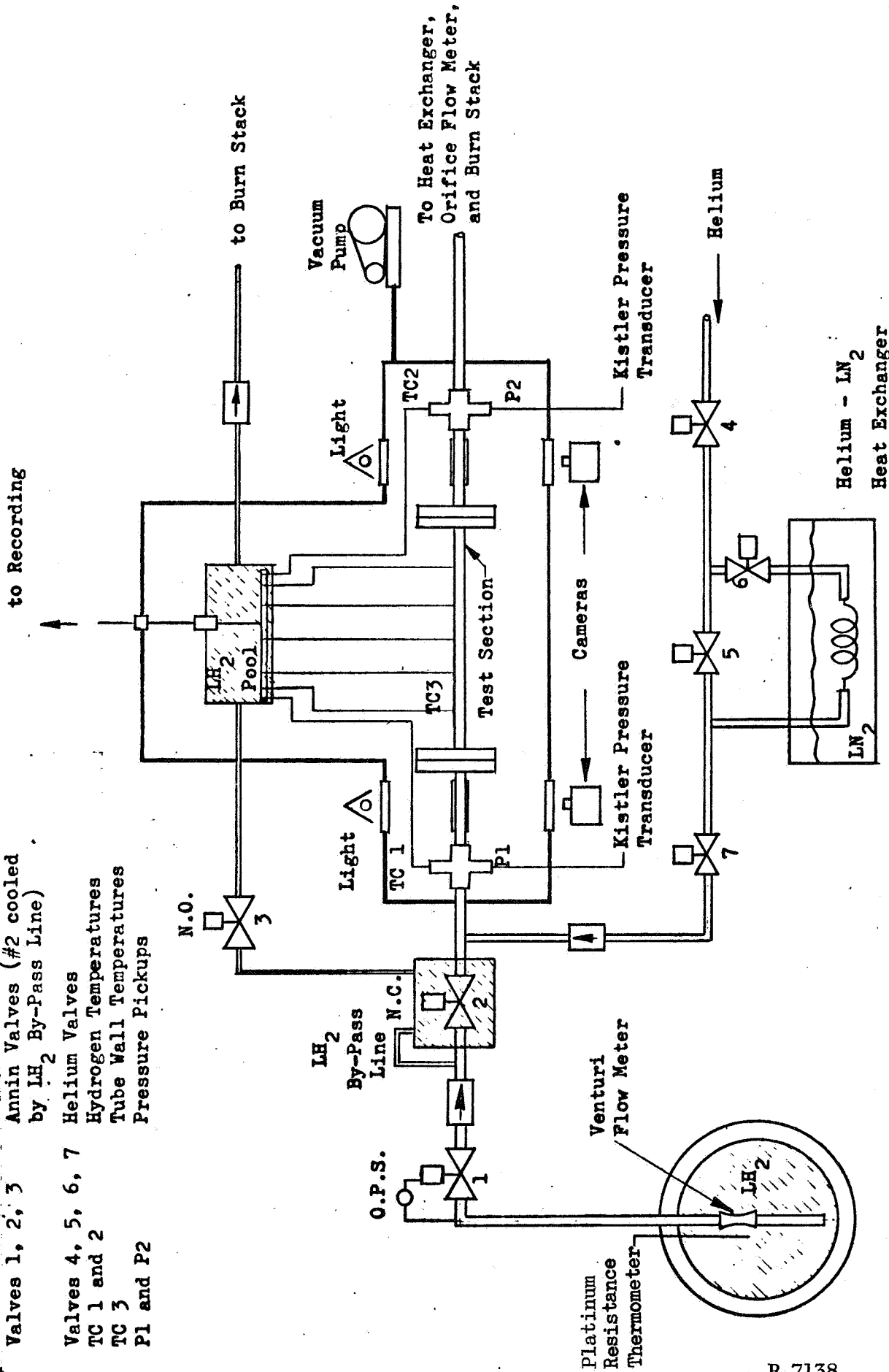


Figure 85. Flow Schematic

4. Pressures records from Wiancko and Statham transducers located in the liquid hydrogen tank, upstream pressure and pressure drop in the liquid hydrogen flow venturi, orifice inlet and orifice pressure drop in the hydrogen gas flow downstream from the test section
5. Gas temperature upstream of the orifice measured by an iron-constantan thermocouple
6. Pressure variations in the flow channel immediately upstream and immediately downstream of the test section recorded by Kistler transducers

The above measurements permitted calculation of hydrogen flowrates, Reynolds numbers and temperature-time curves for the hydrogen flow and for the test specimens.

#### Experimental Test Results

Figures 86 through 91 show the chilldown rates for typical test runs of various tube materials and reflect transient backwall temperature histories. A trend of chilldown rate with hydrogen pressure is shown and a higher pressure condition, indicative of higher hydrogen mass flowrates, resulted in a rapid cooling of the test specimen. For the cases shown the controlling resistance for heat dissipation was the effective boundary layer resistance ( $N_{Bi} < 0.1$ ). As expected the entrance thermocouple (No. 15) recorded temperatures that show a slightly quicker chilldown rate than did the other two thermocouples, No. 18 and 21. Thermocouple No. 18 and 21 were located at the tube midpoint and exit point, respectively. These differences in chilldown rate can be attributed to the higher heat transfer rates at the entrance region and lower coolant bulk temperature.

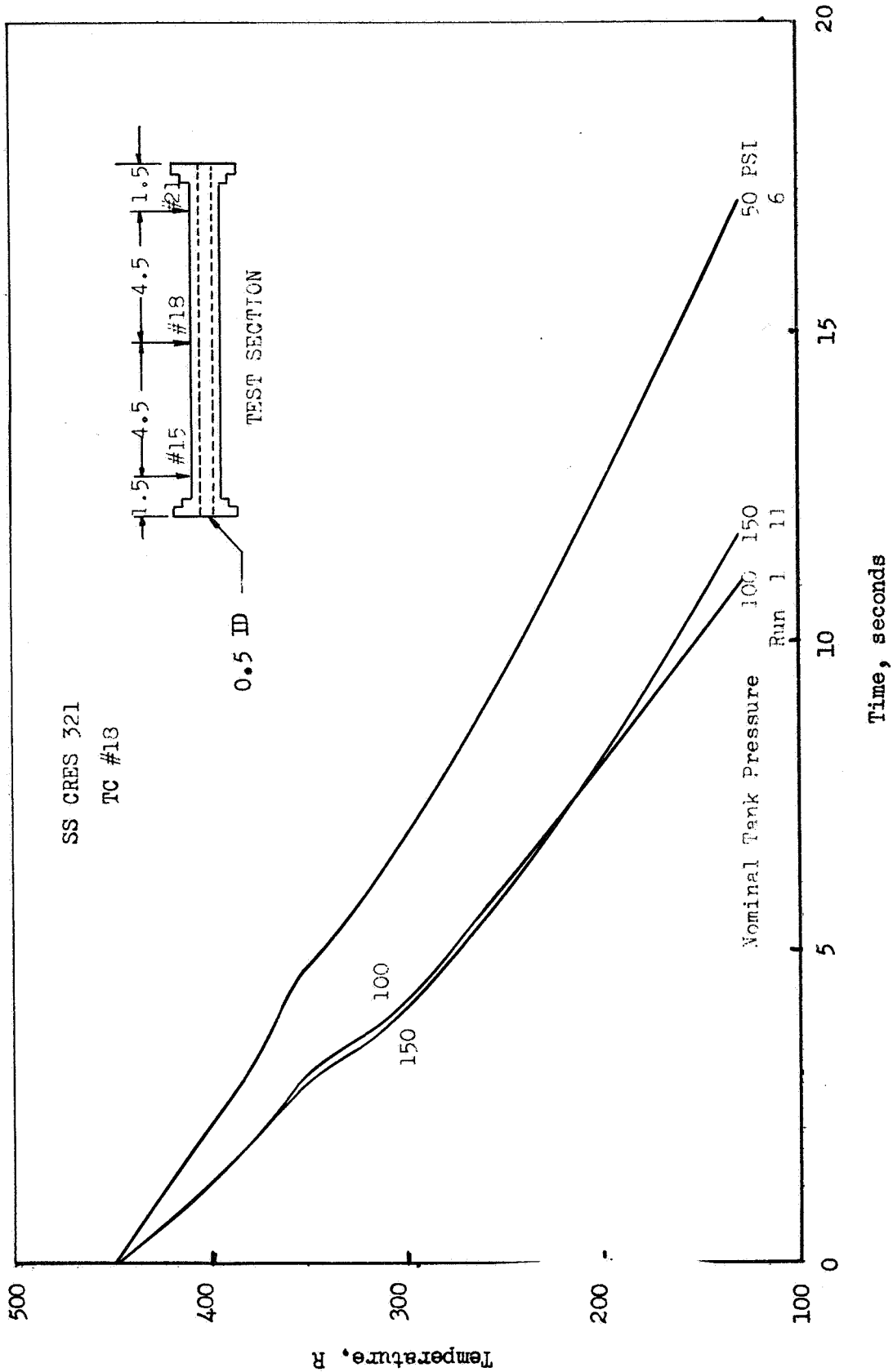


Figure 86. Cooldown of a Stainless Steel Tube in Hydrogen Flow  
(Backwall temperature at midpoint vs time)

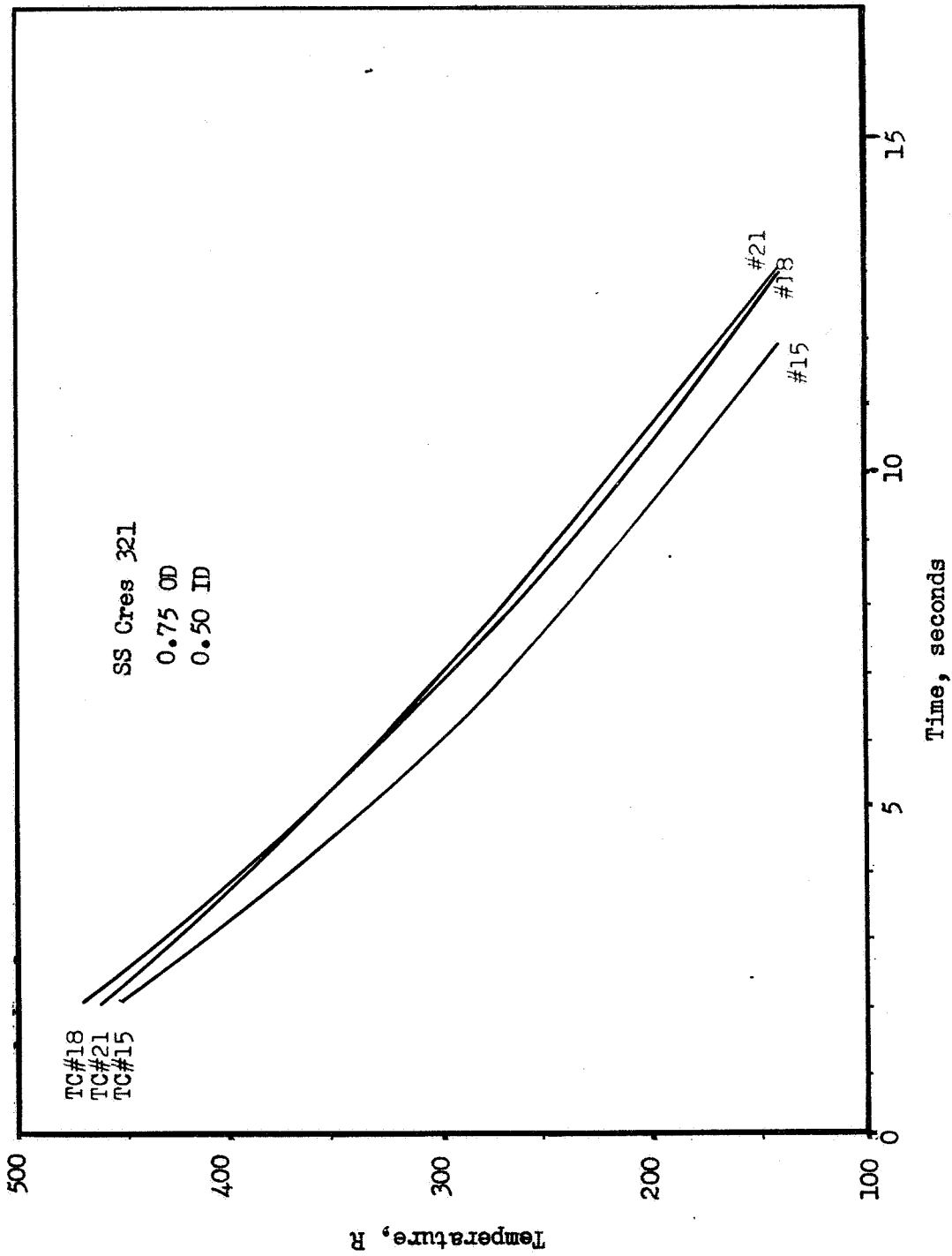


Figure 87. Cooldown of a CRES 321 Tube in Hydrogen Flow (Backwall temperatures vs time; nominal tank pressure, 100 psi; run 1)

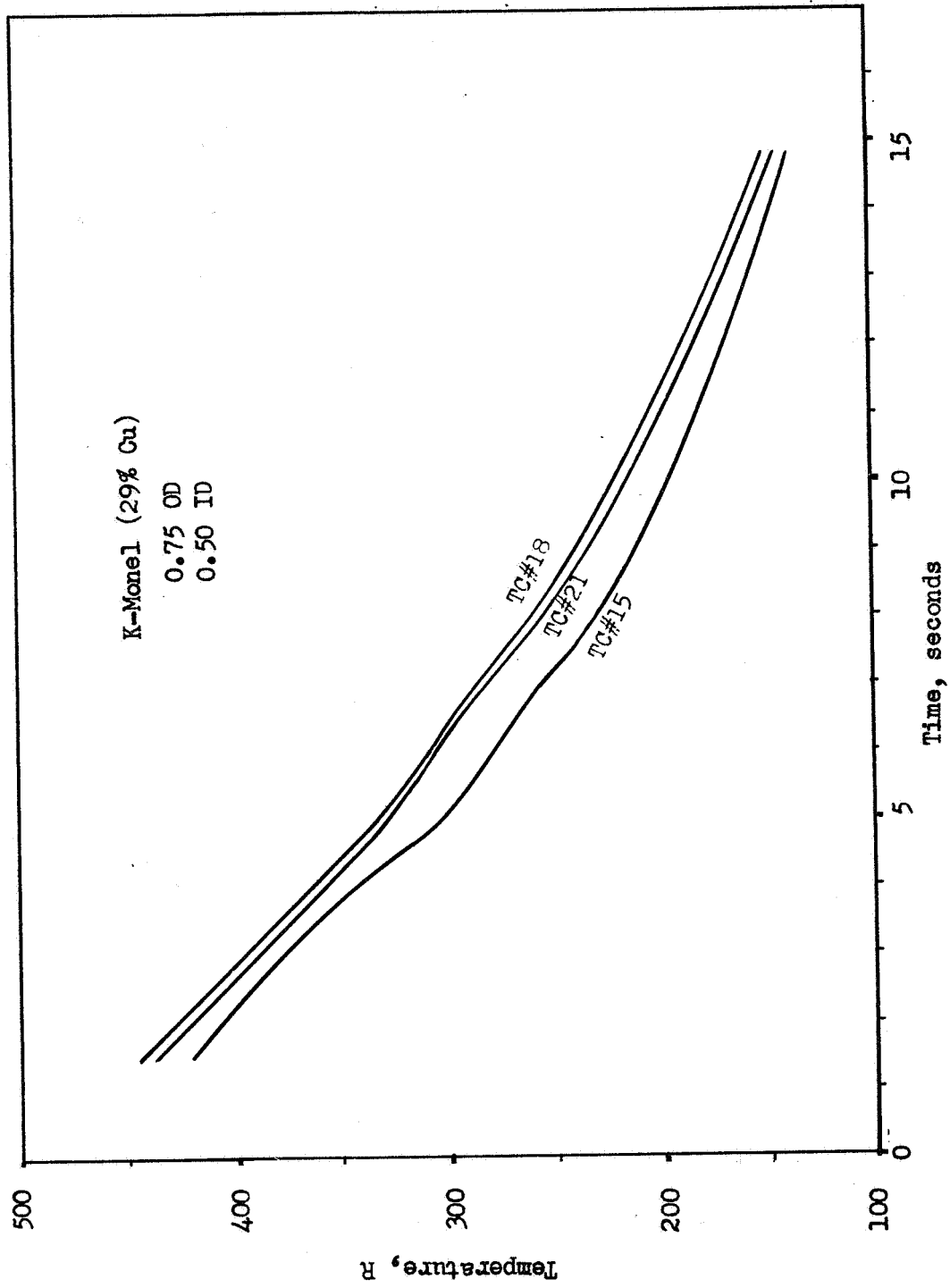


Figure 88. Cooldown of a K-monel (29-percent Cu) Tube in Hydrogen Flow (Backwall temperature vs time; nominal tank pressure, 100 psi; run 31)

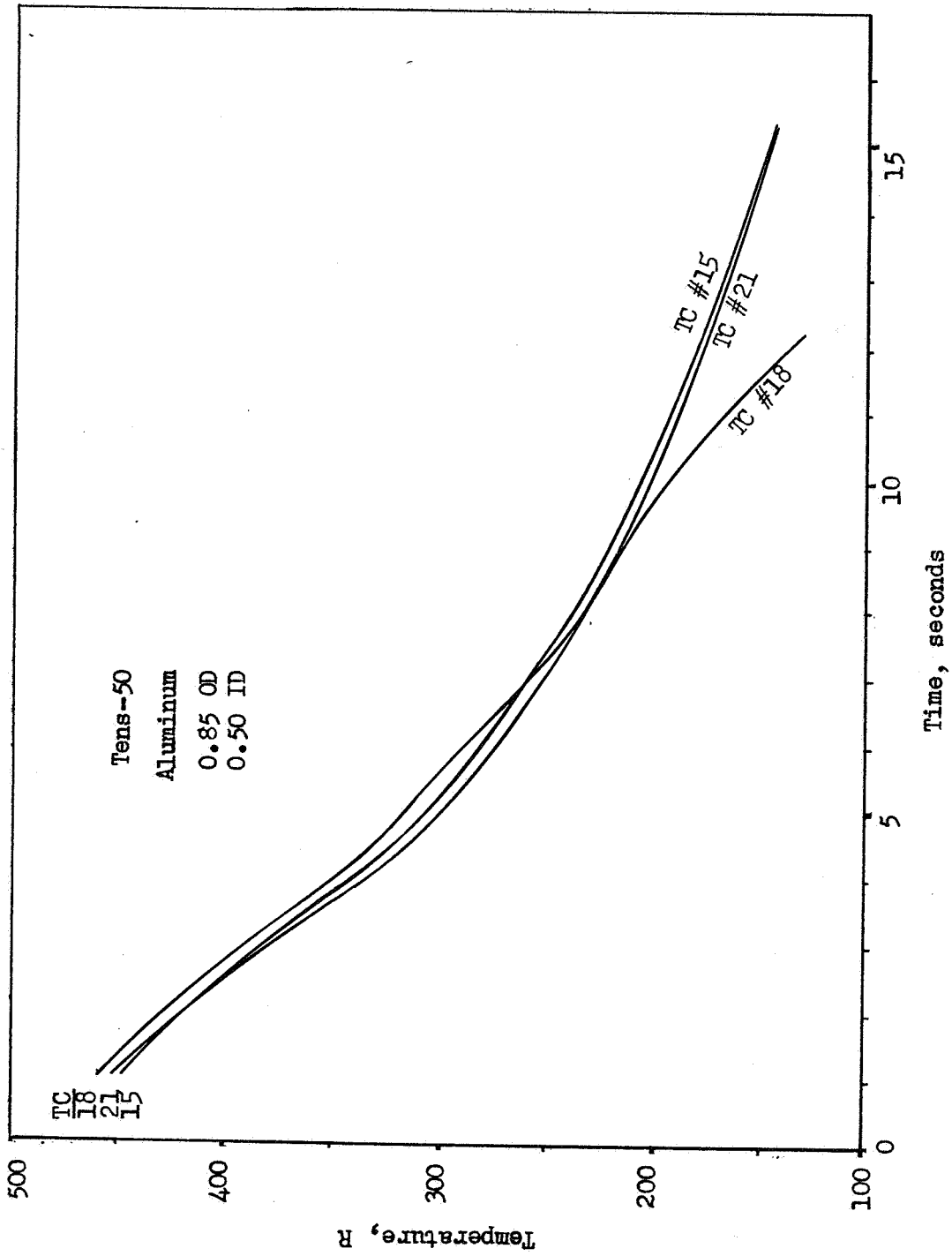


Figure 89. Cooldown of a Tens-50 Aluminum Tube in Hydrogen Flow (Backwall temperatures vs time; nominal tank pressure, 100 pis; run 49)

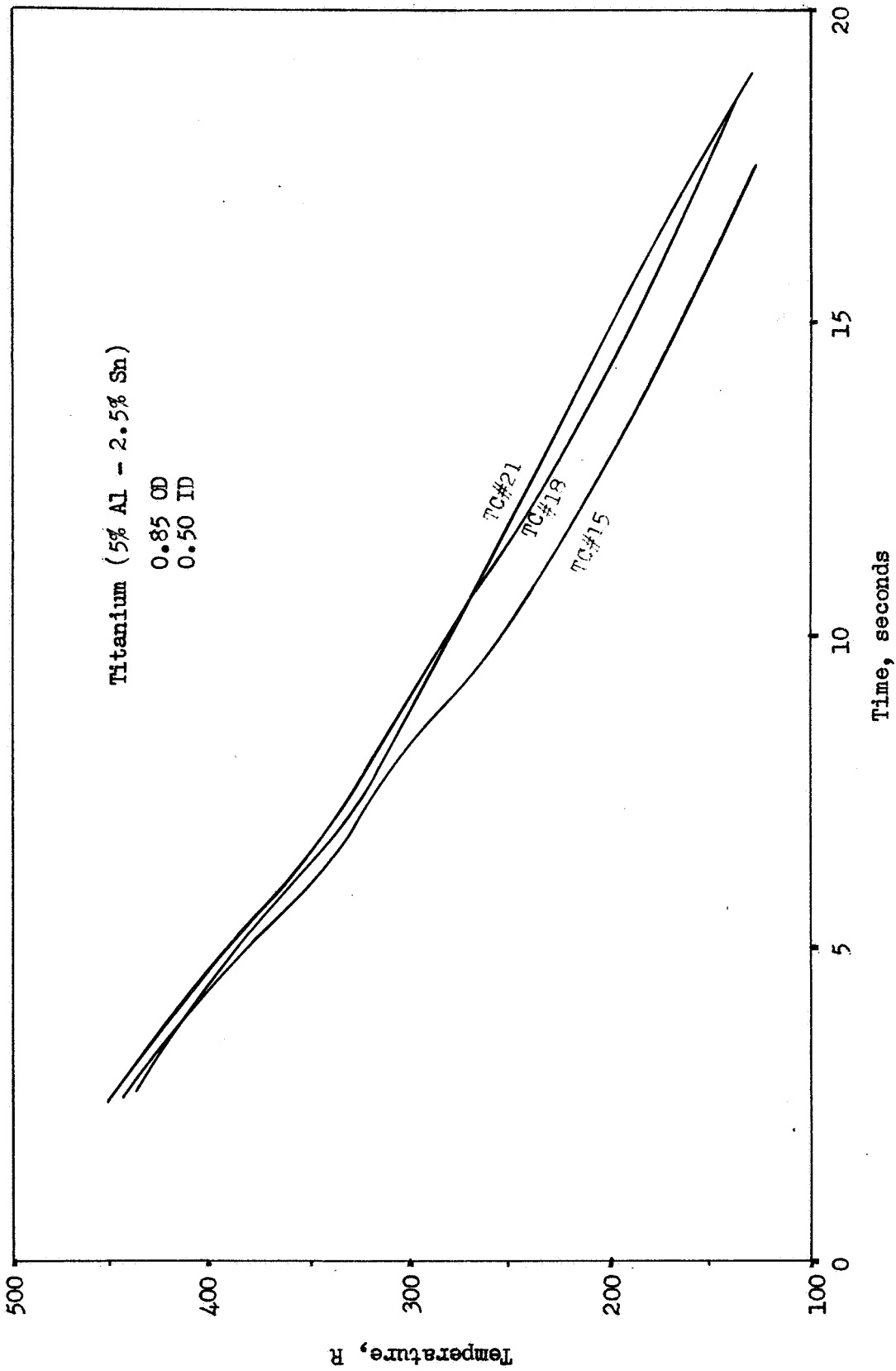


Figure 90. Cooldown of a Titanium (5-percent Al, 2.5-percent Sn) Tube in Hydrogen Flow (Backwall temperature vs time; nominal tank pressure, 100 psi; run 64)

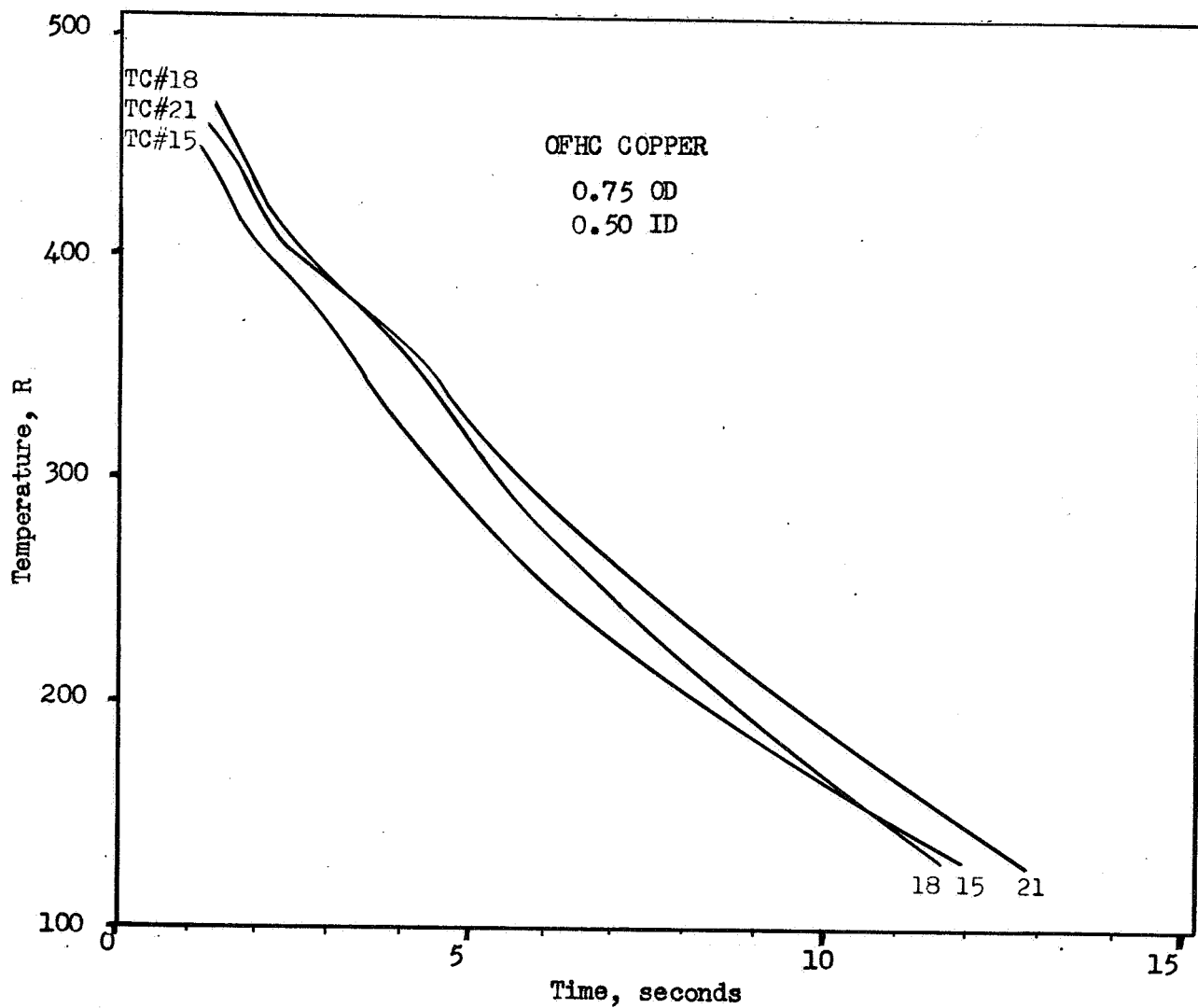


Figure 91. Cooldown of an OFHC Copper Tube in Hydrogen Flow (Backwall temperatures vs time; nominal tank pressure, 100 psi; run 14)

Table 22 illustrates the selected seven film coefficient test runs based on slow chill ( $N_{Bi} < 1.0$ ) conditions. Calculated low Biot numbers indicate that the wall responded as an entity for these tests.

Further testing with higher Biot numbers, longer L/D's and with coated test sections is presently in progress at the Rocketdyne research laboratory.

TABLE 22

TYPICAL TUBE CHILLDOWN PARAMETERS FOR LH<sub>2</sub> TESTS

Material	Run No.	P <sub>1</sub> , psia	P <sub>2</sub> , psia	τ, seconds at α = (1/e)	G <sub>c</sub> , lb/in. <sup>2</sup> -sec	N <sub>Bi</sub>
CRES (321)	1	115.8	97.3	8.3	0.154	0.273
CRES (321)	11	163.3	144.8	8.3	0.228	0.273
CRES (321)	6	69.8	56.8	13	0.0905	0.137
K-monel	31	123.3	97.8	11.0	0.186	0.182
Tens 50	49	123.8	101.3	10.4	0.195	0.041
Titanium (5Al-2.5 Sn)	64	123.8	102.3	14	0.177	0.22
Copper (OFHC)	14	119.8	86.8	8.5	0.187	0.0078

### TASK III: PRECONDITIONING AND THERMAL PROTECTION

During the Task III study, development of pump criteria for external insulation requirements and thicknesses as well as other isolation methods to restrict heat input to the pump from sources including the turbine after shutdown was accomplished. Additional studies included pump chill-down requirements and a pump inlet feed line chilldown evaluation. Alternate preconditioning approaches considered, other than those employed presently with the J-2 engine system, included the evaluation of idle mode conditioning and continuous tank to pump venting.

#### EXTERNAL INSULATION

In addition to coatings for internal wetted-surface insulation, external coatings are required for the LH<sub>2</sub> pump to maintain shutdown temperature or ground chilldown conditions. Prevention of heat radiation from surrounding turbine, vehicle structure, solar, and earth heat inputs is important between restarts and for long orbital or space storage periods. In addition, for ground prechilled pumps, the natural convection and radiation during ground hold and forced convection during ascent make external insulation mandatory for nearly all LH<sub>2</sub> pumps and missions.

The controlling influences for coatings on pump surfaces were examined by equating the heat gain of the pump to heat conducted by external insulation and heat radiation from a source condition. A heat balance was made as follows:

$$\begin{aligned} \text{heat gain of pump} + \text{heat gain of insulation} &= \text{conduction} \\ \text{of insulation} &= \text{radiation from source} \end{aligned}$$

The heat content of the insulation was allowed to be small with respect to the pump heat content, and the pump internal thermal resistance was

assumed negligible due to the long time periods examined. Denoting the pump, source, and insulation conditions by p, s, and i subscripts, respectively,

$$W_p C_{p_p} \left( \frac{d T_p}{d \tau} \right) = \frac{A_i K_i}{X_i} (T_i - T_p) = A_i \sigma \epsilon F (T_s^4 - T_i^4) \quad (77)$$

The solution after integration with respect to time and temperature becomes

$$\frac{\sigma \epsilon F A_i \tau T_s^3}{W_p C_{p_p}} = -1/4 \log_e \left\{ \frac{\left( \frac{T_i}{T_s} - 1 \right) \left( \frac{T_{p_0}}{T_s} + 1 \right)}{\left( \frac{T_i}{T_s} + 1 \right) \left( \frac{T_{p_0}}{T_s} - 1 \right)} \right\} +$$

$$\frac{1}{2} \left\{ \tan^{-1} \left( \frac{T_i}{T_s} \right) - \tan^{-1} \left( \frac{T_{p_0}}{T_s} \right) \right\} - \frac{\sigma X_i \epsilon F T_s^3}{K_i} \log_e \left\{ \frac{\left( \frac{T_i}{T_s} \right)^4 - 1}{\left( \frac{T_{p_0}}{T_s} \right)^4 - 1} \right\} \quad (78)$$

The temperature  $T_{p_0}$  in this expression represents the pump and insulation temperature at time zero. The two dimensionless controlling parameters are seen from the above equation as the relative insulation resistance parameter:

$$\phi = \frac{\sigma \epsilon F T_s^3 X_i}{K_i} \quad (79)$$

and the nondimensional time parameter:

$$\psi = \left[ \frac{A_i \sigma \epsilon F T_s^3}{W_p C_{p_p}} \right] \quad (80)$$

Figure 92 illustrates the relationship of  $\phi$  and  $\psi$  for insulation outside surface temperature approaching 0.9 of the equilibrium temperature ( $T_s$ ). The case of  $\phi = 0$  represents the uninsulated case. Figure 93 represents a conversion chart of the pump temperature from the insulation temperature with various values of  $\phi$ . For large relative insulation thicknesses Fig. 94 was developed. For a time period for the pump to achieve a temperature within 1/e of its final value, approximate values of the controlling parameter requirements may be developed. For rough estimation purposes to warm the pump to within 1/e of the final value,

$$\frac{A_i \sigma \epsilon F T_s^3 \tau_c}{W_p C_{p_p}} \approx 1.5 \quad \begin{array}{l} 0 < \phi < 1.0 \\ \text{lightly insulated case} \end{array} \quad (81)$$

$$\frac{A_i K_i \tau_c}{W_p C_{p_p} X_i} \approx 2.75 \quad \begin{array}{l} \phi \gg 1.0 \\ \text{heavily insulated case} \end{array} \quad (82)$$

It is seen that the time required becomes directly proportional to the pump heat content and inversely to the insulation surface area. As a result LH<sub>2</sub> pumps which most closely approach a spherical shape will warm up the slowest from a prechilled condition. For lightly insulated cases the time required to warm is inversely proportional to the third power of final equilibrium temperature. For the heavily insulated case the time required becomes directly proportional to the insulation resistance ( $\phi \gg 1.0$ ). Values of the pump weight to surface area are shown in Table 7 from the empirical study of existing pumps (Table 27) and from the analysis of geometric shapes (Table 6).

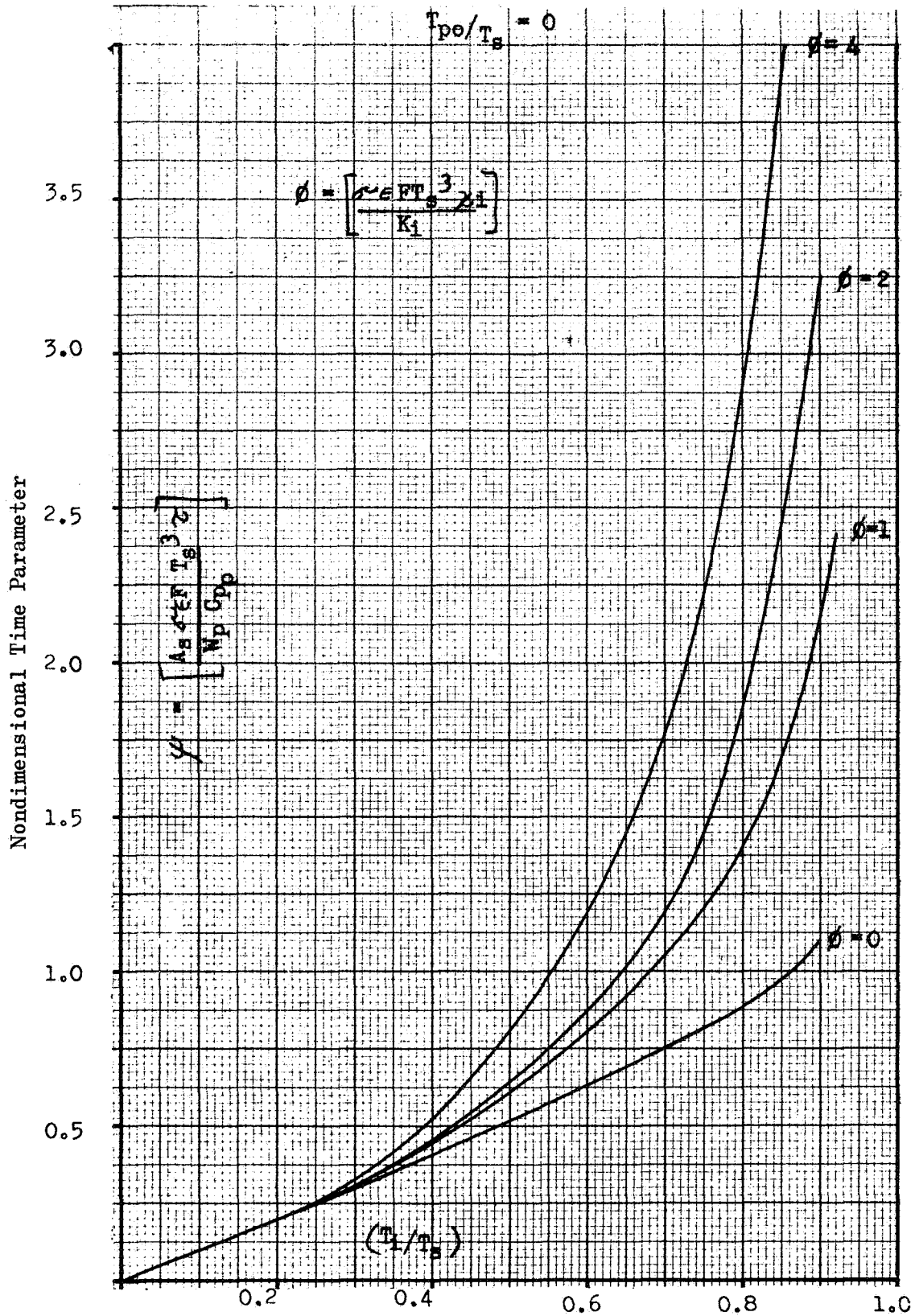


Figure 92. Nondimensional Time Parameter vs Insulation Temperature-Radiation Control Case

$$\phi > 1.0, \frac{T_{p0}}{T_s} = 0$$

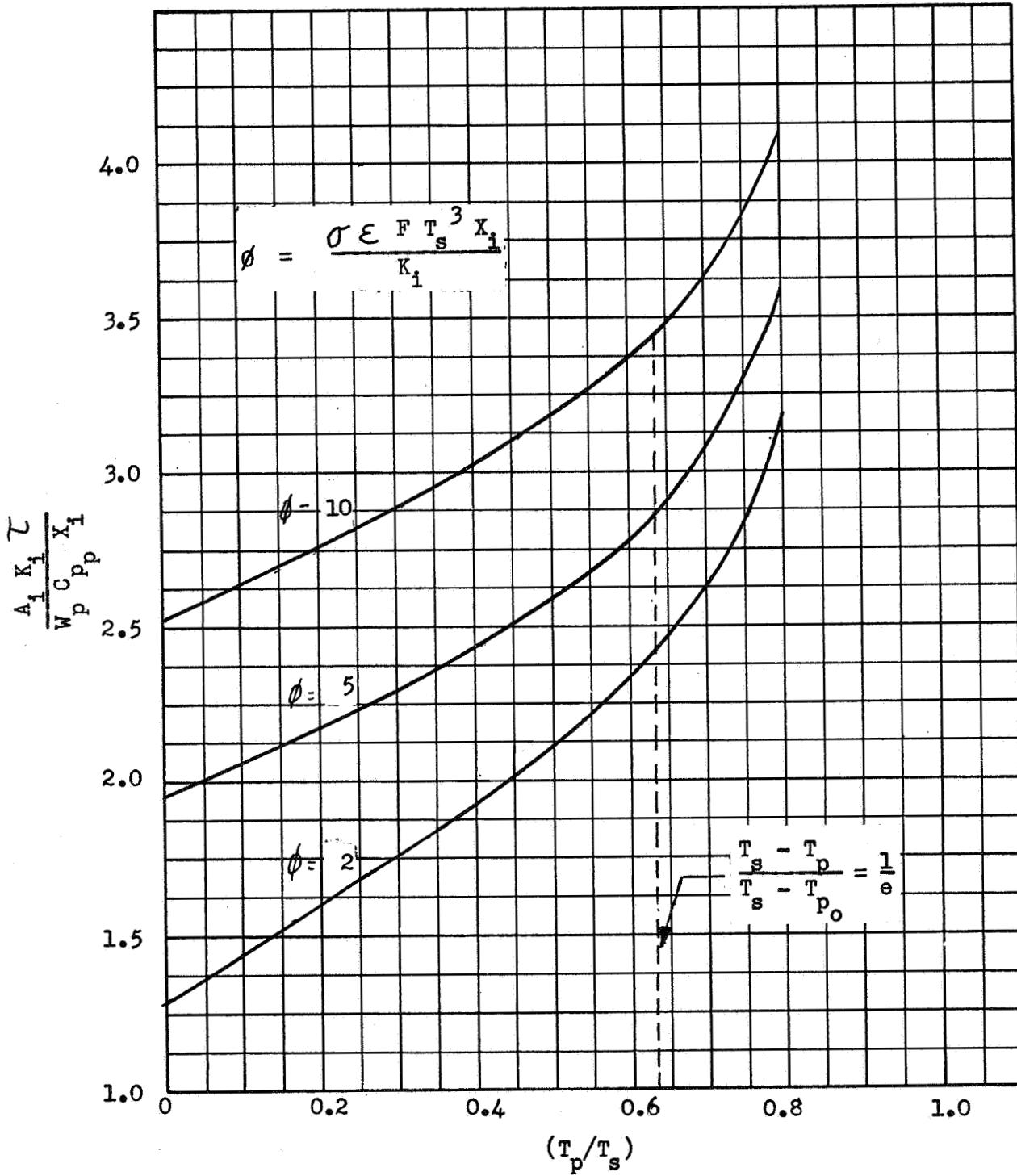


Figure 93. Time vs Pump Temperature-Insulation Control Case

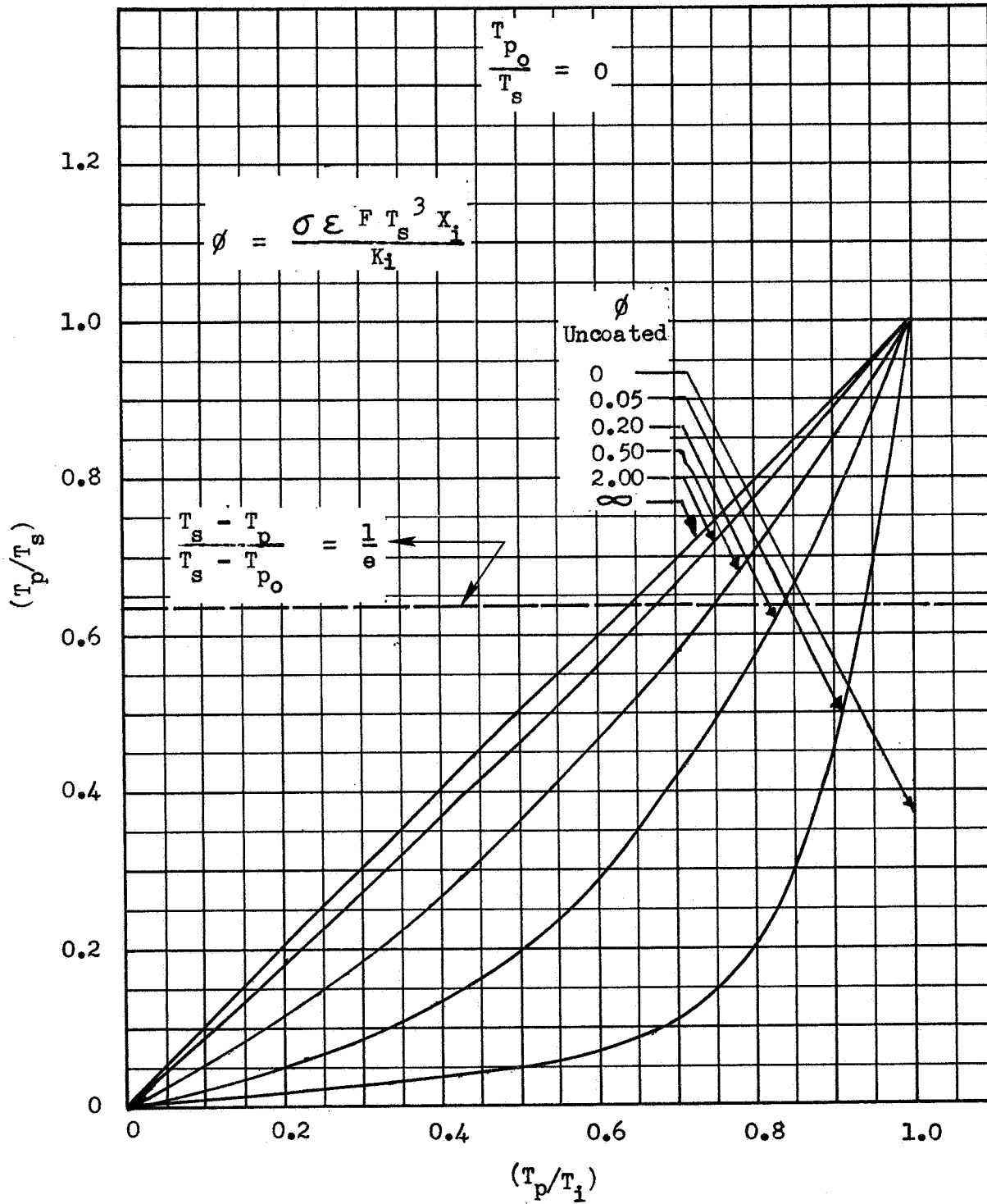


Figure 94. Pump Temperature vs Insulation Temperature

## Insulation Thickness Requirements

Analysis of insulations for the pump and lines from heat sources indicated a wide range in thermal conductivity for available superinsulations under ground and altitude vacuum conditions. Insulators employed in ground environments and subject to atmospheric conditions generally become limited by the air conduction within the insulation matrix. As a result, most ground hold (non-evacuated type) insulators approach (as a lower limit) the conductivity of air or about  $1.5 \times 10^{-2}$  Btu/hr-ft-F. Insulators for vacuum conditions become radiation or material conduction limited and superinsulators for this purpose are generally composed of multiple thin layers of closely spaced aluminized Mylar separated by low-conducting glass mesh. Insulators of this type approach conductivities of  $1.0 \times 10^{-5}$  Btu/hr-ft-F but are very sensitive to small loading pressures which can increase conductivity 25 to 50 times the nominal value, and also to penetrations into the insulating material by struts, supports, etc. A number of insulating materials of interest and their conductivity values are listed in Table 23.

Two materials that could be considered for use as effective turbopump external insulation are polyurethane foam, which has a thermal conductivity of  $k = 1.3 \times 10^{-2}$  Btu/hr-ft-R (ambient value), and Linde S.I.-91, with  $k = 1.0 \times 10^{-5}$  Btu/hr-ft-R (vacuum value). A general curve relating required insulation thickness for a given time and pump surface area to weight ratio, for any insulation material, is shown in Fig. 95. The basis for this curve is the solution to the equation for heat balance between gain of the pump to heat conducted by external insulation and heat radiation. The two dimensionless controlling parameters are seen from Eq. 78 as the relative resistance parameter

$$\phi = \frac{\sigma \epsilon F T_s^3 X_i}{K_i} \quad (83)$$

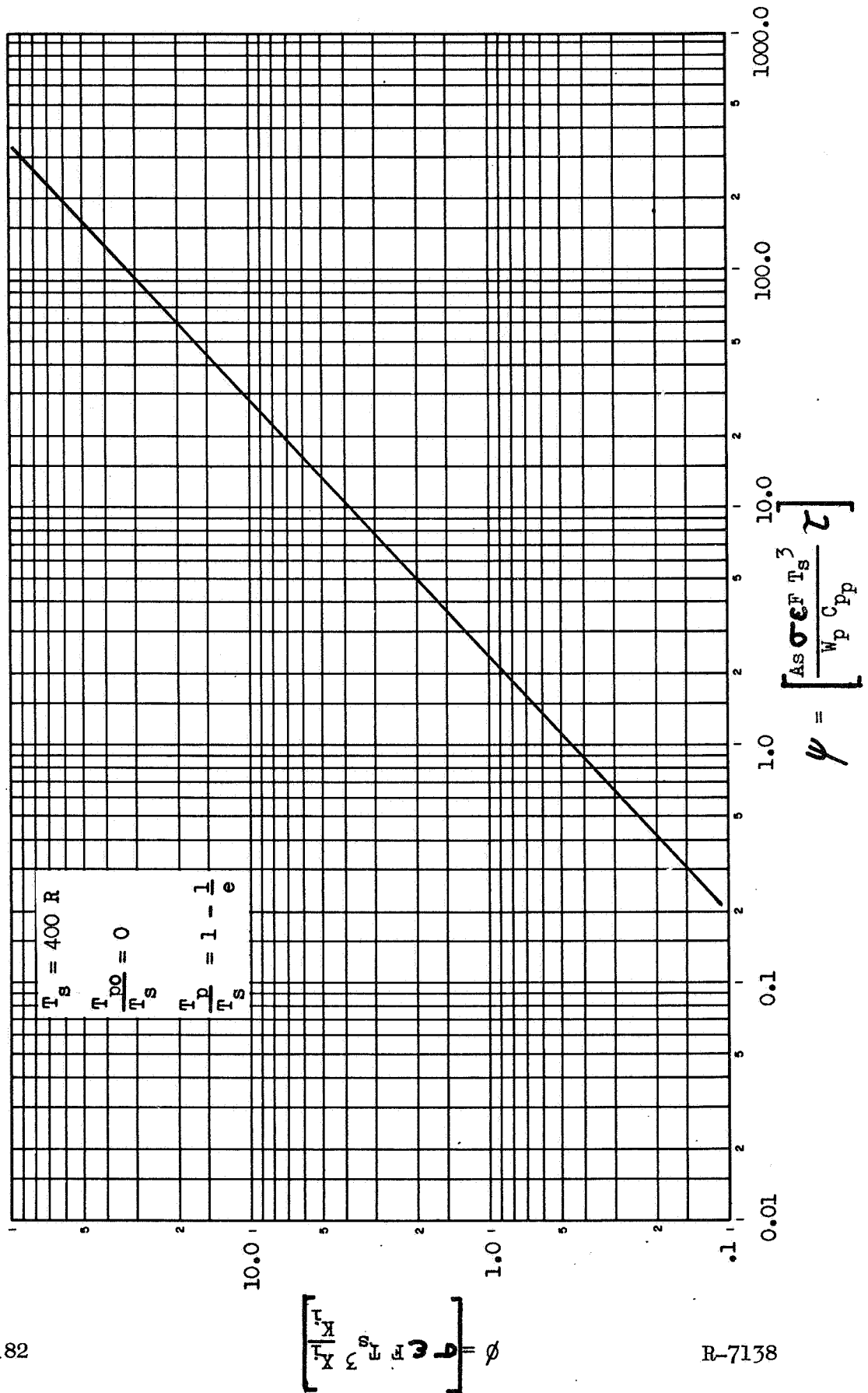


Figure 95.  $\psi$  (Insulation Thickness) for LH<sub>2</sub> Pumps vs  $\tau$  (Time)

TABLE 23

COMPARATIVE EVALUATION OF THERMAL CONDUCTIVITY AND  
DENSITY FOR EXTERNAL INSULATIONS

Material	K (Ambient Pressure), Btu/hr ft F	K (Vacuum), Btu/hr ft F	Density, lb/ft <sup>3</sup>
Dimplar 0.5 Mil (Shallow)	$5.9 \times 10^{-2}$	$13.1 \times 10^{-5}$	-
Embossed Aluminized Mylar (1/4 Mil)	$3.6 \times 10^{-2}$	$6.5 \times 10^{-5}$	-
Dimplar 0.5 Mil (Deepset)	$5.9 \times 10^{-2}$	$39 \times 10^{-5}$	-
Dimplar 1.0 Mil (Deepset)	$6.4 \times 10^{-2}$	$50 \times 10^{-5}$	-
Aluminized Mylar (1/4 Mil)	-	$4.9 \times 10^{-5}$	-
Goodyear (1/4-Mil Mylar)	$1.42 \times 10^{-2}$	$3.0 \times 10^{-5}$	1.9 to 3.0
NRC - 2 (1/4-Mil Aluminized Mylar)	-	$2 \times 10^{-5}$	-
Polyurethane Foam	-	$1.3 \times 10^{-2}$	3.3
Corkboard	-	$1 \times 10^{-2}$	8.7
CRP 314 Urethane	$1.2 \times 10^{-2}$	-	2.0
Glass Fiber at 150 F	$3.3 \times 10^{-2}$	$1.1 \times 10^{-2}$	0.55
Glass Fiber at 150 F	$2 \times 10^{-2}$	$0.25 \times 10^{-2}$	4.6
Silicone Elastomer	$4.7 \times 10^{-2}$	-	30 to 40
Linde SI-62	-	$1.8 \times 10^{-5}$	5.5
Linde SI-91	-	$1.0 \times 10^{-5}$	7.5
Perlite	-	$72 \times 10^{-5}$	8.0
Air at 70 F 1 Atmosphere	$1.5 \times 10^{-2}$	-	-

and the nondimensional time parameter

$$\psi = \frac{A_i \sigma \epsilon F T_s^3 \tau}{W_p C_{p_p}} \quad (84)$$

The insulation thickness required for corkboard and Linde as a function of time is shown in Fig. 96. For example, if Linde S.I.-91 is used for the liquid hydrogen pump for a Mars trip (24,000 hours), a typical insulation thickness of only 0.130 inch would be required if the final pump temperature is allowed to approach to within 1/e of its final value.

#### THERMAL ISOLATION OF PUMP FROM TURBINE

An approach to increase the turbine heat radiating capability by (1) better isolation of the pump and (2) increasing the heat radiating capability of the turbine inlet and exhaust ducts was analyzed by using a closed-form solution for radiation and conduction heat transfer in the ducting. The resulting increase in turbine heat-radiating capability, over an unisolated turbine with minimum ducting, was found to be quite large. For a typical duct thickness of 0.080 inch an improvement in capability of 14 percent was obtained for a turbine temperature of 1600 R, and 60 percent was obtained for 600 R. At the lower temperature there is a greater tendency for heat to be conducted into the duct, which would subsequently be radiated. Both the turbine inlet and exhaust ducting can be modified by design to obtain a significant benefit in heat rejection, through conduction and radiation at the lower turbine temperatures, to reduce substantially the problem of pump chilldown time. A tradeoff between ducting weight increase and hydrogen flow required to chill a warm pump, however, must be evaluated for a specific pump design.

A typical analysis of the heat transferred to a long turbine shaft compared to the heat radiated from the turbine body is illustrated in Fig. 97.

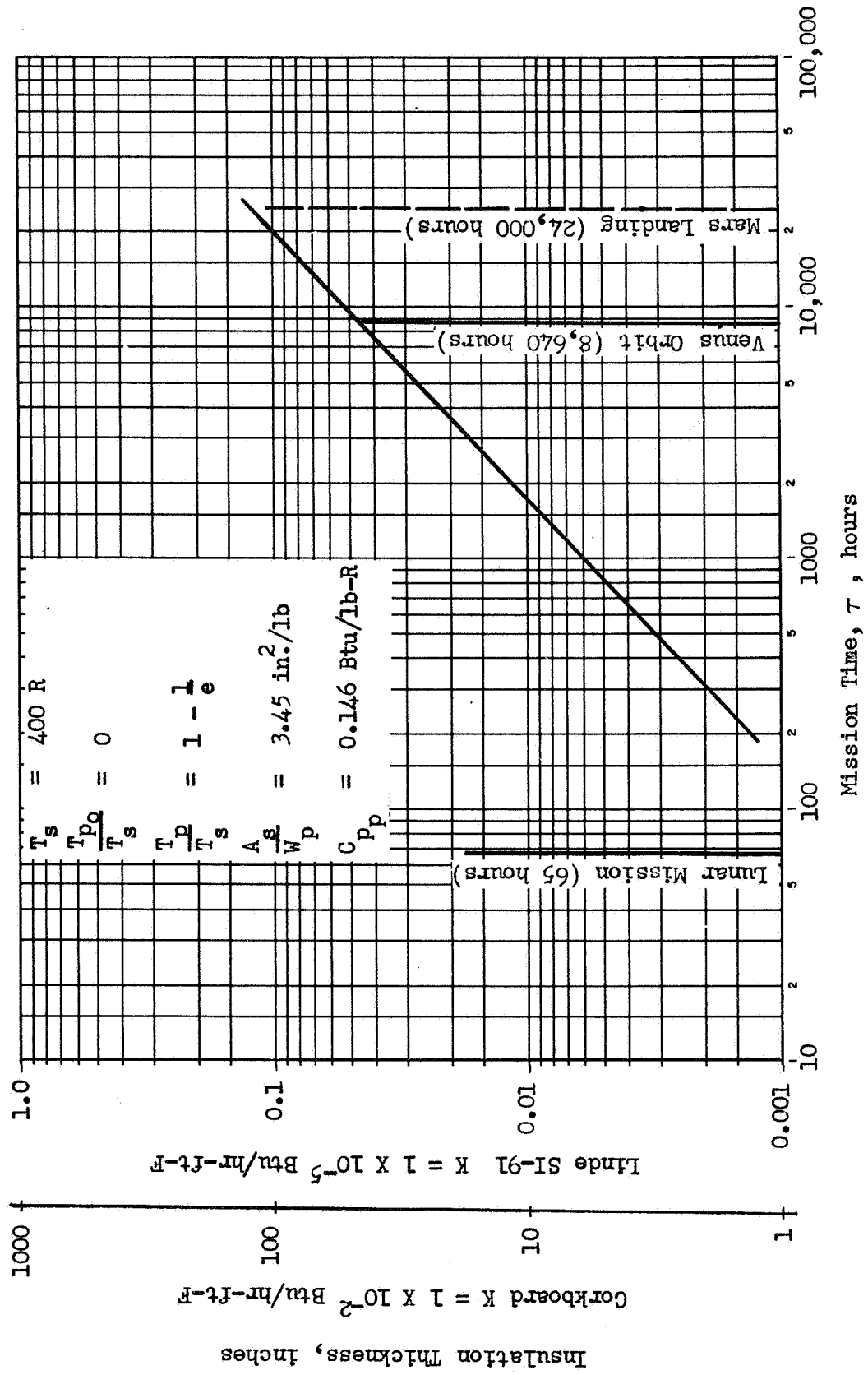


Figure 96. Insulation Thickness vs Mission Time for LH<sub>2</sub> Pump (Mark 15-F)

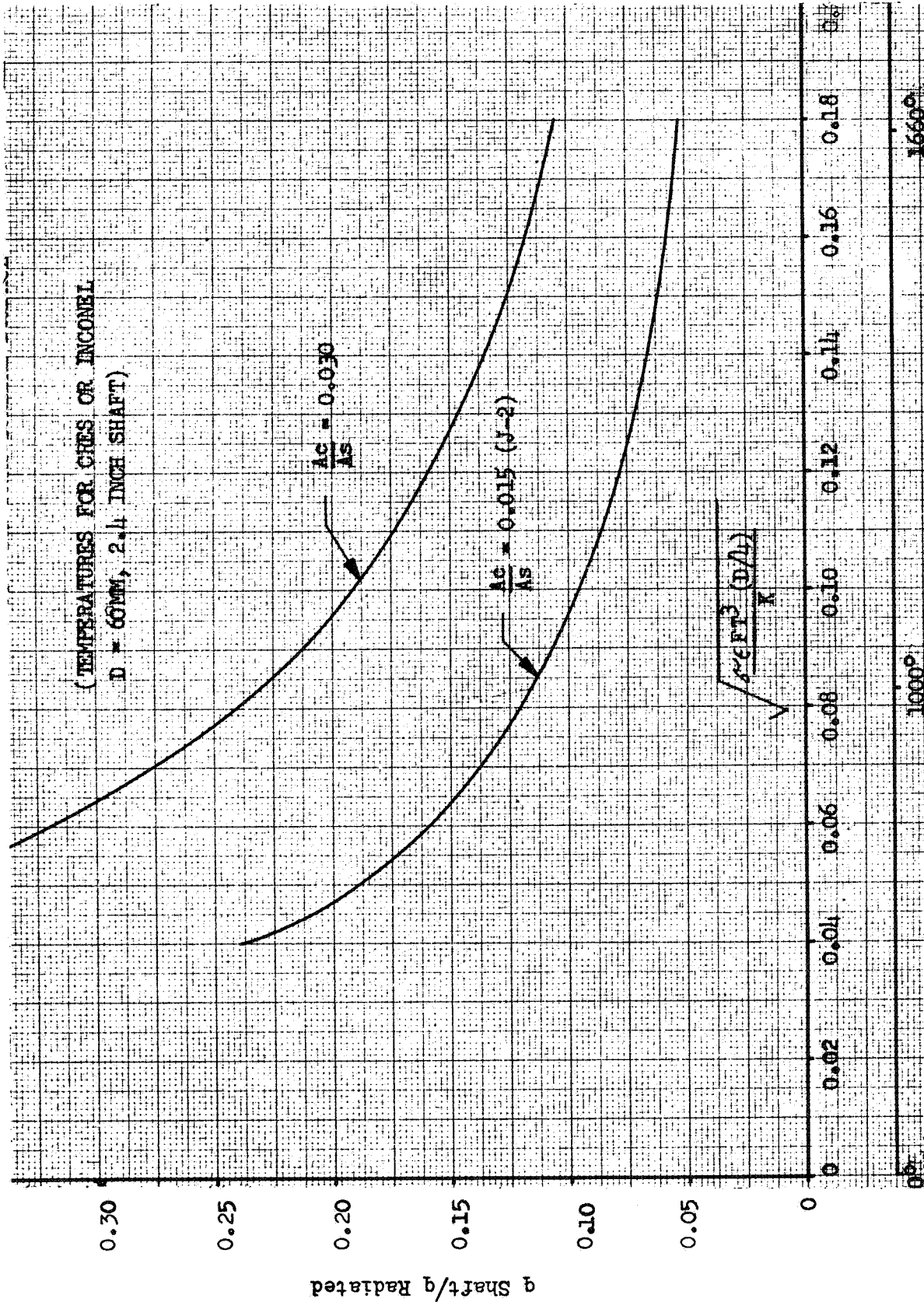


Figure 97. Heat Transferred by Turbine Shaft to Heat Radiated From Turbine Surface

Heat transferred by conduction along the shaft compared to heat radiated from the turbine body after shutdown can range from 5 to 11 percent at turbine temperatures of 1600 and 1000 R, respectively. The equation derived for the ratio of shaft heat conduction to heat radiation from the turbine body was determined as

$$\frac{q_s}{q_r} = \frac{\sqrt{2/5} \frac{A_c}{A_s}}{\frac{\sigma \epsilon F T_r^3 (D/4)}{K}} \quad (85)$$

Figure 98 illustrates a typical (60MM) turbine shaft heat dissipation rate. Figure 99 illustrates short turbine shaft heat conduction rates. Further increases in percentage heat conduction are shown for lower turbine temperatures. Soakback of heat from the turbine to the pump by conduction through the shaft and supports represents the major turbine heat input for insulated pump conditions. For short and intermediate mission times, where the pump insulation is of benefit, the isolation of an uninsulated turbine from pump supports and pump shaft becomes important.

#### Turbine Isolation Scaling Studies

Scaling studies of shaft and ducting influences on heat diversion to and away from the pump were conducted. Turbine diameter and shaft size as a function of thrust were examined on the basis of bearing DN, pump NPSH, turbine tip speed, and shaft stress.

The relationship derived for heat radiated from the downstream ducting of the turbine compared with turbine body surface radiation was

$$\frac{q_{duct}}{q_{body}} = \frac{\sqrt{2/5} \frac{\pi D_d t}{A_s}}{\frac{\sqrt{\sigma \epsilon F T_s^3} t}{k}} \approx \frac{\sqrt{2/5} \left(\frac{t}{L}\right)}{\frac{\sqrt{\sigma \epsilon F T_s^3} t}{k}} \quad (86)$$

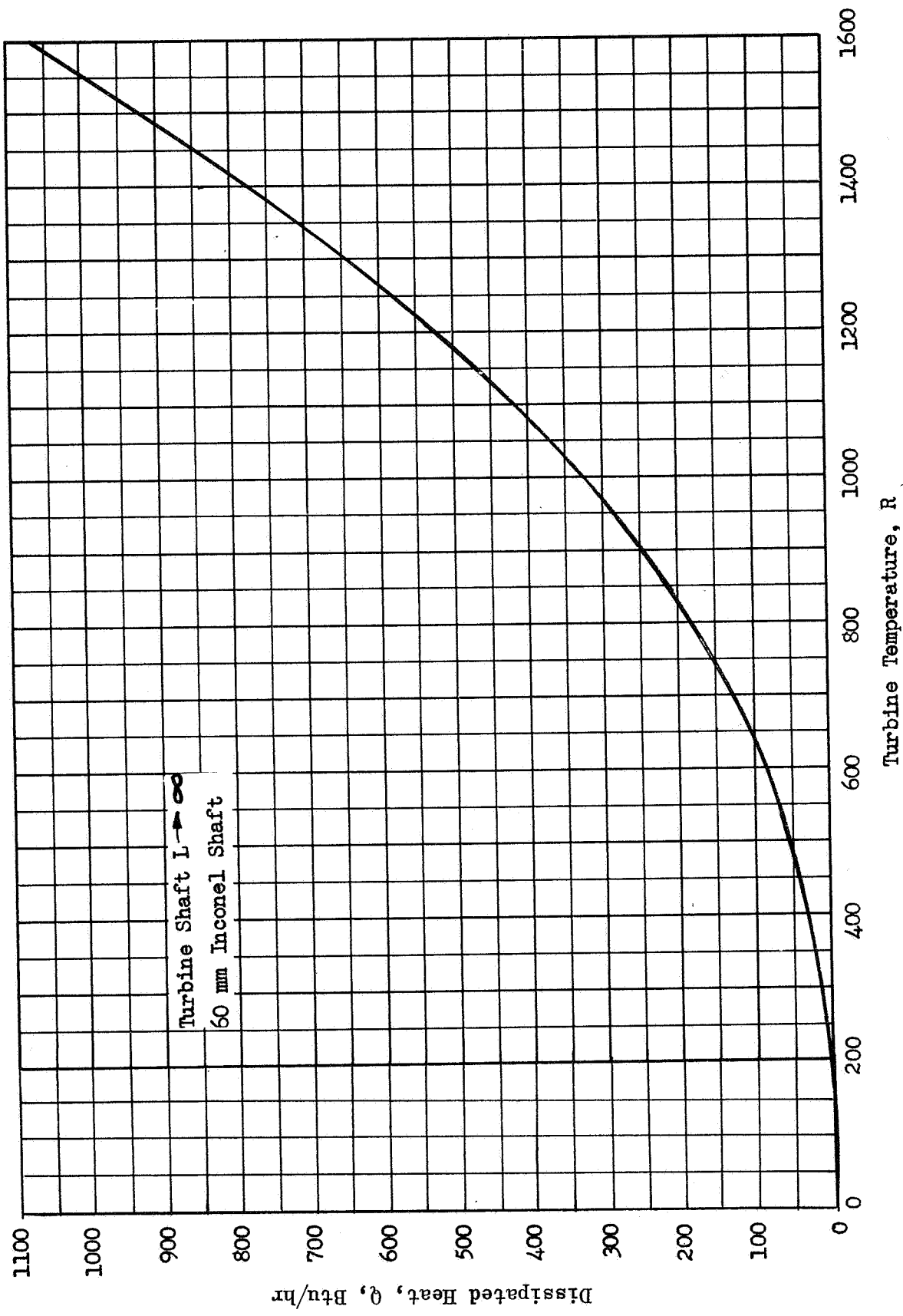


Figure 98. Maximum Turbine Shaft Heat Dissipation vs Turbine Temperature

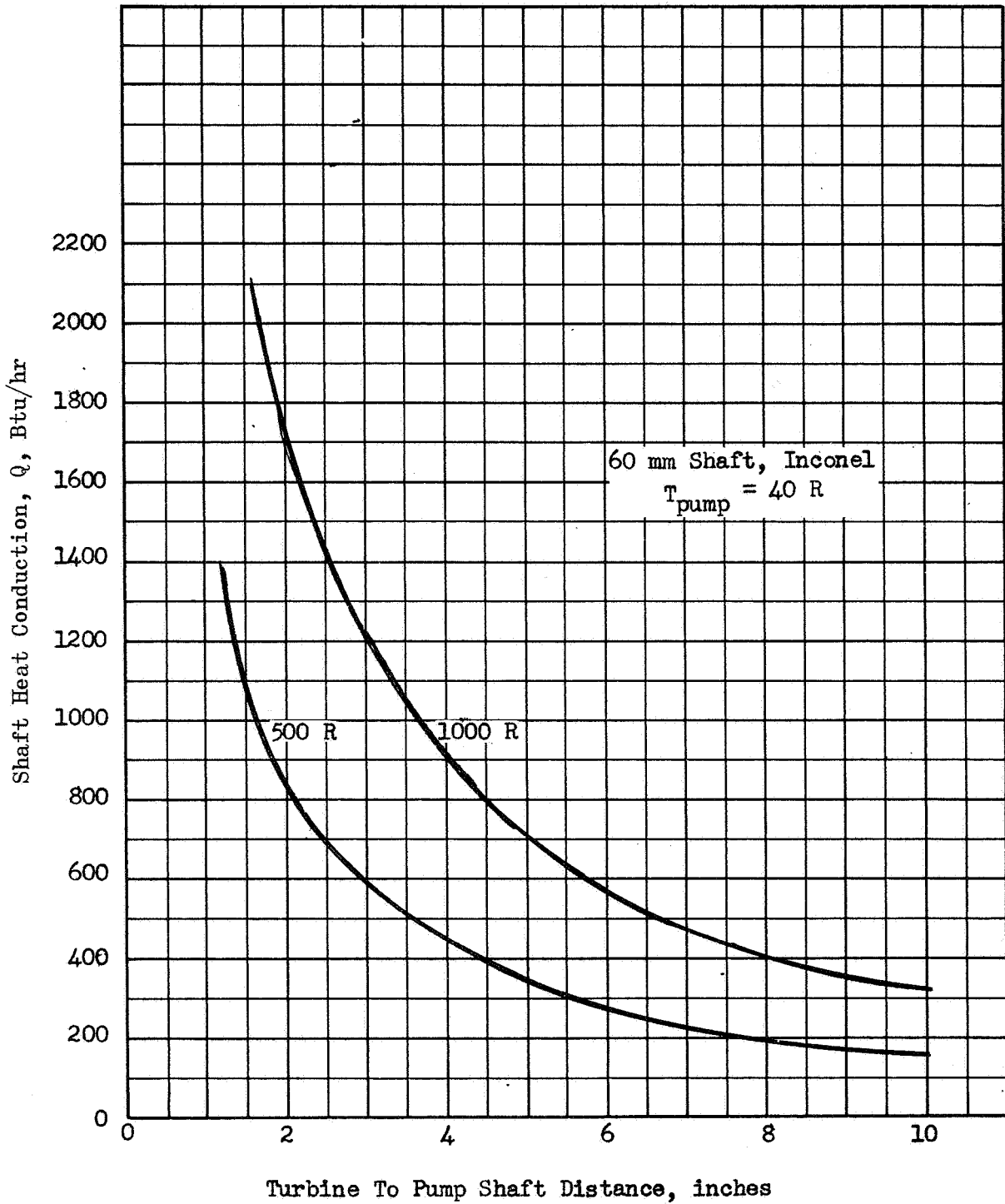


Figure 99. Turbine Shaft Heat Conduction vs Distance—Radiation Neglected

It is shown that the greater the ducting thickness (t) is in relationship to the pump body length (L), the greater the percentage heat radiated by the exhaust ducting. Figure 100 illustrates the heat transferred by downstream ducting compared to the heat radiated from the turbine surface. Substantial percentages of heat can be removed by the ducting at lower surface temperatures.

Cases where the turbine was isolated from the pump body by a standoff housing illustrated in Fig. 100 were also investigated during the concluded study. Typical analysis shown in Fig. 101 for a 0.1-inch-thick housing of various materials indicates an increase in isolation length and a choice of a low conductivity material such as Inconel or titanium can result in a considerable radiation from the housing and an isolation of the heat from the pump body. The resultant increases in turbopump weight and the disadvantage of long shaft connections between the pump and turbine require further detailed study for specific design cases.

Scaling of shaft heat conduction area to turbine surface heat radiating area were conducted for three specific cases where imposed limitations of (1) shaft stress limits, (2) pump NPSH limits, and (3) turbine tip speed-limited designs. The scaling results with thrust were as follows:

$$\left( \frac{A_c}{A_s} \right) \propto F^0 \quad (\text{shaft stress limited}) \quad (87)$$

$$\left( \frac{A_c}{A_s} \right) \propto F^{1/2} \quad (\text{NPSH limited}) \quad (88)$$

$$\left( \frac{A_c}{A_s} \right) \propto F^2 \quad (\text{turbine tip speed limited}) \quad (89)$$

For other than shaft stress limited designs, it is seen that small thrust turbopumps will suffer less from shaft heat conduction. Very large turbopumps with a large shaft conduction area ( $A_c$ ) to radiating surface area ( $A_s$ ) will, as shown above, require proportionately better isolating approaches.

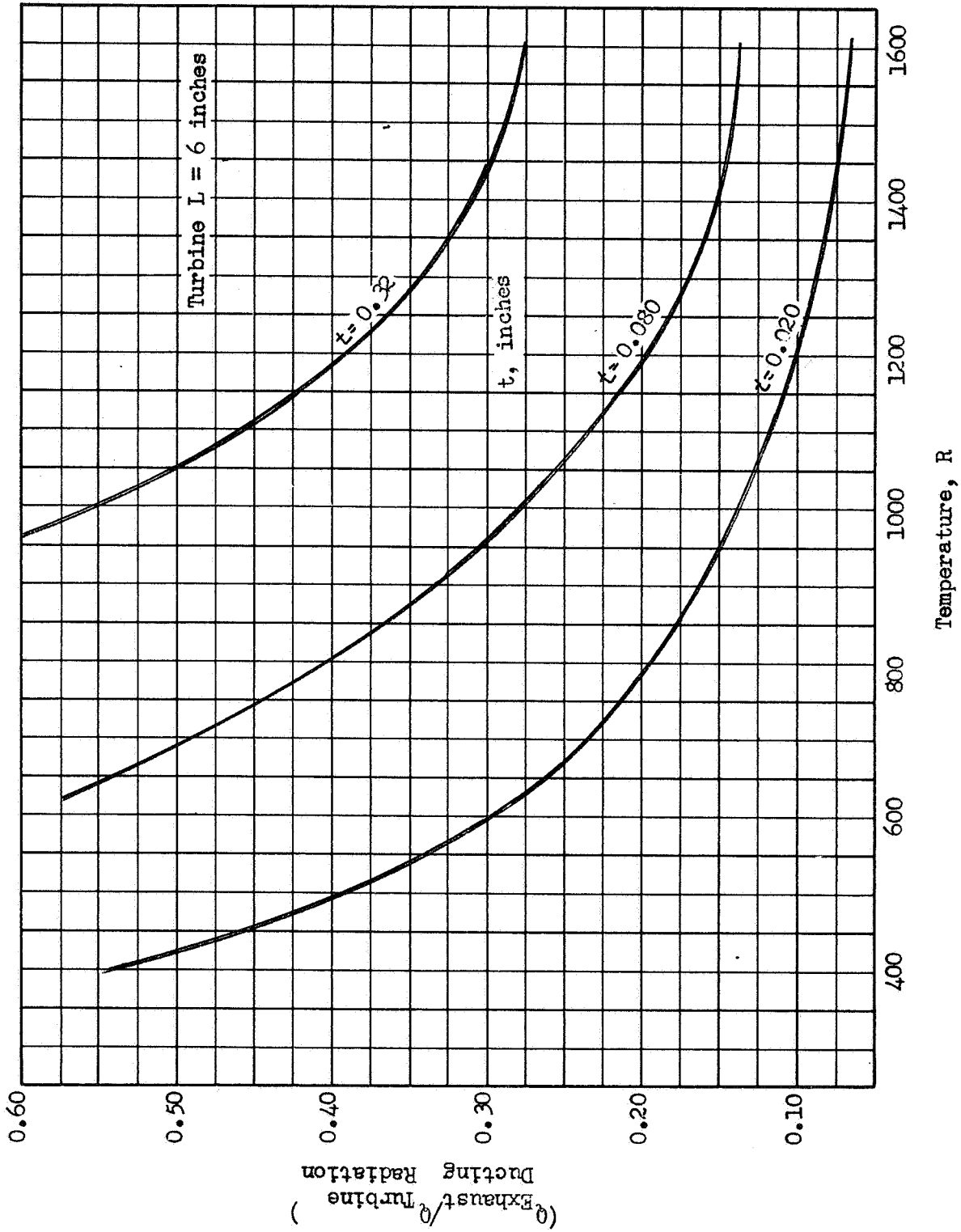


Figure 100. Heat Transferred by Downstream Ducting Compared to Heat Radiated From Turbine Surface

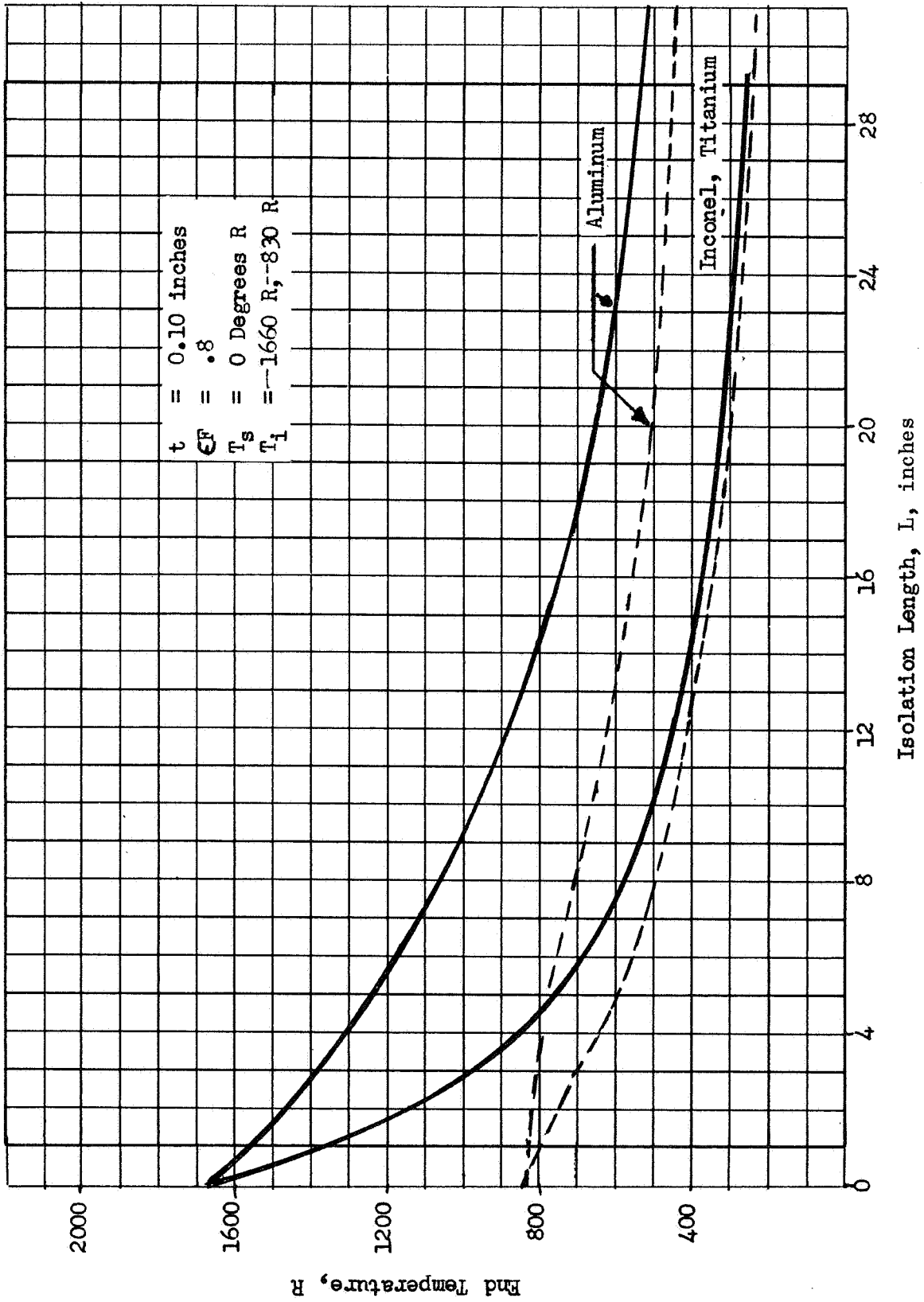


Figure 101. Turbine to Pump Isolation Distance vs Temperature

## TURBOPUMP THERMAL EQUILIBRIUM CONDITIONS

The case for turbopump equilibrium temperature achievement without benefit of the turbine heat radiation to environmental surroundings and where the turbine and pump unit are isolated from the surroundings was examined. A heat balance between the pump warming and the turbine chilling to the final equilibrium temperature  $T_f$  became

$$W_T C_{PT} (T_T - T_f) = W_P C_{PP} (T_f - T_P) \quad (90)$$

The equilibrium temperature  $T_f$  was finally expressed as

$$T_f = \left[ \frac{\delta T_T + T_P}{(\delta + 1)} \right], \quad \delta = \left( \frac{W_T C_{PT}}{W_P C_{PP}} \right) \quad (91)$$

As would be anticipated a lighter turbine to pump weight ratio and lower turbine housing and rotor temperature will contribute to a reduced equilibrium temperature.

A more exact heat balance by employing enthalpy values in an iterative solution to allow for variable heat capacity was performed for existing pumps and design layouts, and the results are illustrated in Table 24. It is seen that turbine to pump weight ratios vary from 1.0 for lower pressure pumps to 0.25 for higher pressure pumps. As a result where a greater pump mass is present the equilibrium temperature is reduced. LH<sub>2</sub> pump equilibrium temperatures are illustrated in Table 24 to range from -120 to +378 F. Effective isolation of the pump and turbine sections will result, of course, in much lower equilibrium temperatures due to the allowance for turbine radiation and duct and structural support heat conduction.

TABLE 24

## COMPARISON OF ISOLATED TURBOPUMP EQUILIBRIUM TEMPERATURES

Data Reference Code	Thrust, lbs X 10 <sup>-3</sup>	Thrust Chamber Pressure, psia	Pump Discharge (P <sub>D</sub> ), psia	Weight, pounds		Equilibrium Temperature After Shutdown, F
				Pump	Turbine	
LH <sub>2</sub> Turbopumps						
I	15	292	920	--	--	--
II	30	1000	1530	37	18	35
III	200	630	1200	180	151	378
IV	250	1500	2550	253	196	235
V	280	1000	1530	364	175	35
VI	350	3000	5950	533	122	-120
VII	350	3000	5950	403	122	-75
VIII	365	1000	1530	180	151	255
IX	1500	1000	1800	2660	2110	225
X	1500	1000	1530	2400	1900	255
XI	3000	1000	1530	4700	3900	255
XII	6000	1000	1530	9400	7800	255
LO <sub>2</sub> Turbopumps						
I	15	292	435	--	--	--
III	200	630	885	156	129	67
IV	250	1500	2090	88	199	575
VI	350	3000	6420	271	299	227
VII	350	3000	6420	178	299	353
IX	1500	1000	1520	1400	1240	113

### Turbopump Transient Heat Conduction

This problem was analyzed to determine the effect of general pump geometry on the time to reach a given equilibrium temperature. For this case the turbopump assembly was assumed to be totally insulated with no heat conduction to other parts of the engine through appendages. It was further assumed that the pump and turbine have infinite conductances within each body such that the resulting temperature will be uniform throughout the turbine and pump at any given time. The shaft was also assumed to have no heat storage capacity. A simple sketch of the turbopump arrangement is shown in Fig. 102, and a heat balance equation between the pump and turbine is given by

$$-W_t C_{P_t} \left( \frac{dT_c}{d\tau} \right) = \frac{kA}{X} (T_t - T_p) = W_p C_{P_p} \left( \frac{dT_p}{d\tau} \right) \quad (92)$$

When Eq. 92 is integrated and the limits are substituted, the following solution is obtained in terms of a nondimensional time and heat content parameters as

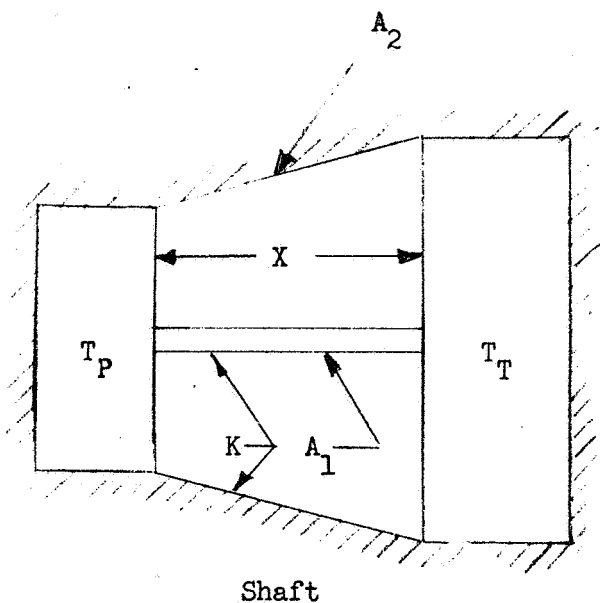
$$\frac{Ak\tau}{XW_t C_{P_t}} = \frac{1}{1+F} \ln \left[ \frac{T_{t_i} - T_{p_i}}{(1+F)T_{t_f} - FT_{t_i} - T_{p_i}} \right] \quad (93)$$

where the pump temperature at any given time is given by

$$T_{p_f} = F (T_{t_i} - T_{t_f}) + T_{p_i} \quad (94)$$

and the turbopump parameter  $F$  and the  $\Omega$  ratios are defined as

$$F = \frac{W_t C_{P_t}}{W_p C_{P_p}}, \quad \Omega = \frac{Ak\tau}{X W_T C_{P_T}} \quad (95)$$



$$A = A_1 + A_2$$

Pump Initial Conditions

$W_P$   
 $C_{P_P}$   
 $T_{P_i}$

Turbine Initial Conditions

$W_T$   
 $C_{P_T}$   
 $T_{T_i}$

$$A = A_1 + A_2$$

Figure 102. Sketch of Pump, Shaft and Turbine for Derivation of Eq. 1

Under specialized conditions of varying F values the above equation may be simplified to

$$\text{I} \quad F \rightarrow 0 \quad \Omega = \ln \frac{T_{T_i} - T_{P_i}}{T_{T_f} - T_{P_i}} \quad (96a)$$

$$\text{II} \quad F \approx 1.0 \quad \Omega = 0.5 \quad (96b)$$

$$\text{III} \quad F \rightarrow \infty \quad \Omega \rightarrow 0 \quad (96c)$$

It can be seen that the time for heat conduction can be varied both by a variation of turbine heat content and by resistance control in the following relationships.

$$\tau \propto W_T C_{PT} \quad (97)$$

$$\tau \propto \frac{X}{kA} \quad (98)$$

The solution represented by Eq. 93 is graphically presented in Fig. 103 for an initial turbine temperature of 1700 R and pump temperature of 40 R for various values of the turbopump parameter F. The results are shown in terms of the lefthand member of Eq. 93 and the ratio of pump final temperature to turbine initial temperature,  $T_{P_t}/T_{T_i}$ . From the curves a small pump temperature rise is obtained if the distance between the pump and turbine (X) is large, the thermal conductivity (k) is low (or good insulation between pump and turbine), and the cross-sectional area for conduction (A) is low. Thus, if X/kA is large the time ( $\tau$ ) to reach any given temperature or the time for the pump to warm up due to turbine heat soakback would be long.

Since it takes an infinite time for the pump turbine temperatures to equalize, dotted curves are shown in Fig. 103 to indicate points of near-equilibrium temperature (1/e) and points where there would be only a 10-degree difference

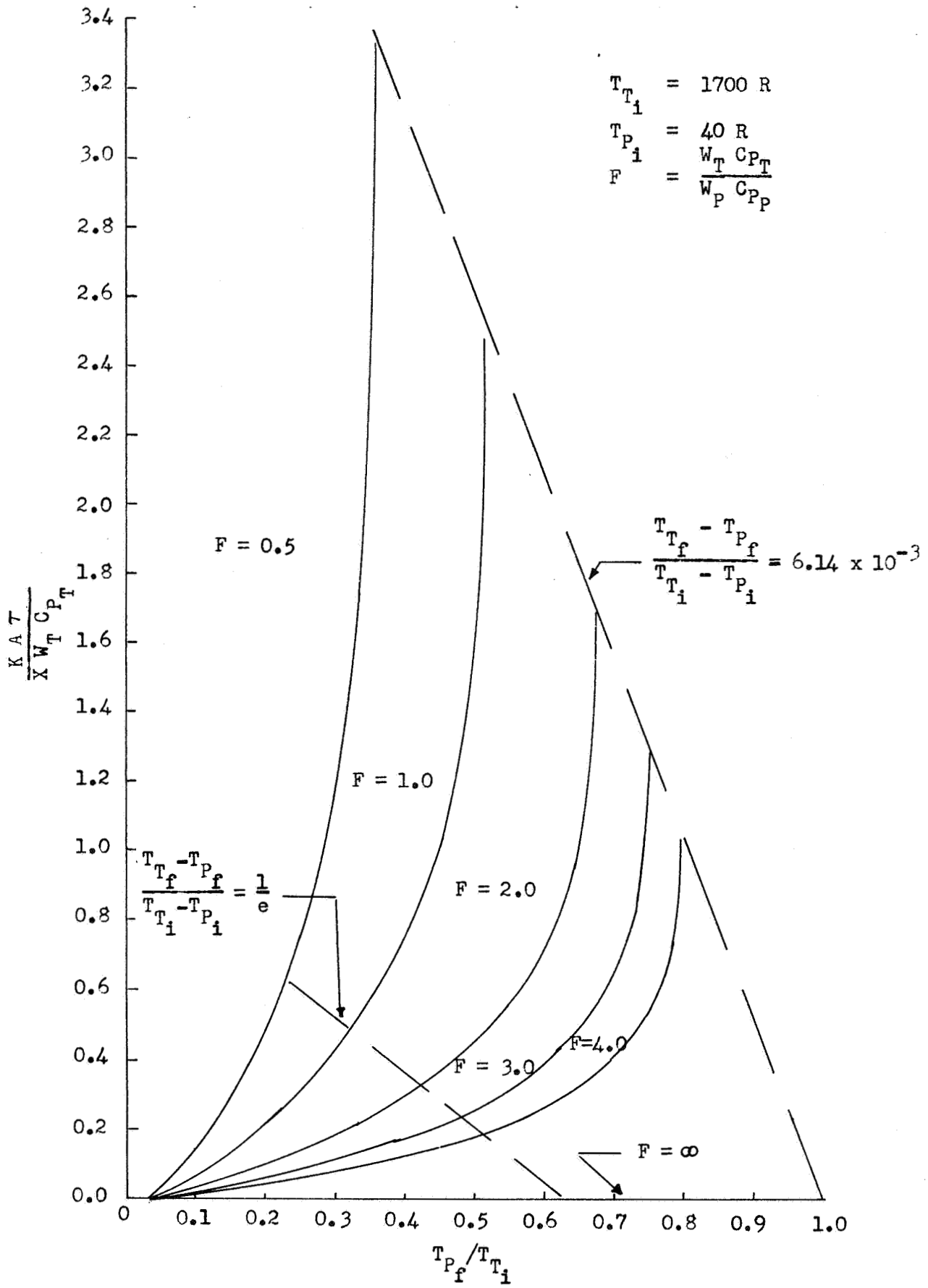


Figure 103. Time vs Pump Temperature, Insulation Control Case

between the final pump and turbine temperatures. In general, minimum pump temperature is obtained if the turbopump parameter F is small or approaches zero.

A detailed heat soakback analysis of typical existing LH<sub>2</sub> turbopumps using digital computer analysis was undertaken under Task IV study to correlate with analyses developed under the Task III study. Good order of magnitude agreement with the more complex analysis was obtained.

#### ENGINE PRECONDITIONING

The J-2 engine requires two basic types of preconditioning. One is chilling of the thrust chamber to reduce the rapid gasification which occurs when at start the liquid hydrogen is heated as it passes through the considerably warmer thrust chamber jacket. The second type of preconditioning required is propellant feed duct and pump chilling. This is required for both the LOX and LH<sub>2</sub> feed systems. Bleed valves below the propellant pumps allow propellants to be recirculated from the stage propellant tanks through inlet ducts and pumps and then returned to the tanks. The LOX and LH<sub>2</sub> recirculation systems operate before engine start to assure that propellants at the pumps are cold enough at start to meet pump NPSH requirements.

For each operation of the J-2 engine preconditioning is required. For missions requiring multiple starts additional preconditioning requirements exist. The thrust chamber prechill requirement is met by GSE cold helium for a second-stage single-burn application; however, for a restart the cold helium must be supplied by a stage cold helium system. After a coast (zero g) phase the stage ducting is warm and filled with all gas—a more severe condition than that for the first burn. On the S-IVB stage the inlet ducting and pump chilldown is accomplished by settling the propellants using an auxiliary propulsion system and then using the same recirculation systems used for the first burn. The J-2S eliminates the auxiliary

propulsion system by incorporating idle mode capability in the J-2. The idle mode operation moves enough propellant through the feed systems so that, with a SPTS system, start recirculation systems are not required. For each restart, however, an additional SPTS cartridge must be added to the engine.

For applications of the J-2 where neither stage coast or stage restart are required the J-2 thrust chamber is chilled before launch using GSE supplied helium, and consequently no stage preconditioning hardware is required. Applications of this type are use of one J-2 in the S-IVB stage when it is used as the second stage of a S-IB, and use of five J-2's in the S-II stage as the second stage of a S-V.

In the same type of application, however, stage hardware is required for the preconditioning of inlet ducts and engine pumps. On the S-IVB stage similar recirculation systems are used for both LOX and LH<sub>2</sub>. Each system has a tank-mounted centrifugal pump driven by an a-c electric motor. Inverters are required to convert the stage battery d-c power. From the pump the recirculation propellant is piped into the inlet ducting just below the stage prevalves. In this line between the pump and inlet duct are a shutoff valve, flowmeter, filter, and check valve. Returning from the engine the recirculation propellant is returned to the tank through a stage line and check valve.

On the S-II stage with five J-2 engines the LH<sub>2</sub> recirculation system uses five recirculation pumps driven by a-c electric motors. As in the S-IVB, inverters are used to convert battery d-c power. From the recirculation system pumps, bypass lines pipe the recirculation propellant into the engine inlet ducts below the prevalves. After flowing through the inlet ducts and engine pumps the LH<sub>2</sub> returns to a stage LH<sub>2</sub> recirculation system manifold and from there by a return line into the LH<sub>2</sub> tank. For LOX recirculation five recirculation duct systems are used on the stage but no pumps are required.

### Engine Modifications to Eliminate Preconditioning

In the J-2S program engine improvement features were incorporated to eliminate the need for engine preconditioning. To eliminate the need for chilling the thrust chamber a duct and valve were provided to bypass fuel around the thrust chamber jacket directly to the injector until turbopump speed has been built up. The buildup of back pressure from  $\text{LH}_2$  gasification in the jacket will then no longer cause turbopump stall. The elimination on the J-2S of the requirement for LOX and  $\text{LH}_2$  recirculation is primarily made possible by a solid-propellant turbine starter (SPTS). The SPTS provides about three times the energy for start as the J-2 hydrogen start tank bottle. The SPTS duration is such that a large portion of the propellant in both ducts has been evacuated and burned in the engine by the time the SPTS burnout occurs. At this point the propellant conditions at the interface are such that steady-state NPSH has been obtained. The elimination of the recirculation requirement on the J-2S is also aided by the use of a thrust chamber tapoff cycle and idle mode start.

### Effect on Weight by Eliminating Preconditioning

Elimination of thrust chamber chill requirement adds about 100 pounds to each J-2 engine because of the addition of the thrust chamber bypass system. No engine hardware is deleted by this modification. The SPTS system, which is added to the J-2 engine to eliminate the recirculation systems, weighs about 114 pounds. It, however, eliminates the start tank system and the two propellant bleed valves—a total of about 153 pounds. This modification, therefore, reduces each engine's weight about 40 pounds.

No change in stage hardware results from the thrust chamber prechill elimination. LOX and  $\text{LH}_2$  recirculation systems are eliminated from both the S-IVB and S-II stages, however. These systems on the S-IVB weigh about 230 pounds. A stage weight reduction of over 2000 pounds would result

from the use of J-2S engines in place of J-2 engines. Most of the stage hardware deletions result from the elimination of the propellant recirculation systems. A value of 80 percent of the total weight reduction (1600 pounds) can therefore be assumed to result from the recirculation system elimination.

#### CLOSED-CYCLE SYSTEM PRECONDITIONING FLOW REQUIREMENTS

Closed cooling cycle system analysis was undertaken for the development of the required LH<sub>2</sub> coolant weight flow relative to the pump weight to achieve a conditioned pump. A closed-form analytical solution was developed for the case of a slow bleed through the pump where equilibrium of the hydrogen and pump body occurred. An equated heat balance on the pump heat transferred and the LH<sub>2</sub> coolant temperature rise becomes

$$-\rho_w C_{P_w} t_w A_w (T_{wi} - T_{H_2}) = W_{H_2} C_{P_{H_2}} (d T_{H_2}) \quad (99)$$

Integrating this results in

$$\frac{W_{H_2} C_{P_{H_2}}}{W_w C_{P_w}} = \frac{1}{\ln_e \left( 1 - \frac{T_{w_2} - T_{H_2i}}{T_{wi} - T_{H_2i}} \right)} = R \quad (100)$$

For a chilldown to 1/e of the initial temperature difference

$$R = -1/\ln_e (1 - 1/e) = 2.2 \quad (101)$$

From this analysis the weight heat capacity product of the hydrogen coolant flow becomes approximately 2.2 times that for the pump. Therefore, to reduce the amount of the coolant required to chill the pump, the size or weight of the LH<sub>2</sub> pump must be reduced.

OPEN-CYCLE SYSTEM PRECONDITIONING FLOW REQUIREMENTS

A second definitive case considering a high wall thermal conductivity may be developed from the relationships

$$h dA_s (\bar{T}_w - T_H) = \dot{w}_H C_{pH} dT_H \quad (102)$$

$$h d\tau (T_w - T_H) = \rho_w C_{pw} t_w dT_w \quad (103)$$

Integration of the first equation above yields

$$\left( \frac{\bar{T}_w - T_H}{\bar{T}_w - T_{Hi}} \right) = e^{-\left( \frac{h A_s}{\dot{w}_H C_{pH}} \right)} \quad (104)$$

which can be reduced to

$$\left( \frac{T_w - T_{Hi}}{T_{wi} - T_{Hi}} \right) = e^{-\left( \frac{N_{Bi} N_{Fo}}{(4 N_{ST} (L/D))} \right)} \quad (105)$$

The Biot Fourier product may be expressed as

$$N_{Bi} N_{Fo} = \frac{W_H}{W_W} \left( \frac{C_{pH}}{C_{pw}} \right) N_{ST} (4L/D) \quad (106)$$

Inserting in the above results in

$$\frac{W_H}{W_W} \left( \frac{C_{pH}}{C_{pw}} \right) = - \frac{e^{N_{ST} (4L/D)}}{N_{ST} (4L/D)} - \ln_e \left( \frac{T_w - T_{Hi}}{T_{wi} - T_{Hi}} \right) \quad (107)$$

As illustrated in Fig. 104 the coolant flow required to chill the pump to a given temperature becomes a function of the Stanton number  $4L/D$  product. Values of this product much less than one result in a coolant which is dumped overboard without full usage. Values greater than one would appear to imply an excessive coolant temperature rise resulting in a diminished efficiency of cooling due to a decreased coolant to wall temperature difference.

Further work comparing the chill condition for surface temperatures brought to the minimum temperature and for complete chilling with finite wall thermal conductivity was conducted under Task II study. Some comparative experimental preconditioning test results are illustrated in a following section.

Results of Ref. 42 were translated into average flows and average weight heat capacity ratios for M-1 slow prechill test results and shown in Table 25. Chilledown weight flow for chilledown to  $1/e$  and to the final temperature are indicated. Chilledown required flows were seen to be approximately twice the simplified equation values.

Integrated weight heat capacity ratio values for the P-W 350K long pre-chill study (outlined in a later section) were approximately

$$\frac{W_{H_2} (C_p)_{H_2}}{W_p (C_p)_p} = 2.0$$

which agrees more favorably with simplified theoretical predictions.

#### CHILLDOWN OF FEED LINE COMPONENTS

Assessment of the time required for chilledown of pump feed lines was developed by considering the heat input to the transiting coolant. A heat balance on the coolant neglecting change in phase and assessing a constant heat capacity becomes

$$h_c dA_s (T_{wc} - T_c) = w_c c_{p_c} dT_c \quad (108)$$

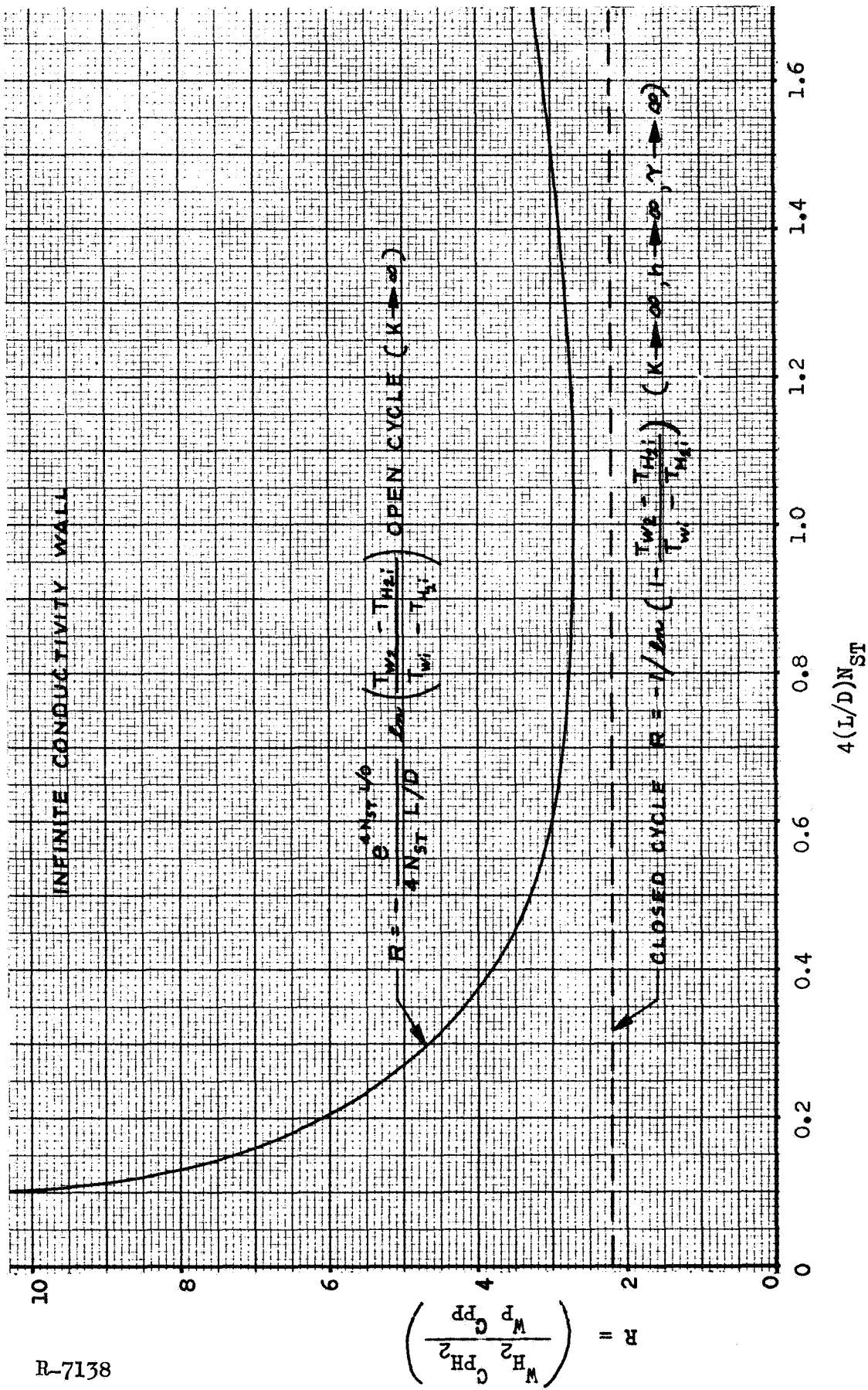


Figure 104. Hydrogen Coolant Flow to Pump Weight vs Stanton—L/D Parameter at ( $\alpha = 1/e$ )

TABLE 25

## M-1 PUMP CHILLDOWN FLOW REQUIREMENTS

Test No.	$\dot{W}_{H_2}$ , lb/sec	$\dot{W}_{H_2}$ (total), pounds	$\tau$ , hours	Childdown to -420 F $\left(\frac{\dot{W}_{H_2} C_{PH_2}}{\dot{W}_p C_{pp}}\right)^*$	Childdown to $\alpha = 1/e$ $\left(\frac{\dot{W}_{H_2} C_{PH_2}}{\dot{W}_p C_{pp}}\right)^*$
1	0.51	3860	2.1	27.2	-
2	-	-	-	-	-
3	0.14	2080	4.25	14.7	7.6
4	0.29	950	0.9	6.7	5.1
5	0.46	1780	1.08	10.5	-
6	0.52	1480	0.80	10.5	-
7	0.36	1130	0.88	7.95	-

$$* \left( \frac{C_{PH_2}}{C_{pp}} \right) \cong 48 \quad (\text{Data from Ref. 42})$$

where the wall temperature is considered at an average value within a time period. Defining the nondimensional values

$$\alpha = \left( \frac{T_{wc} - T_c}{T_{wi} - T_c} \right) \quad (109)$$

$$N_{ST} = \left( \frac{h_c A_c}{\dot{w} C_p} \right) \quad (110)$$

the above relationship becomes

$$N_{ST} \int_0^{A_S} \frac{d(A_S)}{A_c} = + \int_{T_{ci}}^{T_{cf}} \left( \frac{dT_c}{T_{wi} - T_c} \right) \quad (111)$$

If the ratio of surface area ( $A_s$ ) to cross-sectional area ( $A_c$ ) is considered for a cylindrical line component

$$\frac{A_s}{A_c} = \frac{\pi D ds}{\pi/4 D^2} = 4 \left( \frac{ds}{D} \right) \quad (112)$$

Integrating the above relationships results in

$$4 \frac{L}{D} N_{ST} = \ln \left( \frac{T_{wi} - T_{co}}{T_{wi} - T_{ci}} \right) = \ln \left( 1 - \left( \frac{T_{co} - T_{ci}}{T_{wi} - T_{ci}} \right) \right) \quad (113)$$

A graph of this relationship for a Stanton number of 0.0025 is shown in Fig. 105. It is seen that at time zero ( $\alpha = 1.0$ ) the coolant temperature outlet value is maximum and diminishes as a function of time ( $\alpha < 1.0$ ). The controlling influences on a component chilldown are consequently seen as

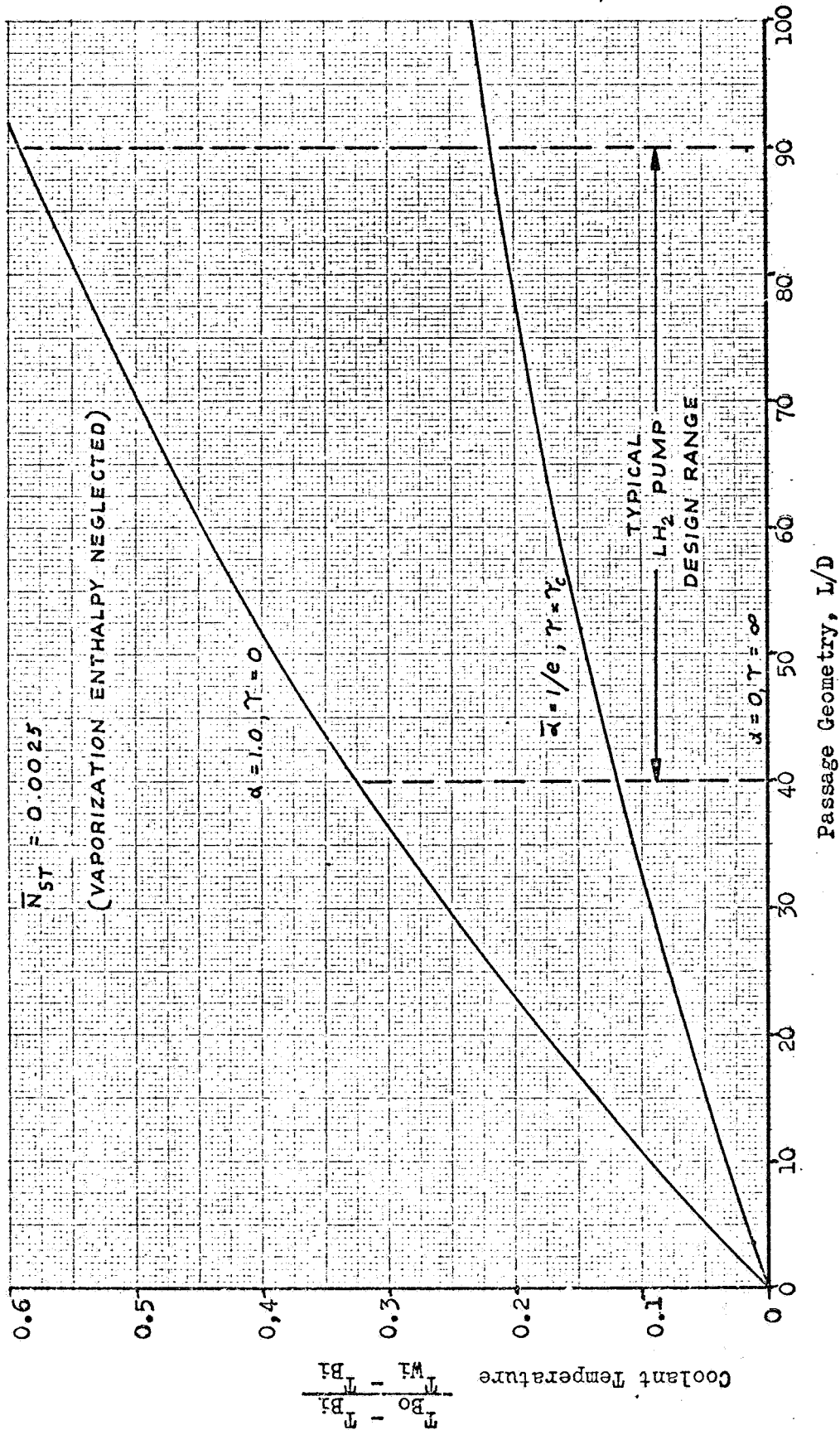


Figure 105. Coolant Outlet Temperature vs Passage Geometry

$$\alpha (Fo, Bi), L/D, N_{ST}$$

(114)

where the Stanton number is a relatively insensitive function of flowrate (Reynolds number).

Computer approaches aimed at discretization of the components, both in length and thickness, were outlined under Task II study. This approach is also valid for feedline study.

Experimental line cooldown data of Ref. 20 were reviewed and are shown typically reduced to nondimensional temperature in Fig. 106. For the range in coolant velocities chosen during this experimental study ( $LN_2$  coolant) a low-wall Biot number condition was prevalent during the runs. Coolant velocities chosen (5 to 9 ft/sec) were such that the film and nucleate boiling effects predominated over forced convection effects resulting in effective enhancement of the line chilldown with coating by reduction of the coating surface temperature to the nucleate boiling range. Study with higher film coefficient conditions with hydrogen or significantly higher  $LN_2$  coolant velocities is necessary to produce the case outlined in Task II where surface chill and coating insulation effects occur to restrain heat input to the coolant from the wall surface.

In considering a rapid pump start condition, delivery of an  $LH_2$  flow with a low percentage vapor to the pump inducer inlet is critical due to the low flow area present in the inducer inlet and criticality of the inducer to the pump start. Future engine designs should limit line  $L/D$  and heat capacity and allow for internally coated insulation surfaces.

#### CONTINUOUS VENT SYSTEM BLEED CONDITIONING

In addition to the pump preconditioning approach currently employed by the J-2 engine system (described under Task IV), two alternate approaches to pump prechill prior to start are available. These include  $LH_2$  pump

Data From Ref. 20

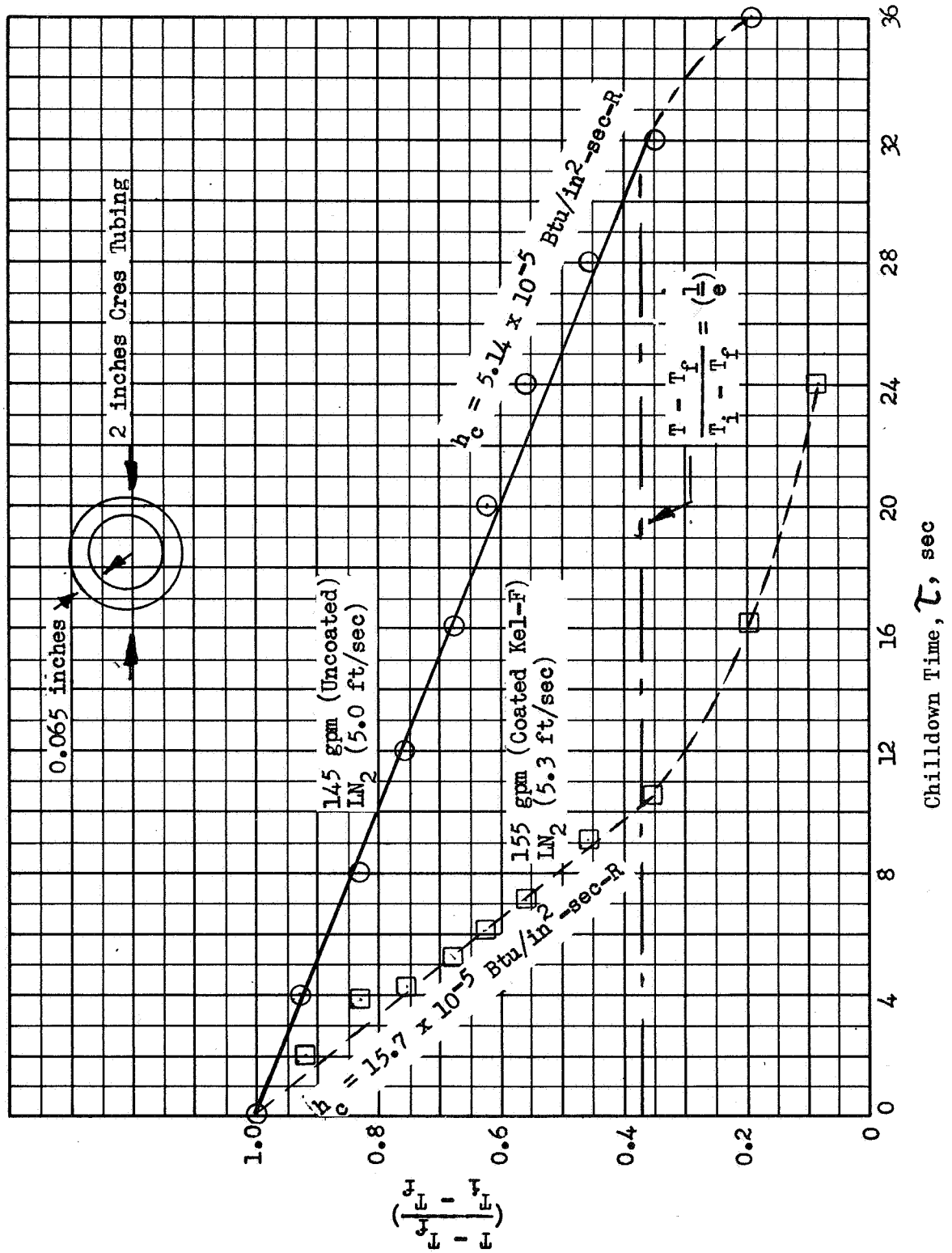
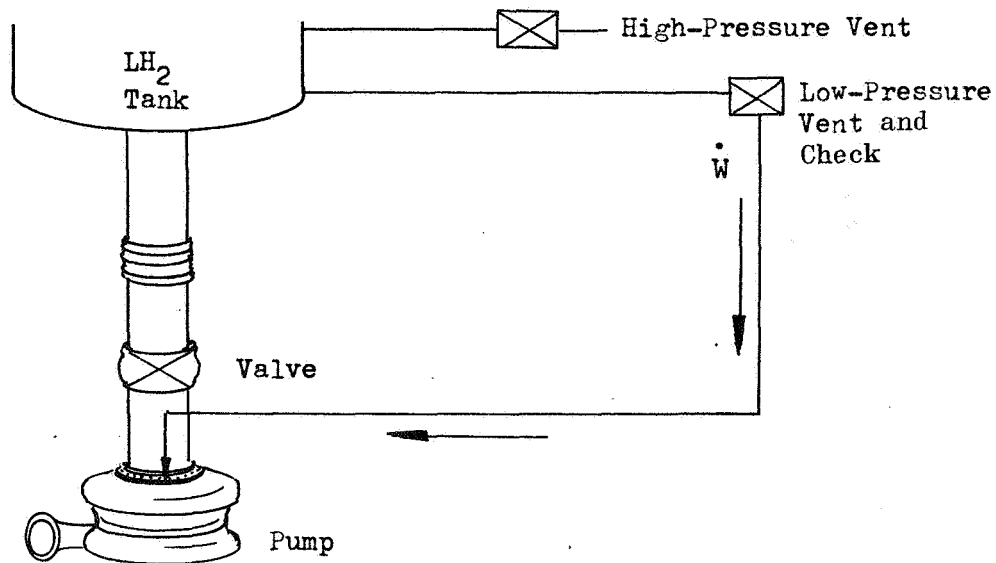


Figure 106. Line Cooldown Test Data (Midpoint Temperature) (T.C. #5) L/D = 5

prechill by "idle mode conditioning" where a small LH<sub>2</sub> bleed is opened through the pump and thrust chamber system for propellant settling or orbit correction purposes. A tank vent blowdown alternative approach can also be employed. A feed system schematic of this approach is shown below:



In this prechill system warm tank ullage gases would be vented through a low-pressure vent and check valve into the pump inlet. A high-pressure vent valve would be employed for tank over pressure precautionary purposes. Data from Saturn flight AS203 (Ref. 56) on the SIV stage LH<sub>2</sub> tanking indicated initial ground hold maximum and third-orbit minimum heating rates of 90 and 15 Btu/sec, respectively, corresponding to approximately 20 to 145 Btu/hr-ft<sup>2</sup> (cylindrical tank area). During a 1.49-hour orbit approximately 250 pounds of LH<sub>2</sub> were vaporized and vented due to solar and earth albedo heating to the LH<sub>2</sub> tank which corresponds to 168 lb/hr vaporization rate. Based upon slow bleed requirements less than 1-hour interval to restart would be possible employing this preconditioning technique. Continuing improvements in insulation techniques and the lesser percentage tank heat input for larger-thrust stages would indicate a possible problem employing this preconditioning approach for large-thrust stages.

Assuming an equal insulation resistance approach for a constant run duration scaling,

$$W_{\text{pump}} \propto F \propto V_{\text{tank}} = \frac{\pi}{4} D^2 L \quad (115)$$

$$\dot{W}_{\text{vapor}} \propto \dot{q} \propto \pi DL \quad (116)$$

$$\frac{\dot{W}_{\text{vapor}}}{W_{\text{pump}}} \propto \left(\frac{L}{D}\right) \quad (117)$$

It is consequently illustrated that the larger tank diameter attendant with significantly larger-thrust engines will either require relatively longer prechill periods by this technique or augmenting methods for supplementing the tank vent gas chilldown approach.

#### DESIGN STUDIES

In support of analysis efforts a number of design studies were undertaken. These design studies included development of methods for reducing turbine heat content by cooling and preventing heat soakback from the turbine by thermal barriers, separations or joints. Additionally a review of internal insulation coating progress to date is presented.

#### Effect of Turbine Cooling

Turbine cooling is an effective method of improving the chilldown characteristics of hydrogen pumps and is also a means of increasing the turbopump performance. By using turbine cooling the allowable operating stress at the turbine blade roots which generally sets the limit to the turbopump speed is increased; thereby higher design speeds can be used to reduce pump flow passage L/D ratios and pump mass to be cooled. The effect is a reduced chilldown time for the pump.

Since the rotational speed, weight, and turbine flowrates of the turbopump can be related to the amount of turbine cooling and the turbine inlet temperature, the advantages of turbine cooling for a hydrogen turbopump for a 250,000 pounds thrust, 1500-psia chamber pressure tapoff cycle,  $\text{LO}_2/\text{LH}_2$  engine was investigated for a no-loss turbine drive gas system. For a given turbine inlet temperature, increasing the amount of turbine blade cooling in the last rotor will increase the design rotational speed and thus decrease the design weight of the turbopump. For example, at an inlet temperature of 2000 R, cooling the last rotor blade to a temperature that is 1000 R below the uncooled blade will increase the allowable design speed 40 percent and, consequently, decrease the weight 20 percent.

This effect is shown in Fig. 106-a. Since the pump design specific speed is increased by 40 percent, the pump impeller L/D ratio is decreased and the pump chilldown time is thereby reduced. Also, since the weight is down by 20 percent while the propellant flowrate is the same, the propellant flowrate to pump mass ratio is increased, thereby further reducing the chilldown time.

An added advantage of turbine cooling is a reduction in the turbine flowrate with a consequent increase in engine specific impulse. For the example previously discussed, 1000 R of turbine cooling ( $\Delta T_c$ ) reduces the turbine flowrate by 5 percent. However, for the same amount of cooling raising the turbine inlet temperature to 3200 R would reduce the turbine flowrate by 13 percent relative to the case of the uncooled turbine, but the advantage of reduced turbopump weight would not be obtained.

From the results of the study illustrated in Fig. 106-b, the turbine flowrate is seen to reach a minimum with turbine inlet temperature and the minimum points are seen to move to the right. This results from energy and lower gas property variations with increasing turbine inlet gas temperature and from a decrease in pump efficiency at low speeds. At low turbine temperatures the effect of a higher available energy predominates,

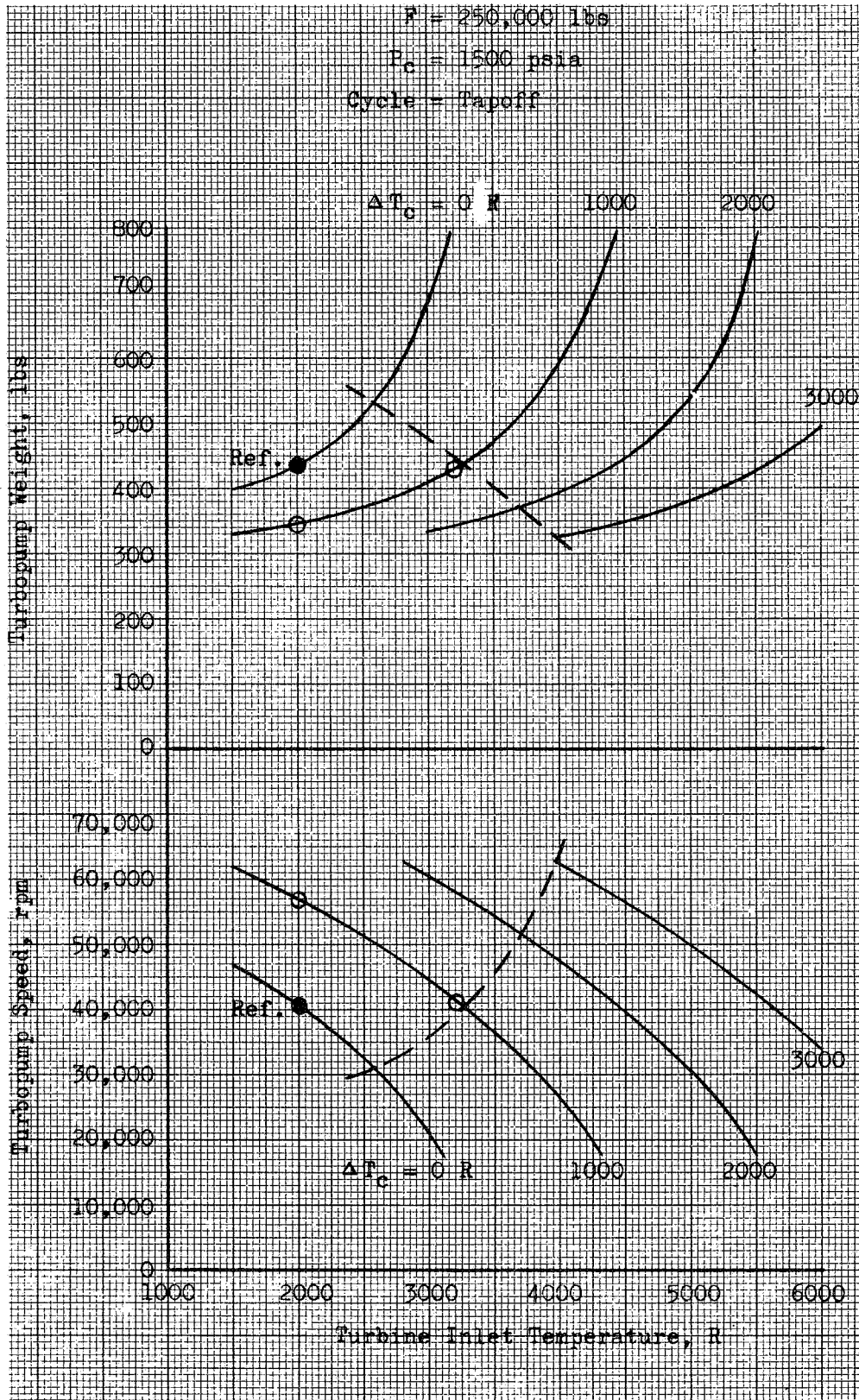


Figure 106-a. Effect of Turbine Cooling on LH<sub>2</sub> Turbopump Performance

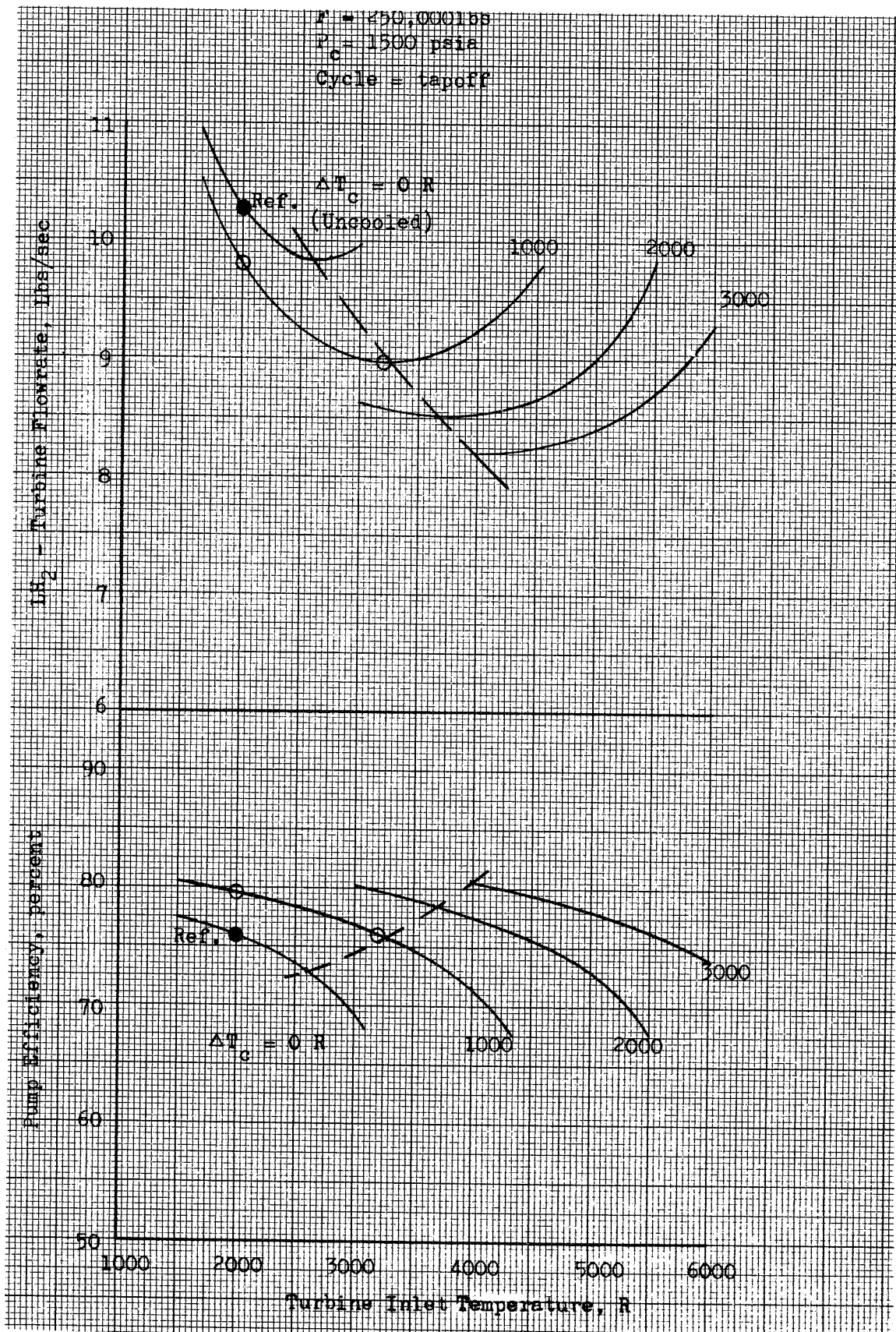


Figure 106-b. Effect of Turbine Cooling on LH<sub>2</sub> Turbopump Performance

and for a given amount of cooling the turbine flowrate decreases with rising inlet temperature. At high turbine temperatures the gas property variations begin to reduce the turbine gas available energy and, since the pump speed is low, the pump efficiency begins to drop off at a high rate. Therefore, at higher temperatures the turbine flowrate rises with increasing temperature. Finally, the reason why the minimum turbine flowrate points occur, for higher amounts of cooling, at higher inlet temperatures than those with less cooling is that the turbopump speed can be increased with increasing amounts of cooling (see dotted curves).

From the above analysis it may be concluded that turbine cooling can lead to pump designs that will have significantly better chilldown characteristics. However, there is a tradeoff between pump chilldown performance for rapid engine start and high engine performance obtained for full thrust operation. Turbine cooling can be used in an optimum manner to maximize the pump chilldown performance and to obtain improved engine performance.

### Cooled Turbine Design

The operation of a hot-gas turbine in a cold environment can best be solved with the regeneratively cooled turbine. All components (the housing and the rotors) are cooled by recirculation of a cryogenic fluid. The housing is constructed similarly to a regeneratively cooled combustion chamber whereby the housing is formed from a multiple stackup of tubes, structurally reinforced. Cryogenic fluid is tapped off the pump and piped into an annulus located downstream of the turbine housing. From there the fluid enters the tubes forming the outer wall of the combustion chamber. It is then circulated through the hollow first-stage nozzle vanes and returned through the tubes forming the inner wall of the combustion chamber. The flow then enters the injector annulus from where it is injected into the combustion chamber, then mixed with a propellant and

ignited. The geometric contour of the combustion chamber indicates a large  $L^*$  which means that complete and uniform combustion can be achieved before the gas reaches the nozzle exit.

The sketch of such a cooled turbine also shows a cooling method for the rotor and turbine buckets as shown in Fig. 107. The rotor as shown is an integral part of the turbine assembly and is connected to the pump shaft with a ball-spline drive. Cryogenic fluid is introduced into the center of the shaft, then transferred into the hollow discs and into the space between both discs from where centrifugal force will push it through the turbine buckets and the interstage stator. Seal rings on the tip of the inlet and exit edge of the buckets which are continuous prevent to a large extent the escape of the cooling fluid, enabling recovery and the possible injection into the turbine combustion manifold or another suitable point within the system. Heat soakback into the pump from a regeneratively cooled turbine would be at a minimum or nonexistent. The regeneratively cooled turbine would have other advantages; for instance it could operate at a higher gas temperature and higher pressure which, for the same power output, would mean smaller size and consequently allow higher rotational speed, resulting in a smaller overall envelope and lighter weight.

#### Cooling of Critical Turbopump Components

A design in which the major turbopump components (such as the fuel inlet, the volute and the turbine housing) are enveloped by liquid hydrogen supplied from the tank is shown in Fig. 108. An installation is provided whereby a sheet metal double wall is welded to the exterior of the fuel inlet and volute. The double wall is not required on the turbine since the reverse-flow configuration lends itself ideally to cooling. Liquid hydrogen flows from the tank into the fuel inlet envelope and through a crossover feedline to the volute and into the turbine filling the cavity between the pump volute backplate and the turbine discharger liner. The expanded hydrogen is then returned to the tank.

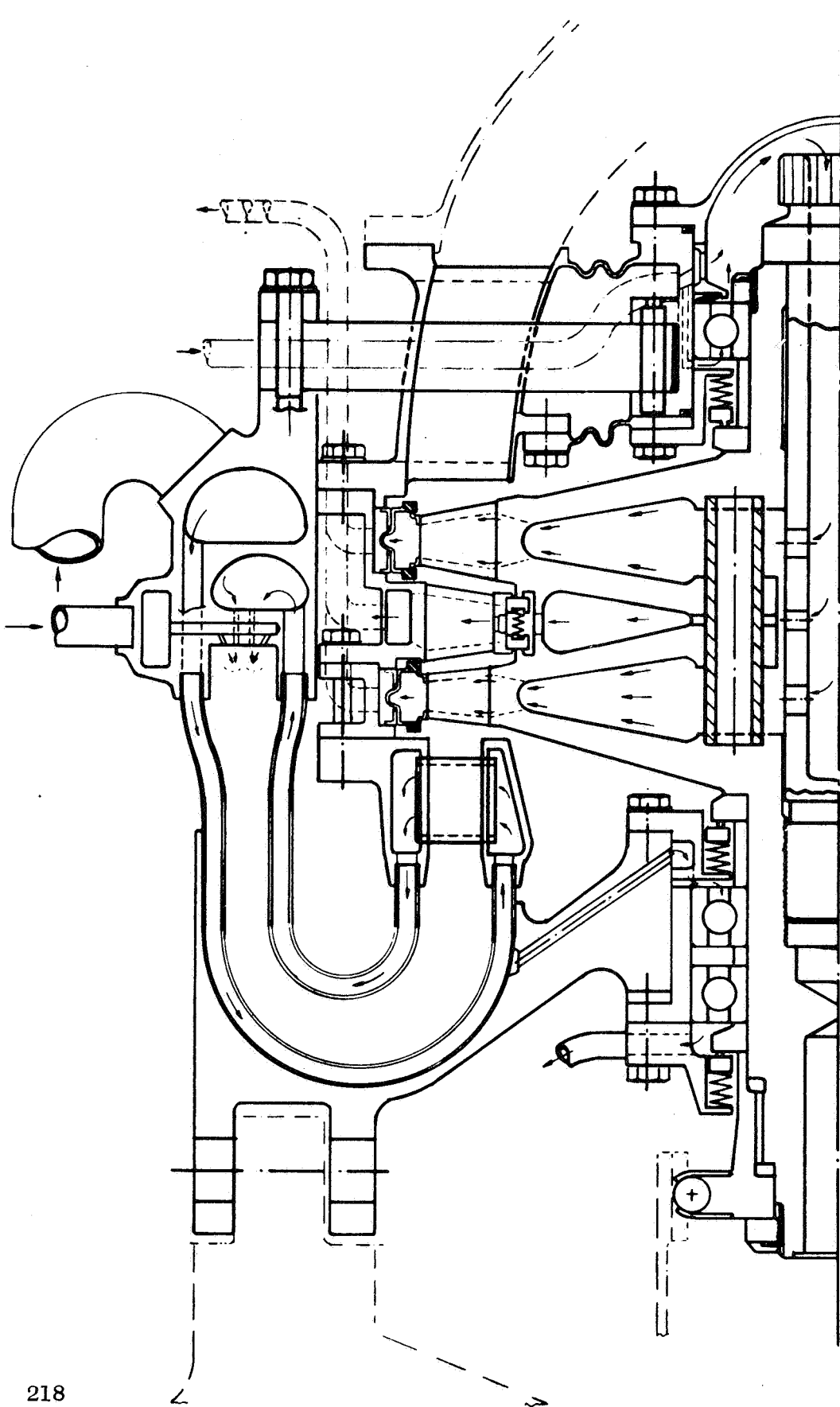


Figure 107. Schematic of a Hydrogen-Cooled Turbine

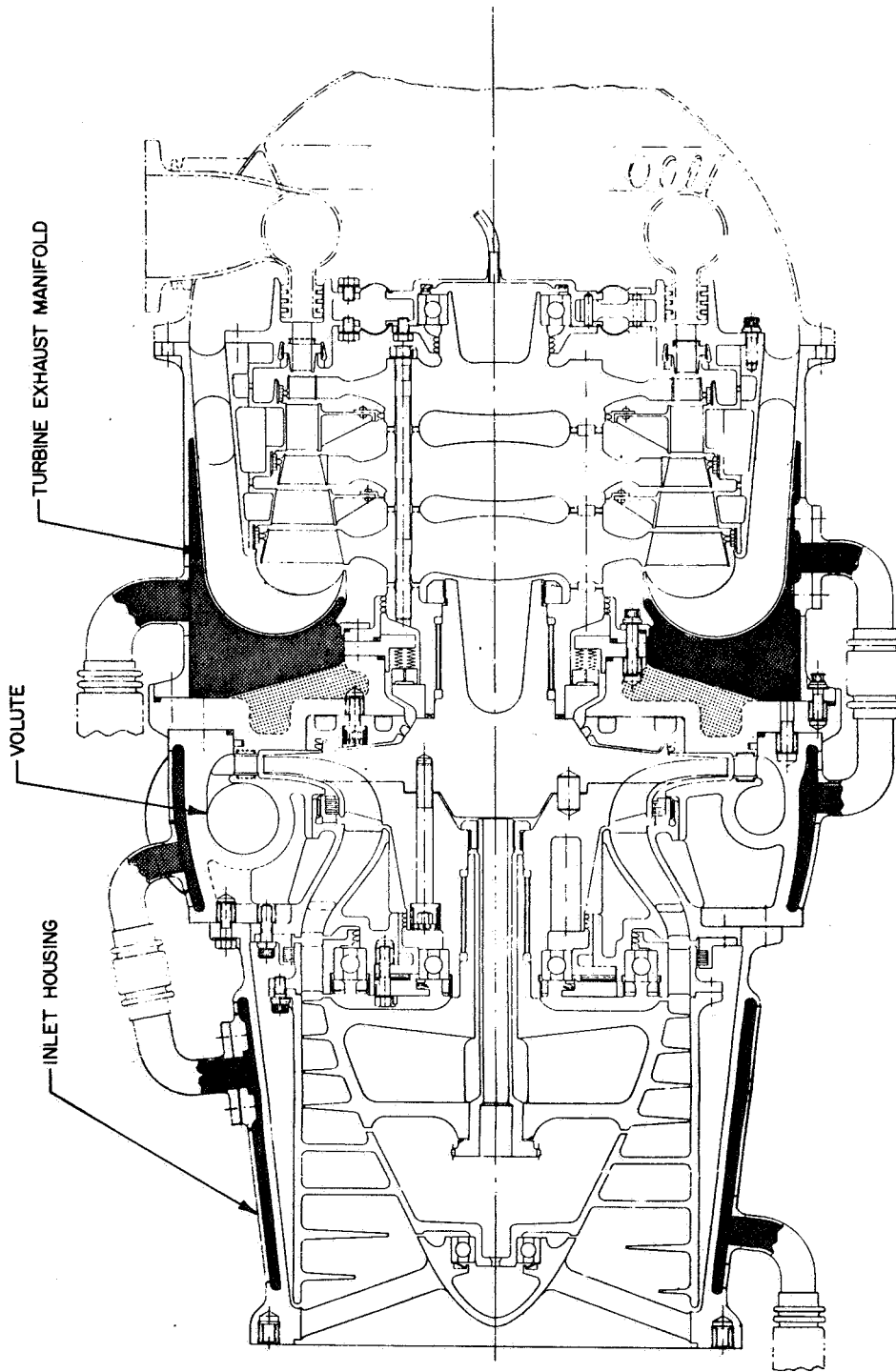


Figure 108. Cooling of Critical Turbopump Components: Inlet Housing, Volute, and Turbine Exhaust Manifold

### Thermal Barrier

Heat soakback from the hot-gas turbine can be prevented effectively with a thermal barrier (Fig. 109). Designed like a spacer, it is clamped between the turbine and the pump mounting flanges (Fig. 110). The thermal barrier is a manifolding device with internal passages through which cryogenic fluid is circulated. Generating a cold interface between the turbine and the pump, the fluid is passed continuously through the thermal barrier or after turbopump shutdown. Suitable materials for the construction of this barrier are aluminum, CRES, K-monel or titanium.

### Ball Spline Application

Separate shafts for the turbine and pump rotor are necessary if heat transfer from the hot turbine into the cryogenic pump is to be prevented. Although retractable spline couplings or face spline couplings could be used, a ball spline coupling offers several distinct advantages. This coupling (Fig. 111) is designed specifically for minimum surface contact during operation and is capable of transmitting high torque and accommodates misalignment due to thermal conditions. It is an ideal thermal barrier in that the balls, fitted relatively loosely in the retainer grooves, separate (fall away) themselves from the torque-contacting surfaces when the turbopump shuts down. The ball spline is constructed like a sprocket and can be made from ASI 9310 with the balls being similar to those in a ball bearing and are usually made from 440C steel.

### Thermal Separation of Turbine and Pump

In addition to the installation of a thermal barrier between the hot turbine and a cryogenic pump, additional thermal protection of the pump can be achieved by mechanical separation of the turbine and pump with a slotted

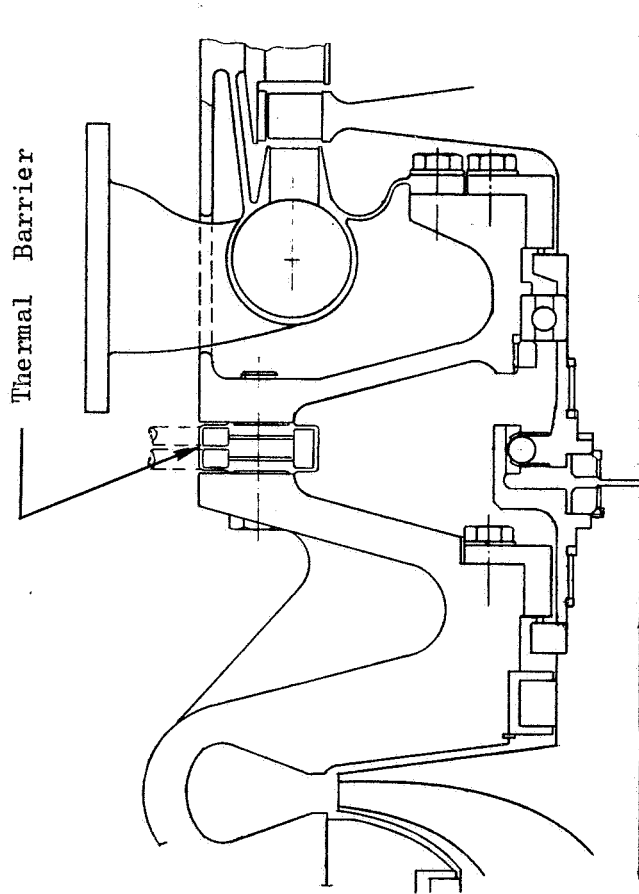
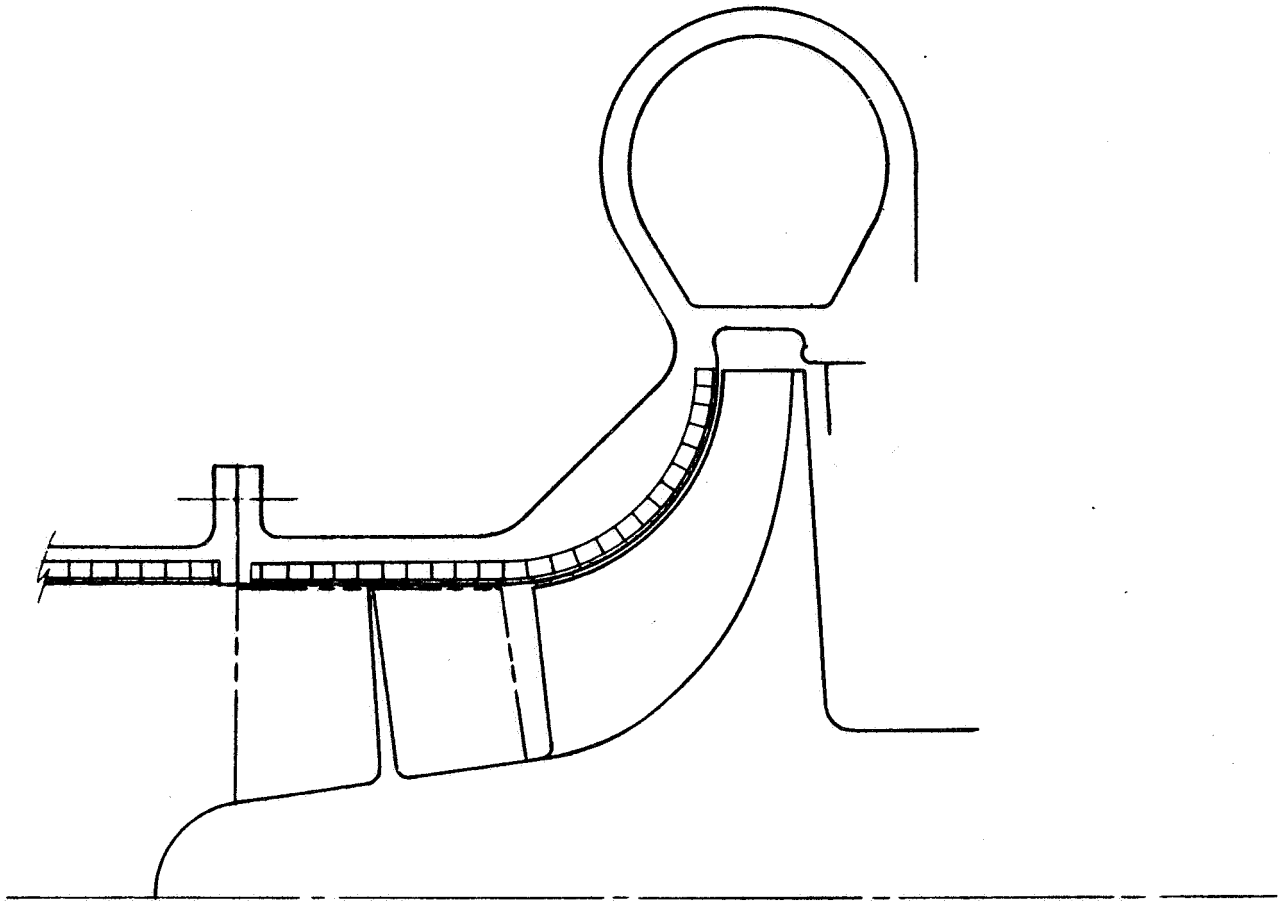
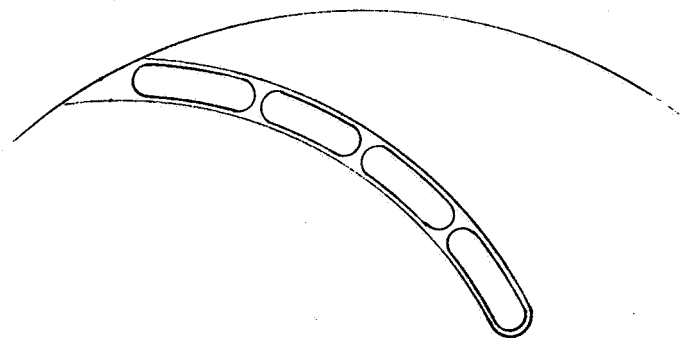


Figure 109. Thermal Barrier for Turbopumps



**PUMP WITH LOW HEAT CAPACITY  
FLUID FLOW SURFACES**



**VANE DETAIL**

**Figure 110. Schematic of Vented Flow Surface  
Liner and Vane**

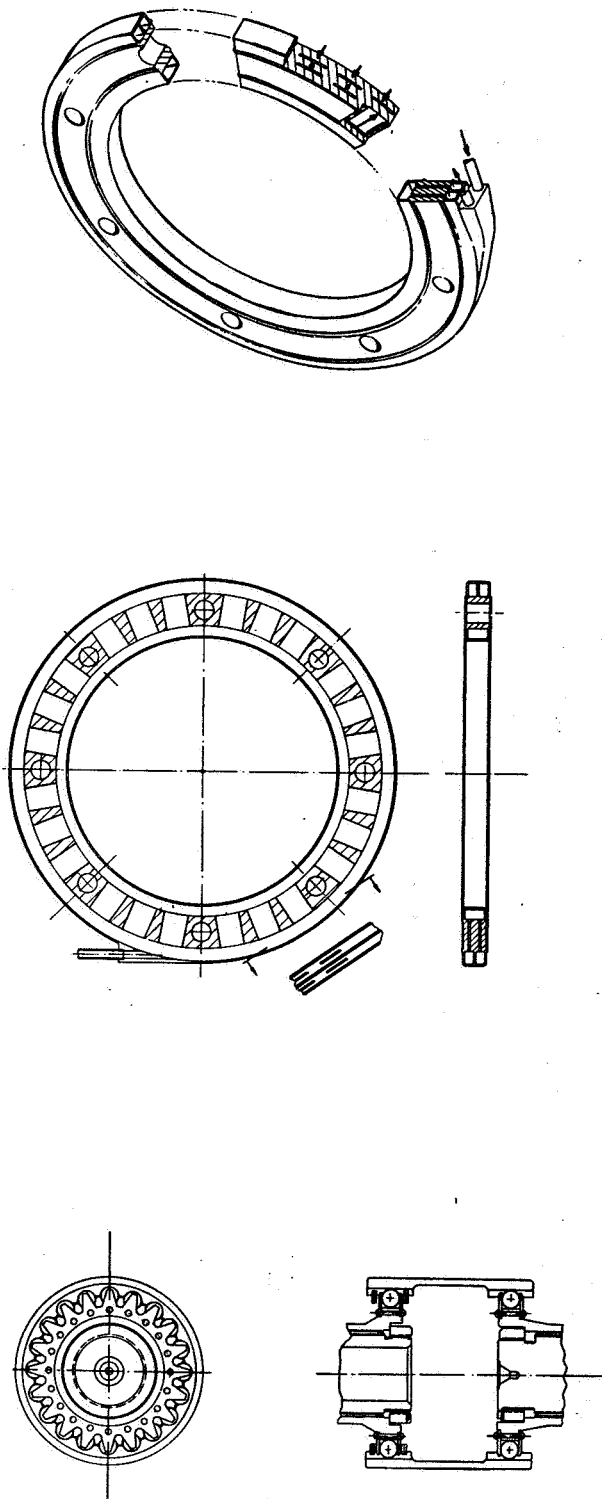


Figure 111. Regeneratively Cooled Thermal Barrier and Ball Spline Details

cylinder. Such a slotted cylinder will increase the thermal resistance; however it may increase the length of the turbopump assembly. Figure 112 illustrates this concept.

#### Coating and Insulation Methods for Pump Passages

To prevent liquid hydrogen from flashing into vapor as it enters a turbopump and contacts ambient-temperature metal surfaces, these materials may be treated by surface oxidization or covered with organic or inorganic low-conductivity coatings.

Metal surfaces may be treated by chemical or electrolytic oxidization, of which the latter is an anodizing process. Aluminum and its alloys may be anodized in chromic, sulfuric and oxalic acid electrolytes. A durable, porous surface will form as the result of such treatment with a porosity up to 20 percent and a potential unlimited growth in thickness. On the boundary between the porous growth and the metal, a very fine glass-like film forms which is of great hardness. The bonding strength of such an oxide film is very high, and a separation of this film from the metal is mechanically not possible. Study of the insulation thicknesses obtainable by this method is required.

The use of KX635 as an internal insulative coating had been evaluated in the "instant start" RL10 turbopump (Ref. 43). Components such as the impeller housings and impellers were coated and evaluated by actual pump tests. The capability of the coating material to withstand the initial thermal shock and the resistance to peeling makes this material an excellent candidate for further evaluation under full performance conditions.

The KX635 coating material (Fig. 113) has been extensively tested in the Rocketdyne Chemical and Nonmetallics section. KX635 is a glass microballoon-filled Kel-F dispersion material. Using KX635 as the coating material for

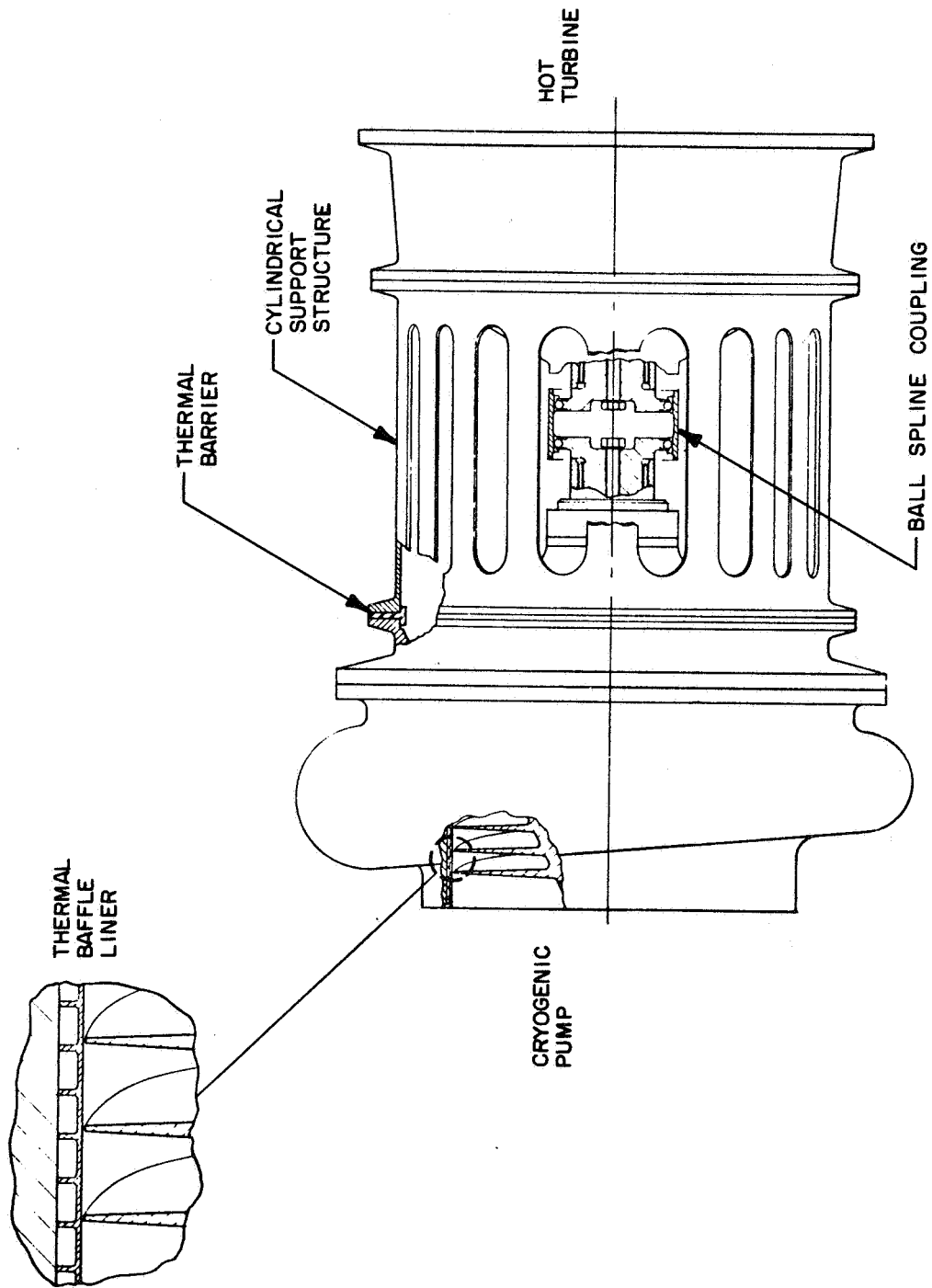


Figure 112 Thermal Isolation of Cryogenic Pump and Hot Turbine

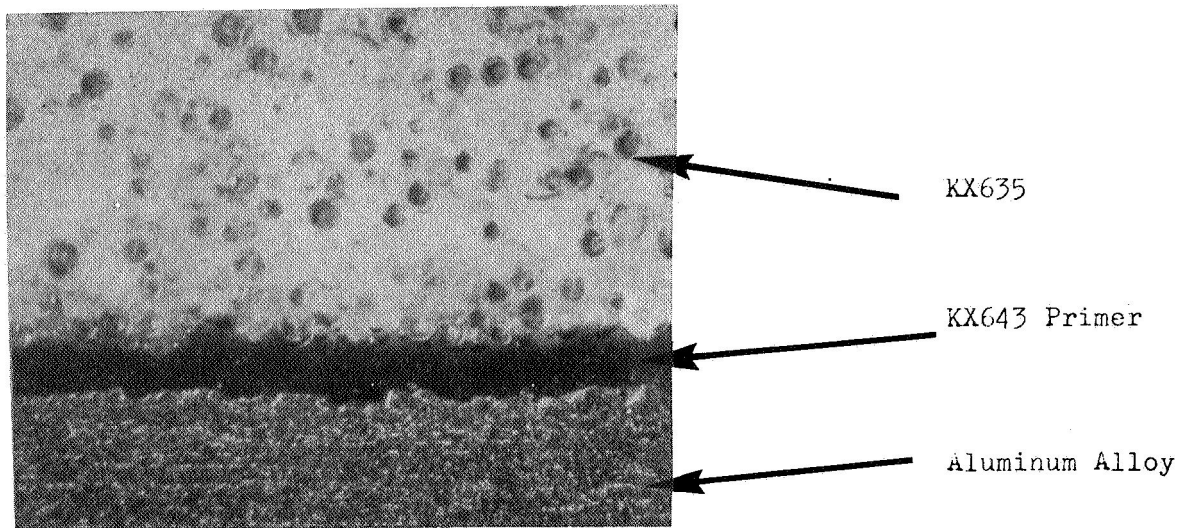
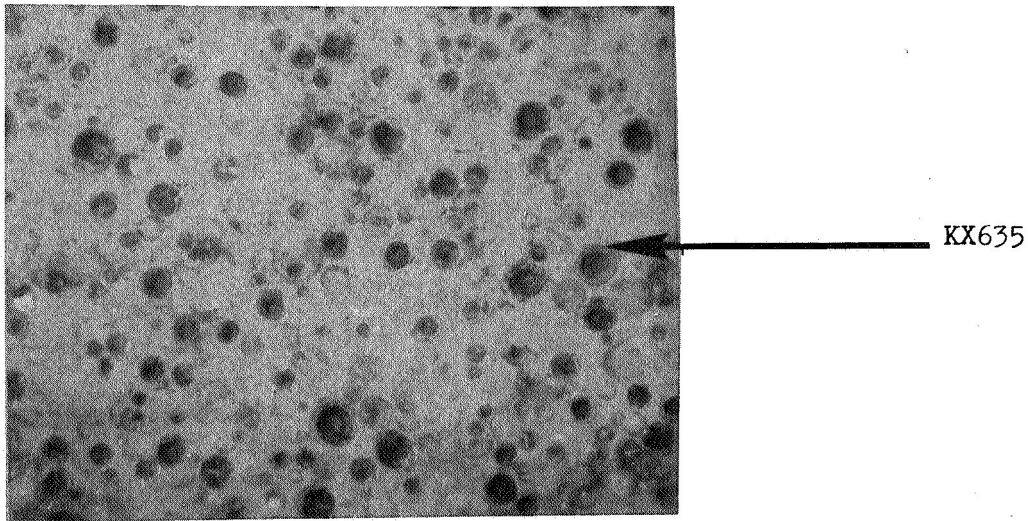
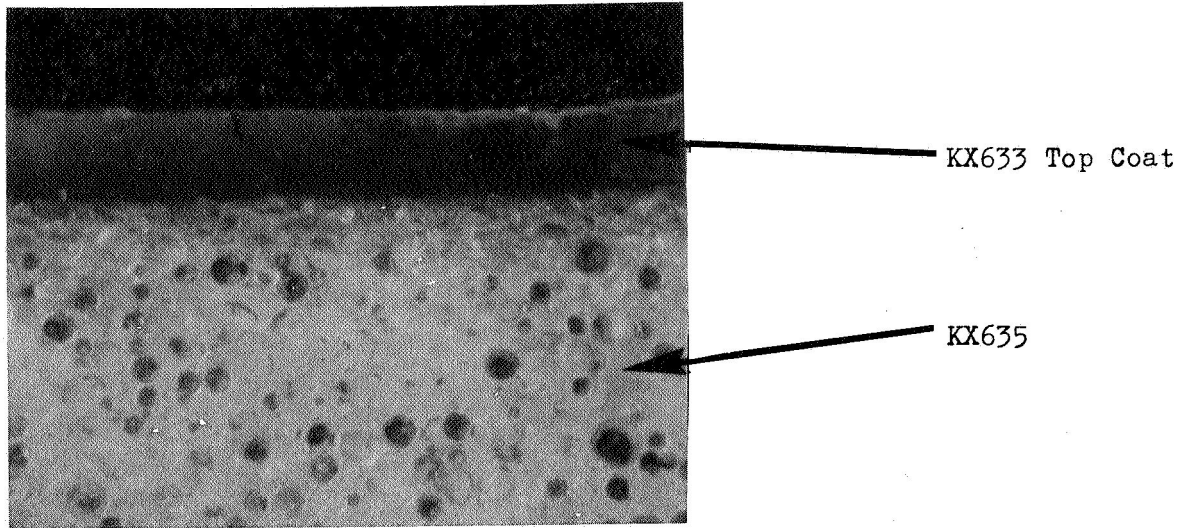


Figure 113. Photomicrograph (100X) of KX635 Coated Aluminum With Top Coat

internal turbopump components, the development and evaluation included in the following efforts:

1. Determination of the bond strength between KX635 and K-monel or Tens-50 aluminum by the methods described below:
  - a. Flexural fatigue life of coated-metal specimens at -320 F
  - b. Static tensile tests of coated-metal specimens at elevated, ambient and cryogenic temperatures
  - c. Cyclic thermal shock tests of coated MK-10 inlets from ambient to -320 F
2. Determination of the thermal contraction and thermal conductivity of KX635 from ambient temperatures to -423 F
3. Development and modification of coating processes that were compatible with the limitations imposed by the types of metals being coated
4. Detailed investigations into the causes for and the elimination of the variation in the KX635 materials used during this period of time
5. Investigations of the sensitivity of KX635 and its constituents to reactions with  $LO_2$

The summary of the program and the information obtained during the investigation of KX635 as an internal coating for liquid oxygen and liquid hydrogen turbopumps is described below.

Test specimens machined from K-monel and Tens-50 aluminum ranging in thickness from 0.065 to 0.140 inch with coating thicknesses from 0.020 to 0.180 inch were tested at ambient and cryogenic temperatures at 4300 cpm, using a specially modified deflection flexural fatigue machine. Total deflection ranged from 0.030 to 0.300 inch. The results of these fatigue tests, whereby the specimens were cycled  $1 \times 10^5$  at ambient temperature

from 0.030 to 0.300 inch and cycled  $1 \times 10^6$  at the cryogenic temperature of -320 F, 0.100 to 0.200 inch, indicated no separation between K-monel and KX635 and Tens-50 aluminum and KX635. Tensile tests were performed at 0.05 in/min at temperatures of 160, 75 and -320 F. The average elongation for KX635 or K-monel was 30, 26 and 12.5 percent, respectively. There was no separation between the KX635 and the Tens-50 or K-monel at any temperature. Cyclic thermal shock tests were performed with MK-10 and MK-15 fuel pump components such as inlets and stators coated with KX635. There was no visible indication of cracking or separation of the coating from the substrate. Thermal contraction data for the KX635 from 70 to -423 F are 0.00675 in./in. compared to 0.0108 in./in. for Kel-F 81. Thermal conductivity data for the KX635 from 150 to -400 F show that K decreases from 1.01 to 0.360 Btu-in./ft<sup>2</sup>-hr-F<sup>2</sup> over that temperature range.

An alternative method of lining the pump passages is with the application of a Kel-F and metal wire-enforced dispersion coating. The lining of the passages is accomplished by spot welding the wire mesh to the passage and then spraying the Kel-F with high pressure at elevated temperature. Final machining is done after the spraying and depositing operation. Samples of coatings of this type have been successfully fabricated.

#### Thermal Liner for Cryogenic Turbopumps

Lining the inlet line and the internal pump flow passages with a thin metal shell should definitely improve the warm-start capability of a cryogenic turbopump. The double-wall passage consisting of the outer structure and sandwich- or honeycomb-type construction of the inner liner separates the flow from the heavier metal walls. The thin liner contacted by the cryogenic flow will cool down very rapidly and because of its small cross section transfer little heat into the cryogenic propellant, thereby reducing the formation of vapor during start. Thermal exchange will take place gradually with a more uniform formation of vapor until thermal equilibrium is reached. The liner material should be titanium in combination with either a titanium or CRES or K-monel outer structure.

## TASK IV: STUDY OF EXISTING LH<sub>2</sub> PUMPS

A detailed examination of existing LH<sub>2</sub> pump designs was undertaken under Task IV study. This included characterization of the flow, geometrical and heat transfer parameters for available pump designs. Moreover, the J-2 MK 15 and a 350K pump were detailed and studied with the thermal analyzer program for startup and shutdown behavioral characteristics. Study of existing data for pump and turbine chilldown in orbit and under ground conditions was accomplished for the J-2 MK 15, M-1, and a 350K LH<sub>2</sub> turbopump.

Existing pump limitations were shown based upon restrictive pump flow areas and upon the choice of material for slow and fast chill circumstances.

### PUMP CHARACTERIZATION

Completion of characterization of both existing pumps and pump designs for geometric and flow parameters was accomplished during this study. In addition to tabulation of the operating conditions, the flow passage overall length to hydraulic diameter ratio from the inducer inlet to the outlet flange was determined for each of the pumps listed in Table 26. Discrete examination of the individual flow passages throughout each pump was also made.

Analysis of the mean velocity weighted on a length basis and evaluation of average pump Reynolds number, flow transit time, mean hydraulic diameter and mass velocity was completed for 12 LH<sub>2</sub> pumps and 6 LO<sub>2</sub> pumps. A summary of the characterization of the pumps for these parameters is listed in Table 27. The parameters were developed to provide an indication of the approximate average values for the pump nondimensional heat transfer parameters of Stanton number, Fourier number, Reynolds number, Biot number, and passage L/D ratio.

TABLE 26

## LIQUID HYDROGEN PUMPS

Data Reference Code Number	Pump Description
1	Inducer plus two centrifugal impellers (external preinducer submerged in propellant tank) All data estimated. Model RL-10
2	Inducer plus one centrifugal impeller (scale model)
3	Inducer plus seven axial stages. Model J-2
4	Preinducer plus inducer plus hydraulic turbine plus two centrifugal impellers (preinducer and hydraulic turbine are integral in pump). Model 30X
5	Inducer plus one centrifugal impeller. Model 29X
6	External preinducer and hydraulic turbine, plus inducer plus two centrifugal impellers (external hydraulic turbine feed line omitted). All data estimated.
7	Same as VI for main pump only. Inducer plus two centrifugal impellers. All data estimated.
8	Inducer plus four axial stages. Model 25X.
9	Inducer plus nine axial stages. All data estimated. Model M-1.
10	Inducer plus four axial stages (scale model).
11	Inducer plus four axial stages (scale model).
12	Inducer plus four axial stages (scale model).

TABLE 26A

## LIQUID OXYGEN PUMPS

Data Reference Code Number	Pump Description
1	Inducer plus two centrifugal impellers (external preinducer submerged in propellant tank). All data estimated. Model RL-10.
3	Inducer plus one centrifugal impeller. Model J-2.
4	Preinducer plus inducer plus hydraulic turbine plus one centrifugal impeller (preinducer and hydraulic turbine are integral in pump). Model 30X.
6	External preinducer and hydraulic turbine plus inducer plus one centrifugal impeller (external hydraulic turbine feed line omitted). All data estimated.
7	Same as VI for main pump only. Inducer plus one centrifugal impeller. All data estimated.
9	Inducer plus one centrifugal impeller. All data estimated. Model M-1.

TABLE 27

PUMP CHARACTERISTICS

IH <sub>2</sub> Pumps													LO <sub>2</sub> Pumps												
Code Number	Name	Type	Thrust, lb x 10 <sup>-3</sup>	Chamber Pressure, psia	Volume Flow (0) gpm	Weight Flow, lb/sec	Developed Head, feet	Developed Pressure, psi	Speed, rpm	Σ L/D, Mean Diameter, inches	Σ L <sub>i</sub> /V <sub>i</sub> /L <sub>b</sub> Mean Velocity, in./sec	Σ L <sub>i</sub> D <sub>i</sub> /L <sub>b</sub> Mean Diameter, inches	T <sub>1</sub> /V <sub>m</sub> Transit Time, T sec x 10 <sup>-3</sup>	V <sub>D</sub> /V <sub>m</sub> Mean, Re x 10 <sup>-6</sup>	ρ V <sub>mean</sub> ' lb-sec/in. <sup>3</sup> x 10 <sup>3</sup>										
1	PRWA RL-10	Centrifugal inducer plus two impellers	15	292	601	5.93	29,300	910	28,400	205.17	3873	0.7708	27.44	9.88	25.72										
2*		Centrifugal inducer plus one impeller	30	1000	1,089	10.75	49,700	1530	48,000	88.63	8326	0.8540	6.74	25.54	55.29										
3	MK 15-F	Inducer plus seven stages axial	200	630	7,830	77.3	38,970	1200	25,950	89.80	4189	1.4091	20.94	19.54	27.82										
4	MK 30-F*	Centrifugal with preinducer	250	1500	8,452	83.4	81,669	2550	36,000	90.70	3682	1.7971	31.58	23.09	25.78										
5	MK 29-F*	Inducer plus one impeller centrifugal	280	1000	12,000	118.5	49,700	1520	28,000	88.63	8326	1.4636	11.55	40.39	55.29										
6	High Pressure**	Centrifugal with preinducer	350	3000	11,392	112.5	193,535	5950	37,300	185.90	5083	3.2931	56.46	55.41	33.75										
8	MK 25-F*	Inducer plus four stages axial	365	1000	13,250	130.8	49,000	1510	30,000	65.26	5716	2.0111	12.77	38.05	37.96										
9	Aerojet M-1	Inducer plus nine stages axial	1500	1000	60,000	502.5	38,500	1800	13,225	107.56	6118	3.7770	38.25	76.49	40.63										
10*		Inducer plus four stages axial	1500	1000	54,450	537.7	49,000	1510	14,800	65.26	5716	4.0825	25.92	77.25	37.96										
11*		Inducer plus four stages axial	3000	1000	108,900	1075.5	49,000	1510	10,460	65.26	5716	5.7658	36.61	109.10	37.96										
12*		Inducer plus four stages axial	6000	1000	217,800	2151.0	49,000	1510	7,400	65.26	5716	8.1550	51.78	154.30	37.96										
7	High Pressure	Data for main pump only								150.23	8194	1.4715	18.36	39.91	54.41										
1	PRWA RL-10	Centrifugal	15	292	184.5	29.33	877	435	11,350	43.09	998	0.4190	30.66	1.62	106.78										
2		Centrifugal	200	630	2,870	466.2	1,780	885	8,008	51.88	1839	1.5924	38.93	11.37	196.82										
3	MK 15-0	Centrifugal with preinducer	250	1500	3,107	493.9	4,217	2090	25,000	53.76	1669	1.5929	43.32	10.32	178.58										
4	MK 30-0**	Centrifugal	350	3000	4,248	675.3	12,939	6420	22,500	98.63	1994	3.1068	77.09	24.03	213.32										
5	High Pressure***	Centrifugal	1500	1000	18,900	3004.5	3,070	1520	3,635	120.44	1869	5.6076	78.65	26.16	199.94										
6	Aerojet M-1	Centrifugal																							
7	High Pressure	Data for main pump only								61.11	3623	1.1327	16.48	15.92	387.61										

NOTE: For IH<sub>2</sub> Pumps: IH<sub>2</sub>: 36.7 B; P<sub>sat</sub> = 14.7; δ = 4.43 lb/ft<sup>3</sup>; ρ = 6.64 x 10<sup>-6</sup> lb-sec/in.<sup>4</sup>; 1/ν = 3.31 x 10<sup>3</sup> sec/in.<sup>2</sup>

For LO<sub>2</sub> Pumps: LO<sub>2</sub>: 162.3 R; P<sub>sat</sub> = 14.7; δ = 71.36 lb/ft<sup>3</sup>; ρ = 1.07 x 10<sup>-4</sup> lb-sec<sup>2</sup>/in.<sup>4</sup>; 1/ν = 3.88 x 10<sup>3</sup> sec/in.<sup>2</sup>

\*Latest State of the art

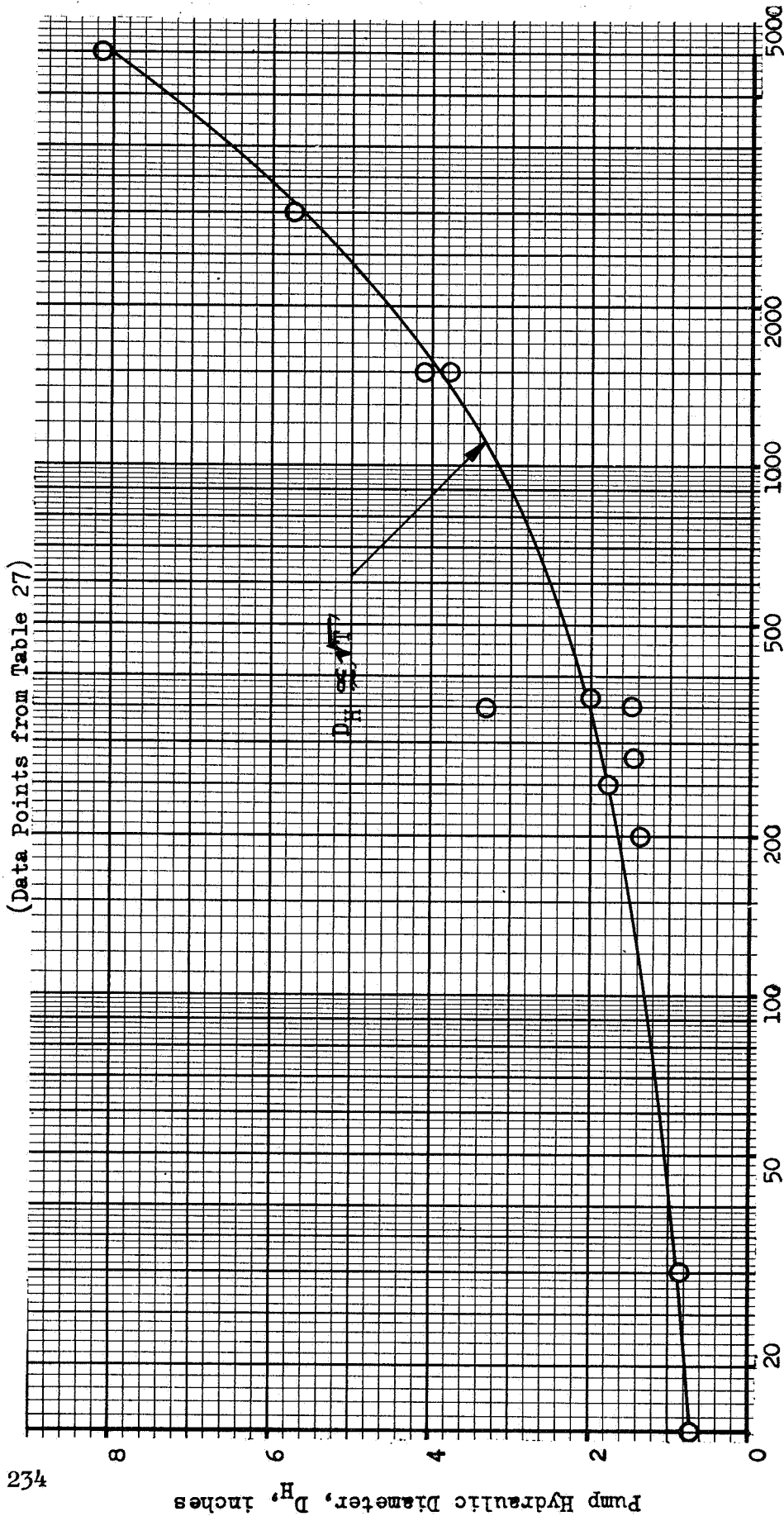
\*\*Preinducer and hydraulic turbine integral in pump, no external circuit required

\*\*\*Preinducer hydraulic turbine external feed circuit not accounted for in data shown

Analysis of the results illustrated in Table 27 illustrates that no specific trend of coolant passage L/D ratio is shown. Length-to-diameter ratio of the LH<sub>2</sub> pump passages ranges from a low of 65 to a high of 205, with the majority of pumps in the vicinity of L/D = 100. Mean pump velocity and fluid mass velocity were also seen to remain fairly constant over a wide thrust range. Passage mean hydraulic diameter and Reynolds number were graphed in Fig. 114 and 115 and illustrate an approximate square root dependence with thrust increase. Coolant transit time values as shown in Table 27 are quite small.

#### EFFECT OF ENGINE THRUST SIZE ON PUMP CHILLDOWN

The characterization of existing pump designs into the nondimensional heat transfer parameters of Fourier and Biot numbers was made based on mean pump wall thickness values and on an average velocity in the pump during an assumed 2.5-second start transient (50 percent of through flow velocity at full design speed). The purpose of this study was to establish thrust scaling rules with regard to pump thermal design. Figure 116 illustrates the average pump Biot number obtained for pump designs listed in Table 27 during the start transient without considering either pump material or operating pressure. The Biot number for all the pumps shown was found to be significantly greater than one, thus indicating that the hydrogen film-coefficient resistance is low with respect to the wall thermal conduction, and a rapid surface chilldown of the pump would result assuming pump toleration of vapor at start. A square root relationship of Biot number with thrust was found. Figure 117 illustrates the pump average Fourier number during the assumed 2.5-second start, and an inverse linear dependence of Fourier number with thrust was found. In a 2.5-second start period all but the smallest-thrust pumps are seen to have a Fourier number less than one. This indicates that for large pumps complete chilling of the wall will not occur during the start period, and heat will continue to bleed into the propellant during mainstage operation.



Thrust Level, pounds  $\times 10^{-3}$

Figure 114. Pump Mean Hydraulic Diameter vs Thrust Level

Data Points from Table 27  
 (Full Thrust Flow Conditions Assumed)

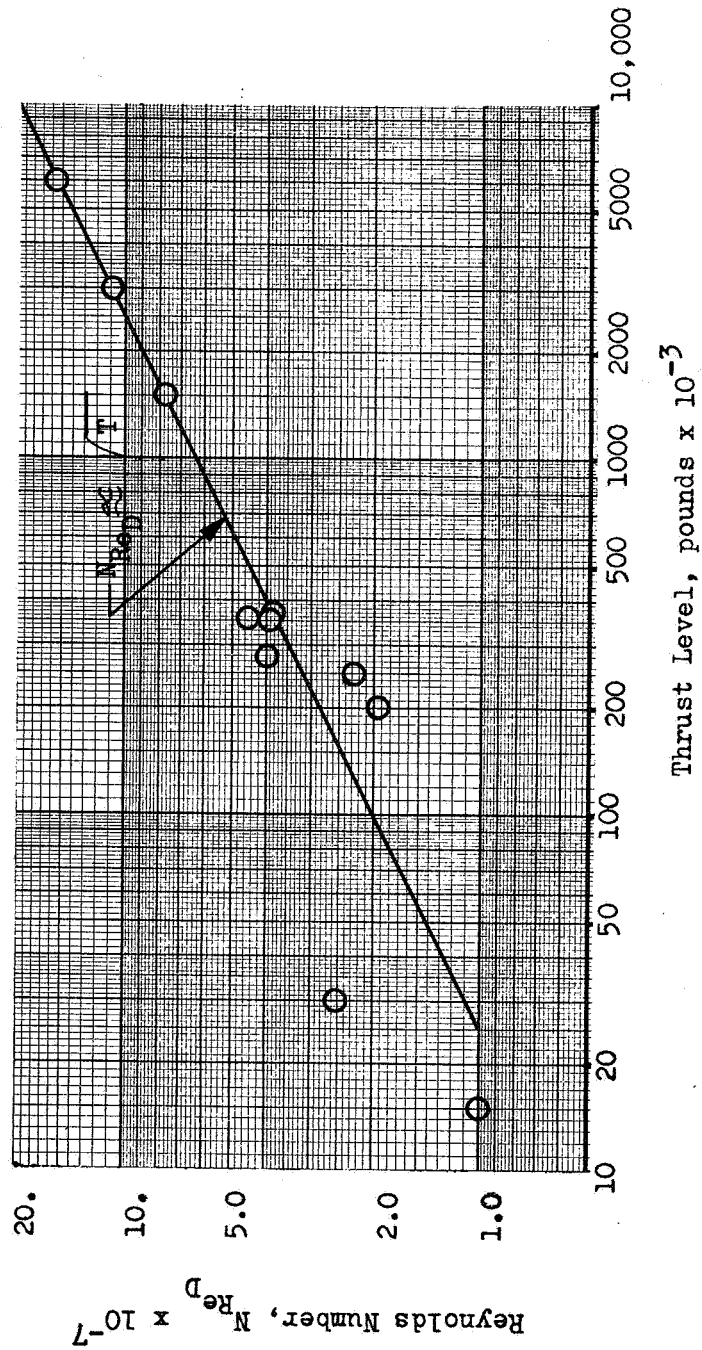


Figure 115. Pump Mean Reynolds Number vs Thrust Level

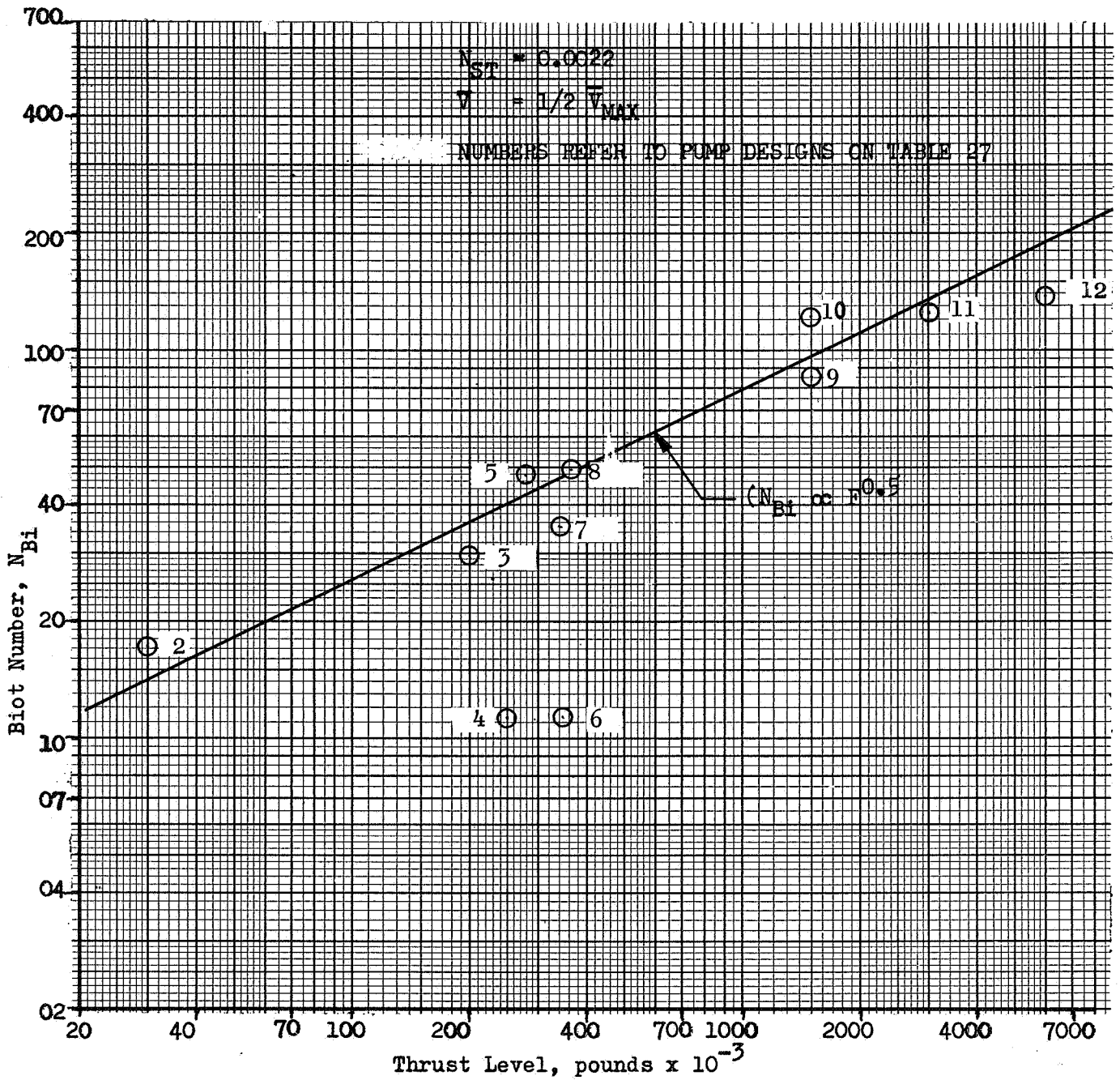


Figure 116. LH<sub>2</sub> Pump Average Biot Number vs Thrust Level

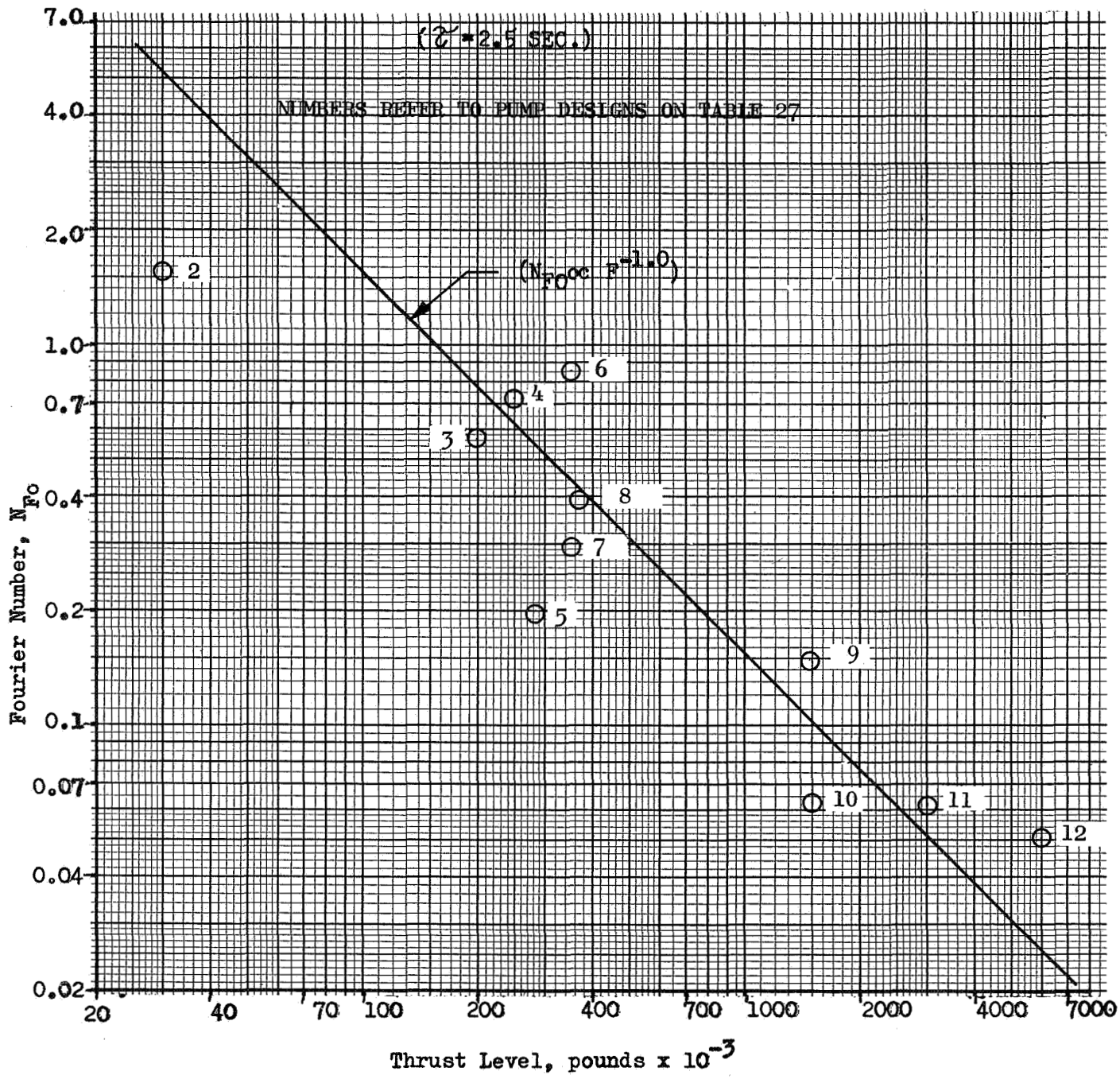


Figure 117. Average Fourier Number vs Thrust Level

The above analysis assumed neither a prechill prior to start nor a "thermodynamic" stall during the start transient. Within the simplifying constraint of using an average Fourier number, improvement in the pump warm-starting characteristics, i.e., a reduction in the film coefficient or Biot number, can be achieved by either enlarging the pump flow area or by reducing the length-to-hydraulic diameter ratios of the pump passages.

### Pump Blade Scaling

In the examination of the chilldown time requirements for axial flow pumps, attention was directed to the blading surfaces which provide the pressure rise. Rapid chilldown of the blade surfaces is required as a result for a nonprechilled pump in order to prevent blade stall induced by gaseous hydrogen vapor formation from the warm blade surface. A scaling of the following heat transfer related nondimensional parameters was considered for the J-2 type blade profiles typically illustrated in Fig. 118:

$$N_{Re}, N_{ST}, N_{Bi}, N_{Fo}, l/t$$

For the definition of the approximate value of these parameters a selection of a typical axial flow machine blade was made. Velocity change of the fluid with respect to the blade along the blade surface length was assumed as shown in Fig. 119. For approximate analysis purposes a 50 percent of rated-flow velocity was considered as representing the transient start period average velocity condition. For nonlinear pump start conditions an alternative average-velocity weighting factor can be employed.

### Blade Reynolds Number Scaling

For blade Reynolds number scaling the length dimension chosen was the half-chord length. The reference viscosity chosen was a liquid value at inducer

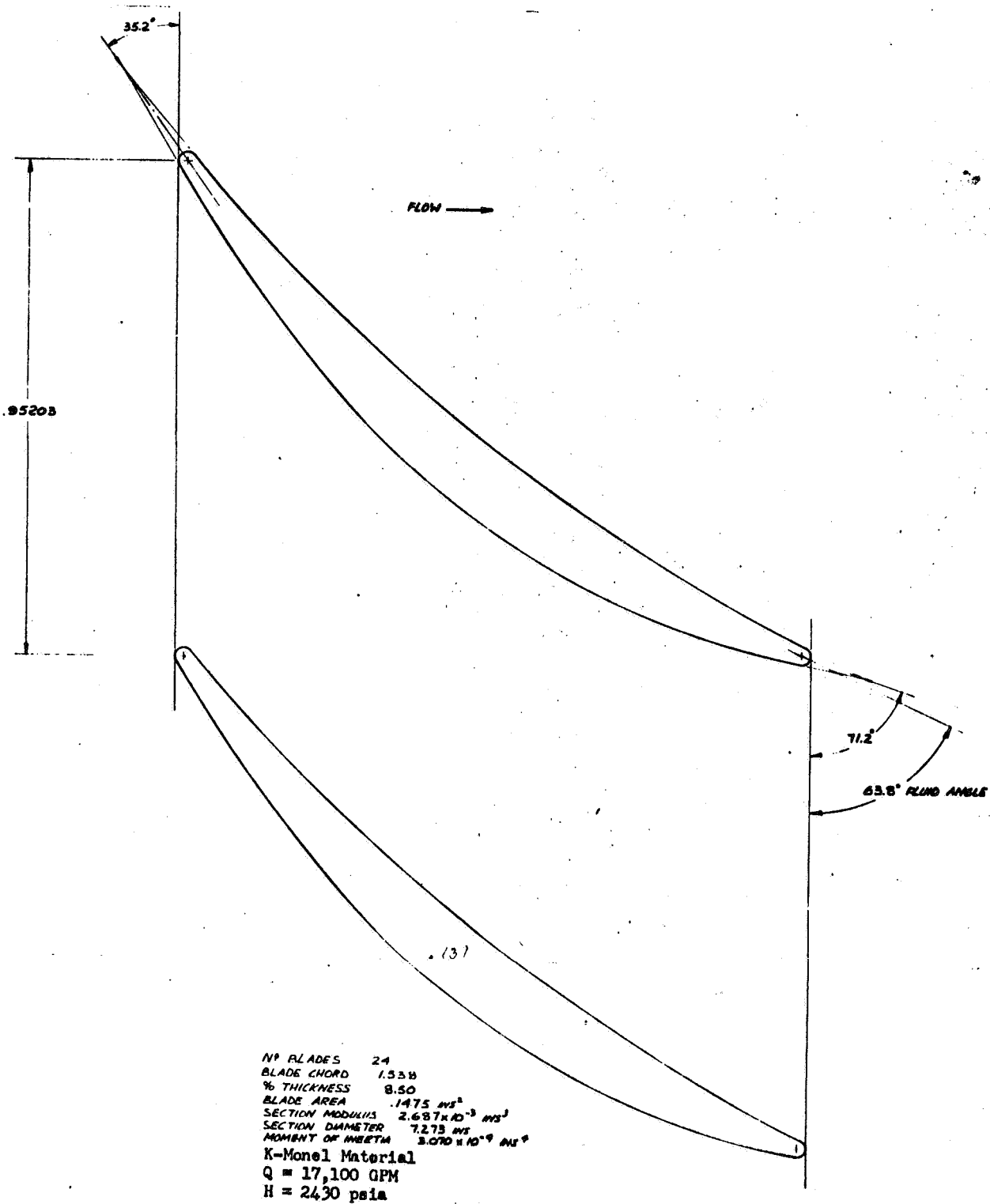


Figure 118. Turbopump Stator Blade

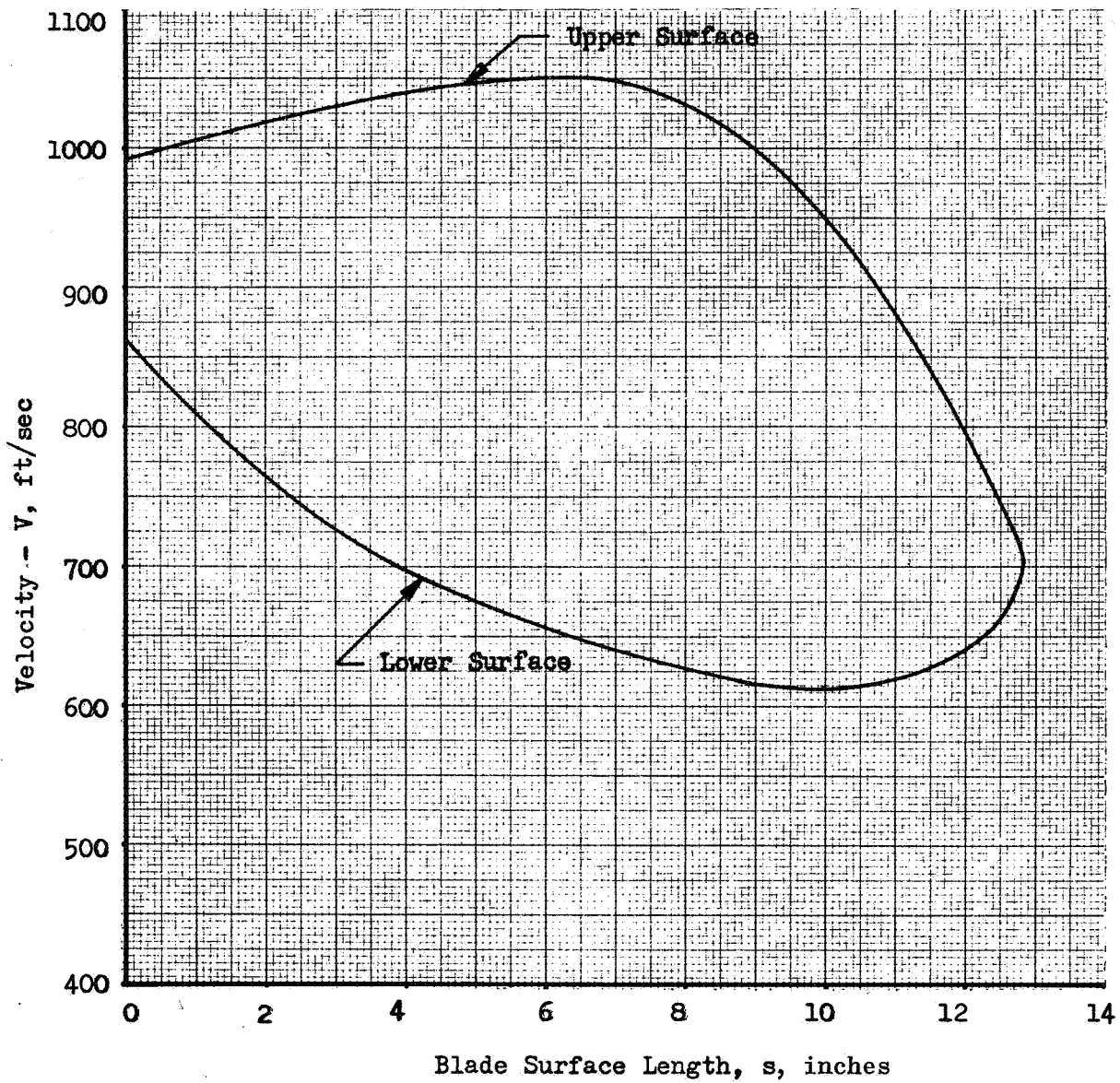


Figure 119. Typical Rotor Tip Blade Surface Velocities

pressure conditions. The blade chord length for an axial flow machine is found to scale according to the following relationship:

$$\frac{l_c}{2} \propto \sqrt{T} \quad (118)$$

As a result the blade Reynolds number can be shown to scale with thrust as

$$N_{Re} = \frac{\rho_\infty V_\infty (l_c/2)}{\mu} \propto \sqrt{T} \quad (119)$$

For nearly all machines the free stream mass velocity remains nearly constant with thrust.

#### Stanton Number Scaling

The Stanton number based on a chord length Reynolds number may be described as

$$N_{ST} = \frac{h}{\rho_\infty V_\infty C_p} \propto N_{Re}^{-0.2} \quad (120)$$

#### Fourier Number Scaling

Evaluation of the Fourier number variation with thrust was made considering an equal pump start time for small and large thrust pumps as a reference 5-second value. During further analysis, refinement of this assumption will be made. Basing the critical dimension on the half-blade thickness,

$$N_{Fo} = \frac{\alpha \tau}{(t/2)^2} \quad (121)$$

a variation of the blade thickness with thrust from above results in a first order dependence as

$$N_{Fo} \propto T^{-1.0} \quad (122)$$

It may as a result be seen that larger axial flow machines will have a slower blade chilling time compared to small thrust machines.

#### Blade $l/t$ Ratio Scaling

The blade length to thickness ratio for axial flow pumps remains the same with thrust scaling due to a square root dependence of both the length and thickness with thrust. Therefore,

$$\frac{l}{t} = \text{constant} \quad (123)$$

As a result the Stanton number dependence upon thrust becomes

$$N_{ST} \propto T^{-0.1} \quad (124)$$

#### Biot Number Scaling

The Biot number represents the ratio of the applied film coefficient to the blade internal conduction ability. For the analysis the characteristic dimension chosen was the half blade thickness at the maximum thickness point due to the fact that flow is occurring over the upper and lower surfaces and because the thickest point in the blade chills the slowest. Describing the Biot number as

$$N_{Bi} = \left( \frac{h (t/2)}{k} \right) \quad (125)$$

and considering from the Stanton number and blade geometric relationships

$$h \propto T^{-0.1} \quad (126)$$

$$t/2 \propto T^{0.5} \quad (127)$$

the scaling of the Biot number becomes:

$$N_{Bi} \propto T^{0.4} \quad (128)$$

In summary the parameter dependences with thrust level is shown below:

$$N_{Re} \propto T^{0.5} \quad (129)$$

$$N_{ST} \propto T^{-0.1} \quad (130)$$

$$N_{Bi} \propto T^{0.4} \quad (131)$$

$$N_{Fo} \propto T^{-1.0} \quad (132)$$

$$l/t \propto T^0 \quad (133)$$

Variations of these parameters with thrust level based on a J-2 reference blade is shown in Fig. 120 and 121. Consideration of the degree of blade chill accomplished within the start period can be categorized, in terms of Biot and Fourier numbers, into a slow and moderate fast-chill circumstance as illustrated below:

$$N_{Bi} N_{Fo} \approx 1.0 \quad \text{slow chill} \quad (134)$$

$$N_{Bi} N_{Fo}^{1/2} \approx \sqrt{\frac{e}{\pi}} \quad \text{moderate chill} \quad (135)$$

$$N_{Fo} \approx \frac{e^2}{\pi} \quad \text{rapid chill } (N_{Bi} > 1.0) \quad (136)$$

Critical Dimension: Half Chord Length  
 Propellants =  $O_2/H_2$   
 Mixture Ratio = 5:1  
 Specific Impulse = 426 seconds  
 Zero Surface Roughness

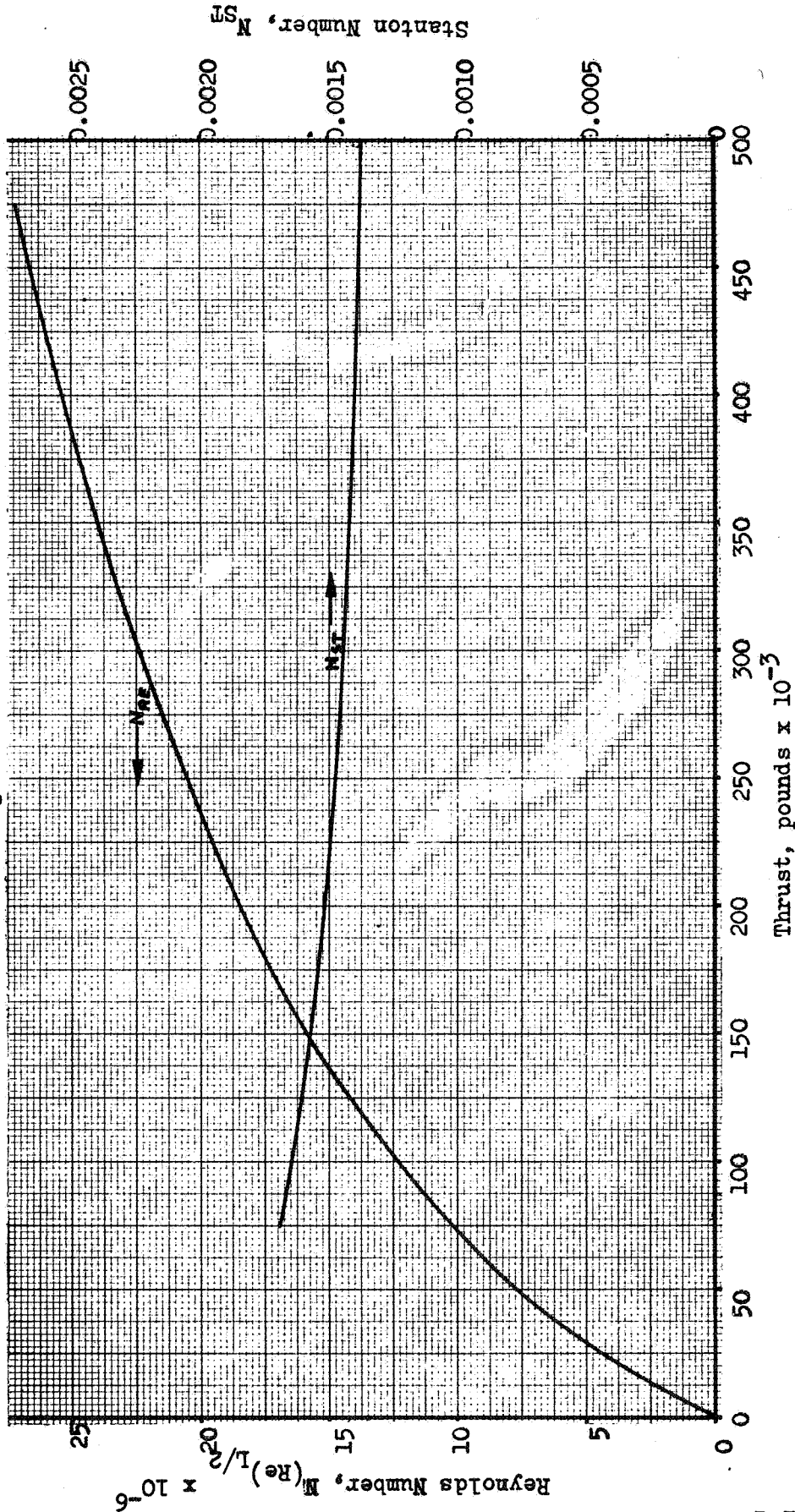


Figure 120. Axial Pump Blade Scaling: Reynolds Number and Stanton Number

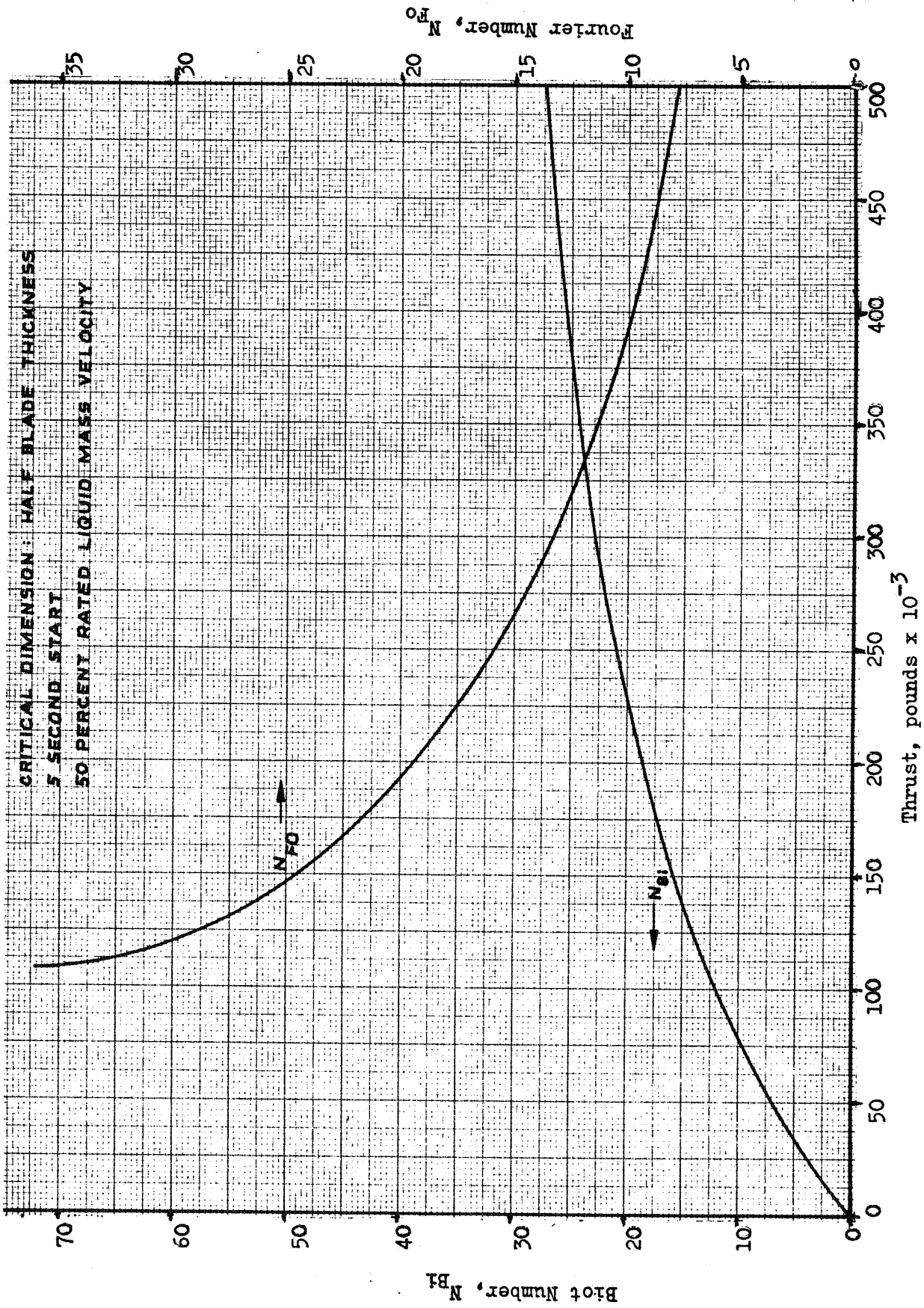


Figure 121. Axial Pump Blade Scaling: Biot and Fourier Numbers

From the large values of Biot and Fourier number calculated for the blading it is apparent that rapid chilling of the axial pump blades occurs unless upstream conditions result in low-density warm hydrogen flowing over the surfaces.

Treatment of the centrifugal flow pump impeller and pump inducers can be made to indicate the severity of thrust scaling problem for the centrifugal pump. A first examination indicates approximately the same Reynolds and Stanton number behavior. Biot and Fourier numbers become strongly dependent upon specific design impeller pressure wall thicknesses. It is expected that in general the above scaling approaches for these latter two non-dimensional parameters will apply for centrifugal pump impellers.

#### ORBITAL PRECONDITIONING OF J-2 TURBOPUMP

Telemetered data for engine J-2019 during orbital flight AS-203 was examined to determine the J-2 turbopump chilldown characteristics during flight. The fuel side instrumentation and prefill flow circuit used in this flight are illustrated schematically in Fig. 122. The electrically driven recirculation pump circulates fuel from the tank, into the main fuel line (downstream of the main fuel pre valve), through the fuel pump, into the return line at the main fuel pump discharge, and back into the tank. The recirculation pump is put into operation 5 to 10 minutes before engine start. During the flight the conditions of the fuel and the fuel circuit components were monitored by the instrumentation.

The telemetered data for the initial four-orbit, 6-hour period of flight AS-203 are presented in Fig. 123 and 124. The instrumentation code shown corresponds to that indicated in Fig. 122. During the first orbit, after the J-2 second-stage shutdown, heat inputs by conduction from the warm turbine and by solar radiation raised the LH<sub>2</sub> pump discharge temperature

Orbital Flight AS-203  
 Engine J2019  
 Date: 5 July 1966

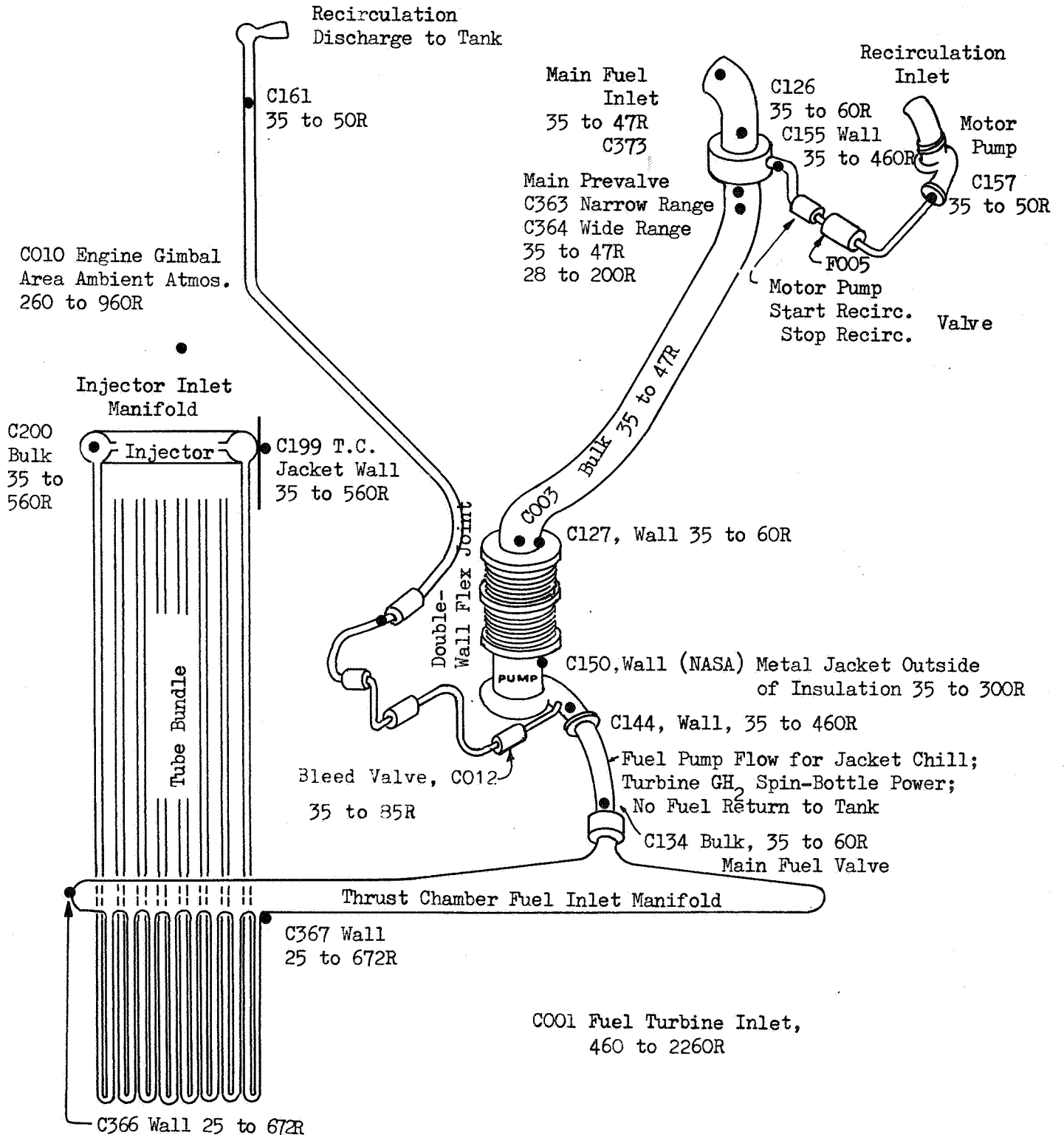


Figure 122. Orbital Flight AS-203 Code Schematic, Code: C = Temperature; F = Flow, Fuel Side

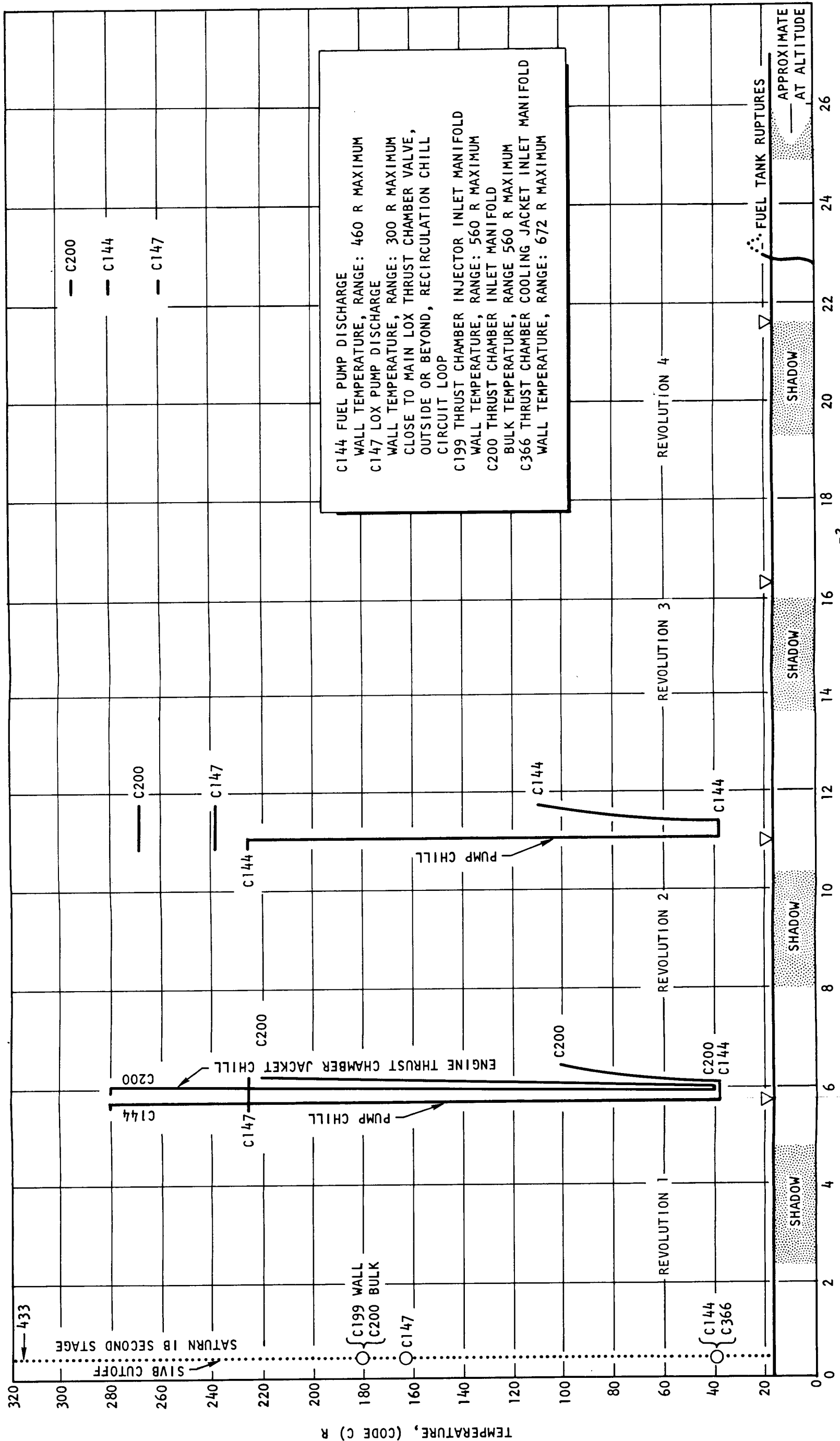


Figure 123. Pump Temperature History for Saturn Orbital Flight AS203

248A

FOLDDOUT FRAME

FOLDDOUT FRAME



from 163 to 226 R. During the early part of the second orbit (at approximately 5600 seconds after liftoff), the fuel preconditioning recirculation pump was operated for approximately 6 minutes and the LH<sub>2</sub> pump discharge temperature was returned to a temperature of 38 R. During the remainder of the second orbit the LH<sub>2</sub> pump reconditioning process was repeated, and the temperature was returned to near storage tank temperature of 40 R. At the end of the fourth orbit both the LH<sub>2</sub> and LO<sub>2</sub> pump discharge wall temperatures were nearly of equal value at 280 and 260 R, respectively.

From flight results, the heating up of the turbopumps, due to solar radiation and turbine heat soakback of approximately 240 R temperature rise for the LH<sub>2</sub> pump and 100 R temperature rise for the LO<sub>2</sub> pump, would require pump preconditioning if the engine were to be restarted.

From additional telemetered data on the fuel and oxidizer turbine housing thermocouples, a graph of the turbine temperature vs time is shown in Fig. 125. With a four-orbit period, radiation and conduction of heat accomplished reduction in turbine temperature to nearly equilibrium temperature. Engine gimbal area ambient temperatures were taken as the equilibrium temperature (-90 F).

Figure 126 illustrates the radiation equation solution (Eq. 14) of the chill-down compared to orbital data. A longer period of time is predicted from analysis due to conduction to the cold adjacent pump and conduction to radiation from the turbine ducting. A comparison of the LO<sub>2</sub> pump chilldown illustrates much closer agreement of the analytical and experimental chilldown curve due to an apparent lesser heat conduction to the pump and lines (Fig. 127).

Comparison of the ground operation cooldown temperature vs time for the turbopump is shown in Fig. 128. A considerably shorter time period of equilibrium results due to combined radiation and forced convection due to air circulation. As a result it is apparent that ground simulation studies of turbine chilldown would be inadequate for prediction of flight conditions.

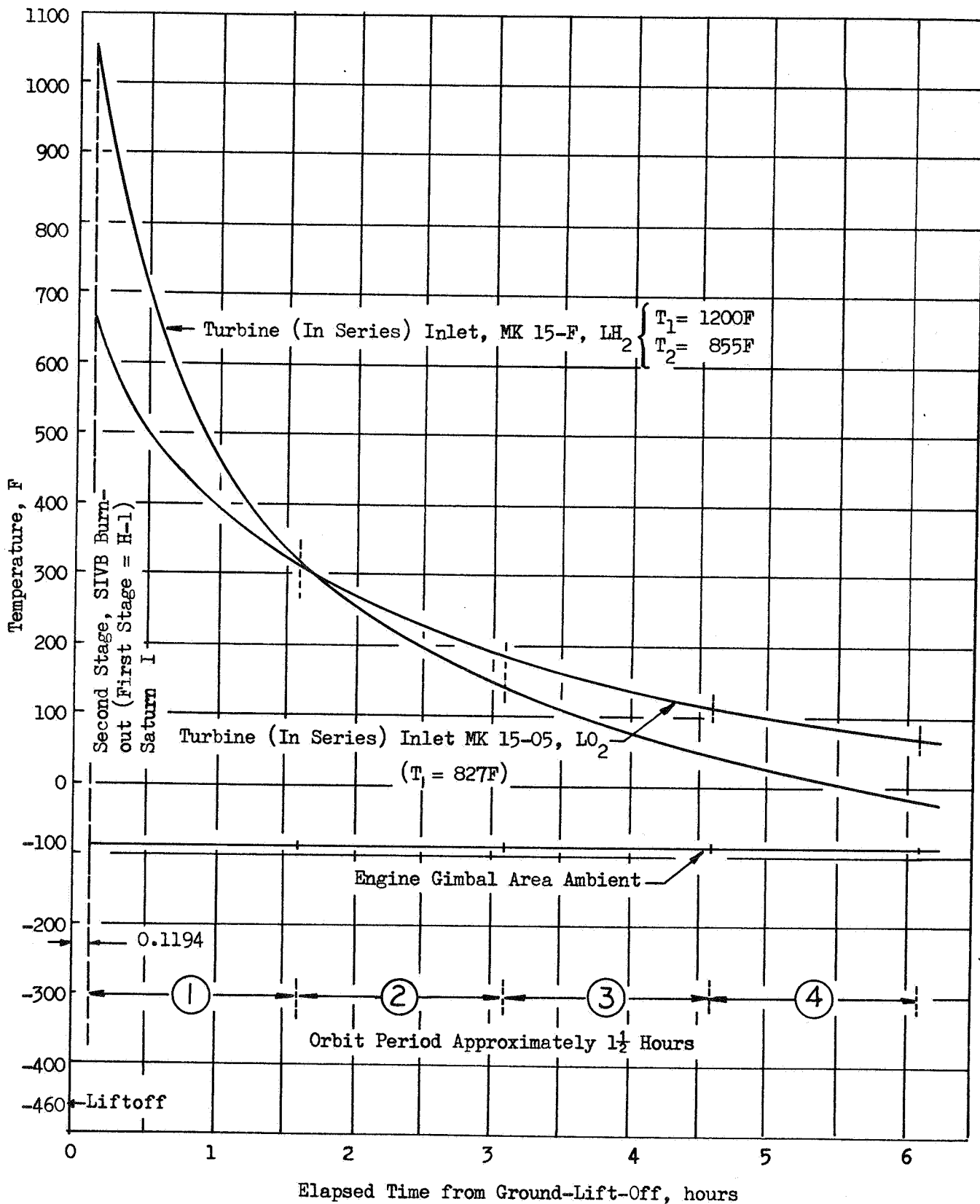


Figure 125. Orbital Flight AS-203, Engine J2019, Date 5 July 1966

$$T_i = 1570 \text{ R} \quad T_s = 370 \text{ R}$$

Fuel Turbine

$W = 151 \text{ lbs}$

$A_s = 283 \text{ in.}^2$

$\epsilon = 0.80$

$F = 1.0$

(Conduction to Pump and Lines Neglected)

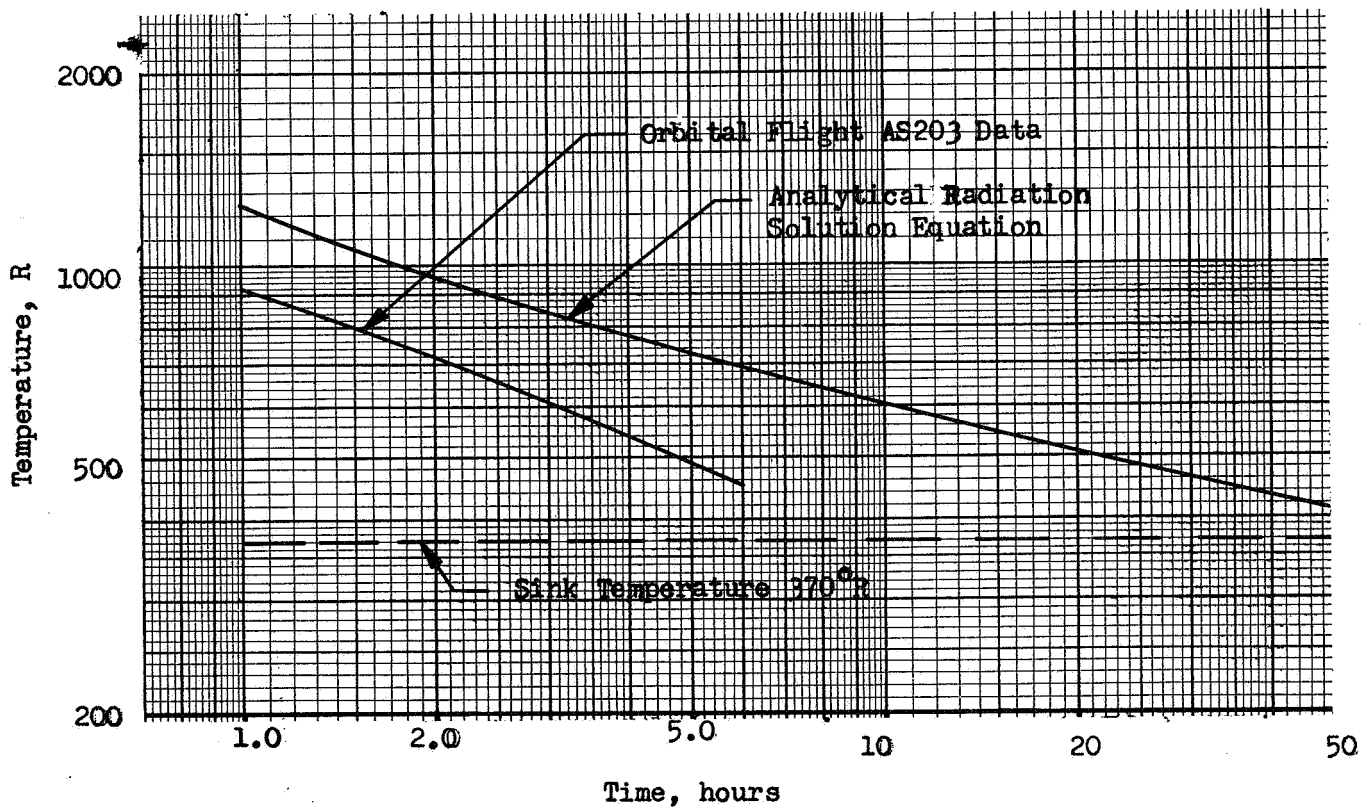


Figure 126. J-2 Turbine Cooldown Temperature vs Time

$$T_i = 1260 \text{ }^\circ\text{R} \quad T_s = 370 \text{ }^\circ\text{R}$$

LO<sub>2</sub> Turbine

$$W = 129 \text{ lbs}$$

$$A_s \approx 378 \text{ in.}^2$$

$$\epsilon = 0.8, F = 1.0$$

(Conduction to Pump and Lines Neglected)

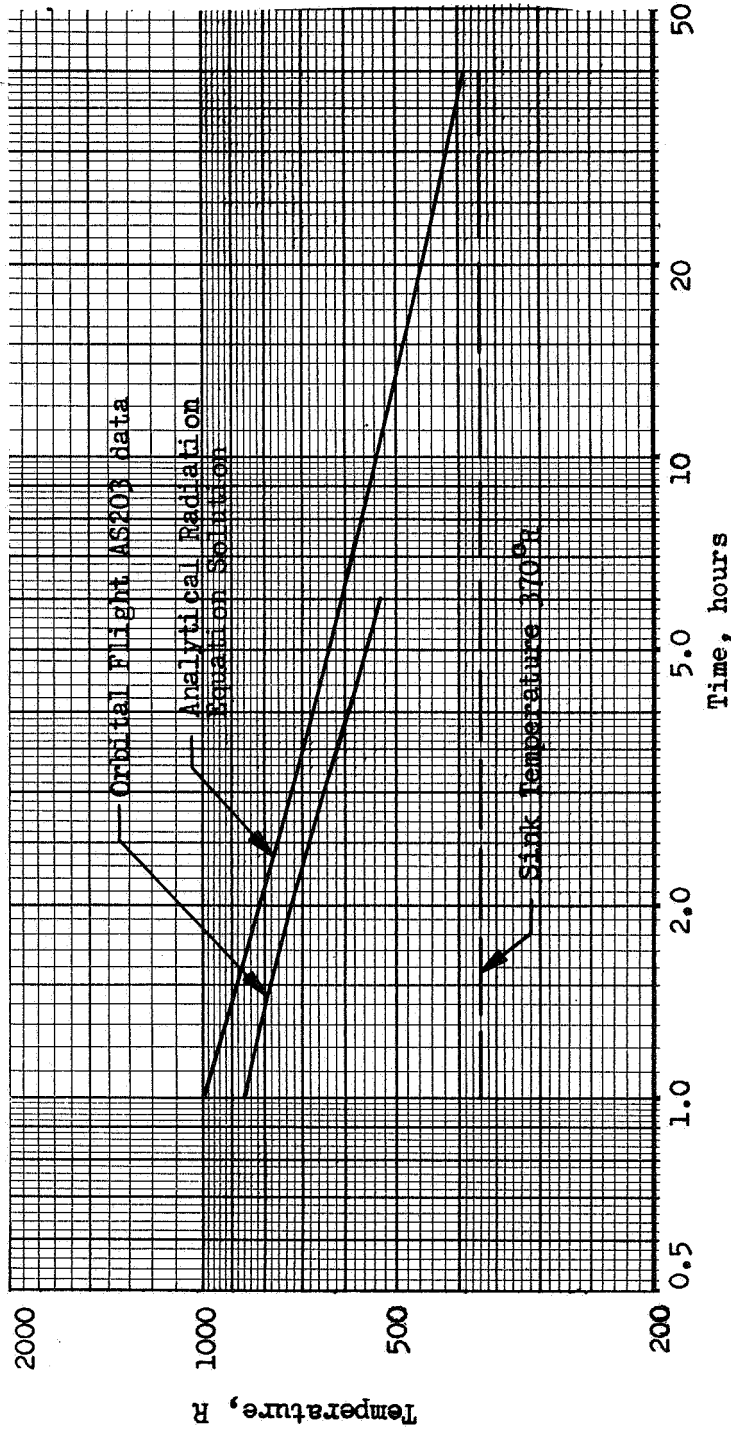


Figure 127. J-2 Turbine Cooldown Temperature vs Time

Steady-State Gas Temperatures at Cut-Off, F

- (1) 1200 °F
- (2) 855 °F
- (3) 827 °F
- (4) 710 °F

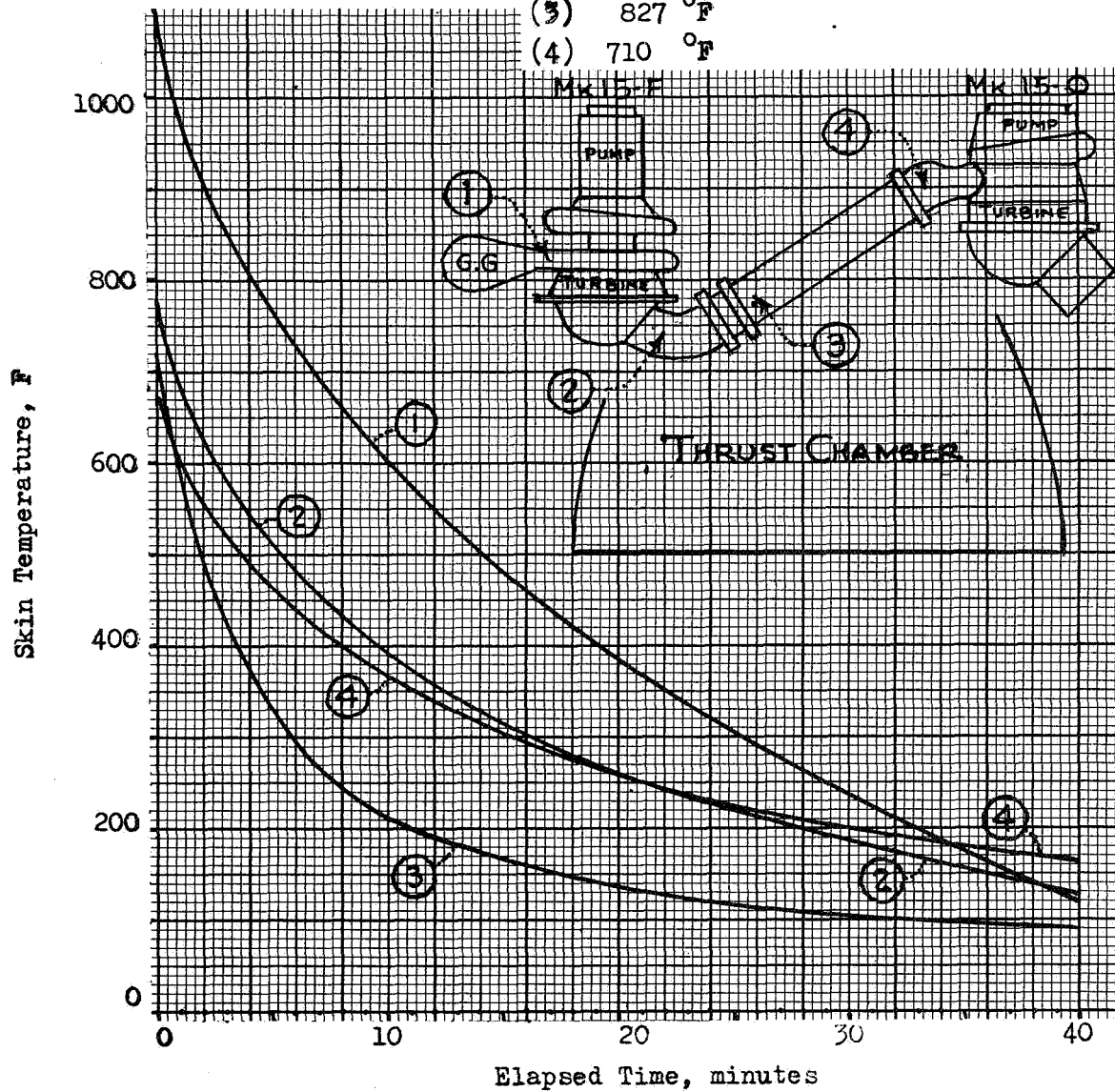


Figure 128. J-2 Turbopumps, Engine Test, Skin Temperatures at Sea Level Ambient, Average of 4 Tests

## MARK-15 LH<sub>2</sub> TURBOPUMP HEAT SOAKBACK ANALYSIS

The thermal analyzer described previously was utilized to determine the temperature distribution in the Mark-15 turbopump after 500 seconds of test firing.

In these analyses, forced convection heating of turbine blades and turbine parts, forced convection cooling of pump parts, radiation from the turbine hot casing, and conduction were considered. The results of these analytical heat transfer studies were in very good agreement with temperature of various locations measured during a 500-second test. Using these initial temperature distributions, the thermal analyzer was further used to study the heat soakback condition of the Mark-15 LH<sub>2</sub> turbopump. To avoid excessive computer machine run time, the complex geometry of the J-2 turbopump was simplified by lumping small adjoining parts (using weighted average thermal properties). For the larger parts, such as turbine wheels and pump rotor, tables of physical properties covering the temperature range of interest were used. Figure 129 shows the J-2 axial flow turbopump with its nodal points as used in the thermal analyzer. Figure 130 depicts the results of the heat soakback analysis for a period of 18 hours after turbopump shutdown.

As it can be seen, the temperature gradient is very steep at the beginning of the heat soakback, but as the time increases the temperature throughout the turbopump tends to become uniform. After 18 hours of heat soakback time, the temperature variation is approximately 130 F (approximately 50 F at the pump inducer and rotor and approximately 180 F in the turbine wheel regions). The heat soakback rate is very low after approximately 18 hours due to the low-temperature driving force. The highest final equilibrium temperature is estimated to be approximately 100 F. As the shutdown period increases above that required for the establishment of the

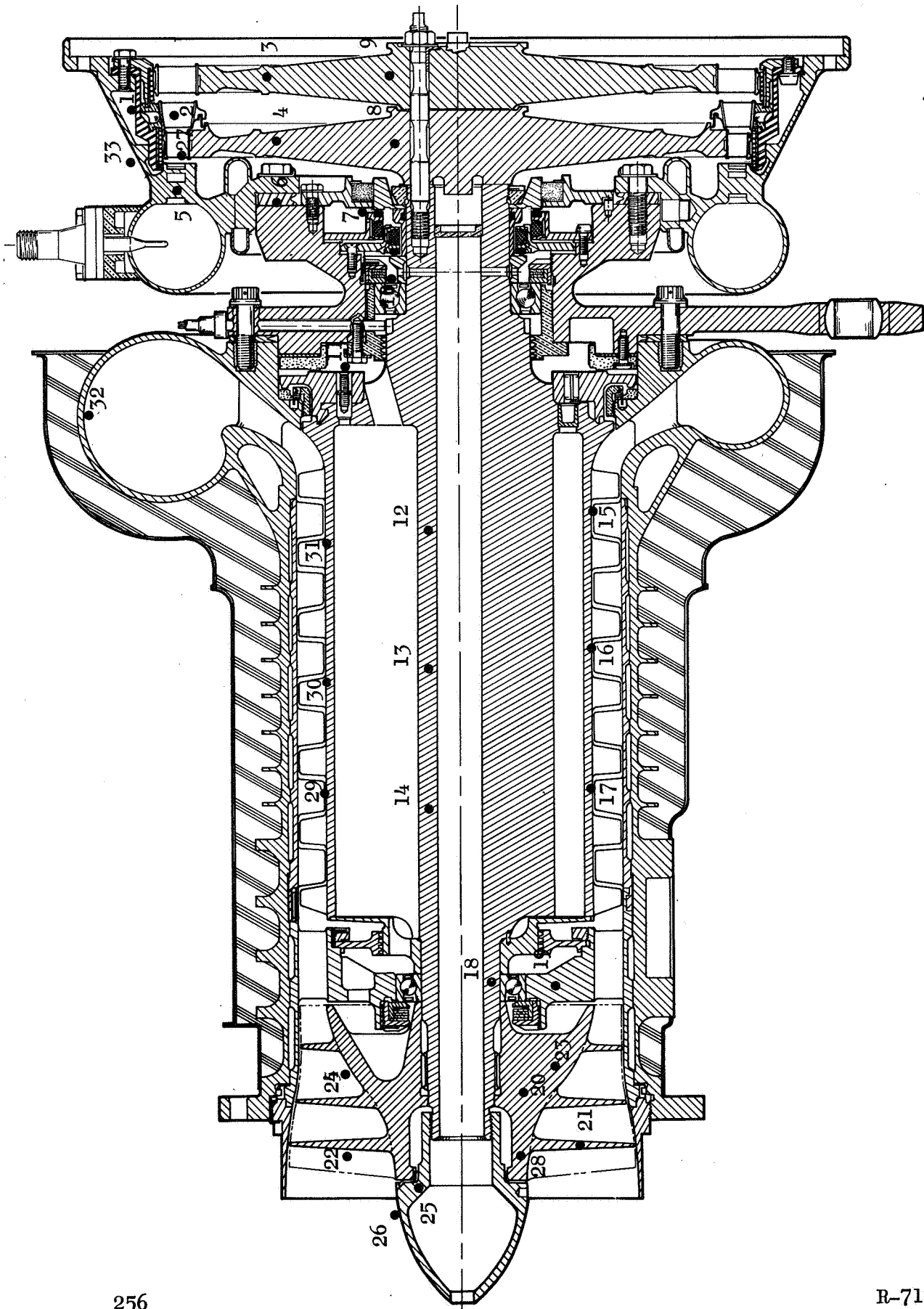


Figure 129. Mark-15 Liquid Hydrogen Turbopump Nodal Points for a Thermal Analyzer Network

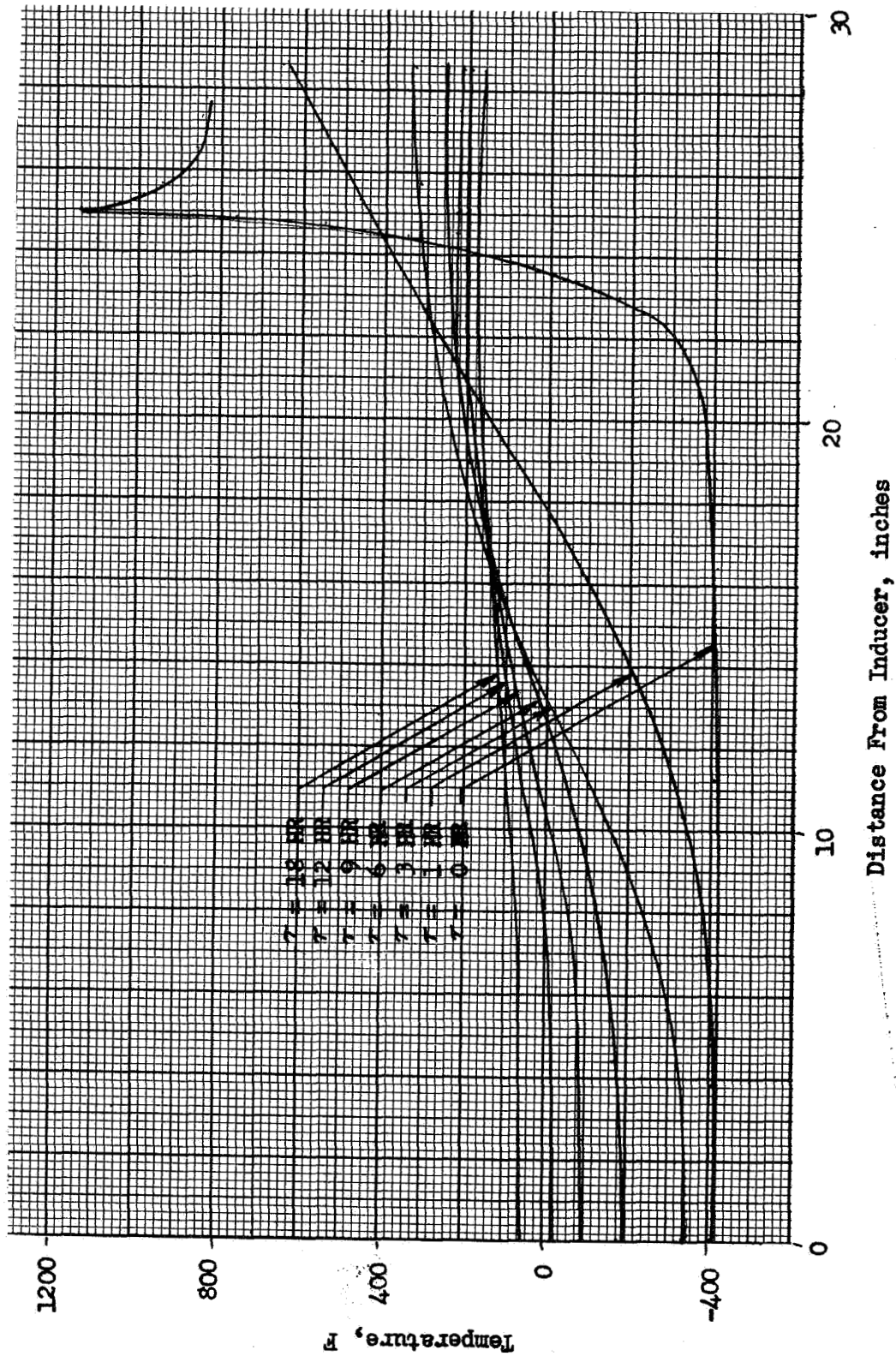


Figure 130. Mark-15 Hydrogen Turbopump Average Internal Temperature Distribution During Soakback

equilibrium temperature, the temperature of the turbopump will decrease through the radiation process to the surrounding surfaces. Therefore, the maximum temperature attained by the inducer and rotor of the J-2 turbopump is expected to be approximately 100 F.

#### MARK-15 LH<sub>2</sub> TURBOPUMP CHILLDOWN ANALYSIS

Following the heat soakback analyses studies, the boundary conditions and the initial temperature distribution of the turbopump were changed and the chilldown analyses were begun using Fig. 129 as the model. In these studies a 3-minute prechill followed by a 2.5-second start transient were considered. The prechill conditions were varied while the start transient conditions were assumed to remain constant. The prechill conditions considered were:

1. Zero percent of the total flowrate
2. 1.44 percent of the total flowrate
3. 5 percent of the total flowrate

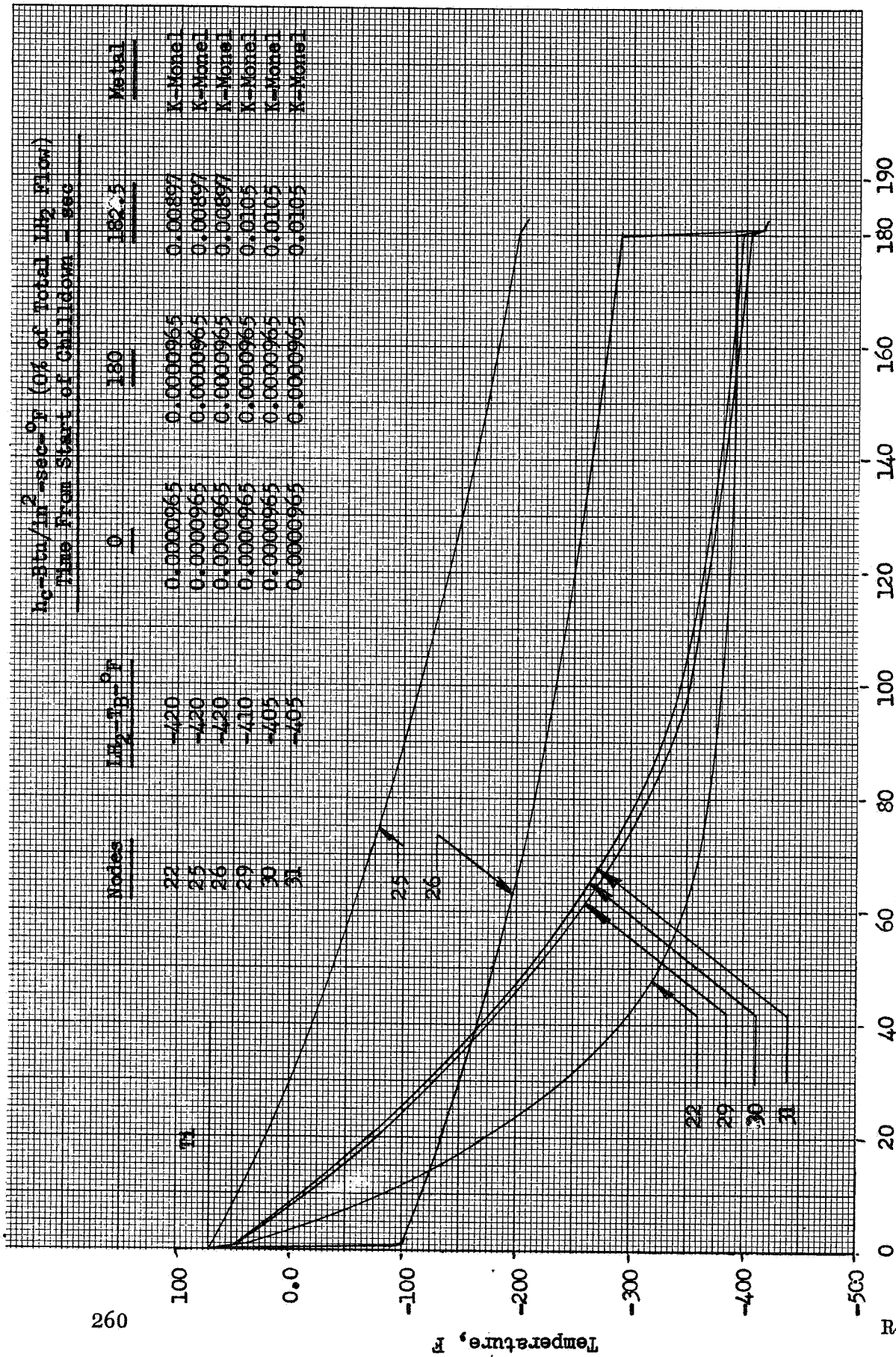
Condition one assumes that the lines and the pump are filled with -420 F LH<sub>2</sub>. Although no LH<sub>2</sub> is flowing through the pump, nevertheless the pump parts will be chilled down by means of LH<sub>2</sub> as the LH<sub>2</sub> goes through the film and nucleate boiling processes. During the film boiling process, the heat flux rate is lower than during the nucleate boiling process due to a low LH<sub>2</sub> film coefficient. As the film boiling converts to nucleate boiling, due to a drop in temperature difference between the LH<sub>2</sub> saturation temperature and the warm pump surfaces, the heat flux rate will increase. The surface temperature drops and the heat will flow from the internal segment to the surface and from the surface the heat will be absorbed by the LH<sub>2</sub>.

The determination of the LH<sub>2</sub> film coefficient for boiling conditions was based on the work previously presented in Fig. 5. The results are plotted in

Fig. 131 as temperature vs time from the start of chilldown. It is seen that the temperatures of some nodes (25 and 26) are still fairly high after 3 minutes of prechill. However, after 2.5 seconds of start transients, the surface temperature reaches almost that of the bulk temperature of the LH<sub>2</sub>. Node 25 is an internal node connected to the surface node 26. Temperature of node 25 changes very little at the start of chilldown, whereas the temperature of node 26 drops quite sharply. After approximately 2 seconds the temperature of the two nodes decreases in similar manner up to 3 minutes of the prechill.

During the 2.5 seconds of start transient, the temperature of the surface node 26 takes a sharp drop, whereas the temperature of node 25 does not appreciably change. This is due to the resistance between the two nodes caused by the low thermal conductivity of the metal. The results are plotted on Fig. 132 and 133. These figures show that the temperature gradient between nodes 25 and 26 is fairly high during the early part of the chilldown, but the two nodes' temperatures approach one another near the end of chilldown period. The surface temperatures are generally close to the LH<sub>2</sub> bulk temperature at the end of the 2.5-second start transient.

Other areas where the rotor wall thickness is greater than the region investigated should be analyzed. Also, a great deal of the accuracy of the entire study depends on the type of LH<sub>2</sub> cooling taking place. It is very important that the LH<sub>2</sub> cooling process be isolated and a thorough investigation be made. A detailed model which considers the very first drop of LH<sub>2</sub> coming in contact with the pump part (within a short time of the start of the chilldown) to the time when the full flow is established should be further analyzed.



Time, seconds

Figure 131. Pump Chilldown Temperature vs Time for Mark-15 LH<sub>2</sub> Turbopump

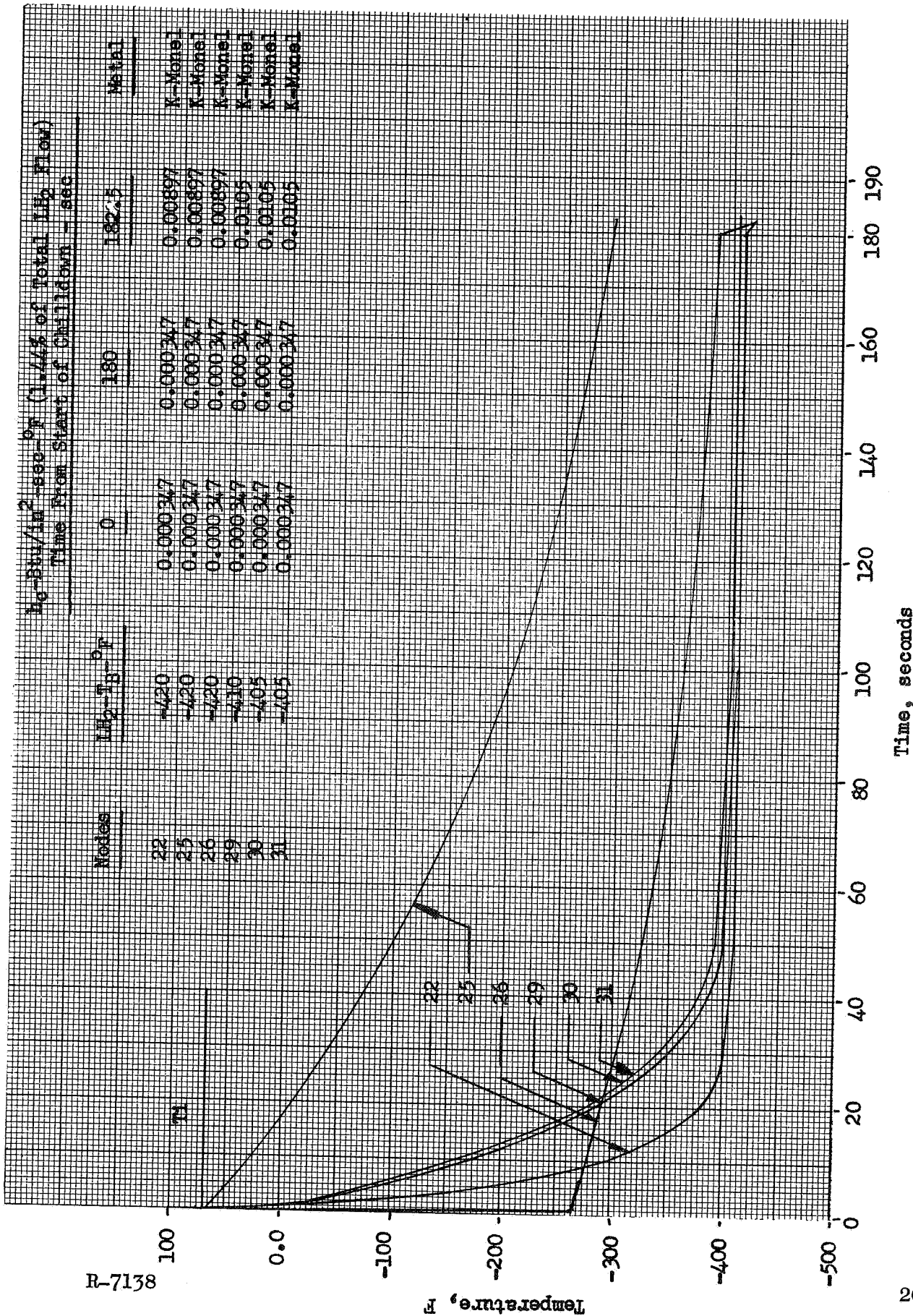


Figure 132. Pump Chilldown Temperature vs Time for Mark-15 LH<sub>2</sub> Turbopump

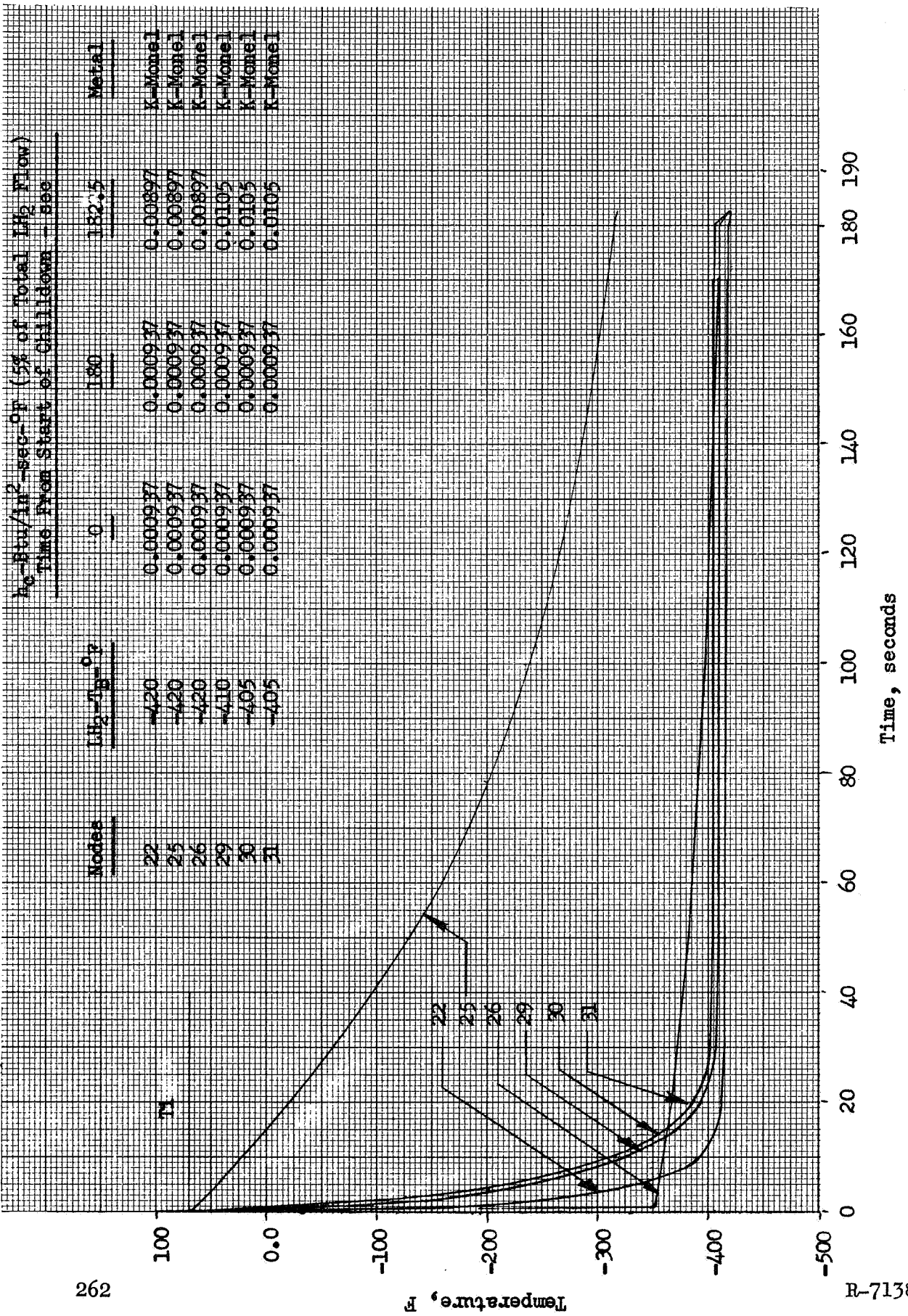


Figure 133. Pump Chilldown Temperature vs Time for Mark-15 LH<sub>2</sub> Turbopump

## MARK 29 TURBOPUMP

The Mark 29 single-stage liquid hydrogen turbopump nodal distribution (Fig. 134) and computer setup were initiated during the eleventh monthly report period. However, due to lack of time, no further heat transfer analysis was carried out for this turbopump. This work can be carried out in the future.

## 350K LH<sub>2</sub> TURBOPUMP HEAT SOAKBACK STUDY

The high-pressure, 5000-psi, 350K LH<sub>2</sub>-pump nodal distribution is shown in Fig. 135. Attempt was made to isolate the different materials involved in order to be able to use physical property tables for each material. In areas where this isolation led to creating a small node, thus increasing the computing machine time, two or more materials were lumped into one and their weighted average properties were used. Since experimental temperature distribution for the end of 500 seconds test was not available, as in the case of the J-2 turbopump, the initial condition of the high-pressure, 5000-psi LH<sub>2</sub> pump was estimated based on the J-2 results, weight ratio of the two turbopumps, turbine inlet gas temperatures, etc. The thermal analyzer program was again used and the heat soakback analysis was carried out for a duration of 6 hours. The results are plotted in Fig. 136. It can be seen that this figure resembles Fig. 130 which is the soakback temperature distribution for the Mark-15 turbopump. The equilibrium temperature of this turbopump can be estimated to be approximately 50 F. Further detailed heat transfer analysis can be carried out for this turbopump considering longer time periods, and turbine isolation and pump insulation approaches.

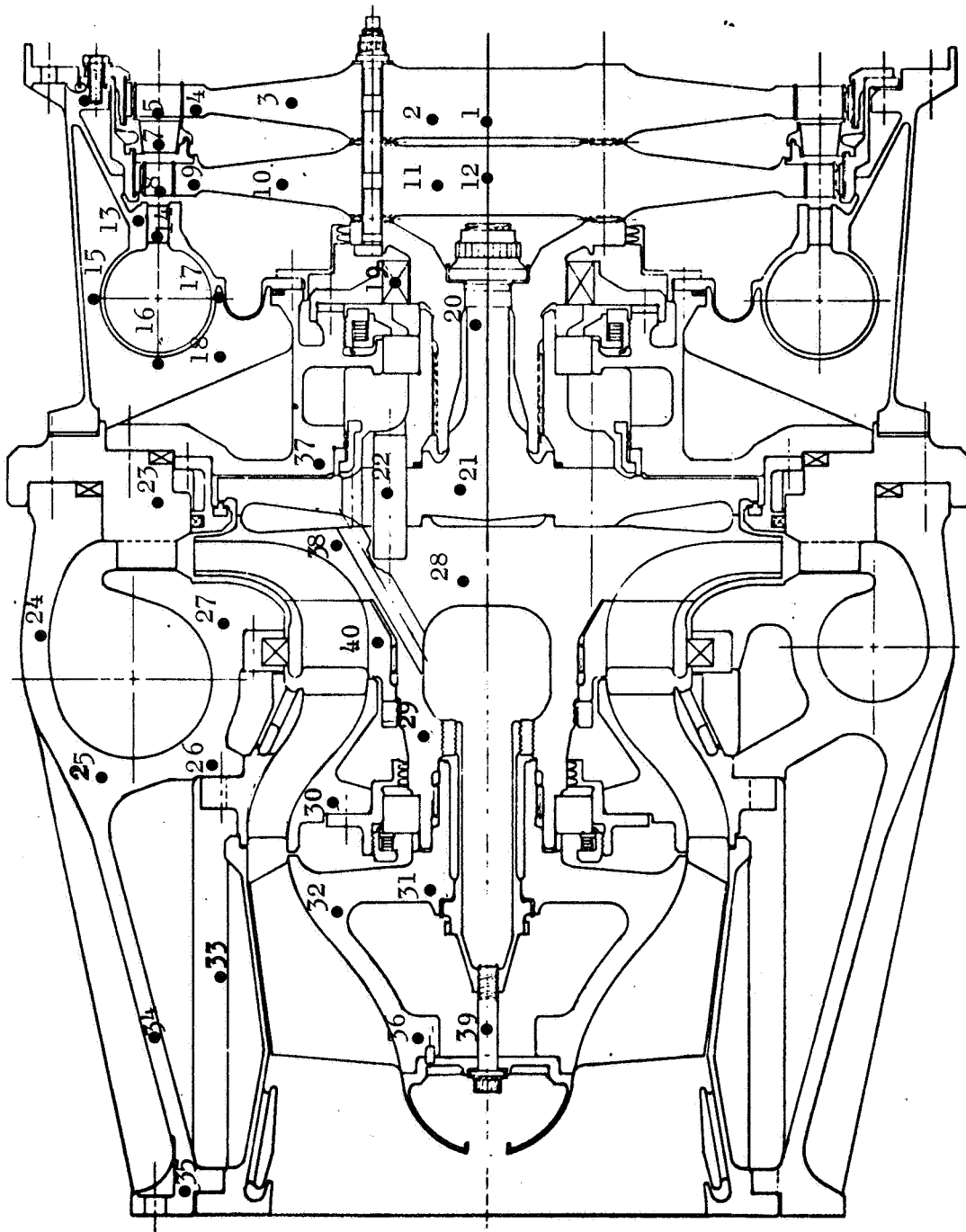


Figure 134. Mark-29 Single-Stage Liquid Hydrogen Turbopump Nodal Point Distribution

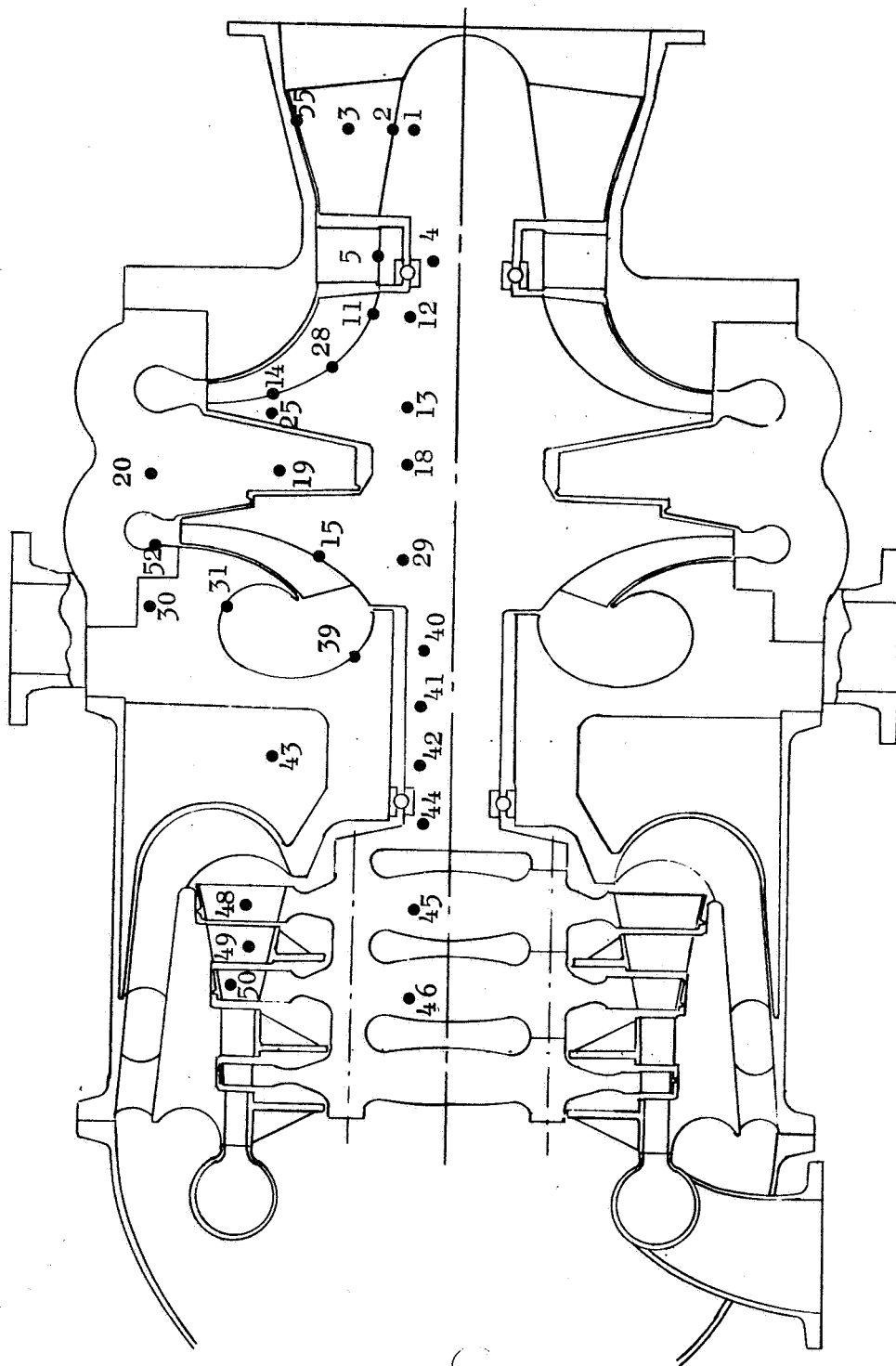


Figure 135. A 350K LH<sub>2</sub> Turbopump Nodal Point Description

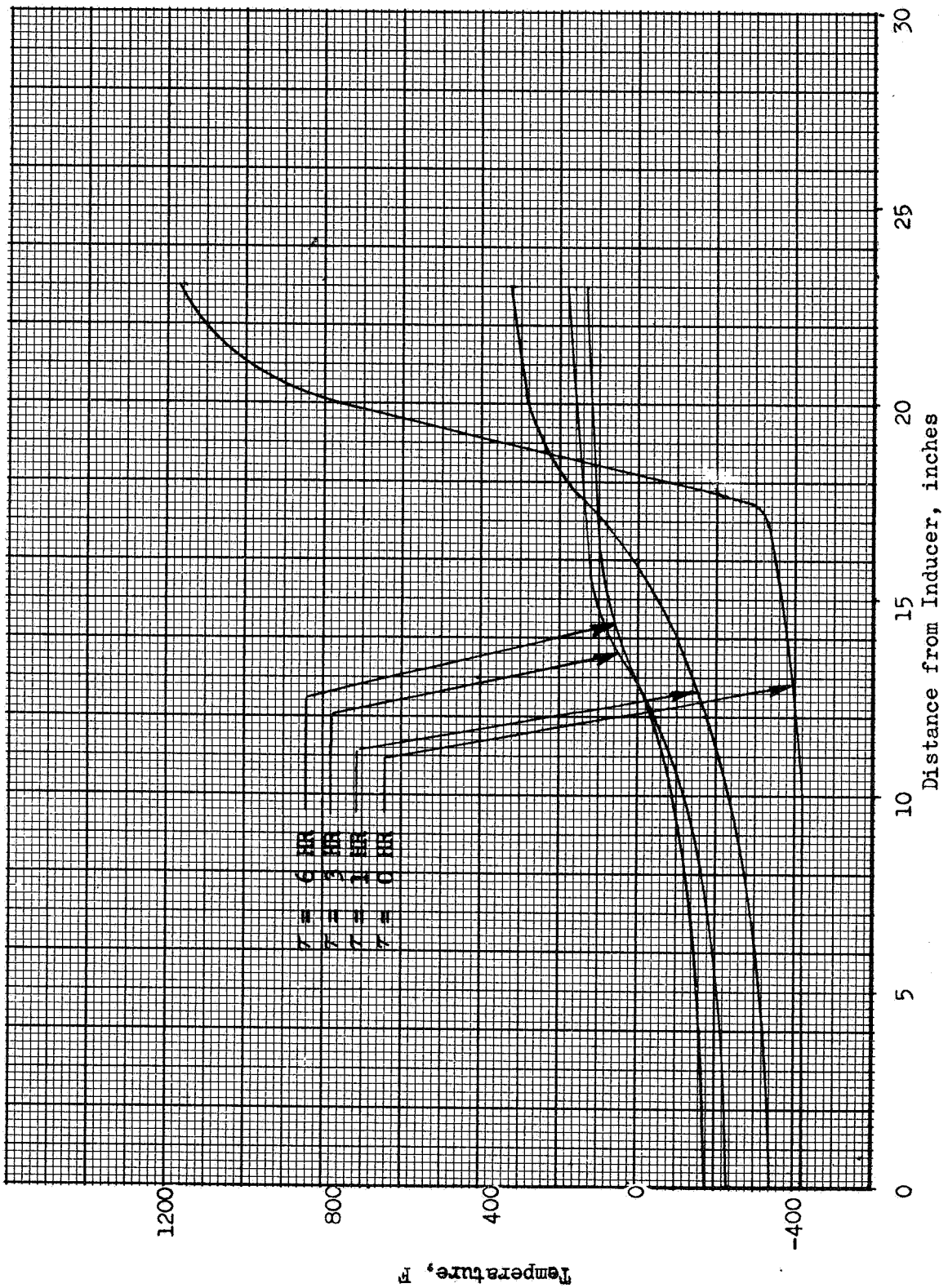


Figure 136. A 350,000 lbf LH<sub>2</sub> Turbopump Average Internal Temperature Distribution During Heat Soakback

## 350K LH<sub>2</sub> TURBOPUMP CHILLDOWN ANALYSIS

For the purposes of the chilldown analyses the nodal distribution shown in Fig. 135 was modified and the appropriate boundary and initial conditions were used in conjunction with the thermal analyzer. The LH<sub>2</sub> bulk temperature was assumed to be slightly different at various locations of the pump such as the inlet, impeller, and volute region. A 3-minute prechill followed by a 2.5-second start transient were considered. During the prechill period three LH<sub>2</sub> film coefficients were used which were based on zero percent of full flow (the pump being just full of LH<sub>2</sub>), 1.44 and 5 percent of full flow. For zero percent flow the film coefficient was determined based on the experimental data of Fig. 4. For other conditions the film coefficient was based on experimental data of Fig. 5.

The results of these analyses are plotted on Fig. 137, 138, and 139. As was explained previously the effect of different materials is quite evident. For example, Fig. 137 indicates that the temperatures of nodes 30 and 52, which are internal node and surface node, respectively, are very close together. The material of these nodes is aluminum with high thermal conductivity. On the other hand the temperatures of nodes 29 (internal) and 15 (surface) are quite different even at the end of 3 minutes of prechill period. The material of these nodes is titanium whose thermal conductivity is very low when compared to aluminum. A temperature difference of approximately 300 F exists between nodes 29 and 15.

Figures 138 and 139 essentially tell the same story as Fig. 137. The temperature of nodes 30 and 52 (aluminum material) are only approximately 25 F apart at the end of 3 minutes of prechill, whereas the temperature difference between nodes 15 and 29 (titanium material) is approximately 200 F.

From the results of the foregoing analyses it can be concluded that for the purposes of a rapid chilldown a material with very low density, low

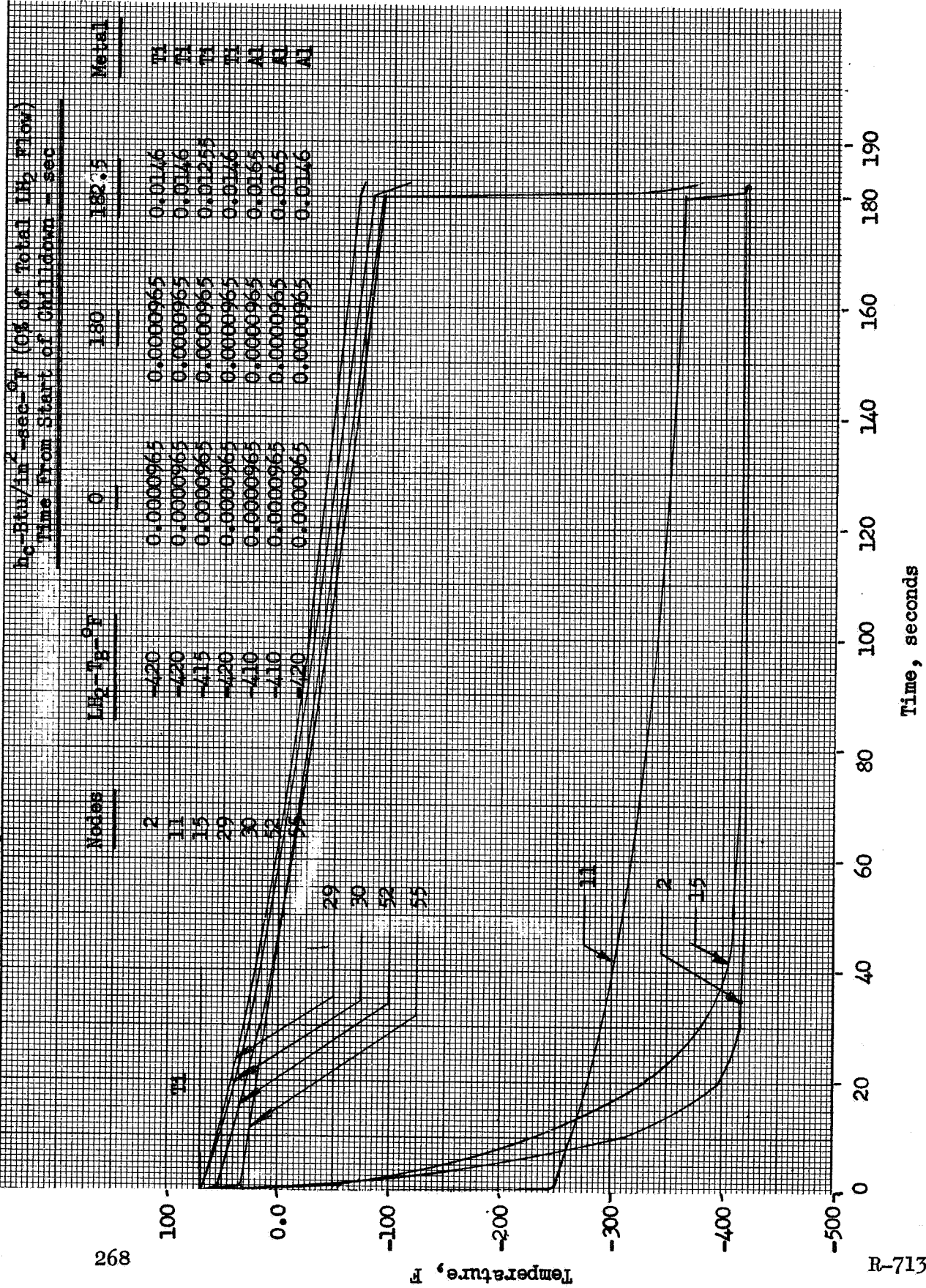


Figure 137. Pump Chilldown Temperature vs Time For a 350,000 lbf Breadboard LH<sub>2</sub> Turbopump

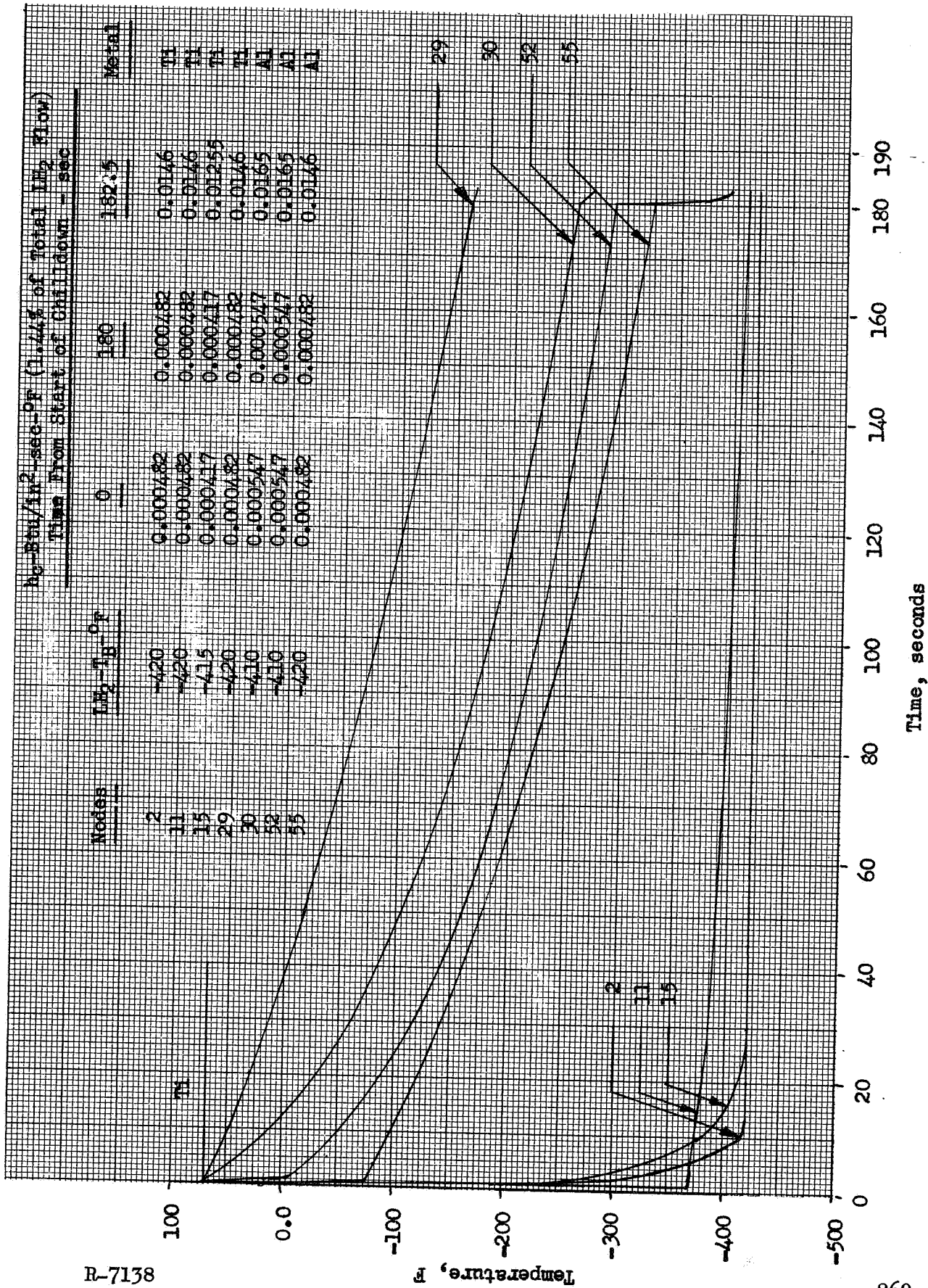


Figure 138. Pump Chillotdown Temperature vs Time For a 350,000 lbf Breadboard LH<sub>2</sub> Turbopump

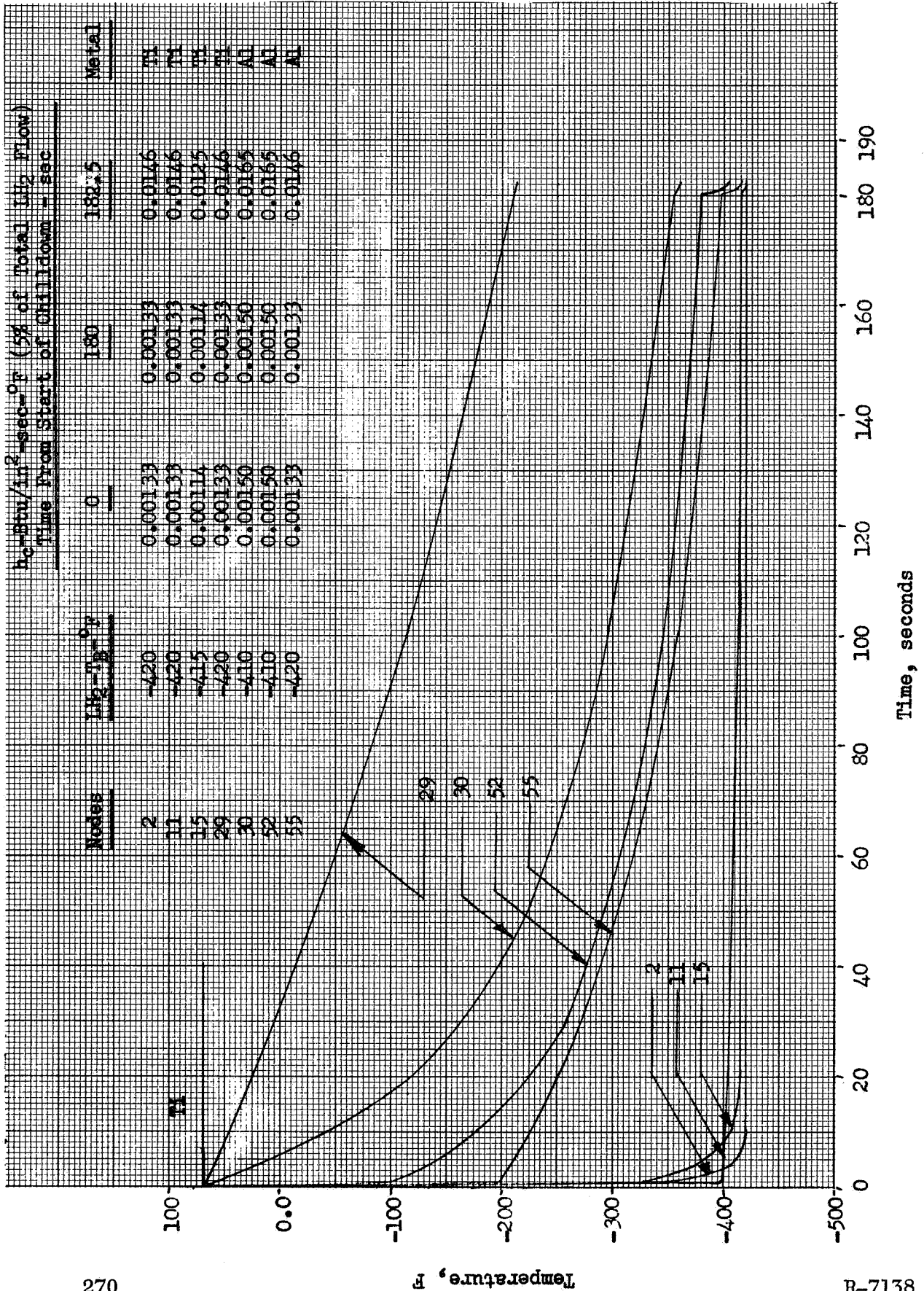


Figure 139. Pump Chilldown Temperature vs Time for a 350,000 lbf Breadboard LH<sub>2</sub> Turbopump

specific heat, and extremely high thermal conductivity is preferred for uniform chilldown. Since theoretically such material has negligible heat content, the chilldown time is exceedingly short and the material temperature will be uniform at all times, thus causing no thermal stresses. When conventional materials are used the selection should be based on low heat content and very low thermal conductivity. In this case the wetted surface temperatures drop rapidly to that of the LH<sub>2</sub> bulk temperature, and thus a short start transient time will be required. However, the material must be capable to withstand the thermal shock which will be set up due to transient temperature variations.

In order to eliminate the stress problem, two methods of chilldown seem to be applicable. The first one is a very slow chilldown, causing a slight amount of the boiloff H<sub>2</sub> to pass through the pump. In this case the surfaces and the internal part of the pump will chill down at a very slow rate. Therefore, temperature gradient will be small causing no thermal stress.

The second method is to use a very low thermal conductivity material and coat the wetted surfaces of the pump. The coating itself will chill down very rapidly and will also resist the flow of heat from the base metal to the LH<sub>2</sub>. Since the heat flux will be very low, there will be no large temperature gradient established in the metal and thus no thermal stresses. However, the coatings themselves might present problems such as peeling off, cracking, etc. Coating application approaches were described in Task III. The method of passing the required amount of boiloff H<sub>2</sub> through the pump also appears advantageous even though a long prechill time is necessary.

A further conclusion that can be drawn from these studies is that based on the influencing properties (such as weight, specific heat, thermal conductivity, yield stress, etc.) among the conventional materials, titanium seems to be a better material than stainless steels and aluminum for LH<sub>2</sub>

turbopump application for rapid starts. This is due to its low thermal conductivity, light weight and low heat content when compared to other materials under similar conditions.

The thermal analyzer program which was used to determine the temperature distribution in the above-mentioned turbopumps solves N-dimensional (Ref. 48) transient heat transfer problems by the analysis of an analogous network of nodes joined by conductors. A capacitance, C, a heat generation rate, Q, and a temperature, T, are associated with each conductor. In order to analyze the temperature distribution of an object due to changes of some boundary or internal condition(s), the pump under investigation is divided into convenient volumes which are called nodes. Identifying numbers are assigned to these nodes. The required inputs to the thermal analyzer are the initial conditions, the boundary conditions, the capacitances (mass times specific heat), and the resistances (thermal conductivity multiplied by the ratio of the heat flow area to the distance the heat travels). The smaller the volumes the larger the number of nodes a part can be broken into and thus the greater is the accuracy of the analysis. However, as the number of nodes increases for a given part, the higher will be the computer time consumption. Therefore, a compromise must be made between the desired accuracy and the expenses incurred. Also, options are built in the thermal analyzer that can make use of tables for variable properties (specific heat, thermal conductivity, film coefficient). These options were used in the analysis of the turbopumps discussed.

### 350K LH<sub>2</sub> TURBOPUMP GROUND PRECHILL STUDY

A comparison of the analysis techniques and some existing test results was accomplished. In an effort to determine the chilldown time of a 350K high-pressure hydrogen pump, preliminary test results supplied by NASA are plotted in Fig. 140 and were used in the current study to compare experimental data with the developed analytical model.

In the pump, hydrogen coolant passages were drilled tangent to the cylindrical contour of a relatively thick-wall aluminum pump housing. The tangent passages intersected to form a circuit around the pump perimeter. Four such circuits were then connected in series pairs by longitudinal passages to provide two parallel flow paths as shown in Fig. 141. Measured wall temperatures near the inlet and outlet are shown in Fig. 140. Operating conditions from this test were input to the modified Thermal Analyzer Program in an attempt to predict analytically this temperature distribution with time. Property values were based on the average value of the inlet and outlet temperatures, assuming coolant and wall temperatures are close for this slow-chill case. The coolant temperature and the corresponding hydrogen heat capacity are plotted in Fig. 142. Coolant mass velocity  $G$  was determined from the passage area and total coolant flowrate given in Fig. 140 and plotted as a function of time in Fig. 143.

Assuming a typical average Stanton number of 0.002, a hydrogen film coefficient  $h$  was calculated as a function of chilldown time and plotted in Fig. 143. Integrated mean values of mass velocity, heat capacity, and film coefficient were calculated to represent operating conditions during the chilldown period. A mean coolant passage wall thickness was determined for the entire passage length by summing the average thickness of each passage section weighted by length and dividing by the total length of the entire coolant passage. This resulted in a mean wall thickness of approximately 1.5 to 1.6 inches. The ratio of passage  $L/D$  from Fig. 141 is 400. The above values were input to the modified Thermal Analyzer Program including bulk temperature rise to calculate the wall temperature distribution with time. The results are plotted in Fig. 144 for a portion of the chill period. The design examined involved a long network of passages in a thick wall pump housing. Analysis indicates the chilldown time for the pump configuration could have been predicted, however, with fair accuracy with reasonable approximations included. Improvements in minimization of chilldown time for this configuration would include the addition of more parallel cooling paths, larger coolant inlet pressure, larger diameter chilling passages, smoother flow passages, and a smaller pump mass.

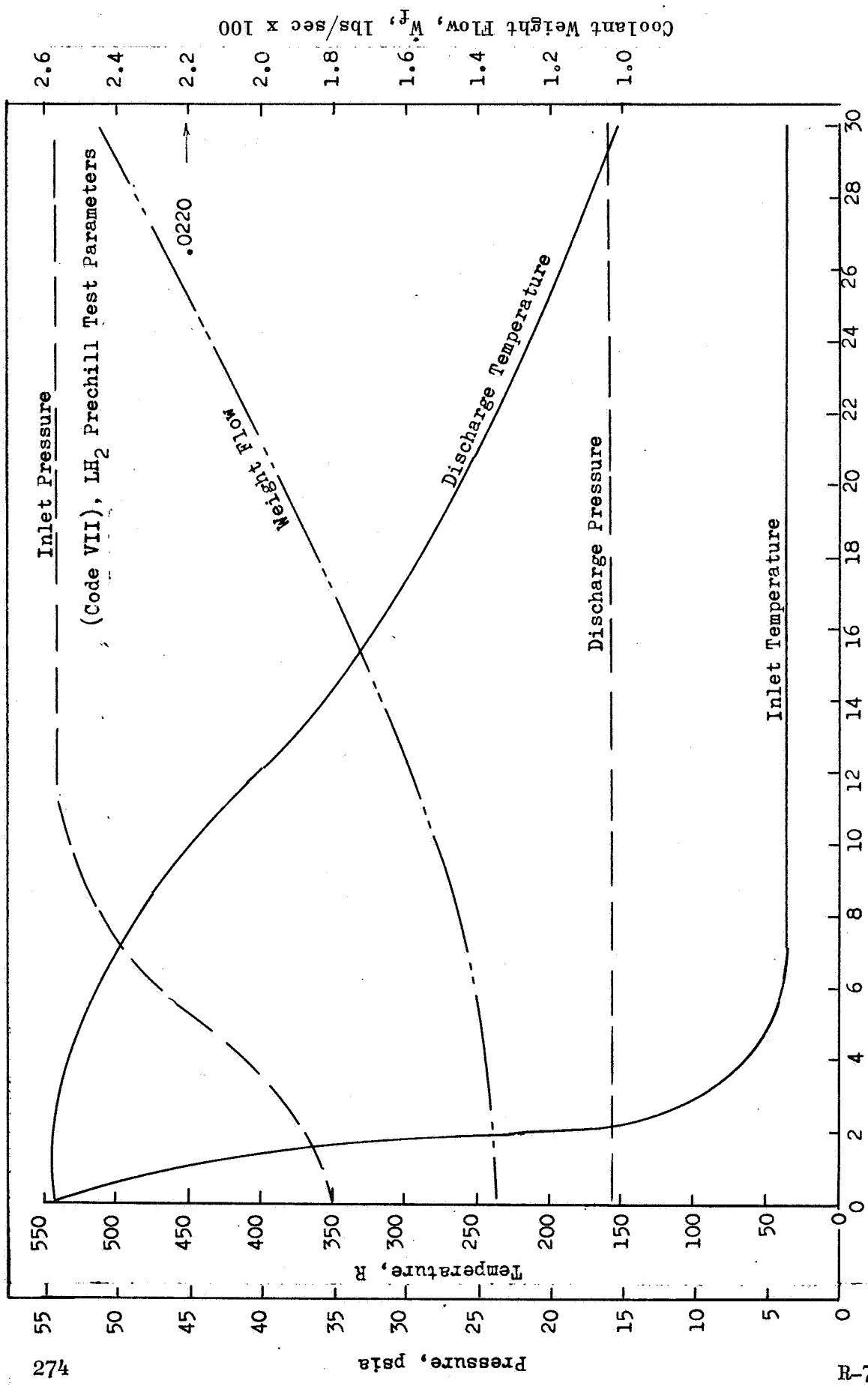


Figure 140. A 350K LH<sub>2</sub> Turbopump Chillover vs Time

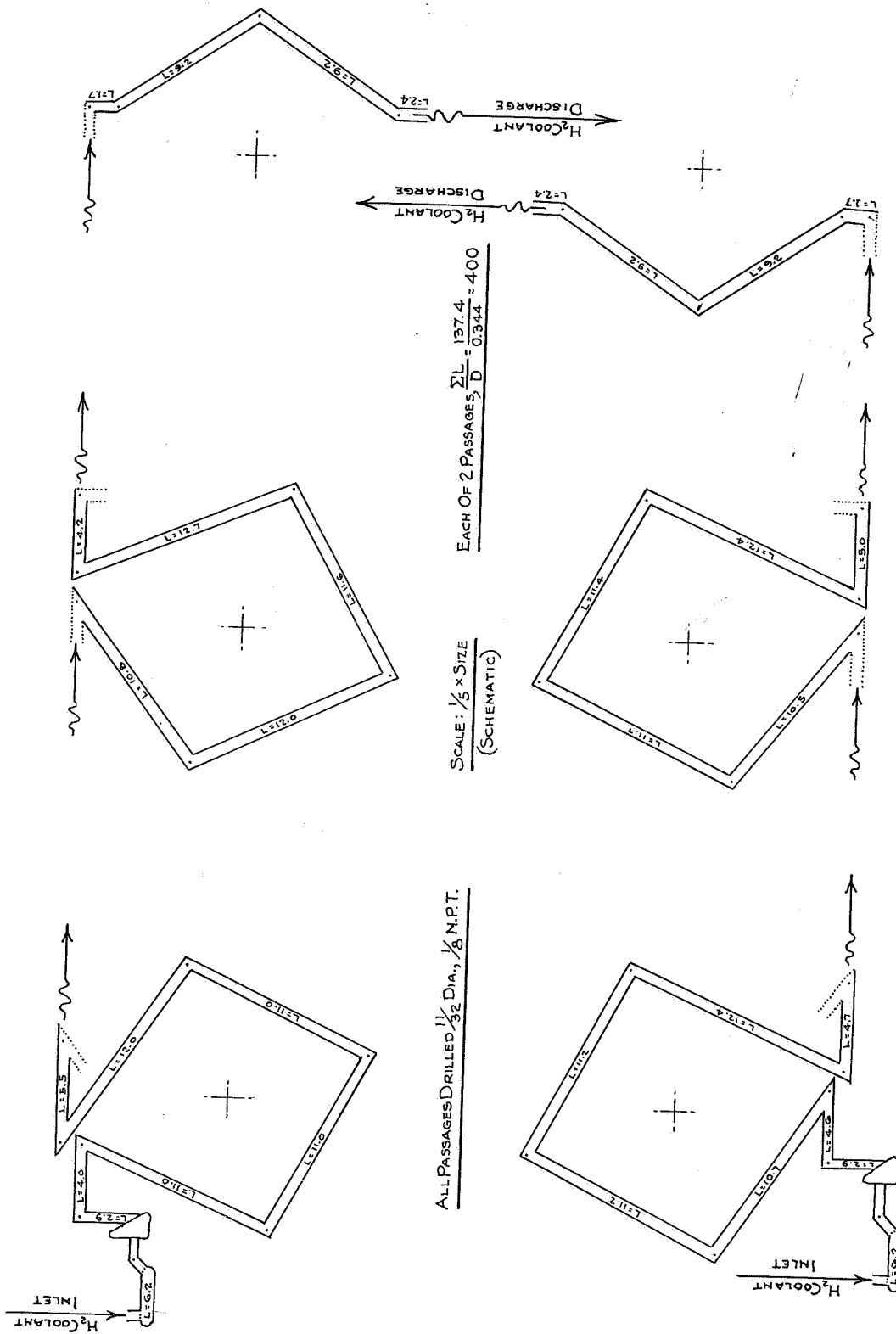


Figure 141. Prechill Coolant Passages of 350K LH<sub>2</sub> Pump

Mean Values  $\left\{ \begin{array}{l} C_{PM} = 3.256 \\ \gamma_m = 1.474 \end{array} \right.$

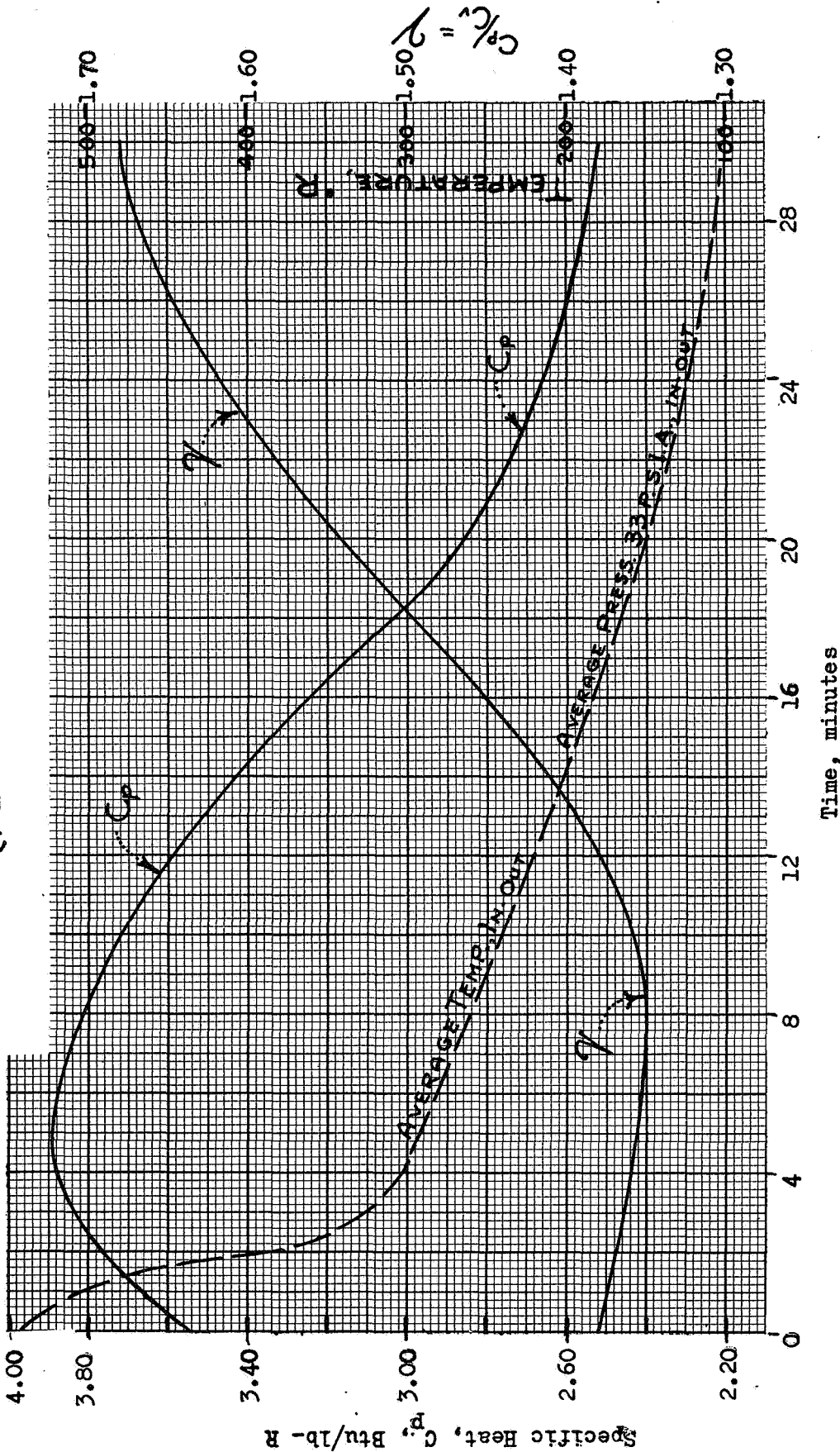


Figure 142. A 350,000 lbf LH<sub>2</sub> Pump, Prechill Coolant Parameters

Heat Transfer Coefficient,  $h = 0.00218G_p^2$ , BTU/sec in.<sup>2</sup> R x 1000

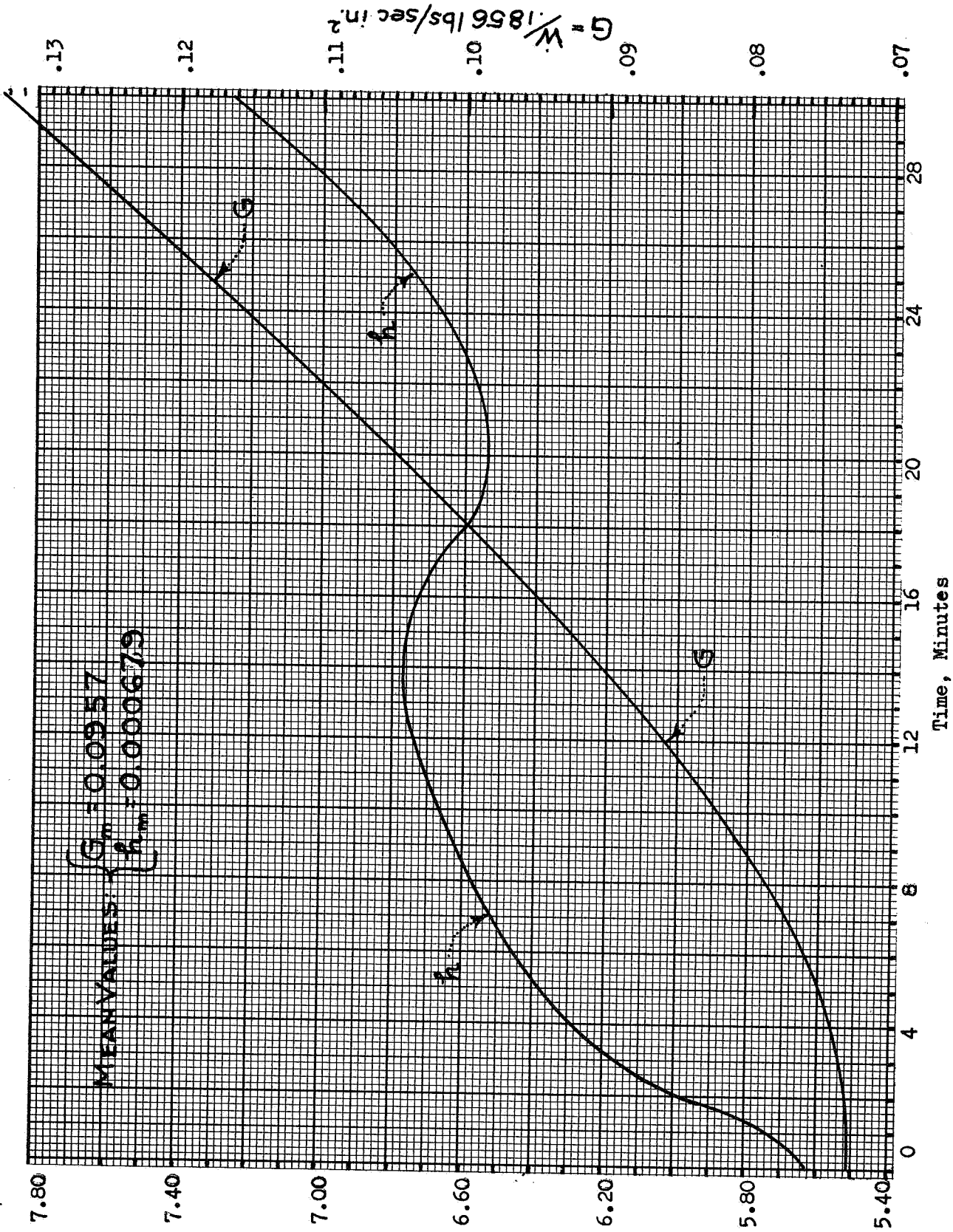


Figure 143. A 350,000 lbf Prechill Coolant Parameters, Test 5.01

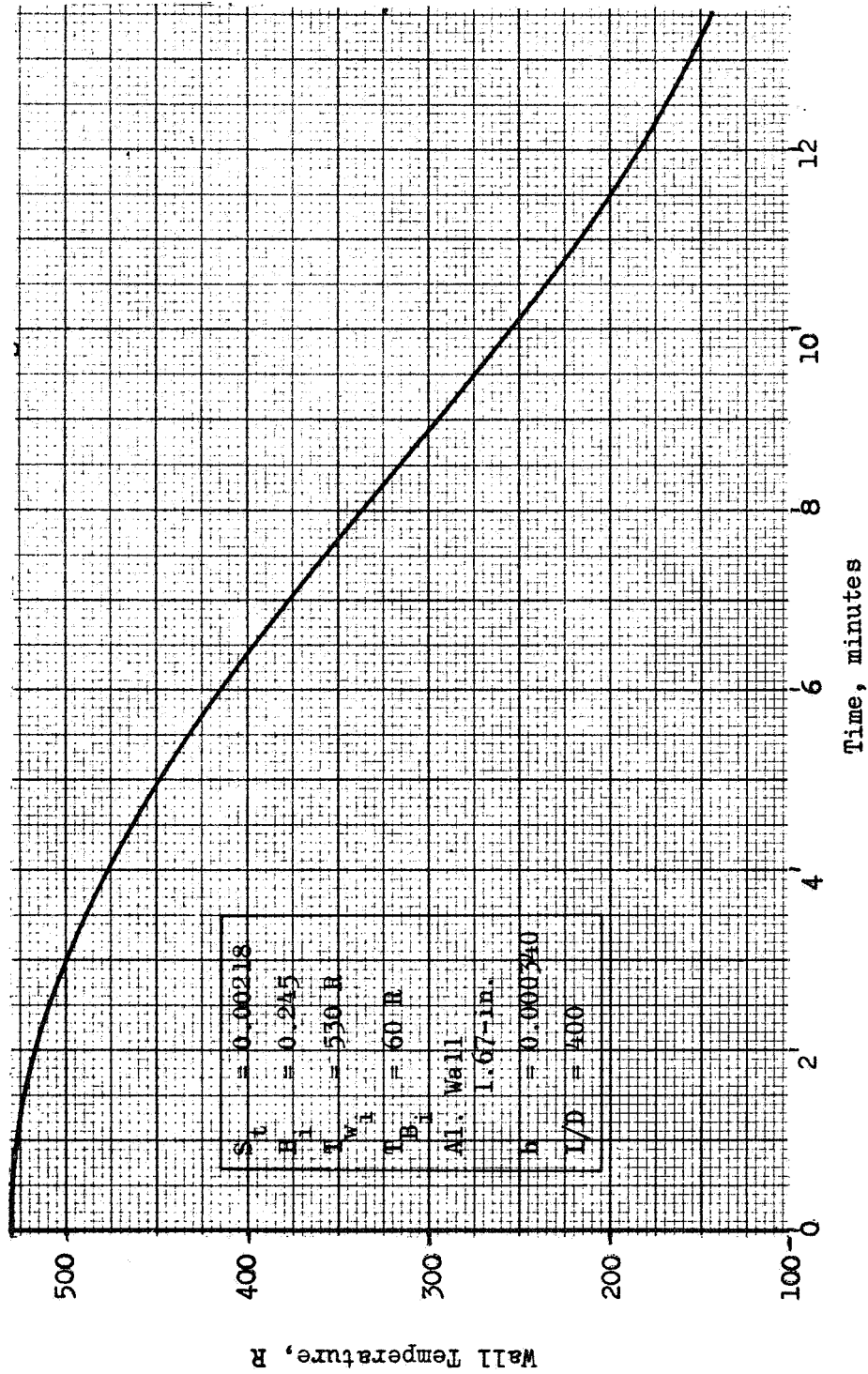


Figure 144. Analytical Wall Temperature Variation for a 350,000 lbf LH<sub>2</sub> Pump Prechill Coolant Passage

For the high-pressure prechill study a comparison of the choked-flow relationship for hydrogen was compared with the flow actually obtained in the flow passages shown in Fig. 140. In the described study a choked-flow pressure ratio (3.5) existed during the entire 30 minutes of chilldown. The theoretical value for an isentropic choked-flow for gaseous hydrogen is:

$$\frac{\dot{W} \sqrt{T}}{A P_{\text{inlet}}} = 0.139 \quad \gamma = 1.4 \quad (137)$$

(isentropic)

A comparative value for the measured parameter based on discharge temperature conditions and inlet pressure value becomes

$$\frac{\dot{W} \sqrt{T_{\text{outlet}}}}{A P_{\text{inlet}}} = 0.032 \quad (\text{experimental measured values}) \quad (138)$$

or roughly 23 percent of the isentropic value.

Consideration of the Fanno friction effects in a passage with  $L/D = 400$ , temperature at the outlet value and  $f = 0.0022$  resulted in:

$$\frac{\dot{W} \sqrt{T_{\text{outlet}}}}{A P_{\text{inlet}}} = 0.0765 \quad (\text{flow with friction}) \quad (139)$$

( $4fL/D = 3.5$ )

From Fig. 145 it may be seen that the inlet, exit and drilled passage turn losses result in a further flow reduction over that expected theoretically.

Figure 146 illustrates additional study data on tests conducted on a 350K LH<sub>2</sub> pump where a 1-hour slow prechill (wall temperature reduced to 200 R) was followed by a shorter period with the pump inlet valve open. Tests 6.01 to 9.01 represent successive tests where the cooldown period was reduced from an 80 to a 5-second period.

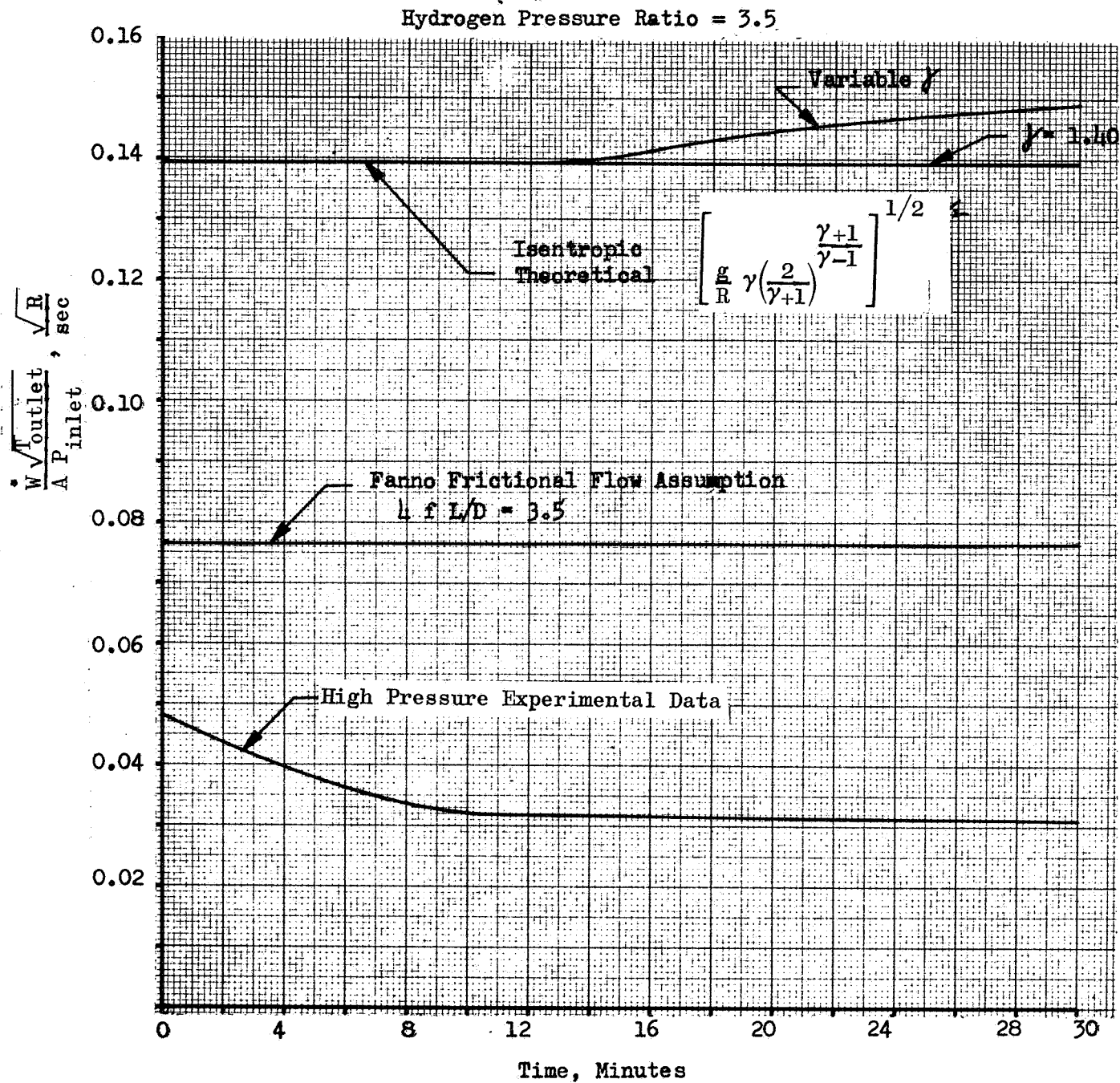


Figure 145. Study of a 350,000 lbf LH<sub>2</sub> Pump Prechill

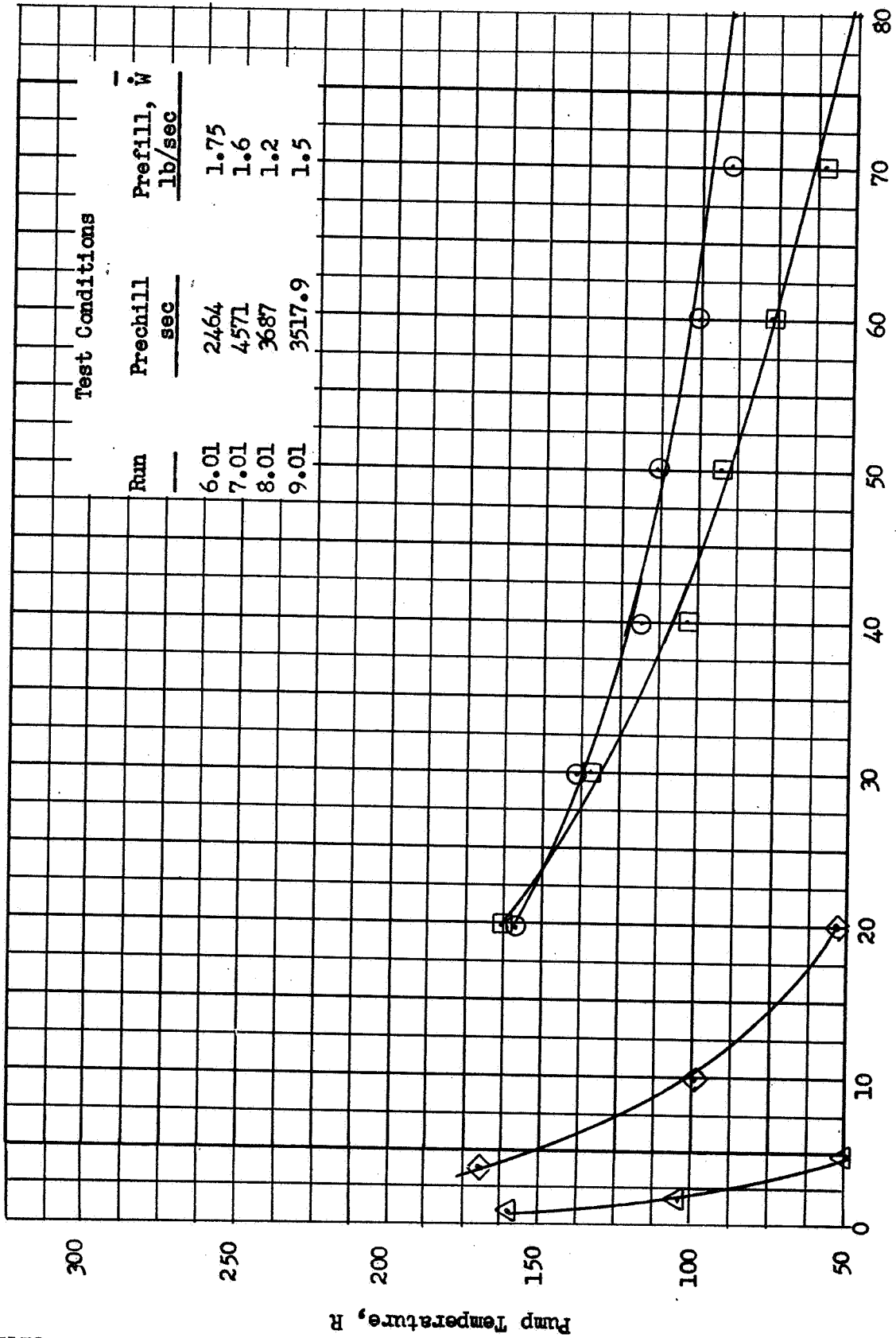


Figure 146. A 350K Pump Prechill Test Data

## M-1 PUMP CHILLDOWN STUDY

Data were taken from Ref. 42 on the M-1 pump cooldown study. This was reviewed as partially outlined in Task III where flow requirements were compared with theoretical values. Figure 147 compares test data for test 3 and 4 where average prechill flowrates were varied from 0.14 to 0.29 lb/sec. A substantial reduction in wall temperature with time was noted for test 4 with about the same total flow expended to the 1/e chill point. Further tests, however, were not conducted with larger chill flowrates.

## SLOW-CHILL REQUIREMENTS OF EXISTING PUMPS

Examination of limiting prechill flow conditions to provide a suitable prechill state prior to engine start was made based upon the minimum flow passage area for existing pumps shown in Fig. 148. An allowable choked vapor flow relative to the mainstage liquid flow is shown for a selected 80 R vapor temperature condition. Improvements in the chill flow during line blowdown of the hydrogen flow can result from increased tank pressure verifying the pressure effect outlined under Task I. Limiting percentage chill flows to provide entire pump chilling are noted in Fig. 149 for the various pump materials. It is shown that a high stagnation pressure of the prechill flow cannot be used to advantage with the choice of low thermal conduction materials such as titanium and stainless steel. Figure 150 illustrates the thrust dependence upon the allowable prechill flow percentages. It is shown that the larger thrust designs are somewhat limiting more in regard to allowable chilldown flow.

Figure 151 illustrates a translation of the required minimum time required for chill vs the percentage chilldown flow. It can be seen that if the entire pump is to be chilled, a long time with a small chill flow percentage is required for stainless and titanium pumps. A high flow with a shorter allowable time is indicated for the aluminum pump material.

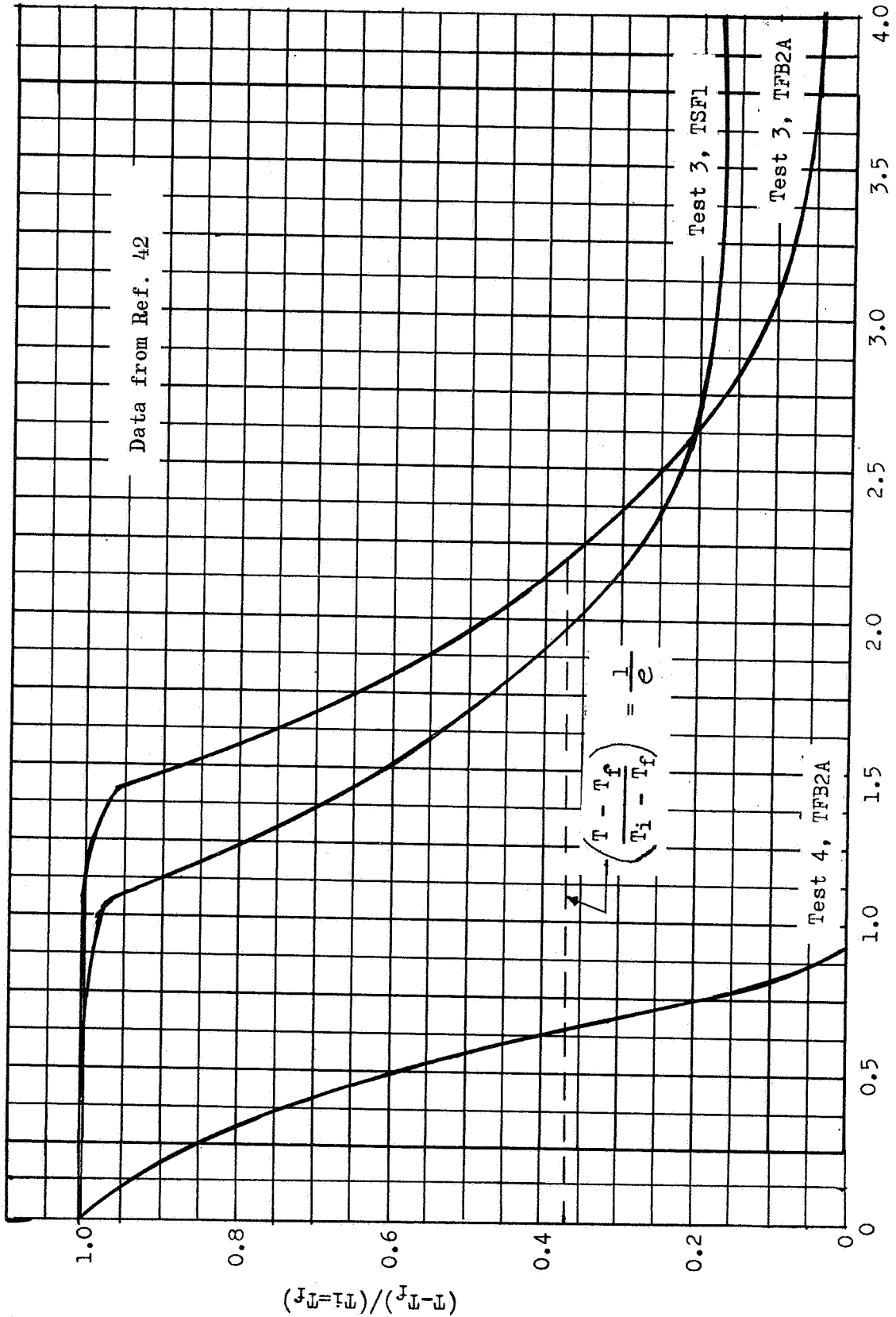


Figure 147. M-1 Pump Wall Chilldown vs Time

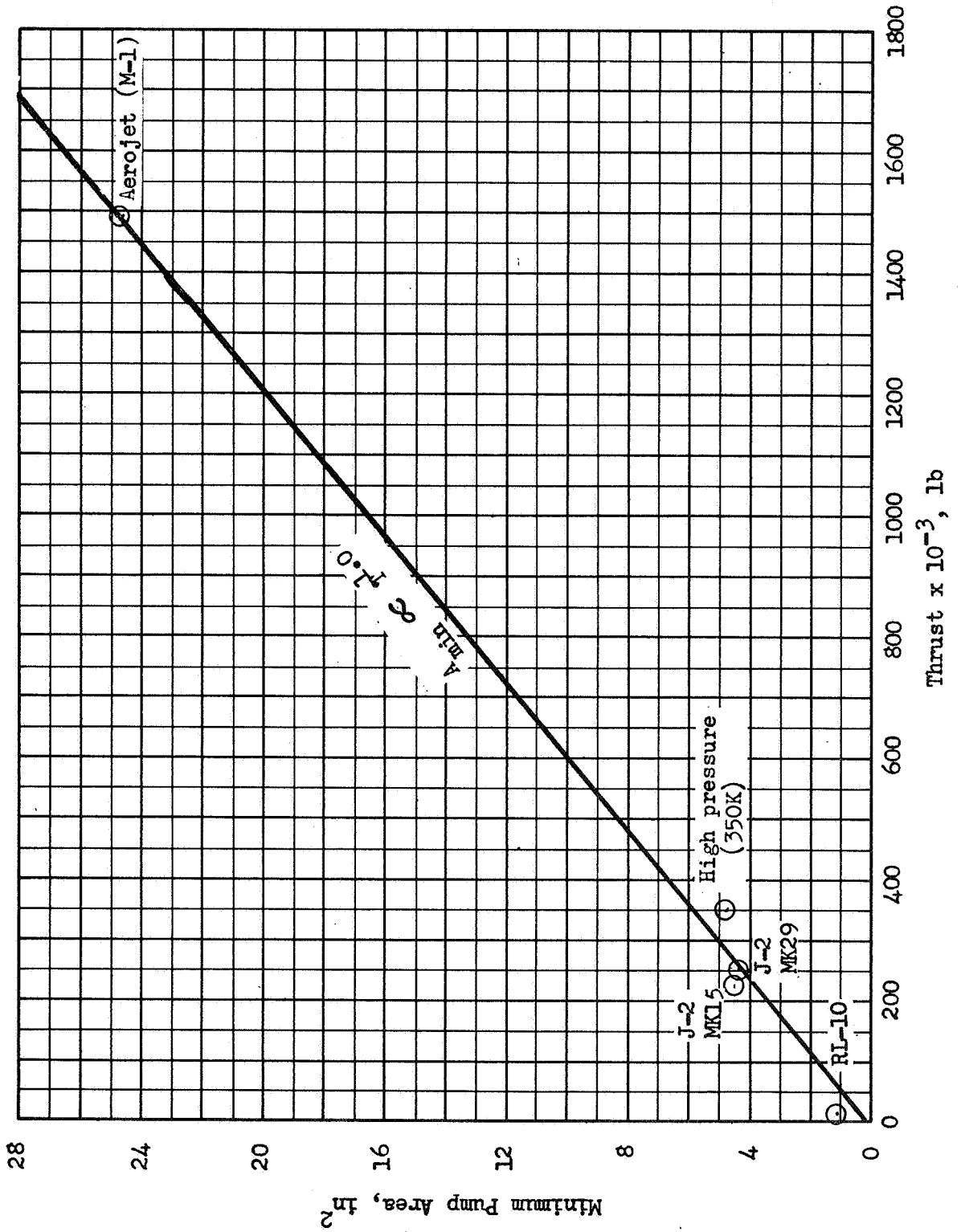
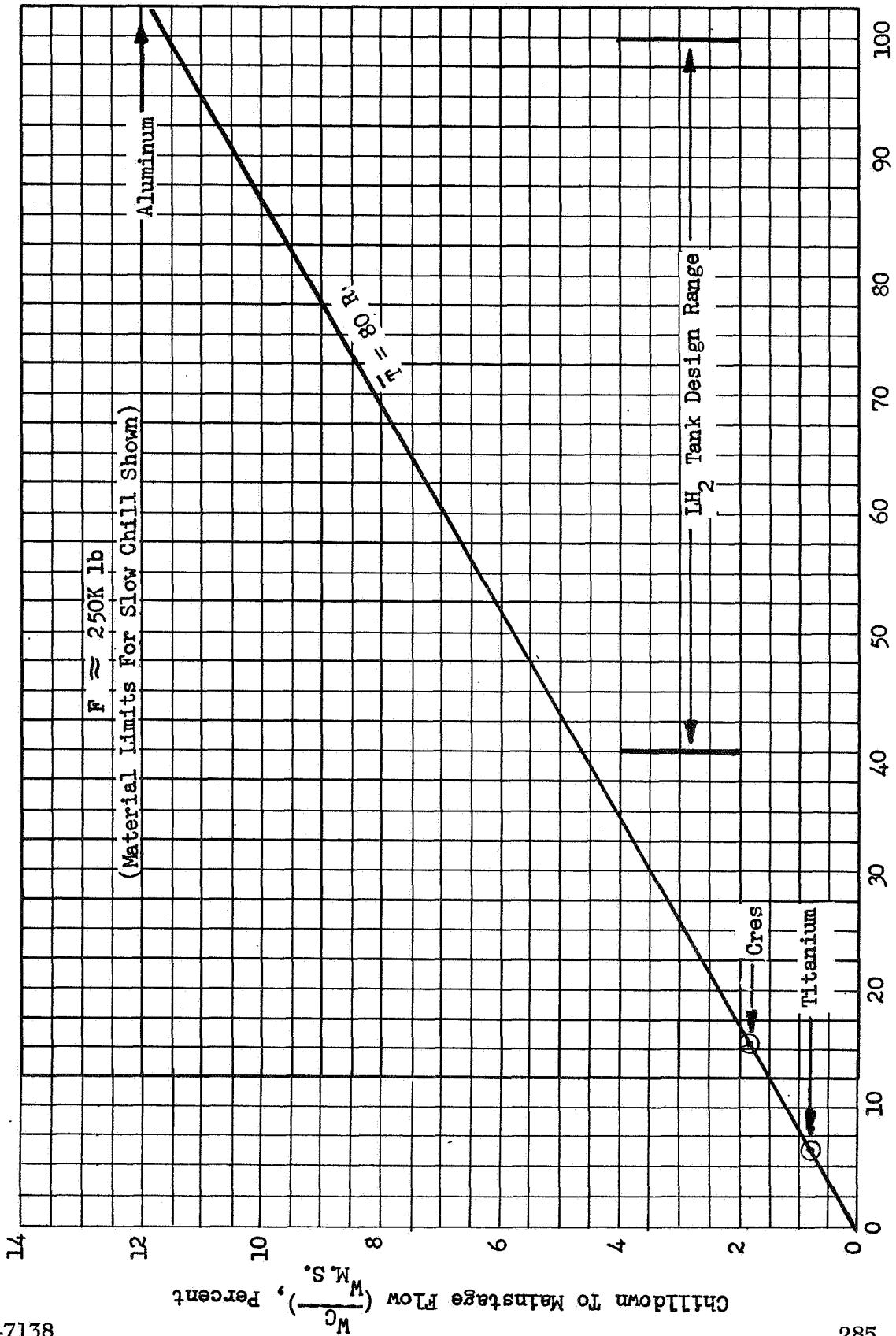


Figure 148. Pump Minimum Flow Passage Area vs Thrust Level



Tank Stagnation Pressure,  $P_0$ , psia

Figure 149. LH<sub>2</sub> - Limiting Chilldown Flow vs Tank Pressure

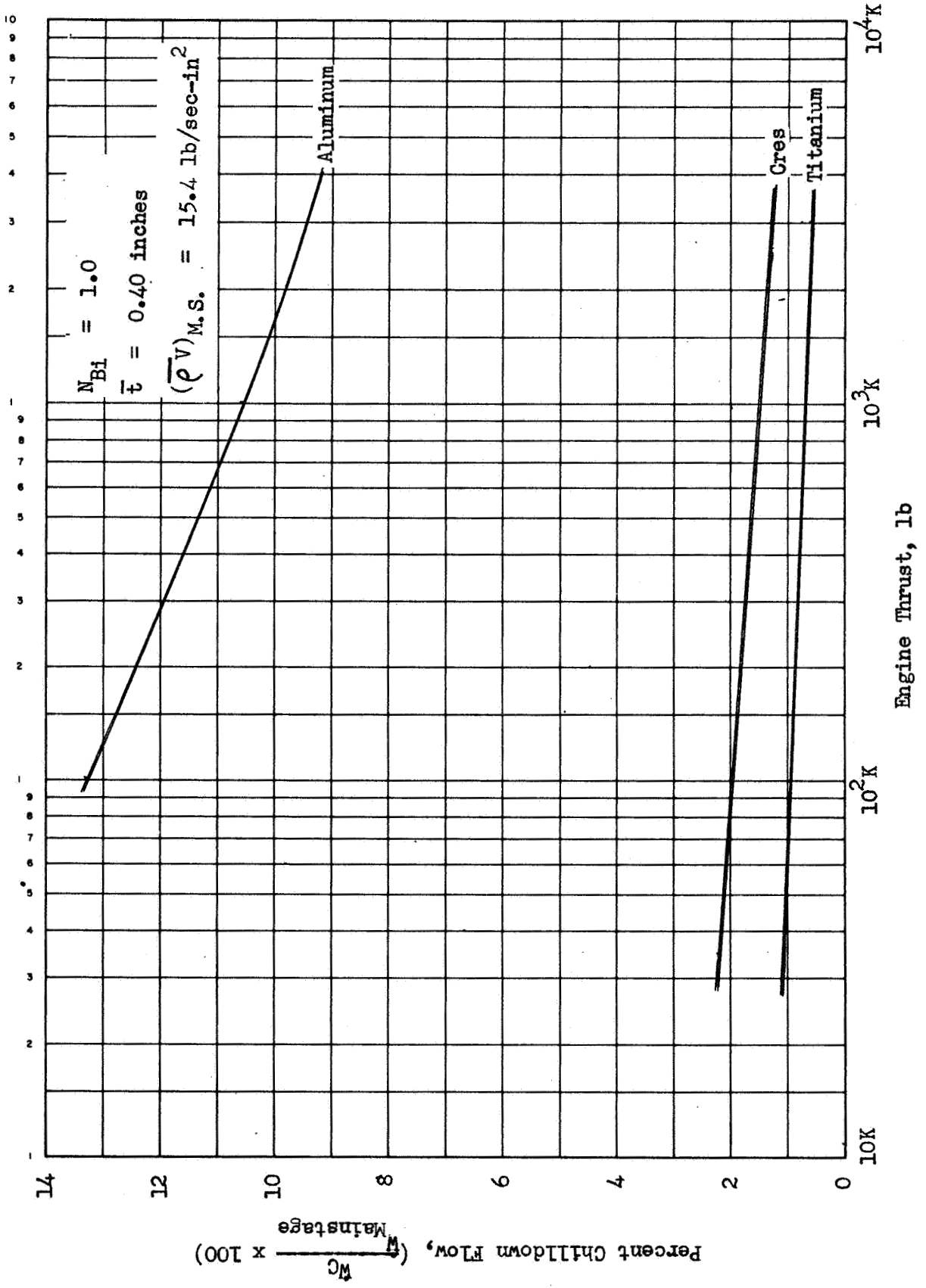


Figure 150 Comparison of Maximum Chill Flow Attainable

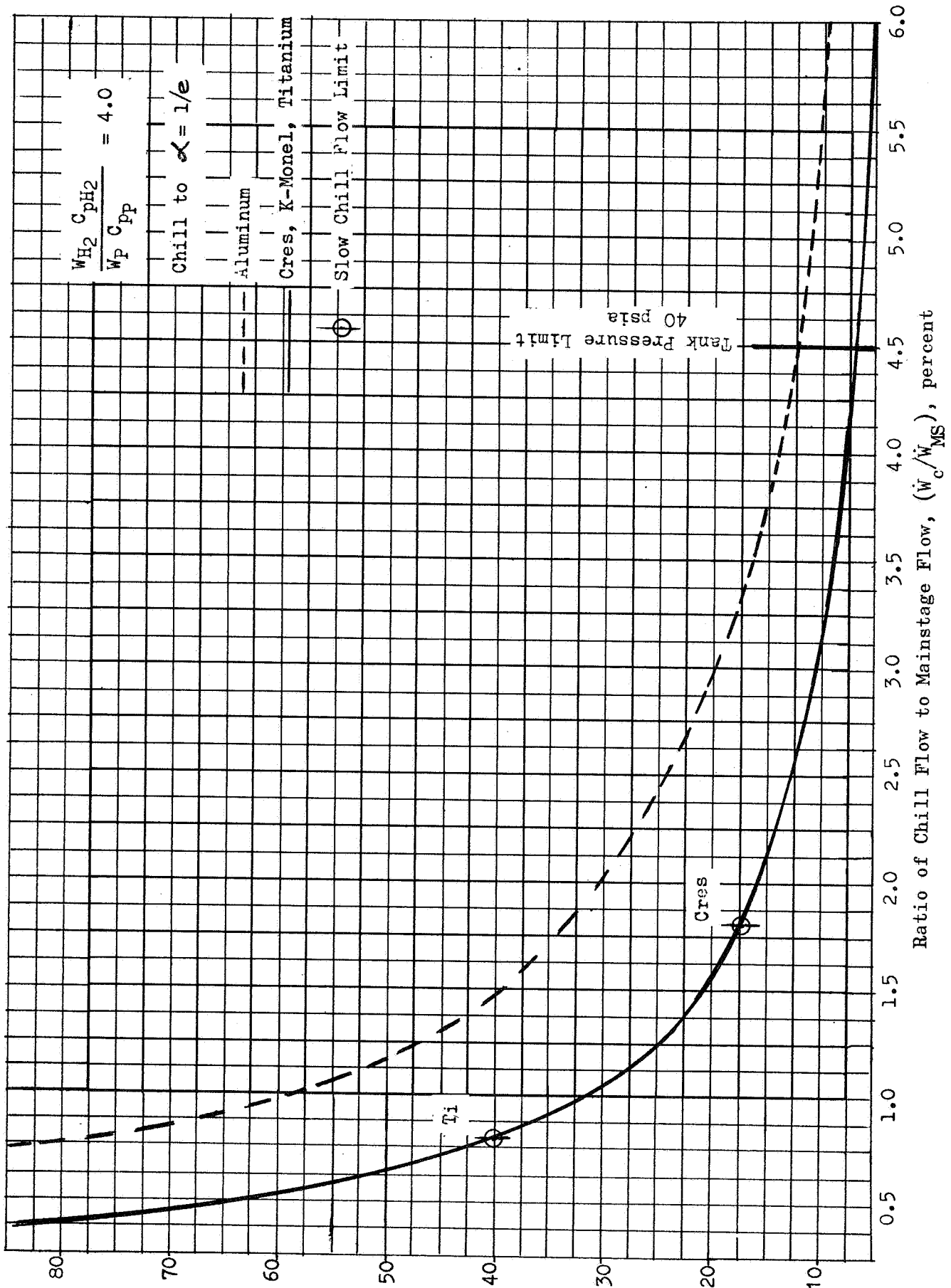


Figure 151. Limiting Chilldown Time vs Percent Mainstage Flowrate

## PUMP VAPOR TOLERANCE

Analysis of the pump vapor tolerance conditions was conducted under Task I study. Based on the criteria of a limiting 35-percent volume vapor ingestion by the pump, a solution of the equation derived for the relationship between heat transfer from the wall surfaces and coolant heat absorption is given by

$$\frac{A_s}{A_c} \bar{N}_{ST} = \frac{(T_{SAT} - T_i) + f\left(\frac{\lambda}{C_p}\right)}{(\bar{T}_w - T_{SAT})} \quad (140)$$

Solution for the allowable wetted wall surface temperature  $\bar{T}_w$  for typical J-2 pump conditions is shown in Fig. 152. Allowable wall temperature at start is shown to increase with start condition stagnation pressure. The decreased wetted surface area of the pump is shown to allow a proportionately less prechill prior to pump start. For proposed future designs for limited chill prior to start, the selection of configurations on these criteria is mandatory.

A comparison of flow areas throughout the J-2 engine system (Table 28) shows a limiting flow area condition existing in the pump inducer and staging locations. As a result the pump inlet is shown to provide the greatest flow area restriction within the feed system. Consequently both prechill time is increased and start behavior becomes extremely sensitive for obtaining liquid flow in the inducer and first staging sections of the pump.

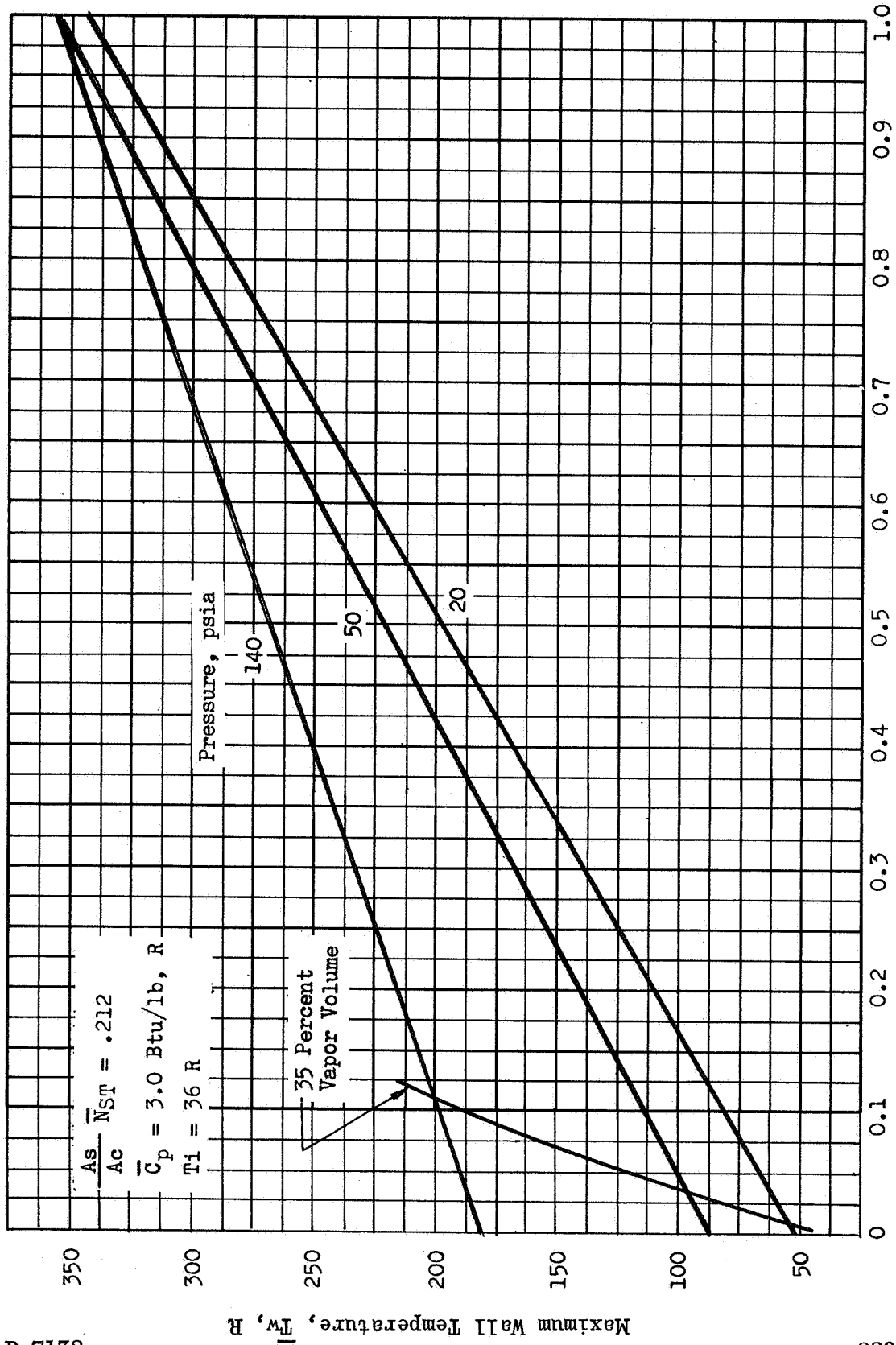


Figure 152.  $LH_2$  Pump Start Chilldown Temperature vs Allowable Vapor Fraction

TABLE 28

COMPARATIVE J-2 LH<sub>2</sub> FEED SYSTEM FLOW AREAS

Location	A <sub>c</sub> Flow Area, in. <sup>2</sup>	Mainstage G, lb/in. <sup>2</sup> -sec
Pump Inlet (MK 15)	41.2	1.87
Pump Inducer	4.96	15.6
Staging (Rotor)	4.45	17.3
Staging (Stator)	8.35	9.25
Volute Exit	12.5	6.17
Thrust Chamber Tube Inlet	13.4	5.76
Thrust Chamber Throat Tube	10.2	7.57
Thrust Chamber Tube Exit	19.1	4.04
Injector Orifice Area	25.8	3.0

## NOMENCLATURE

A	area
B	vapor-volume to liquid-volume ratio
C	perimeter
c	acoustic velocity
$C_f$	skin friction coefficient
$C_H$	Stanton coefficient
$C_I$	internal node capacitance
$C_L$	coefficient of lift
$C_m$	meridional velocity
$C_p$	specific heat ratio
$C_v$	void coefficient
D, d	hydraulic diameter, diameter, ductility, blade spacing
e	exponential
eff	effective
erf	error function
E	elastic modulus
F	shape factor for radiation, thrust, weight heat capacity ratio
f	function, friction factor
G	mass velocity
g	acceleration of gravity
H	enthalpy, head
h	film heat transfer coefficient, cavity height

I	indicates an internal node, dimensionless
i	initial
J	Joule constant (778 ft-lb/Btu)
$k_e$	cavitation number
K, k	conductivity
L, $l$	length
M	summation limit
M*	critical Mach number
m	exponent for velocity profile
N	thermal shock parameter, speed
n	distance normal to contour wall, number of blades
NPSH	net positive suction head
$N_{Bi}$	Biot number
$N_{Fo}$	Fourier number
$N_{Pr}$	Prandtl number
$N_{Re}$	Reynolds number
$N_{ST}$ , St	Stanton number
o	stagnation condition
P	pressure, pump
$P_d$	pump discharge pressure
Q	heat rate, internal heat generation rate, volume flowrate
Q/A	heat flux
R	gas constant, relative velocity ratio
r	radius

s entropy, blade surface length  
 S distance along contour wall, inches, surface  
 SAT saturation  
 $S_s$  suction specific speed  
 T temperature, thrust  
 t thickness, depth  
 $T_i$  temperature at node i, F  
 $T_j$  temperature at node j, F  
 $T_R$  Eckert reference temperature  
 $T_l$  fluid temperature, F  
 U local freestream velocity, tangential velocity of pump impeller  
 u velocity in boundary layer, internal energy  
 V vapor, velocity  
 W weight, flow velocity relative to impeller  
 $\dot{W}$  weight flowrate  
 w wall  
 WG wall gas side value  
 $W_o$  passage velocity  
 x distance, vapor fraction by weight  
 y radial distance of contour

**GREEK LETTERS**

$\alpha$  thermal diffusivity, temperature ratio, incidence angle  
 $\beta$  blade angle  
 $\beta^*$  cavitation parameter

$\Gamma$	vapor energy to liquid energy ratio
$\gamma$	specific heat ratio
$\delta$	pump heat content ratio, boundary layer thickness
$\delta^*$	displacement thickness
$\Delta$	differential
$\epsilon$	surface emissivity, wall roughness
$\xi$	hub-to-tip ratio
$\theta$	momentum thickness
$\lambda$	pump inlet hub-to-tip ratio
$\mu$	viscosity, Poisson's ratio
$\rho$	density
$\sigma$	Stephan Boltzmann constant
$\tau$	time, cavitation coefficient
$\phi$	temperature ratio, nondimensional resistance ratio, flow coefficient, energy thickness
$\phi_{IT}$	pump inlet flow coefficient at tip
$\psi$	nondimensional time parameter, head coefficient
$\Omega$	nondimensional time parameter
$\infty$	freestream condition

#### SUBSCRIPTS

$A_w$	adiabatic wall
$b$	bulk coolant
$c$	critical value, coolant, cross section, chord
$e$	earth
$f$	final

h	hub
H	hydrogen, hydraulic
i	initial, insulation
L	liquid
m	root mean square
o	orbit
P	pump
r	radiated
s	sink or source, surface
T, t	turbine, tip
v	vapor
w	wall
y	yield
1	inlet
2	discharge
$\infty$	freestream

## REFERENCES

1. Acosta, A. J., and L. B. Stripling, "Cavitation in Turbopumps," Journal of Basic Engineering, Trans. ASME, September 1952.
2. Apisa, J. N. et al., Development of Materials and Materials Application Concepts for Joint Use as Cryogenic Insulation and Micrometeoroid Bumpers, Proceed. of L.T.C.S. in Space, Huntsville, Alabama, October 1966.
3. Brentari, E. G. et al., Boiling Heat Transfer for Oxygen, Nitrogen, Hydrogen, and Helium, National Bureau of Standards TN 317, September 1965.
4. Bursik, W. J., Pseudo-Sonic Velocity and Pseudo-Mach Number Concepts in Two-Phase Flows, NSFC NASA TN D-3743, December 1966.
5. Campi, F. A. et al., Transient Two-Phase Heat Transfer and Flow Characteristics of Liquid Hydrogen, Westinghouse Astronuclear Laboratory Report, WANL-TNR-N2, April 1963.
6. Class, C. R., J. R. Deham, M. Piecone, and R. B. Cost, "Boiling Heat Transfer to Liquid Hydrogen From Flat Surfaces," Advances in Cryogenic Engineering, 5m p. 224-253 (1959).
7. Cody, J. C., and E. H. Hyde, Thermal Problems Associated With the Development of a Flight Configured Cryogenic Insulation System, Proceed. of L.T.C.S. in Space, Huntsville, Alabama, 1966, p. 67.
8. Compendium of the Properties of Materials at Low Temperature (Phase 1), WADD TR 60-56, Part II, Wright-Patterson AFB, Ohio, October 1960.
9. Corruccini, R. J. (NBS), "Temperature Measurements in Cryogenic Engineering," Advances in Cryogenic Engineering, Vol. 8, Plenum Press, N.Y., 1963.
10. CPR Technical Information Bulletin 314, CRP Division, Upjohn Company.
11. Data Obtained from P&VE MSFC, Huntsville, Alabama.
12. Design, Fabricate and Test Breadboard Liquid Hydrogen Pump Interim Report, PWA FR-1461, 30 July 1965, Section II.

13. Design, Fabricate and Test Breadboard Liquid Hydrogen Pump Interim Report, PWA FR-1937, 30 July 1966, Section II.
14. Dipprey, D., and R. Sabersky, Heat and Momentum Transfer in Smooth and Rough Tubes at Various Prandtl Numbers, Institute of Heat and Mass Transfer, 6, 1963.
15. Dorsey, J. W., and C. L. Kleder, Thermal Mass Penalties Associated With Cryogenic Storage on Manned Mars and Venus Missions, Proceed. of Long Term Cryo. Propellant Storage in Space, Huntsville, Alabama, October 1966.
16. Durham, T. F., R. M. McClintock, and R. P. Reed, Cryogenic Materials Data Handbook, Cryogenic Engineering Laboratory, Boulder, Colorado.
17. Eddington, R. B., Investigation of Shock Phenomena in a Supersonic Two-Phase Tunnel, AIAA Paper No. 66-87, Third Aerospace Sciences Meeting, New York, N.Y., January 1966.
18. Eldridge, E. A., and H. W. Deem, Physical Properties of Metals and Alloys From Cryogenic to Elevated Temperatures, ASTM No. 296, 1961.
19. Elliot, D. G., D. R. Bartz, and S. Silver, Calculations of Turbulent Boundary Layer Growth and Heat Transfer in Axisymmetric Nozzles, TR No. 32-387, Jet Propulsion Laboratory, California Institute of Technology, Pasadena, California.
20. General Dynamics, Liquid Hydrogen Suction Line Insulation Research and Development, NASA Contract NAS8-20167, GDC Report GDC-00866-07, July 1966.
21. Giedt, W. H., Principles of Engineering Heat Transfer, pp 293-311, Van Nostrand, New York, 1957.
22. Gouse, S. W., Jr., and G. A. Brown, A Survey of the Velocity of Sound in Two-Phase Mixtures, ASME Paper No. 64-WA/FE-35, Winter Annual Meeting, New York, 29 November-4 December 1964.
23. Handbook of Thermal Design Data for Multilayer Insulation System, Lockheed Missiles and Space Company Report IMSC-A742593-V1, Contract NAS8-11347, August 1965.

24. Hendricks, R. C., R. W. Graham, Y. Y. Hsu, and R. Friedman, Experimental Heat Transfer and Pressure Drop of Liquid Hydrogen Flowing Through a Heated Tube, NASA TN D-765, 1961.
25. Hummel, F. A., and C. A. Laren, Thermal Analyzer Program, International Letter 4114-131, Rocketdyne, 17 November 1964.
26. Interim T-S Diagram for Parahydrogen, NBS, Boulder, Colorado.
27. R-6199, Investigation of Cooling Problem at High Chamber Pressures, Final Report, Period July 1963 - May 1965, Contract NAS8-4011, Rocketdyne, a Division of North American Aviation, Inc., Canoga Park, California.
28. Jakobsen, J. K., "On the Mechanism of Head Breakdown in Cavitating Inducers," Journal of Basic Engineering, Volume 86, Series D, No. 2, June 1964, 291-305.
29. Karplus, H. B., Propagation of Pressure Waves in a Mixture of Water and Steam, ARF 4132-12, Armour Research Foundation, Illinois Institute of Technology, Chicago 16, Illinois, January 1961.
30. Launder, B., "An Improved Pohlhausen Type Method of Calculating the Two-Dimensional Laminar Boundary Layer With a Pressure Gradient," Trans. ASME Journal of Heat Transfer, August 1964.
31. Lindquist, C. R., and L. R. Niendorf, Experimental Performance in Model Liquid Hydrogen Space Tankage With Compressible Super Insulation, Bulletin F-1730, Union Carbide, Linde Division.
32. Liguori, R. R., and J. W. Stephenson, The Heating Program, ASTRA, Inc. Raleigh, North Carolina, January 1961.
33. Manson, L., and J. D. Seader, Study of Boiling Heat Transfer With LOX, LH<sub>2</sub>, and LN<sub>2</sub>, R-6259, Rocketdyne, a Division of North American Aviation, Inc., Canoga Park, California.
34. Matson, L. C., Advances in Multilayer Insulation, Bulletin F-1761, Union Carbide, Linde Division, 1961.

35. McCarthy, J. R., and H. Wolf, "Forced Convection Heat Transfer to Gaseous Hydrogen at High Heat Flux and High Pressure in a Smooth, Round, Electrically Heated Tube," ARS Journal, April 1960.
36. McCarthy, J. R., and H. Wolf, The Heat Transfer Characteristics of Gaseous Hydrogen and Helium, Rocketdyne RR 60-12, Rocketdyne, a Division of North American Aviation, Inc., Canoga Park, California, December 1960.
37. Mikesell, R. P., and R. B. Scott, "Heat Conduction Through Insulating Supports in Very Low Temperature Equipment," Journal of Research of the National Bureau of Standards, V 57, December 1956.
38. Moses, R. A., Physical and Thermodynamic Properties for Heat Transfer Analysis, Pub. 575-A-5, Lecture 2 of Advanced Heat Transfer Seminar, Rocketdyne, a Division of North American Aviation, Inc., Canoga Park, California, 1966.
39. Physical Properties of Metals and Alloys From Cryogenic to Elevated Temperatures, ASTM STP No. 296, American Society for Testing Materials, April 1961.
40. Powell, R. L., and L. P. Caywood (NBS), "Low Temperature Characteristics of Some Commercial Thermocouples," pp 517-521, in Advances in Cryogenic Engineering, Vol. 7, Plenum Press, N.Y., 1962.
41. Powell, W. B., Heat Transfer to Fluids in Region of the Critical Temperature, JPL, PR 20-285, April 1966.
42. Ritter, J. A., Summary of Observed Results When Chilling the M-1 Fuel Turbopump, NASA Contract NAS3-2555 Aerojet General Corporation, AGC 8800-65, June 1966.
43. Saucier, S. P., Investigation of the Instant Start Capabilities of the RL-10 Engine With Internally Insulated Fuel Pumps, R-P&VE-PA-65-M-702 memo, July 1965.
44. Seader, J. D., W. S. Miller, and L. A. Kalvinskis, Boiling Heat Transfer in Cryogenics, Rocketdyne, a Division of North American Aviation, Inc., Canoga Park, California, February 1964; also available as NASA CR-243, June 1965.

45. Schlichting, H., Boundary Layer Theory, 4th Edition, McGraw-Hill, New York, 1960.
46. Scott, R. B., Cryogenic Engineering, Chapter 5, Van Nostrand, Princeton, 1959.
47. Supercritical Pressure Liquid Hydrogen Heat Transfer Data Compilation, Rocketdyne, a Division of North American Aviation, Inc., Canoga Park, California, 21 April 1965.
48. Thermal Network Analyzer Program, Lockheed Aircraft Corporation, Missiles and Space Division, Sunnyvale, California, 28 April 1961.
49. R-6187, Thermal Protection of the J-2 Engine From S-II Stage In-Flight Heating, Rocketdyne, a Division of North American Aviation, Inc., Canoga Park, California, August 1965, Contract NAS8-19.
50. Verschoor, J. D., and J. Greebler, "Heat Transfer by Gas Conduction and Radiation in Fibrous Insulations," Transactions of the ASME, August 1952.
51. Wong, J., Multiple Layer Insulations, Bulletin F-1161, Union Carbide, Linde Division, 1961.
52. White, C. K., Experimental Techniques in Low-Temperature Physics, Oxford University Press, London, 1959.
53. Wolf, H., and J. R. McCarthy, Heat Transfer to Hydrogen and Helium With Wall to Fluid Temperature Ratios to 11.09, presented at the AIChE Annual Meeting, 4-7 December 1960, Washington, D.C.
54. Wood, W. D., and W. H. Deem, Thermal Properties of High Temperature Materials, Redstone Scientific Information Center, Redstone Arsenal, Alabama, June 1964.

APPENDIX A

DISTRIBUTION LIST FOR INTERIM REPORT

NAS8-20324

THERMODYNAMIC IMPROVEMENTS IN LIQUID HYDROGEN TURBOPUMPS

<u>COPIES</u>	<u>RECIPIENT</u>	<u>DESIGNEE</u>
	NASA Marshall Space Flight Center Huntsville, Alabama 35812	
2	Office of Technical Information , MS-IP	(X)
1	Technical Library	(X)
1	Purchasing Office, PR-SC	(X)
1	Patent Office, CCP	(X)
1	Keith Chandler, R-P&VE-PA	(X)
1	Technology Utilization Office, MS-T	(X)
2	H. Beduerftig (R-P&VE-P) (Technical Monitor)	(X)
4	Chief, Liquid Propulsion Technology, RPL Office of Advanced Research and Technology NASA Headquarters Washington, D. C. 20546	(X)
25	NASA Scientific and Technical Information Facility P.O. Box 38 College Park, Maryland 20740	(X)
1	Mr. Vincent L. Johnson Director, Launch Vehicles and Propulsion, SV Office of Space Science and Applications NASA Headquarters, Washington, D. C. 20546	(X)
1	Mr. Doug Lord Director, Advanced Manned Missions, MT Office of Manned Space Flight NASA Headquarters, Washington, D. C. 20546	(X)
1	Leonard Roberts Mission Analysis Division NASA Ames Research Center Moffett Field, California 24035	(X)

NASA FIELD CENTERS

<u>COPIES</u>	<u>RECIPIENT</u>	<u>DESIGNEE</u>
2	Ames Research Center Moffett Field, California 94035	H. J. Allen Mission Analysis Div.
2	Goddard Space Flight Center Greenbelt, Maryland 20771	Merland L. Moseson Code 620
2	Jet Propulsion Laboratory California Institute of Technology 4800 Oak Grove Drive Pasadena, California 91103	Henry Burlage, Jr. Propulsion Div., 38
2	Langley Research Center Langley Station Hampton, Virginia 23365	Dr. Floyd L. Thompson Director
2	Lewis Research Center 21000 Brookpark Road Cleveland, Ohio 44135	Dr. Abe Silverstein Director
2	Marshall Space Flight Center Huntsville, Alabama 35812	Hans G. Paul Code R-P&VE-P
2	Manned Spacecraft Center Houston, Texas 77001	Dr. Robert R. Gilruth Director
2	John F. Kennedy Space Center, NASA Cocoa Beach, Florida 32931	Dr. Kurt H. Debus

GOVERNMENT INSTALLATIONS

<u>COPIES</u>	<u>RECIPIENT</u>	<u>DESIGNEE</u>
1	Aeronautical Systems Division Air Force Systems Command Wright-Patterson Air Force Base Dayton, Ohio 45433	Dr. L. Schmidt Code ASRCNC-2
1	Air Force Missile Development Center Holloman Air Force Base, New Mexico	Maj. R. E. Bracken Code MDGRT
1	Air Force Missile Test Center Patrick Air Force Base, Florida	L. J. Ullian
1	Air Force Systems Division Air Force Unit Post Office Los Angeles 45, California	Col. Clark Tech. Data Center

<u>COPIES</u>	<u>RECIPIENT</u>	<u>DESIGNEE</u>
1	Arnold Engineering Development Center Arnold Air Force Station Tullahoma, Tennessee	Dr. H. K. Doetsch
1	Bureau of Naval Weapons Department of the Navy Washington 25, D. C.	J. Kay, Code RTMS-41
1	Defense Documentation Center Headquarters Cameron Station, Building 5 5010 Duke Street Alexandria, Virginia 22314 Attn: TISIA	
1	Headquarters, U. S. Air Force Washington 25, D. C.	Col. C. K. Stambaugh Code AFRST
1	Picatinny Arsenal Dover, New Jersey 07801	I. Forsten, Chief Liquid Propulsion Lab.
1	Air Force Rocket Propulsion Laboratory Research and Technology Division Air Force Systems Command Edwards, California 93523	RPRR
1	U. S. Atomic Energy Commission Technical Information Services Box 62 Oak Ridge, Tennessee	A. P. Huber Oak Ridge Gaseous Diffusion Plant (ORGDP) P. O. Box P
1	U. S. Army Missile Command Redstone Arsenal Alabama 35809	Dr. Walter Wharton
1	U. S. Naval Ordnance Test Station China Lake California 93557	Code 4562 Chief, Missile Propulsion Div.

INDUSTRY CONTRACTORS

1	Chemical Propulsion Information Agency Applied Physics Laboratory 8621 Georgia Avenue Silver Spring, Maryland 20910	Tom Reedy
1	Aerojet-General Corporation P. O. Box 296 Azusa, California	L. F. Kohrs

<u>COPIES</u>	<u>RECIPIENT</u>	<u>DESIGNEE</u>
1	Aerojet-General Corporation P. O. Box 1947 Technical Library, Bldg. 2015, Dept 2410 Sacramento, California 95809	R. Stiff
1	Aeronutronic Philco Corporation Ford Road Newport Beach, California	D. A. Carrison
1	Aerospace Corporation 2400 East El Segundo Boulevard P. O. Box 9508 Los Angeles, California 90045	Owen Dykma MS-2293 Propulsion Dept.
1	Arthur D. Little, Inc. 20 Acorn Park Cambridge 40, Massachusetts	E. Karl Bastress
1	Astropower Laboratory Douglas Aircraft Company 2121 Paularino Newport Beach, California 92663	Dr. Goerge Moc Director, Research
1	Astrosystems International, Inc. 1275 Bloomfield Avenue Caldwell Township, New Jersey	
1	Atlantic Research Corporation Edsall Road and Shirley Highway Alexandria, Virginia 22314	R. Friedman
1	Beech Aircraft Corporation Boulder Facility Box 631 Boulder, Colorado	J. H. Rodgers
1	Bell Aerosystems Company P. O. Box 1 Buffalo 5, New York	Dr. Kurt Berman
1	Bendix Systems Division Bendix Corporation, 3300 Plymouth Rd. Ann Arbor, Michigan	John M. Brueger
1	Boeing Company P. O. Box 3707 Seattle 24, Washington	J. D. Alexander

<u>COPIES</u>	<u>RECIPIENT</u>	<u>DESIGNEE</u>
1	Missile Division Chrysler Corporation P. O. Box 2628 Detroit, Michigan 48231	John Gates
1	Wright Aeronautical Division Curtiss-Wright Corporation Wood-ridge, New Jersey 07075	G. Kelley
1	Missile and Space Systems Division Douglas Aircraft Company, Inc. 3000 Ocean Park Boulevard Santa Monica, California 90406	R. W. Hallet Chief Engineer Advanced Space Tech.
1	Aircraft Missiles Division Fairchild Hiller Corporation Hagerstown, Maryland 10	J. S. Kerr
1	General Dynamics/Astronautics Library & Information Services (128-00) P. O. Box 1128 San Diego, California 92112	Frank Dore
1	Re-Entry Systems Department General Electric Company 3198 Chestnut St. Philadelphia, Pennsylvania 19101	F. E. Schultz
1	Advanced Engine & Technology Dept. General Electric Company Cincinnati, Ohio 45215	D. Suichu
1	Grumman Aircraft Engineering Corp. Bethpage Long Island, New York	Joseph Gavin
1	Aerospace Operations Walter Kidde and Company, Inc. 567 Main Street Belleville, New Jersey 07109	R. J. Hanville Director of Research Engineering
1	Ling-Temco-Vought Corp. Astronautics P. O. Box 5907 Dallas, Texas 75222	Warren C. Trent

<u>COPIES</u>	<u>RECIPIENT</u>	<u>DESIGNEE</u>
1	Lockheed California Company 2555 N. Hollywood Way Burbank, California 91503	G. D. Brewer
1	Lockheed Missiles and Space Company Attn: Technical Information Center P. O. Box 504 Sunnyvale, California	Y. C. Lee
1	Lockheed Propulsion Company P. O. Box 111 Redlands, California 92374	H. L. Thackwell
1	The Marquardt Corporation 16555 Saticoy Street Van Nuys, California 91409	Warren P. Boardman, Jr.
1	Baltimore Division Martin Marietta Corporation Baltimore, Maryland 21203	John Calathes (3214)
1	Denver Division Martin Marietta Corporation P. O. Box 179 Denver, Colorado 80201	J. D. Goodlette (A-241)
1	McDonnell Aircraft Corporation P. O. Box 516/Municipal Airport St. Louis, Missouri 63166	R. A. Herzmark
1	Space & Information Sytems Division North American Rockwell Corp. 12214 Lakewood Blvd. Downey, California 90241	D. Simkin
1	Northrop Space Laboratories 3401 West Broadway Hawthorne, California	Dr. William Howard
1	Florida Research and Development Center Pratt & Whitney Aircraft United Aircraft Corporation P. O. Box 2691 West Palm Beach, Florida 33402	R. J. Coar
1	Astro-Electronics Division Radio Corporation of America Princeton, New Jersey 08540	S. Fairweather

<u>COPIES</u>	<u>RECIPIENT</u>	<u>DESIGNEE</u>
1	Rocket Research Corporation 520 South Portland Street Seattle, Washington 98108	Foy McCullough, Jr.
1	Reaction Motors Division Thiokol Chemical Corporation Denville, New Jersey 07832	Arthur Sherman
1	Republic Aviation Corporation Farmingdale Long Island, New York	Dr. William O'Donnell
1	Rocketdyne (Library, Dept. 586-306) Division of North American Rockwell Corp. 6633 Canoga Avenue Canoga Park, California 91304	E. B. Monteath
1	Space General Corporation 9200 Flair Avenue El Monte, California 91734	C. E. Roth
1	TRW Systems Group TRW Incorporated One Space Park Redondo Beach, California 90278	G. W. Elverum
1	Stanford Research Institute 333 Ravenswood Avenue Menlo Park, California 94025	G. Marxman
1	TAPCO Division TRW, Incorporated 23555 Euclid Avenue Cleveland, Ohio 44117	P. T. Angell
1	Thiokol Chemical Corporation Huntsville Division Huntsville, Alabama	John Goodloe
1	Research Laboratories United Aircraft Corporation 400 Main Street East Hartford, Connecticut 06108	Erle Martin
1	United Technology Center 587 Methilda Avenue P. O. Box 358 Sunnyvale, California 94088	B. Abelman

Security Classification

## DOCUMENT CONTROL DATA - R &amp; D

(Security classification of title, body of abstract and indexing annotation must be entered when the overall report is classified)

1. ORIGINATING ACTIVITY (Corporate author) Rocketdyne, a Division of North American Rockwell Corporation, 6633 Canoga Avenue, Canoga Park, California 91304		2a. REPORT SECURITY CLASSIFICATION UNCLASSIFIED	
		2b. GROUP	
3. REPORT TITLE  THERMODYNAMIC IMPROVEMENTS IN LIQUID HYDROGEN TURBOPUMPS			
4. DESCRIPTIVE NOTES (Type of report and inclusive dates) Interim Report			
5. AUTHOR(S) (First name, middle initial, last name)  Rocketdyne Engineering			
6. REPORT DATE 22 March 1968	7a. TOTAL NO. OF PAGES 327	7b. NO. OF REFS 54	
8a. CONTRACT OR GRANT NO. NAS8-20324	9a. ORIGINATOR'S REPORT NUMBER(S)  R-7138		
b. PROJECT NO.	9b. OTHER REPORT NO(S) (Any other numbers that may be assigned this report)		
c.			
d.			
10. DISTRIBUTION STATEMENT			
11. SUPPLEMENTARY NOTES		12. SPONSORING MILITARY ACTIVITY	
13. ABSTRACT  Analytical and experimental results are presented of an investigation to develop engineering criteria to analyze and improve liquid hydrogen turbopumps for rocket engine applications from the standpoint of alleviating the constraints of extensive pump thermal preconditioning and a narrow starting region envelope.			

14. KEY WORDS	LINK A		LINK B		LINK C	
	ROLE	WT	ROLE	WT	ROLE	WT
Pump Thermal Design						
Material						
Preconditioning						
Thermal Protection						
Existing LH <sub>2</sub> Pumps, Study of						
Heat Transfer Coefficients						
Chiltdown						
Insulation						
Thermal Equilibrium						
Pump Characterization						